INFLUENCE OF THICKNESS ON SOME PHYSICAL CHARACTERIZATION FOR NANOSTRUCTURED MgO THIN FILMS†

Muhammad H. Al-Timimi[a],*, Widad H. Albanda[b], Mustafa Z. Abdullah[c]

[a]Department of Physics, College of Science, University of Diyala, Iraq
[b]Science Department - College of Basic Education, Mustansiriyah University, Iraq
[c]Materials Research Directorate, Ministry of science and technology, Iraq
*Corresponding Author e-mail: muhammadtimimi@yahoo.com

MgO Nanostructured thin films with different thicknesses (200, 400, and 600 nm) have been deposited by the chemical spray pyrolysis technique. The results confirm that the structure, morphology, optical, and electrical properties were all affected by the thickness of the film. MgO films' physical properties were examined using (XRD), (FE-SEM), (EDX), (AFM), (UV-Vis spectrophotometer), and the Hall Effect. According to the structural analysis, the films have a cubic magnesium oxide polycrystalline structure, with a preferred orientation (002). The average Crystalline Size and optical band gap are found in the range (20.79-18.99) nm and (3.439-3.162) eV respectively with an increase in thickness. The surface morphology of the films reveals that they are free of crystal defects such as holes and voids, as well as homogeneous and uniform. The EDS patterns show that the as-grown films contain magnesium and oxygen. The Hall Effect shows that electrical conductivity decreases with thickness. The experimental results show that film thickness influences the physical properties of as-grown MgO thin films and that thicker films can be used as an absorber layer in solar cell applications.

Keywords: *MgO films; Chemical spray pyrolysis; Effect of thickness; Structure; Optical and electrical properties*
PACS: 73.20.At, 78.20._e, 77.55._f

1. INTRODUCTION

Magnesium oxide, which has good electronic, optical, magnetic, electrical, thermodynamic, and mechanical properties, is one of the most intriguing and promising materials in the family of metal oxides [1,2]. MgO is a scientific and industrial substance. It is a crystalline highly ionic insulator that is stable at high temperatures. Magnesium oxide thin films have drawn a lot of interest because of their numerous applications. Because of their high transparency, good protection qualities against ion bombardment, and high durability, they're commonly used as a protective layer for AC-plasma display panels [3,4]. MgO also has a wide band gap and a low refractive index, allowing it to be used in a variety of ferroelectric superconducting and ferroelectric thin film materials and buffer layers, as well as interlayers in the structure of magnetic memory device [5,6,7,8,9]. MgO thin films have also been used as buffer layers for superconducting and ferroelectric thin films as well as interlayers with a magnetic memory device structure. MgO has a wide range of applications, including adsorption, reflecting and antireflecting coatings, electronics, fire retardants, ceramics, catalysis, chemical, toxic waste management [10,11], solar cells, laser diodes, and many other high-tech applications [12,13]. Many researchers prepared magnesium oxide films using physical and chemical methods according to the specific application of each method, such as chemical spray pyrolysis [14], electron-beam [15], Pulsed laser [16], Sol-gel [17], chemical vapor [18], and spin coating [19], etc. In the present work, we have tried to study the effect of thickness on Some Physical Characterization of Nanostructured MgO Films on glass substrates by the chemical spray pyrolysis technique.

2. EXPERIMENTAL PROCEDURES

(MgO) thin films with different thicknesses (200, 400, 600) nm were a fabrication by utilizing the chemical spray pyrolysis technique, The magnesium chloride $MgCl_2 \cdot 6H_2O$ solution was prepared by dissolving it in deionized water while stirring continuously. The substrates (glass) were thoroughly cleaned with ultrasonic and then washed with distilled water and acetone. As the carrier gas, the air was used, and the solution was sprayed onto a heated substrate using a nozzle. The nozzle's diameter was 0.3 mm. The nozzle was (30 cm) away from the heated substrate surface, and the (1.5 bar) compressor and different thicknesses were obtained by changing the number of sprays in each experiment.

X-ray diffraction was used to determine the structural properties, field emission scanning electron microscopy and atomic force microscopy were used to investigate the morphology of the thin films, a (UV-Vis) spectrophotometer was used to measure the optical properties, and Hall effect measurement was used to determine the electrical properties.

3. RESULTS AND DISCUSSION
3.1. Structural and Morphological Characteristics

The XRD exam was carried out to investigate the crystal structure type of magnesium oxide MgO films. Figure 1. shows the XRD patterns of MgO films deposited at different thicknesses (200, 400, and 600 nm) respectively. The

---

detected characteristic peaks at ($2\Theta= 36.88^\circ$, 42.85°, 62.21° and 78.51°) of planes (111) (002) (022) and (222) attributed to the cubic magnesium oxide with space group (Fm-3m no. 225) [20,21], with (a=b=c= 4.2170 A°) and ($\alpha=\beta= 90^\circ$), And matching it with the standard data (JCPDS 98-000-9863) [22]. The results revealed that with the increase of MgO film thickness at (400 and 600 nm); the characteristic peaks of MgO became sharper and more intense [23].
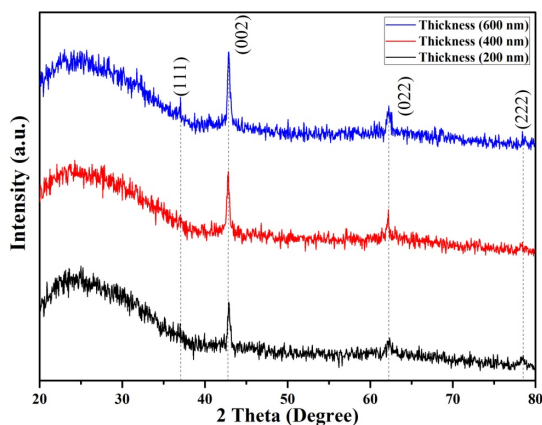

Figure 1. XRD of MgO films at Different Thicknesses.

The XRD Parameters of synthesized MgO nanoparticles was determined by Scherrer's equation at different thicknesses (200, 400, and 600 nm) to be (20.79, 19.83, and 18.99 nm) of the MgO nanoparticles respectively [24,25], the crystalline size of a film decreases with increasing thickness. This is because as the thickness of the film increases, the number of grain boundaries in the film increases, which reduces the average grain size [26, 27], this is because the surface energy of the particle increases with decreasing size, which causes the lattice parameter to contract. The magnitude of this contraction depends on the material and its surface energy [28]. Table (1) presents all synthesized MgO films' obtained parameters from the XRD.

Table 1. XRD Parameters of MgO Films at Different Thickness

Thickness (nm)	2Θ Experimental	2Θ Standard	FWHM (deg)	Crystalline Size (nm)	d_{hkl} (Å) Experimental	d_{hkl} (Å) Standard	(hkl)
200	42.81	42.85	0.3557	20.79	2.1106	2.1085	(002)
400	42.91	42.85	0.3728	19.83	2.1059	2.1085	(002)
600	42.89	42.85	0.3892	18.99	2.1069	2.1085	(002)

The morphology of MgO film surfaces was investigated using (FE-SEM), which provides high-resolution and magnification images of the surfaces. We observe that the surface structures of the prepared films are highly agglomerated aggregates of dense quasi-spherical nanoparticles. and clearly show the voids, nonuniform particle sizes, and irregular shapes in the MgO films. This is consistent with Boo J. H. et al. and Bian, J. M. et al. [29,30], As in Figure (2). The thickness of MgO sheets has a significant impact on particle size. In theory, the atoms diffuse into MgO and arrange themselves into larger particle sizes following deposition for various periods. When the thickness of MgO thin films is raised, small particles coalesce with one another, The recrystallization of particles caused by the increase in thickness encourages the reorientation of the overall microstructure [31,32].
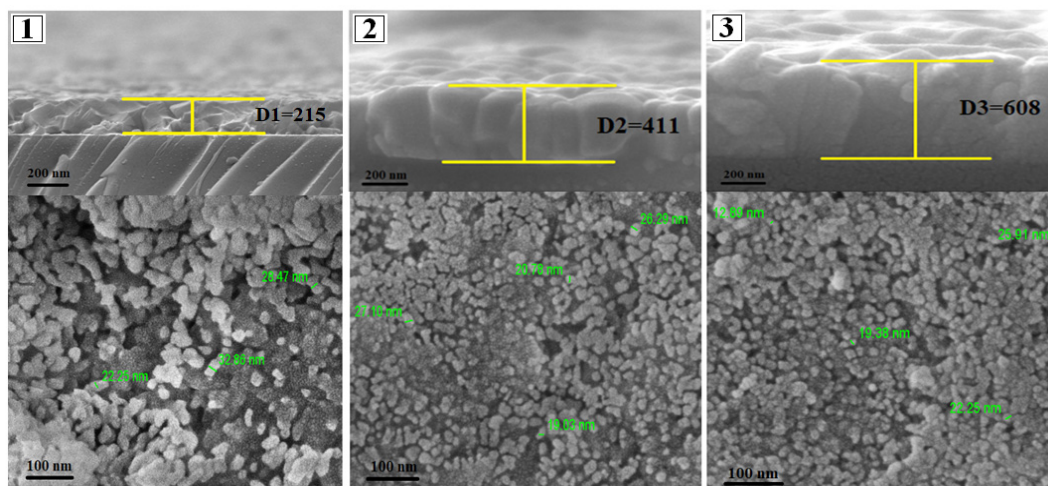

Figure 2. (FE-SEM) of MgO and the cross-section at Different Thicknesses

The Energy Dispersion X-ray Analysis (EDX) in Fig. (3) shows the presence of only the Mg and O. As shown in Table 2. The Mg: O atomic ratio is equal to 0.767 : 1 for sample 1 (200nm), 0.707 : 1 for sample 2 (400nm), and 0.648 : 1 for sample 3 (600nm).
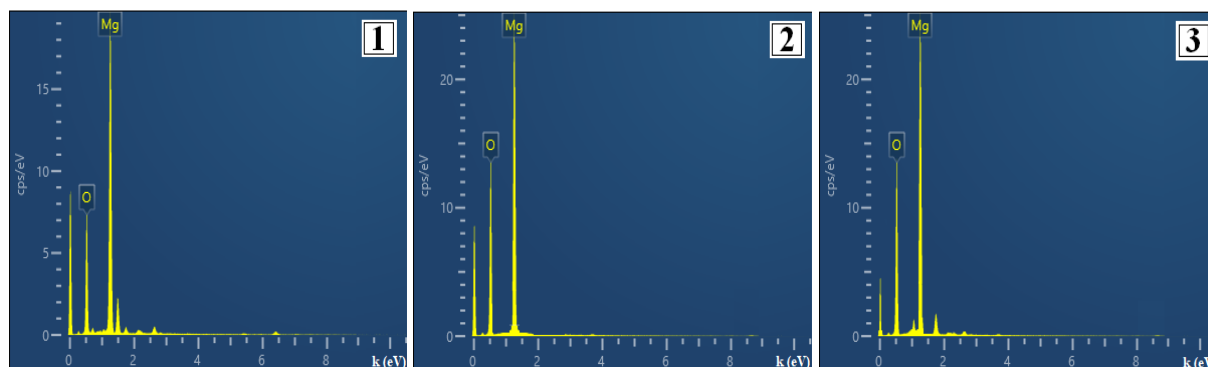

Figure 3. EDX of MgO films at Different Thicknesses

Table 2. The Ratios of the Elements of MgO from EDX

Element	200 nm		400 nm		600 nm	
	Weight %	Atomic %	Weight %	Atomic %	Weight %	Atomic %
Mg	53.84	43.43	52.16	41.45	50.42	39.33
O	46.16	56.57	48.84	58.55	49.58	60.67
Total	100	100	100	100	100	100

To recognize the surface characteristics and particle size distribution of prepared films in the current study, The AFM is presented in Fig. (4) and Table 3.
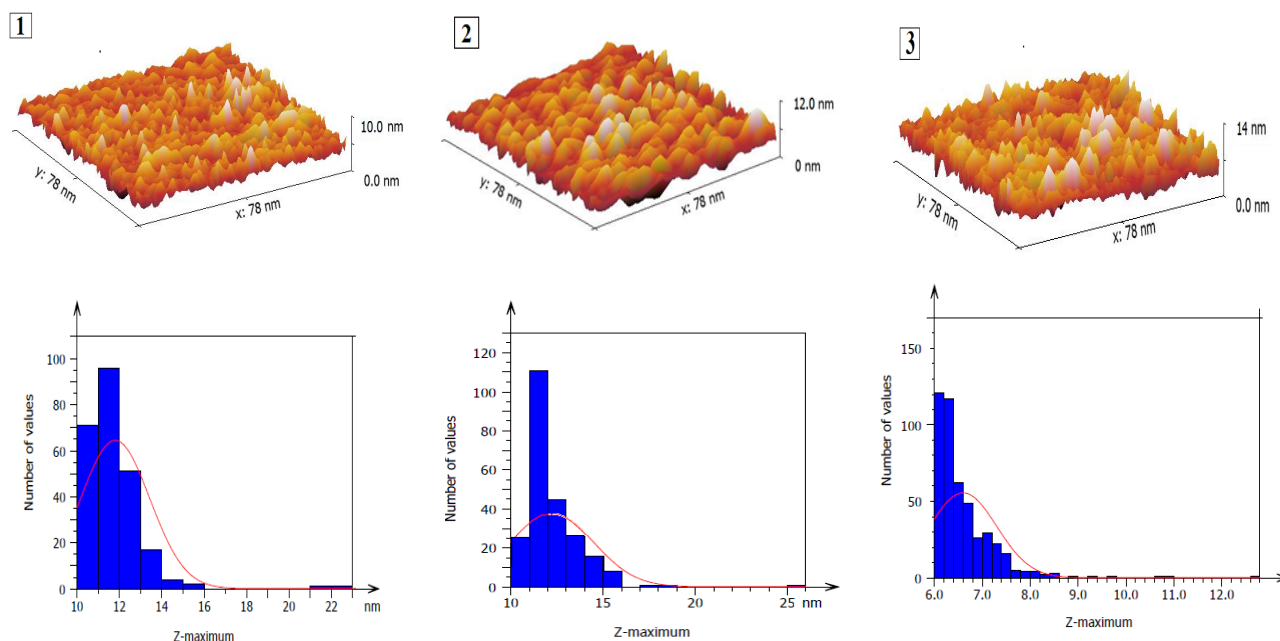

Figure 4. AFM images of MgO at different thicknesses

Table 3. Roughness and RMS of MgO Films at Different Thicknesses.

Thickness (nm)	Roughness Average Sa (nm)	RMS (nm)	Particles Size (nm)	Surface Skewness (RsK) (nm)	Surface Kurtosis (Rku) (nm)	Maximum Height Sz(nm)
200	4.541	5.139	10.970	0.138	1.884	24.77
400	4.231	5.423	10.231	0.327	3.884	27.99
600	3.194	3.833	9.191	0.580	2.493	35.41

The particle size grows with the thickness of the film and it was discovered to be uniformly distributed. Many nucleation centers form on the substrate when deposition begins, resulting in the formation of small crystallites. Because the films are only deposited for a short period of time, the small crystallites on the substrate cannot grow into large crystallites, and thus the thinner films have smaller crystallites than the thicker films [33]. The crystallinity of the

films is related to the surface roughness, which can be improved by increasing the film thickness. The larger crystallite size and higher crystallinity of the films can lead to better electrical and optical properties. The surface roughness of MgO films increases with increasing film thickness, which is due to the increased number of grain boundaries and defects in the film. This can lead to increased scattering of light, resulting in a decrease in optical transmittance [34]. The crystallinity of the films improved as the film thickness increased, and the surface roughness of MgO films increased [35], as shown in Fig. 5, This result is consistent with the thickness XRD observation.
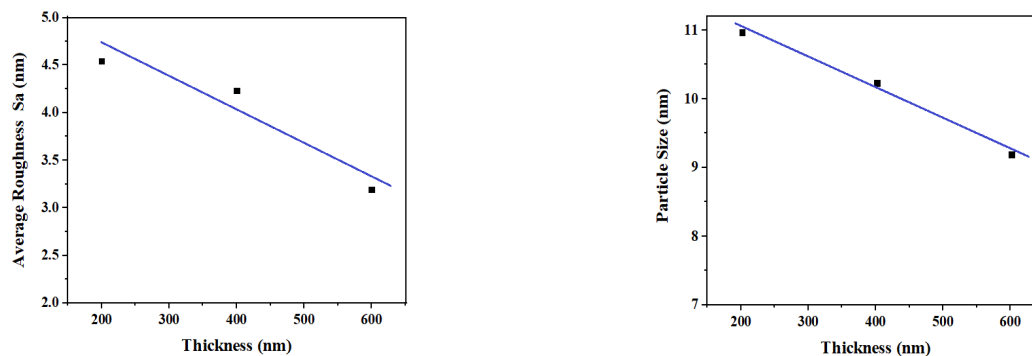

Figure 5. Average roughness and particle size with a thickness of MgO films

3.2. Optical Properties

When different thicknesses of MgO films are used during the preparation method, the optical behavior of MgO films will change dramatically as a result of the new structural and morphological features. Increasing the thickness of a material will generally decrease its optical transmittance. This is because thicker materials absorb more light, reducing the amount of light that can pass through. Additionally, thicker materials are more likely to scatter light, further reducing the amount of light that can pass through [36]. The MgO films' transmittance and reflectance spectra are shown Fig. (6).
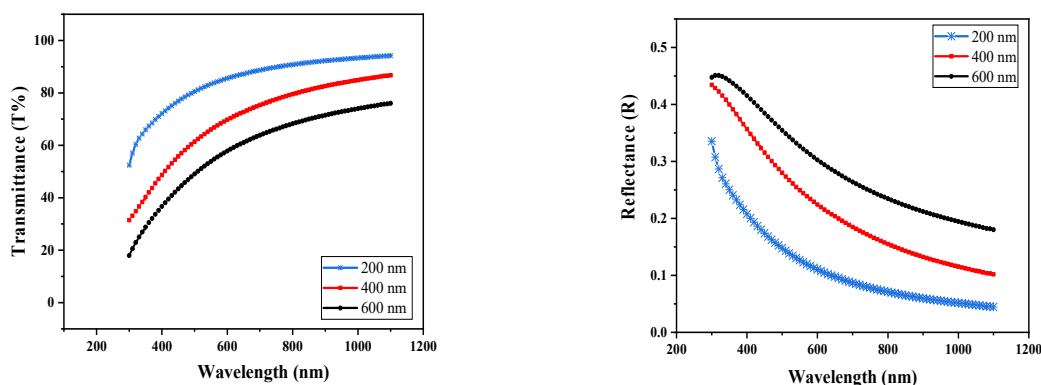

Figure 6. Transmittance and Reflectance of MgO films

In the visible range, MgO thin films have high transmittance values. It can be used in solar cell devices as an optical window. In general, the decrease in (T%) could be attributed to scattering effects, crystalline structure, and surface homogeneity, as reported by [37,38]. Transmittance is a measure of how much light passes through a material. The optical energy gap determines how much light can be transmitted through a material, as materials with larger gaps tend to have higher transmittance values [39]. Reflectance is a measure of how much light is reflected off a surface, while transmittance is a measure of how much light passes through a material. The optical energy gap affects both reflectivity and transmittance, as materials with larger gaps tend to reflect more light and transmit less [40,41].

The absorption coefficients (α) of MgO films were calculated using the Lambert equation (1) [42]:

$$\alpha = \ln\left(\frac{1}{T}\right)/d. \tag{1}$$

where: (T) the transmittance, (d) film thickness.

Figure (7) shows the calculated absorption coefficient of MgO films. The highest absorption coefficient was obtained for the films prepared with higher thickness than those prepared with less thickness.

The energy gap and particle size of the material are both affected by variations in thickness. As the thickness of a material increases, the energy gap typically decreases, while the particle size increases. This is because thicker materials have more electrons and therefore a larger number of states available for electrons to occupy. This reduces the energy gap between the highest occupied molecular orbital and the lowest unoccupied molecular orbital, resulting in a decrease

in the energy gap [43,44]. The increased number of electrons also leads to an increase in particle size, as larger particles are needed to accommodate all of the electrons [45]. The following equation can be used to calculate the energy gap for the as-prepared films [46]:

$$\alpha h\upsilon = A(h\upsilon - E_g)^n. \qquad (2)$$

(A) : constant, $h\upsilon$: energy of the photon, n is determined by the nature of the transition. The value was (1/2) in this case (a direct band transition).
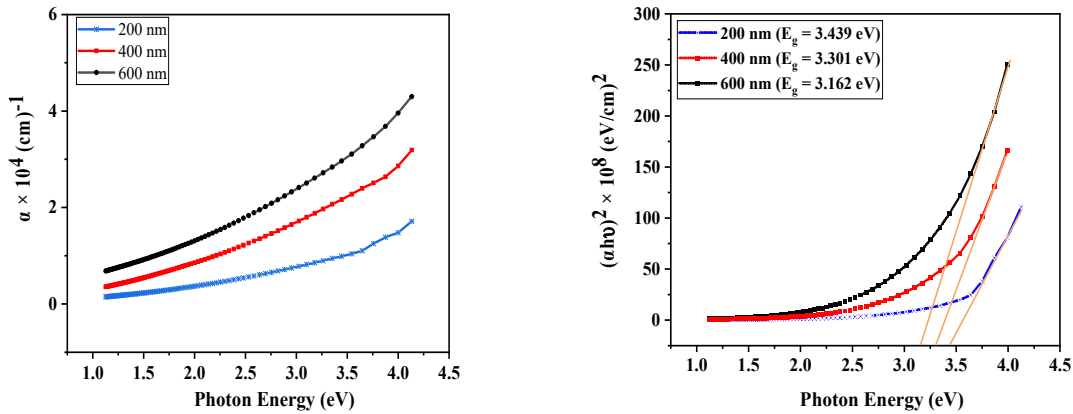

Figure 7. The Absorption coefficient and Energy gap of MgO films

The optical transmittance value is determined by the film's refractive index (no), which is influenced by the thickness of the film. As the thickness of the film increases, the refractive index increases, and the optical transmittance decreases. This leads to a decrease in the Eg value [47]. It is evident that when thickness grows, the Value of Eg rises. The Eg values are comparable to those that Płóciennik, P. et al. [48], and Tamboli, Sikandar H., et al. [49].

The higher the refractive index, the lighter is reflected off a surface, The refractive index (no) is related with reflectance (R) by the relation [50]:

$$n_o = \left[\frac{(1+R)^2}{(1-R)^2} - (k_o^2 - 1)\right]^{\frac{1}{2}} + \frac{(1+R)}{(1-R)} \qquad (3)$$

The refractive index behaves very similarly to reflectance. Figure (8) shows the correlation between refractive index (n_o) and photon energy for MgO films. the refractive index increases with thickness. The equation (4) can be used to calculate the extinction coefficient (ko) [51]:

$$k_o = \frac{\alpha\lambda}{4\pi} \qquad (4)$$

(k_o) extinction coefficient.

$$\varepsilon_r = n_\circ^2 - k_\circ^2 \qquad (5)$$

$$\varepsilon_i = 2n_\circ k_\circ \qquad (6)$$

Figure (8) shows the refractive index and extinction coefficient of MgO films.
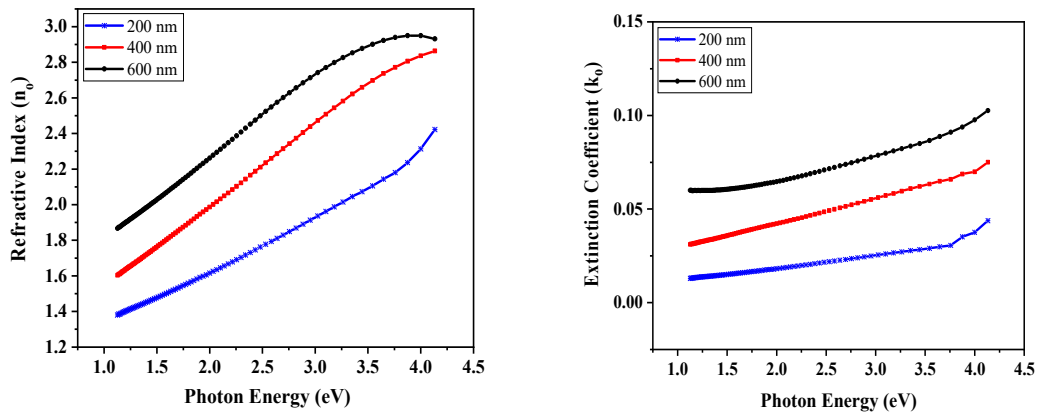

Figure 8. Refractive index and Extinction Coefficient of MgO films

The dielectric constant can be expressed as a complex number, with both real and imaginary parts. The real part of the dielectric constant represents the ability of the material to store energy, while the imaginary part represents losses

due to absorption and other effects. The behavior of the real dielectric constant is associated with the refractive index and the imaginary dielectric constant with the extinction coefficient with the equation (5) and (6) [52,53], as shown in Figure (9). Table 4 shows the optical properties of MgO films at different thicknesses (200, 400, and 600 nm).
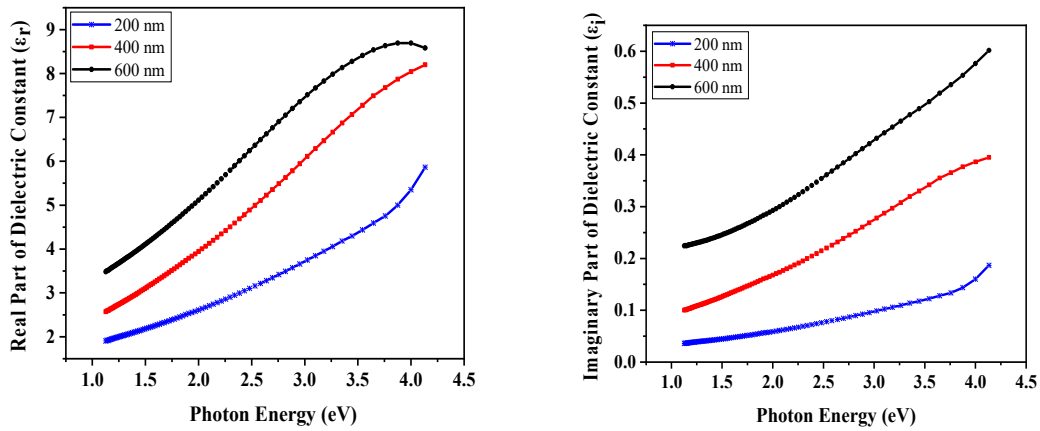

Figure 9. The real and imaginary part of the dielectric constant of MgO films

Table 4. Optical Properties of MgO Films at Different Thicknesses

Thickness (nm)	Eg (eV)	($\alpha \times 10^4$ cm^{-1}) Maximum	(n_o) Maximum	(k_o) Maximum	(E_r) Maximum	(E_i) Maximum
200	3.439	1.7076	2.4241	0.0442	5.8652	0.1888
400	3.301	3.1893	2.8586	0.0742	8.1553	0.3921
600	3.162	4.3024	2.9451	0.1092	8.7144	0.6001

3.3. Electrical Properties

Hall coefficient is a measure of the strength of a material's response to an applied magnetic field [54]. The Hall coefficient can be affected by the thickness of thin films, as thinner films tend to have higher Hall coefficients due to their increased surface area and reduced number of charge carriers [55], As the thickness of the film increases, the electrical resistance increases. This is because as the thickness of the film increases, there are more atoms and molecules in the material that can impede the flow of electrons. The increase in resistance is due to an increase in collisions between electrons and atoms or molecules in the material [56]. As shown in Table 5. Additionally, as the thickness of a thin film increases, its capacitance also increases. This is because as the thickness of a thin film increases, its surface area also increases, which allows for more charge to be stored on its surface, and the decrease in mobility can be attributed to an increase in dislocation density and lattice strain [45], as shown in Fig (10).

Table 5. Electrical Properties of MgO films at Different Thicknesses

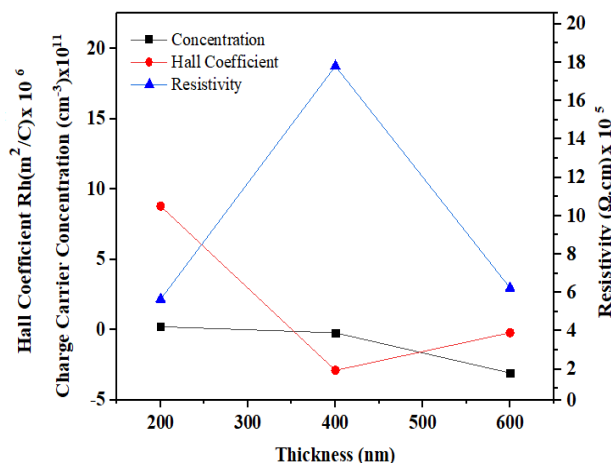| Thickness (nm)	Concentration (cm)$^{-3}$	Hall Coefficient Rh(m^2/C)	Conductivity ($\Omega \cdot$cm)$^{-1}$	Resistivity ($\Omega \cdot$cm)	Mobility (cm^2/v$\cdot$s)
200	0.2244×10^{11}	8.792×10^6	4.590×10^{-6}	2.178×10^5	1.276×10^1
400	-0.2163×10^{11}	-2.886×10^6	5.337×10^{-7}	1.874×10^6	1.54
600	-3.069×10^{11}	-2.034×10^7	3.369×10^{-6}	2.968×10^5	6.852×10^1

Figure 10. Electrical Properties of MgO films at Different Thicknesses

4. CONCLUSIONS

The thickness of the transparent MgO films prepared by chemical spray pyrolysis can be controlled by varying the deposition time. The films are composed of nanocrystalline grains with a size range from 10 to 50 nm, also The films exhibit good adhesion to the glasses substrate and The rate of roughness decreases with increasing the thickness of the film, The crystallite size decreases with increasing the thickness of the thin film, In the visible region, MgO films exhibit high transmittance with values up to 80%, The refractive index of the films increases with increasing film thickness, The films also exhibit low reflectance in the visible region, The energy gap (Eg) of the films increases with increasing film thickness, indicating that they can be used as optical coatings (color filters), and optical absorbers for applications such as photodetectors or solar cells. The electrical resistivity of MgO films decreases with increasing film thickness, indicating that they can be used as conductive layers for electronic devices such as transistors.

ORCID IDs

Muhammad H. Al-Timimi, https://orcid.org/0000-0002-9828-6945; **Widad H. Albanda**, https://orcid.org/0000-0002-3214-395X
Mustafa Z. Abdullah, https://orcid.org/0000-0002-4087-7830

REFERENCES

[1] B. Aspe, X. Castel, V. Demange, D. Passerieux, M.A. Pinault-Thaury, F. Jomard, S. Députier, et al. "Enhanced tunability and temperature-dependent dielectric characteristics at microwaves of K0. 5Na0. 5NbO3 thin films epitaxially grown on (100) MgO substrates," Journal of Alloys and Compounds, **856**, 158138 (2021). https://doi.org/10.1016/j.jallcom.2020.158138

[2] M. Tlili, C. Nefzi, B. Alhalaili, C. Bouzidi, L. Ajili, N. Jebbari, R. Vidu, and N.T. Kamoun, "Synthesis and characterization of MgO thin films obtained by spray technique for optoelectronic applications", Nanomaterials, **11**(11), 3076 (2021). https://doi.org/10.3390/nano11113076

[3] E.H. Choi, H.J. Oh, Y.G. Kim, J.J. Ko, J.Y. Lim, J.G. Kim, D.-I. Kim et al., "Measurement of secondary electron emission coefficient (γ) of MgO protective layer with various crystallinities." Japanese journal of applied physics, **37**, 7015 (1998). https://doi.org/10.1143/JJAP.37.7015

[4] M. Gross, A. Winnacker, and P.J. Wellmann, "Electrical, optical and morphological properties of nanoparticle indium-tin-oxide layers," Thin Solid Films, **515**(24), 8567-8572 (2007). https://doi.org/10.1016/j.tsf.2007.03.136

[5] M.L. Kantam, K. Mahendar, and S. Bhargava, "One-pot, three-component synthesis of highly substituted pyridines and 1, 4-dihydropyridines by using nanocrystalline magnesium oxide," Journal of Chemical Sciences, **122**(1), 63-69 (2010). https://www.ias.ac.in/article/fulltext/jcsc/122/01/0063-0069

[6] B.M. Choudary, R.S. Mulukutla, and K.J. Klabunde, "Benzylation of aromatic compounds with different crystallites of MgO," Journal of the American chemical Society, **125**(8), 2020-2021 (2003). https://doi.org/10.1021/ja0211757

[7] H.M. Hussein, and M.H. Al-Timimi, "Preparation and Study Some Physical Properties of (CMC/PAA: MgO) Nano Composites," Eurasian J. Phys. Chem. Math. **8**, 47-55 (2022). https://www.geniusjournals.org/index.php/ejpcm/article/view/1944

[8] S.S. Chiad, N.F. Habubi, W.H. Abass, and M.H. Abdul-Allah, "Effect of thickness on the optical and dispersion parameters of Cd0.4Se0.6 thin films," Journal of Optoelectronics and Advanced Materials, **18**(9-10), 822-826 (2016).

[9] H.S. Kim, S.M. George, B.K. Park, S.U. Son, C.G. Kim, and T.M. Chung, "New heteroleptic magnesium complexes for MgO thin film application," Dalton Transactions, **44**, 2103-2109 (2015). https://doi.org/10.1039/C4DT03497J

[10] A.O. Mousa, N.A. Nema, and S.H. Trier, "Study of structural and optical properties for MgO films prepared by using chemical spray pyrolysis technique," Materials Science: An Indian Journal, **14**, 426-434 (2016).

[11] M.D. Sakhil, Z.M. Shaban, K.S. Sharba, N.F. Habub, K.H. Abass, S.S. Chiad, and A.S. Alkelaby, "Influence mgo dopant on structural and optical properties of nanostructured cuo thin films," NeuroQuantology, **18**(5), 56 (2020). http://doi.org/10.14704/nq.2020.18.5.NQ20168

[12] M. Tlili, N. Jebbari, W. Naffouti, and N.T. Kamoun, "Effect of precursor nature on physical properties of chemically sprayed MgO thin films for optoelectronic application," The European Physical Journal Plus, **135**(8), 1-12 (2020). https://doi.org/10.1140/epjp/s13360-020-00706-z

[13] S. Visweswaran, R. Venkatachalapathy, M. Haris, and R. Murugesan, "Characterization of MgO thin film prepared by spray pyrolysis technique using perfume atomizer," Journal of Materials Science: Materials in Electronics, **31**(17), 14838-14850 (2020). https://doi.org/10.1007/s10854-020-04046-7

[14] H.S. Al-Rikabi, M.H. Al-Timimi, and W.H. Albanda, "Morphological and optical properties of MgO1-xZnSx thin films," Digest Journal of Nanomaterials and Biostructures (DJNB), **17**(3), 889-897 (2022). https://doi.org/10.15251/DJNB.2022.173.889

[15] A. Chowdhury, and J. Kumar, "Morphology, surface topography and optical studies on electron beam evaporated MgO thin films," Bulletin of Materials Science, **29**(5), 513-521 (2006). https://doi.org/10.1007/BF02914083

[16] R.A. Ismail, A.M. Mousa, and S.S. Shaker, "Pulsed laser deposition of nanostructured MgO film: effect of laser fluence on the structural and optical properties," Materials Research Express, **6**(7), 075007 (2019). https://doi.org/10.1088/2053-1591/ab1208

[17] T. Kawaharamura, K. Mori, H. Orita, T. Shirahata, S. Fujita, and T. Hirao, "Effect of O3 and aqueous ammonia on crystallization of MgO thin film grown by mist chemical vapor deposition," Japanese Journal of Applied Physics, **52**(3R), 035501 (2013). https://doi.org/10.7567/JJAP.52.035501

[18] Z. Bazhan, F.E. Ghodsi, and J. Mazloom, "Effect of stabilizer on optical and structural properties of MgO thin films prepared by sol–gel method," Bulletin of Materials Science, **36**(5), 899-905 (2013). https://www.ias.ac.in/article/fulltext/boms/036/05/0899-0905

[19] A.K. Balta, Ö. Ertek, N. Eker, and İ. Okur, "MgO and ZnO composite thin films using the spin coating method on microscope glasses," Materials Sciences and Applications, **6**(01), 40 (2015). http://dx.doi.org/10.4236/msa.2015.61006

[20] K.R. Nemade, and S.A. Waghuley, "Synthesis of MgO nanoparticles by solvent mixed spray pyrolysis technique for optical investigation," International Journal of Metals, **2014**, 1-4 (2014). https://doi.org/10.1155/2014/389416

[21] H. Güney, and D. İskenderoğlu, "Synthesis of MgO thin films grown by SILAR technique," Ceramics International, **44**(7), 7788-7793 (2018). https://doi.org/10.1016/j.ceramint.2018.01.210

[22] J.P. Villegas, I. Moncayo-Riascos, D. Galeano-Caro, M. Riazi, C.A. Franco, and F.B. Cortés, "Functionalization of γ-alumina and magnesia nanoparticles with a fluorocarbon surfactant to promote ultra-gas-wet surfaces: Experimental and theoretical approach," ACS applied materials and interfaces, **12**(11), 13510-13520 (2020). https://doi.org/10.1021/acsami.9b22383

[23] K.V. Rao, and C.S. Sunandana, "Structure and micro structure of combustion synthesized MgO nanoparticles and nanocrystalline MgO thin films synthesized by solution growth route," Synthesis and Reactivity in Inorganic, Metal-Organic and Nano-Metal Chemistry, **38**(2), 173-180 (2008). https://www.tandfonline.com/doi/abs/10.1080/15533170801926127

[24] M.T. Mhetre, H.M. Pathan, A.V. Thakur, and B.J. Lokhande, "Preparation of Magnesium Oxide (MgO) thin films by spray pyrolysis and its capacitive characterizations," ES Energy and Environment, **18**, 41-46 (2022). http://dx.doi.org/10.30919/esee8c785

[25] A.J. Mawat, and M.H. Al-Timimi, "Structural Properties of (MgO$_{1-x}$CdS$_x$) Thin Films Prepared by Chemical Spray Pyrolysis technique," Journal of the college of basic education, **27**(113) (2021).

[26] N. Revathi, P. Prathap, and K.R. Reddy, "Thickness dependent physical properties of close space evaporated In2S3 films," Solid State Sciences, **11**(7), 1288-1296 (2009). https://doi.org/10.1016/j.solidstatesciences.2009.04.019

[27] M. Ghosh, D. Karmakar, S. Basu, S.N. Jha, D. Bhattacharyya, S.C. Gadkari, and S.K. Gupta, "Effect of size and aspect ratio on structural parameters and evidence of shape transition in zinc oxide nanostructures," Journal of Physics and Chemistry of Solids, **75**(4), 543-549 (2014). https://doi.org/10.1016/j.jpcs.2013.11.007

[28] D. Holec, P. Dumitraschkewitz, D. Vollath, and F.D. Fischer, "Surface energy of Au nanoparticles depending on their size and shape," Nanomaterials, **10**(3), 484 (2020). https://doi.org/10.3390/nano10030484

[29] J.H. Boo, S.B. Lee, K.S. Yu, W. Koh, and Y. Kim, "Growth of magnesium oxide thin films using single molecular precursors by metal–organic chemical vapor deposition," Thin Solid Films, **341**(1-2), 63-67 (1999). https://doi.org/10.1016/S0040-6090(98)01524-7

[30] J.M. Bian, X.M. Li, X.D. Gao, and W.D. Yu, "Growth and characterization of high quality MgO thin films by Ultrasonic Spray Pyrolysis," in: *Key Engineering Materials*, Vol. 280, (Trans Tech Publications Ltd., 2005), pp. 1171-1174.

[31] M. Kongtunmon, L. Supadee, W. Kundhikanjana, P. Janphuang, R. Supruangnet, W. Jongpinit, Dh. Munthala, et al., "Effect of annealing atmosphere on hydration behavior of MgO thin film in tunneling magnetoresistance sensor," Ceramics International, **48**(5), 6966-6970 (2022). https://doi.org/10.1016/j.ceramint.2021.11.253

[32] Y.Q. Zhu, W.K. Hsu, W.Z. Zhou, M. Terrones, H.W. Kroto, and D.R.M. Walton, "Selective Co-catalysed growth of novel MgO fishbone fractal nanostructures," Chemical physics letters, **347**(4-6), 337-343 (2001). https://doi.org/10.1016/S0009-2614(01)00939-3

[33] A. Khan, F. Rahman, R. Nongjai, and K. Asokan, "Optical transmittance and electrical transport investigations of Fe-doped In2O3 thin films," Applied Physics A, **127**, 339 (2021). https://doi.org/10.1007/s00339-021-04490-0

[34] W.S. Liu, W.K. Chen, and K.P. Hsueh, "Transparent conductive Ga-doped Mg$_x$Zn$_{1-x}$O films with high optical transmittance prepared by radio frequency magnetron sputtering," Journal of alloys and compounds, **552**, 255-263 (2013). https://doi.org/10.1016/j.jallcom.2012.10.066

[35] O. Diachenko, A. Opanasuyk, D. Kurbatov, N. Opanasuyk, O. Kononov, D. Nam, and H. Cheong, "Surface morphology, structural and optical properties of MgO films obtained by spray pyrolysis technique," Acta Physica Polonica A, **130**(3), 805-810 (2016). https://essuir.sumdu.edu.ua/bitstream/123456789/48466/1/Diachenko_Surface_Morphology.pdf

[36] D. Alagarasan, S.S. Hegde, S. Varadharajaperumal, R. Aadhavan, R. Naik, M. Shkir, H. Algarni, et al., "Effect of SnS thin film thickness on visible light photo detection," Physica Scripta, **97**(6), 065814 (2022). https://doi.org/10.1088/1402-4896/ac6d19

[37] A.J. Mawat, M.H. Al-Timimi, W.H. Albanda, and M.Z Abdullah, "Morphological and optical properties of Mg1-xCdSx nanostructured thin films," AIP Conference Proceedings, **2475**, 090019 (2023). https://doi.org/10.1063/5.0103955

[38] C. Nefzi, M. Souli, N. Beji, A. Mejri, and N. Kamoun-Turki, "Improvement of structural, optical and electrical properties of iron doped indium oxide thin films by high gamma radiations for photocatalysis applications," Materials Science in Semiconductor Processing, **90**, 32-40 (2019). https://doi.org/10.1016/j.mssp.2018.09.022

[39] A. Kaushal, and D. Kaur, "Effect of Mg content on structural, electrical and optical properties of Zn$_{1-x}$Mg$_x$O nanocomposite thin films," Solar energy materials and solar cells, **93**(2), 193-198 (2009). https://doi.org/10.1016/j.solmat.2008.09.039

[40] J. Al-Zanganawee, M. Al-Timimi, A. Pantazi, O. Brincoveanu, C. Moise, R. Mesterca, D. Balan, et al., "Morphological and optical properties of functionalized SWCNTs: P3OT nanocomposite thin films, prepared by spincoating," Journal of Ovonic Research, **12**(4), 201-207 (2016).

[41] A.T. Abood, O.A.A. Hussein, M.H. Al-Timimi, M.Z. Abdullah, H.M.S. Al-Aani, and W.H. Albanda, "Structural and optical properties of nanocrystalline SnO2 thin films growth by electron beam evaporation," AIP Conference Proceedings, **2213**(1), 020036 (2020). https://doi.org/10.1063/5.0000454

[42] F.M. Tezel, U. Veli, and İ.A. Kariper, "Synthesis of MgO thin films: How heat treatment affects their structural, electro-optical, and surface properties," Materials Today Communications, **33**, 104962 (2022). https://doi.org/10.1016/j.mtcomm.2022.104962

[43] A.M. Smith, and S. Nie, "Semiconductor nanocrystals: structure, properties, and band gap engineering," Accounts of chemical research, **43**(2), 190-200 (2010). https://doi.org/10.1021/ar9001069

[44] O.A. Williams, M. Nesladek, M. Daenen, S. Michaelson, A. Hoffman, E. Osawa, K. Haenen, et al., "Growth, electronic properties and applications of nanodiamond," Diamond and Related Materials, **17**(7-10), 1080-1088 (2008). https://doi.org/10.1016/j.diamond.2008.01.103

[45] H. S. Al-Rikabi, M. H. Al-Timimi, and W.H. Albanda, "Morphological and optical properties of MgO1-xZnSx thin films," Digest Journal of Nanomaterials & Biostructures (DJNB), **17**(3), (2022). https://doi.10.15251/DJNB.2022.173.889

[46] M.H. Saeed, M.H. Al-Timimi, and O.A.A. Hussein, "Structural, morphological and optical characterization of nanocrystalline WO3 thin films," Digest Journal of Nanomaterials and Biostructures, **16**(2), 563-569 (2021). https://chalcogen.ro/563_SaeedMH.pdf

[47] N. Guermat, W. Daranfed, and K. Mirouh, "Extended wide band gap amorphous ZnO thin films deposited by spray pyrolysis," Annales de Chimie-Science des Matériaux, **44**(5), 347-352 (2020). https://doi.org/10.18280/acsm.440507

[48] P. Płóciennik, D. Guichaoua, A. Zawadzka, A. Korcala, J. Strzelecki, P. Trzaska, and B. Sahraoui, "Optical properties of MgO thin films grown by laser ablation technique," Optical and Quantum Electronics, **48**, 1-12 (2016). http://dx.doi.org/10.1007%2Fs11082-016-0536-8

[49] S.H. Tamboli, R.B. Patil, S.V. Kamat, V. Puri, and R.K. Puri, "Modification of optical properties of MgO thin films by vapour chopping," Journal of Alloys and Compounds, **477**(1-2), 855-859 (2009). https://doi.org/10.1016/j.jallcom.2008.11.011

[50] M.H. Abdul-Allah, S.A. Salman, and W.H. Abbas, "Annealing effect on the structural and optical properties of $(CuO)(Fe_2O_3)_x$ thin films obtained by chemical spray pyrolysis," Journal of Thi-Qar Science, **5**(1), (2014). https://www.iasj.net/iasj/pdf/a38620e9241bbe5a

[51] H.M. Hussein, and M.H. Al-Timimi, "Preparation and Study Some Physical Properties of (CMC/PAA: MgO) Nano Composites," Eurasian Journal of Physics, Chemistry and Mathematics, **8**, 47-55 (2022).

[52] O. Diachenko, J. Kováč Jr, O. Dobrozhan, P. Novák, J. Kováč, J. Skriniarova, and A. Opanasyuk, "Structural and optical properties of CuO thin films synthesized using spray pyrolysis method," Coatings, **11**(11), 1392 (2021). https://doi.org/10.3390/coatings11111392

[53] B. Elidrissi, M. Addou, M. Regragui, A. Bougrine, A. Kachouane, and J.C. Bernede, "Structure, composition and optical properties of ZnS thin films prepared by spray pyrolysis," Materials Chemistry and physics, **68**(1-3), 175-179 (2001). https://doi.org/10.1016/S0254-0584(00)00351-5

[54] R. Singh, M. Gupta, and S.K. Mukherjee, "Effect of Ag layer thickness on optical and electrical properties of ion-beam-sputtered $TiO_2/Ag/TiO_2$ multilayer thin film," Journal of Materials Science: Materials in Electronics, **33**(9), 6942-6953 (2022). https://doi.org/10.1007/s10854-022-07873-y

[55] K. Derrar, M. Zaabat, N. Rouabah, R. Nazir, F. Hanini, A. Hafdallah, S.A. Khan, et al., "Preparation of Sb: SnO_2 thin films and its effect on opto-electrical properties," Journal of Materials Science: Materials in Electronics, **33**(13), 10142-10153 (2022). https://doi.org/10.1007/s10854-022-08004-3

[56] G. Yergaliuly, B. Soltabayev, S. Kalybekkyzy, Z. Bakenov, and A. Mentbayeva, "Effect of thickness and reaction media on properties of ZnO thin films by SILAR," Scientific reports, **12**(1), 1-13 (2022). https://doi.org/10.1038/s41598-022-04782-2

ВПЛИВ ТОВЩИНИ НА ФІЗИЧНІ ХАРАКТЕРИСТИКИ НАНОСТРУКТУРНИХ ТОНКІХ ПЛІВОК MgO

Мухаммад Х. Аль-Тімімі[a], Відад Х. Альбанда[b], Мустафа З. Абдуллах[c]

[a]Департамент фізики, Науковий коледж, Університет Діяла, Ірак
[b]Науковий Департамент, Коледж базової освіти, Університет Мустансірія, Ірак
[c]Управління досліджень матеріалів, Міністерство науки і технологій, Ірак

Технологія хімічного розпилювального піролізу осадила наноструктуровані тонкі плівки MgO різної товщини (200, 400 і 600 нм). Результати підтверджують, що товщина плівки вплинула на структуру, морфологію, оптичні та електричні властивості. Фізичні властивості плівок MgO досліджували за допомогою (XRD), (FE-SEM), (EDX), (AFM), (UV-Vis спектрофотометр) і ефекту Холла. Відповідно до структурного аналізу, плівки мають кубічну полікристалічну структуру оксиду магнію з переважною орієнтацією (002). Середній розмір кристала та ширина забороненої зони знаходяться в діапазоні (20,79-18,99) нм і (3,439-3,162) еВ відповідно зі збільшенням товщини плівок. Морфологія поверхні плівок показує, що вони вільні від кристалічних дефектів, таких як отвори та пустоти, а також гомогенні та однорідні. Карти EDS показують, що вирощені плівки містять магній і кисень. Ефект Холла вказує, що електропровідність зменшується з товщиною. Експериментальні результати показують, що товщина плівки впливає на фізичні властивості вирощених тонких плівок MgO. Більш товсті плівки можна використовувати як шар поглинача в сонячних елементах.

Ключові слова: *плівки MgO; хімічний розпилювальний піроліз; вплив товщини; структура; оптичні та електричні властивості*

THE THERMOLUMINESCENCE PARAMETERS OF IRRADIATED K-FELDSPAR[†]

Sahib Mammadov*, Aybeniz Ahadova, Aqshin Abishov, Ahmad Ahadov

Institute of Radiation Problems, ANAS, Azerbaijan
*Corresponding Author e-mail: mammadov_sahib@yahoo.com

Isothermal decay of the TL glow curve has been studied at ambient temperature. Heating of feldspar at 600ºC leads to increased sensitivity of the samples upon irradiation for the whole range of glow curve. In general, we observe a sensitivity increase of about five times. Fading of the glow curve is observed at the low-temperature part of the glow curve while it has been kept in the dark at the ambient, constant temperature. After a certain period, approximately in 40 to 50 days the low-temperature region of the glow curve fades down while the high-temperature part remains unchanged. Peaks at the low-temperature region of the TL glow curve were isolated by the curve subtraction method. Activation energy and frequency factor parameters of the isolated peaks were calculated, taking first and second-order kinetics into account. The values of the calculated activation energy vary between 0.7 to 1.1 eV, and frequency factor values of the isolated peaks change within the order of 10^9 to 10^{13}s^{-1}. The μ values clearly indicate that all isolated peaks are more likely to be second-order kinetics.

Keywords: *Feldspar; Isothermal decay; Activation energy; Frequency factor*
PACS: 78.60.Kn

INTRODUCTION

Feldspar fraction extracted from sediments has been increasingly investigated for the dating of archeological artifacts and the age of geological sediments. The main advantage of using feldspars instead of quartz is their higher luminescence brightness and saturation dose, which could extend the range of dating applications. At the same time, the luminescence emission of feldspar exhibits a large variety due to the substantial natural abundance of the mineralogical composition [1-3]; the presence of adverse luminescent phenomena like anomalous fading and sensitivity changes; irradiation and thermal history [4]. Investigations were mainly made on natural K-feldspars separated from geological sediments and pure feldspar minerals. They were devoted to clarifying the luminescence behavior of such materials, describing the optical bleaching mechanism [5], identifying traps and recombination centers, and assessing a reliable protocol for dating procedures [6-9].

The exact composition of TL luminescence curves in feldspars and their kinetics is still an open question, although numerous studies have been carried out. In particular, it is necessary to find out whether the broad TL luminescence curves consist of individual narrow TL peaks or are the result of a superposition of continuous energy levels [7].

To contribute to the knowledge of the luminescent mechanisms in feldspars, we present the results of a study of activation energy and frequency factor values on the natural feldspar mineral.

MATERIALS AND METHODS

We have taken the feldspar kindly presented by the Institute of Inorganic Chemistry and Catalysis ANAS as a sample. Samples were gently crashed and sieved, and the fraction of 100-160 μm of feldspar was used for TL measurement. Hydrochloric acid (1N) was used to remove carbonates and then rinsed with deionized water. Magnetic separation was applied to remove any magnetic inclusions. Any high-density components were separated using heavy liquid Sodium poly-tungsten. Irradiation was performed at ambient temperature with a ^{60}Co gamma source with a dose rate of 3.73 mGy/s. The dose rate of the ^{60}Co source was determined using a Magnette Miniscope MS400 EPR spectrometer using individually packed BioMax alanine dosimetry films with barcode markings (developed by Eastman Kodak Company). For the experiments, it was used both natural and thermally treated feldspar samples to compare the changes in radiation sensitivity due to thermal treatment. Thermally treated feldspar was heated at 600ºC for one hour before irradiation.

The Harshaw TLD 3500 Manual Reader is used to measure the characteristics of TL samples. TL measurements were performed using a linear heating rate of 20ºC/s from 50ºC to 400ºC. Three aliquots of 5 mg of each sample were used for each measurement. TL data points represent the average of three different aliquots of the sample. A thin and uniform layer of feldspar grains was laid on the planchet surface to get complete contact, ensuring a consistent TL signal from the sample.

Several experimental methods for evaluating the basic trapping parameters from a TL peak are based on the peak shape. The peak shape method enables the evaluation of "activation energy" and "frequency factor" using the temperature at the peak maximum (T_m) and the low (T_1) and high (T_2) half-width temperatures (Fig. 1) of the experimental glow curve.

The formulas for finding the activation energies by these methods usually contain one of the following factors: (a) $\tau=T_m-T_1$, the half-width at the low-temperature side of the peak, (b) $\delta=T_2-T_m$, the half-width towards the falloff of the glow peak, or (c) $\omega=T_2-T_1$, the total half-width. These formulas were developed and systemized by Chen R. [10]. Here are the summarized function and relevant coefficients (Table 1) for the first and second-order kinetics:

$$E = C_\propto \left(\frac{kT_m^2}{\propto} \right) - b_\propto (2kT_m) \tag{1}$$

where $k = 8.617 \times 10^{-5}$ eV/K is the Boltzmann constant and α is δ, τ or ω respectively.
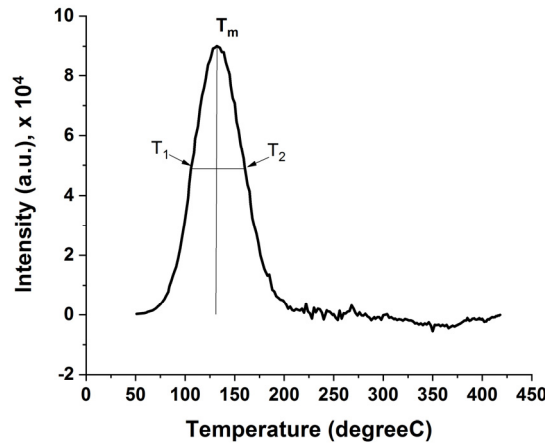
Figure 1. Isolated TL peak. Tm is a temperature at the peak maximum; T1 is a temperature at the point of the left side half-width; T2 is a temperature at the end of the right-side half-width

The values of C_α and b_α for each of the three methods are given in Table 1. Note that the order of kinetics of a peak is usually determined by its symmetry factor, defined as

$$\mu = \delta/\omega, \tag{2}$$

where a characteristic value of μ for the first order peaks is 0.42 and for the second order is 0.52 [11].

Table 1. Coefficients appearing in Eq.1 for the various methods of calculating activation energies [11]

	First order			**Second order**		
	τ	δ	ω	τ	δ	ω
$C_\propto$	1.51	0.976	2.52	1.81	1.71	3.54
$b_\propto$	1.58	0	1	2	0	1

Once the activation energy of a first-order peak is defined, the frequency factor can be determined by using the formula:

$$s = \frac{\beta E}{kT_m^2} \exp(E/kT_m), \tag{3}$$

where β (K/s) is the constant heating rate.
For the second-order kinetics, the formula needs to be written as:

$$s = \frac{\beta E}{kT_m^2(1+\frac{2kT_m}{E})} \exp(E/kT_m) \tag{4}$$

RESULTS AND DISCUSSIONS

The continuum of energy states creates a broad TL glow curve shown in Figs. 2 and 3. This broad spectrum cannot be considered a single peak. It rather can be described as a linear combination of many narrower peaks, each corresponding to a separate but closely spaced energy level. These closely spaced energy levels can be identified by subtracting the TL luminescence curves. For example, Strickertsson et all [12] examined the TL signals from microclines and identified six overlapping peaks using the fractional glow technique to estimate the activation energy E as a function of the temperature T. Applying the T_{stop} –T_{max} method, they reported a continuous distribution of energies between $E \sim 1.0$ eV and $E \sim 1.7$ eV at the low-temperature region (below the 280°C). For higher T_{stop} values, the activation energy E was constant at a value of $E \sim 1.75$ eV [12].

In our case, we used the isothermal decay method. Several aliquots of the material are irradiated with a gamma dose of 34.12 Gy, and the TL glow curve is obtained. The process is then repeated several times using the remaining part of the aliquots after a certain period, i.e., after five days, 15 days, etc. This procedure produces a series of TL glow curves shown in Fig. 2 and 3, essentially corresponding to a gradual isothermal (i.e. at ambient temperature) cleaning of this sample's overall TL glow curve.

The comparison of Fig. 2 and Fig. 3 shows that heating of feldspar at 600°C leads to increased sensitivity of the samples upon irradiation for the whole range of the glow curve. In general, we observe a sensitivity increase of about five times. Fading of the glow curve is observed at the low-temperature part of the glow curve while it has been kept in the dark at the ambient, constant temperature. After approximately 40 to 50 days, the low-temperature region of the glow

curve fades down while the high-temperature part remains unchanged. It is a common phenomenon for irradiated feldspar and anomalous fading. Explanations of the anomalous fading effect have been based on various proposed models, such as the tunneling model, the localized transition model, and a model based on competition with radiationless transitions. Currently, the most accepted explanations of AF are based on quantum mechanical tunneling from the ground state or the excited state of the trap [13 and references therein].
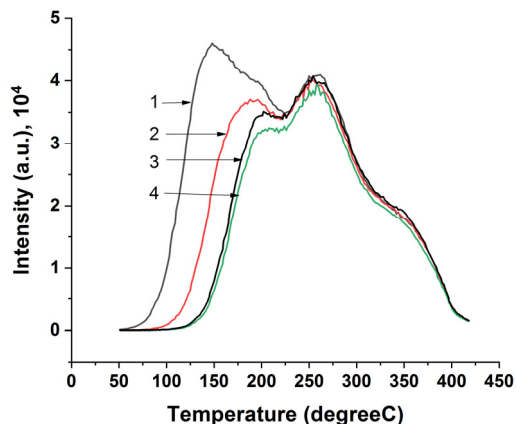

Figure 2. TL glow curve of unheated natural feldspar irradiated at 34.12 Gy (1); TL glow curve of the same sample after 15 days (2), 22 days (3), and 27 days (4)
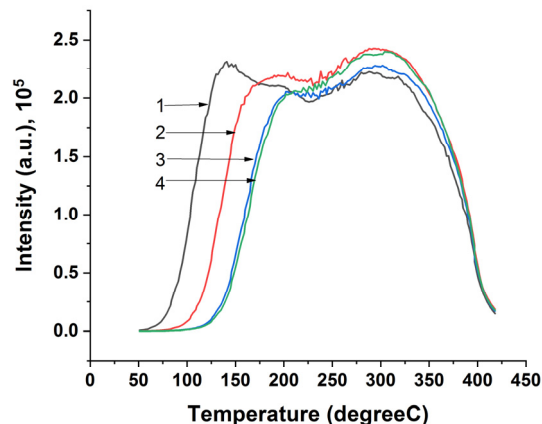
Figure 3. TL glow curve of natural feldspar heated at 600ºC for one hour and irradiated at 34.12 Gy (1); TL glow curve of the same sample after five days (2), 12 days (3), and 40 days (4). Curve (5) represents the isolated peak by subtracting curve (4) from curve (1)

Specifically, Figs. 4 and 5 show the results of subtracting the TL glow curve for the two samples as individual peaks.
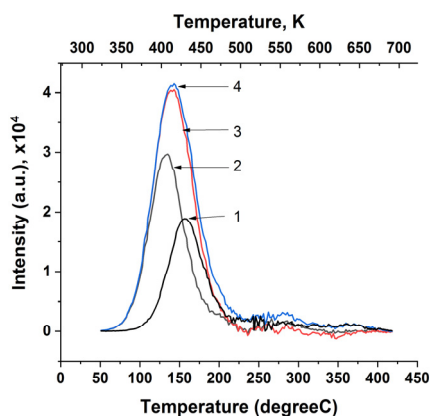
Figure 4. Isolated glow curves were obtained by subtracting method. Curve (1) represents the isolated peak by subtracting glow curve (4) presented in Fig. 2 from curve (2) presented in Fig. 2, i.e (1) = Fig 2 curve (2) – Fig.2 curve (4); and subsequently (2) = Fig 2 curve (1) – Fig. 2 curve (2); (3) = Fig 2 curve (1) – Fig. 2 curve (3); (4) = Fig 2 curve (1) – Fig. 2 curve (4)
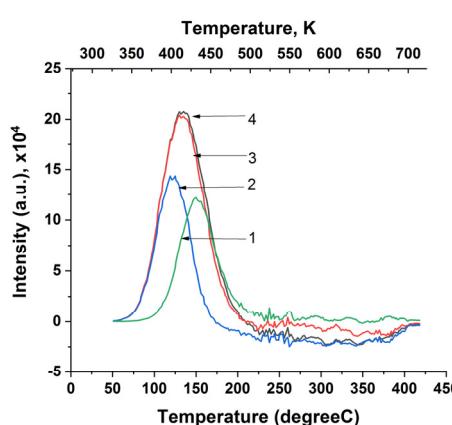
Figure 5. Isolated glow curves obtained by subtracting method: Curve (1) represents the isolated peak by subtracting glow curve (4) presented in Fig. 3 from curve(2) presented in Fig. 3, i.e (1) = Fig 3, curve (2) – Fig. 3, curve (4); and subsequently (2) = Fig 3, curve (1) – Fig.3, curve (2); (3) = Fig 3, curve (1) – Fig. 3, curve (3); (4) = Fig 3, curve (1) – Fig.3, curve (4)

Table 2 illustrates the major geometric parameters of the isolated peaks for the unheated and irradiated feldspar. The values of μ indicate that all isolated peaks belong to second-order kinetics.

Table 2. TL parameters of the isolated peaks for the unheated feldspar irradiated at 34.12 Gy (For the punctuation of the peaks, please, refer to Fig. 4)

Peak identity	T_m, K	T_1, K	T_2, K	ω	δ	τ	μ
1	429	405	457	52	28	24	0.54
2	408	381	433	52	25	27	0.48
3	414	385	444	59	30	29	0.51
4	414	385	447	62	33	29	0.53

However, one hardly observes curves with pure first-order or second-order kinetics. Experimental glow curves usually show values between 0.42 and 0.52 or around them (please refer to Tables 2 and 3). It is suggested [11] to interpolate the constants listed in Table 1 for the first and second-order kinetics to find activation energies. A much more suitable interpolation parameter seems to be μ which is found directly from the peak's geometrical shape (refer to Tables 2 and 3). We have to write general equations so that they would give the first-order case for μ=0.42 and the second-order

case μ=0.52. Thus, with the parameters of μ given in Table 1, the factors in equation 1 for the interpolated-extrapolated τ method would be

C_τ = 1.51 + 3.0 (μ-0.42); $\qquad$ b_τ = 1.58 + 4.2 (μ-0.42)

For the **δ** and **ω** method coefficients would be

C_δ = 0.976 + 7.3 (μ-0.42); $\qquad$ b_δ = 0 and

C_ω= 2.52 + 10.2 (μ-0.42); $\qquad$ b_ω = 1 respectively.

Table 3. Activation energy values of the isolated peaks for the unheated feldspar irradiated at 34.12 Gy (For the punctuation of the peaks, please, refer to Fig. 4)

Peak identity	E_τ (eV)	E_δ (eV)	E_ω (eV)
1	1.08	1.04	1.06
2	0.77	0.81	0.80
3	0.77	0.80	0.79
4	0.79	0.80	0.80

The frequency factor also easily might be calculated using the formula (3) for the first-order kinetics or the second-order kinetics by formula (4) [11]. Table 4 illustrates the values of the frequency factors calculated for the peaks listed in Table 3. The calculation of activation energy and frequency factor was performed using the user-defined function in the Matlab program.

Table 4. Calculated frequency factor values of the isolated peaks for the unheated feldspar irradiated at 34.12 Gy (For the punctuation of the peaks, please, refer to Fig.4)

Peak identity	Values calculated for τ method		Values calculated for δ method		Values calculated for ω method	
	1st order	2nd order	1st order	2nd order	1st order	2nd order
1	6.64E+12	6.22E+12	2.17E+12	2.02E+12	3.79E+12	3.50E+12
2	3.49E+9	3.20E+9	1.15E+10	1.05E+9	8.51E+9	7.82E+9
3	2.45E+9	2.60E+9	5.94E+9	5.45E+9	4.43E+9	4.07E+9
4	4.43E+9	4.07E+9	5.94E+9	5.45E+9	5.95E+9	5.45E+9

Table5. TL parameters of the isolated peaks for the feldspar heated at 600ºC and irradiated at 34.12 Gy(For the punctuation of the peaks, please, refer to Fig.5)

Peak identity	T_m, K	T_1, K	T_2, K	ω	δ	τ	μ
1	423	399	448	49	25	24	0.51
2	394	372	419	47	25	22	0.53
3	405	376	437	61	32	29	0.52
4	406	377	439	62	33	29	0.53

Table 6. Activation energy values of the isolated peaks for the feldspar heated at 600ºC and irradiated at 34.12 Gy (For the punctuation of the peaks, please, refer to Fig.5)

Peak identity	E_τ (eV)	E_δ (eV)	E_ω (eV)
1	1.00	1.01	1.01
2	0.98	0.97	0.98
3	0.75	0.76	0.77
4	0.75	0.77	0.76

Table 7. Calculated frequency factor values of the isolated peaks for the unheated feldspar irradiated at 34.12 Gy (For the punctuation of the peaks, please, refer to Fig.4)

Peak identity	Values calculated for τ method		Values calculated for δ method		Values calculated for ω method	
	1st order	2nd order	1st order	2nd order	1st order	2nd order
1	8.81E+13	8.29E+13	2.12E+13	2.12E+13	3.75E+13	3.52E+13
2	2.91E+9	2.67E+9	3.92E+9	3.60E+9	3.92E+9	3.60E+9
3	2.29E+9	2.09E+9	4.16E+9	3.82E+9	3.09E+9	2.83E+9
4	5.03E+12	4.71E+12	2.74E+12	2.56E+12	3.71E+12	3.47E+12

CONCLUSIONS

The decay of the luminescence curve with time was considered to be an isothermal decay at ambient temperature, and the proposed procedure makes it possible to identify peaks in the low-temperature region of the TL luminescence curve. An analysis of the values of the symmetry factor suggests that bimolecular mechanisms are based on the kinetics of decay processes since the values of this parameter vary within 0.52. The values of the calculated activation energy range between 0.7 to 1.1 eV, and frequency factor values of the isolated peaks change within the order of 10^9 to 10^{13}s^{-1}.

ORCID IDs

Sahib Mammadov, https://orcid.org/0000-0002-4547-4491; **Aubeniz Ahadova**, https://orcid.org/0000-0001-9173-9537
Aqshin Abishov, https://orcid.org/0000-0003-2467-4344; **Ahmad Ahadov**, https://orcid.org/0000-0002-6039-8714

REFERENCES

[1] W.E. Madcour, and S.Y. Afifi, "Thermoluminescence Properties of Local Feldspar from Gattar Mountain Area", Arab J. Nucl. Sci. Appl. **50**(1), 59-66 (2017). https://inis.iaea.org/search/48036670

[2] L.A. Gliganic, R.G. Roberts, and Z. Jacobs, "Natural variations in the properties of TL and IRSL emissions from metamorphic and volcanic K-feldspars from East Africa: Assessing their reliability for dating", Radiat. Meas. **47**(9), 659–664 (2012). https://doi.org/10.1016/j.radmeas.2012.03.001

[3] S. Tsukamoto et al., "A comparative study of the luminescence characteristics of polymineral fine grains and coarse-grained K-and Na-rich feldspars", Radiat. Meas. 47(9), 903–908 (2012). https://doi.org/10.1016/j.radmeas.2012.02.017

[4] L. Panzeri, M. Martini, and E. Sibilia, "Effects of thermal treatments on luminescence features of three natural feldspars", Radiat. Meas. 47(9), 877–882 (2012). https://doi.org/10.1016/j.radmeas.2012.03.021

[5] E. Şahiner, M.K. Erturaç, G.S. Polymeris, and N. Meriç, "Methodological studies on integration time interval's selection for the luminescence ages using quartz and feldspar minerals; sediments collected from Sakarya, Turkey", Radiat. Meas. **120**, 163–169, (2018). https://doi.org/10.1016/j.radmeas.2018.06.024

[6] N.M.M. Doğan, and E. Şahiner, "An Experimental Study Related to Dose Scattering on the Routinely Used Minerals with Comparison of Grain Sizes and Disks Materials", Çankaya Univ. J. Sci. Eng. **13**(2), 054–063 (2016). https://dergipark.org.tr/en/download/article-file/351167

[7] V. Pagonis, P. Morthekai, and G. Kitis, "Kinetic analysis of thermoluminescence glow curves in feldspar: evidence for a continuous distribution of energies", Geochronometria, **41**(2), 168–177 (2014). https://doi.org/10.2478/s13386-013-0148-z

[8] G.S. Polymeris, V. Pagonis, and G. Kitis, "Thermoluminescence glow curves in preheated feldspar samples: An interpretation based on random defect distributions", Radiat. Meas. **97**, 20–27 (2017). https://doi.org/10.1016/j.radmeas.2016.12.012

[9] V. Pagonis, F.M. dos Santos Vieira, A. Chambers, and L. Anthony, "Thermoluminescence glow curves in preheated feldspar: A Monte Carlo study", Nucl. Instruments Methods Phys. Res. Sect. B Beam Interact. with Mater. Atoms, **436**, 249–256 (2018). https://doi.org/10.1016/j.nimb.2018.09.036

[10] R. Chen, "On the calculation of activation energies and frequency factors from glow curves", J. Appl. Phys. **40**(2), 570–585 (1969). https://doi.org/10.1063/1.1657437

[11] R. Chen, "Glow curves with general order kinetics", J. Electrochem Soc. Solid State Sci. 1254–1257 (1969). https://iopscience.iop.org/article/10.1149/1.2412291

[12] K. Strickertsson, "The thermoluminescence of potassium feldspars-Glow curve characteristics and initial rise measurements", Nucl. Tracks Radiat. Meas. **10**(4-6), 613–617 (1985). https://doi.org/10.1016/0735-245X(85)90066-3

[13] I.K. Sfampa, G.S. Polymeris, N.C. Tsirliganis, V. Pagonis, and G. Kitis, "Prompt isothermal decay of thermoluminescence in an apatite exhibiting strong anomalous fading", Nucl. Instruments Methods Phys. Res. Sect. B, Beam Interact. with Mater. Atoms, **320**, 57–63 (2014). https://doi.org/10.1016/j.nimb.2013.12.003

ПАРАМЕТРИ ТЕРМОЛЮМІНЕСЦЕНЦІЇ ОПРОМІНЕНОГО К-ПОЛЬОВОГО ШПАТУ

Сахіб Мамадов, Айбеніз Ахадова, Акшин Абішов, Ахмад Ахадов
Інститут радіаційних проблем НАНА, Азербайджан

Досліджено ізотермічний спад кривої світіння ТЛ при температурі навколишнього середовища. Нагрівання польового шпату до 600ºC призводить до підвищення чутливості зразків при опроміненні на всьому діапазоні кривої світіння. Загалом ми спостерігаємо підвищення чутливості приблизно в п'ять разів. Згасання кривої світіння спостерігається на низькотемпературній ділянці кривої світіння при зберіганні в темряві при постійній температурі навколишнього середовища. Через певний проміжок часу, приблизно через 40-50 днів, низькотемпературна область кривої світіння згасає, а високотемпературна частина залишається незмінною. Піки в низькотемпературній області кривої світіння ТЛ виділені методом віднімання кривої. Розраховано параметри енергії активації та частотного фактору ізольованих піків з урахуванням кінетики першого та другого порядку. Значення розрахованої енергії активації змінюються в межах від 0,7 до 1,1 еВ, а значення коефіцієнта частоти ізольованих піків змінюються в межах порядку від 109 до 1013 с$^{-1}$. Значення μ чітко вказують на те, що всі ізольовані піки, швидше за все, є кінетикою другого порядку.

Ключові слова: *польовий шпат; ізотермічний розпад; енергія активації; частотний фактор*

SOME PROPERTIES OF SEMICONDUCTOR-FERROELECTRIC STRUCTURES[†]

Zakirjan T. Azamatov, ⓘSharifa B. Utamuradova, Murodjon A. Yuldoshev*, Nurlan N. Bazarbayev

Institute of Semiconductor Physics and Microelectronics, National University of Uzbekistan,
20 Yangi Almazor st., Tashkent, 100057, Uzbekistan
*Corresponding Author e-mail: murod.yuldoshev1993@gmail.com
Received March 17, 2023; revised March 27, 2023; accepted March 29, 2023

This paper presents the properties of semiconductor-ferroelectric structures consisting of ZnO nanorods grown at low temperatures by the hydrothermal method on $LiNbO_3$ and $LiNbO_3$:Fe substrates. The resulting structures were analyzed by scanning electron microscope, photoluminescence, and spectrophotometry. SEM images and spectra; absorption spectra; photoluminescence spectra in the ultraviolet and visible ranges are presented. The studies have shown the possibility of using, along with others, the hydrothermal method for the synthesis of $Zn(NO_3)_26H_2O$ and $C_6H_{12}N_4$ to obtain arrays of ZnO nanorods as a sensitive element of surfactant-based UV radiation sensors.
Keywords: *nanorod; photoluminescence; scanning electron microscope; absorption spectrum*
PACS: 68.37.Hk, 78.55.Ap, 42.25.Bs, 61.46.Km

INTRODUCTION

ZnO has a whole set of properties that are well combined with each other, such as: high optical transparency, the presence of piezo and photo effects, low resistivity, radiation resistance, etc. Zinc oxide is a direct-gap semiconductor with a band gap of 3.36 eV and a high binding energy exciton state ~ 60 MeV. This combination of physical parameters, as applied to ZnO thin films, makes this material promising for creating UV, blue, green, and white LEDs, optical and gas sensors, piezo sensors, HUD displays, transparent contacts, etc.

Semiconductor-ferroelectric structures ($ZnO-LiNbO_3$) are currently attracting much attention of researchers due to the possibility of creating radio photonics and functional microelectronics devices on their basis.

Zinc oxide initially has an electronic type (n-type) conductivity with a fairly low resistivity ($\rho \approx 10^{-3} \div 10^{-4}$ Ω·sm), a high concentration of n-type charge carriers (~ $10^{20} \div 10^{21}$ sm^{-3}), and relatively low mobility ($\mu \approx 5 \div 20$ sm^2/V·s) [1].

Lithium niobate can be called a wide gap semiconductor due to the change in the band gap of the crystal (3.4 eV) based on the cross effect. However, due to the high resistivity ($\rho \approx 10^{15} \div 10^{17}$ Ω·sm) and low mobility ($\mu \approx 10^{-3}$ sm^2/V·s), as well as the manifestation of spontaneous polarization and hysteresis properties, it belongs to the ferroelectric group of materials.

ZnO nanostructures have a wide range of applications in various devices. ZnO nanorods (NR ZnO) are interesting for their electronic and optoelectronic properties [2,3] and are often functional elements of such devices as ultraviolet (UV) nanolasers, chemical sensors, solar cells, nanogenerators [4,5]. The creation of UV sensors of surface acoustic waves (SAW) based on zinc oxide nanostructures as sensitive elements is a very urgent task; they are promising for economical wireless and batteryless devices [6-8].

In this regard, semiconductor-ferroelectric structures formed on the surface of a ferroelectric substrate from single-crystal lithium niobate make it possible to create optically and electrically controlled structures according to the topology of a field-effect transistor or a field-controlled photoresistor [9]. To create such microdevices, it is necessary to conduct a comprehensive study of the structural, optical, and luminescent properties of semiconductor-ferroelectric structures.

For example, a highly efficient photodetector was developed based on a surfactant generator with a ZnO nanorod layer sensitive to ultraviolet radiation on the surface of a $LiNbO_3$ substrate [10,11]. In particular, the sensor is capable of detecting UV radiation as low as 1.8 μW/sm^{-2}.

In our work, we present the results of a study of morphological, optical absorption spectra, photoluminescent properties of $ZnO-LiNbO_3$ and $ZnO-LiNbO_3$:Fe structures.

EXPERIMENTAL PART

ZnO were synthesized on a stainless-steel grid by the hydrothermal method [12]. Before growing ZnO nanorods, a seed layer is formed on the surface of the substrates. The dip coating method has been applied to prepare the ZnO seed layer on substrates due to its low cost and simplicity. All reagents (Sigma-Aldrich, 99%) used in the experiment were analytically pure and were used without further purification. Zinc acetate dehydrate ($ZnC_4H_6O_42H_2O$) was dissolved in ethanol with stirring with a stainless-steel shaft mixer at room temperature to obtain a homogeneous solution. The stirred solution is placed in a beaker, the substrates are dipped into the solution at low speed using an automatic dip coating system, and air dried at room temperature.

The growth of ZnO nanorods is carried out in the following sequence: aqueous solutions of zinc nitrate hexahydrate $Zn(NO_3)_26H_2O$ and hexamethylenetetramine $C_6H_{12}N_4$ were prepared. The resulting suspension was transferred to a Teflon

coated stainless steel autoclave. Substrates with a ZnO seed layer were placed on the bottom of the autoclave. Finally, the autoclave was closed and placed in a bath with a water thermostat. The hydrothermal reaction is carried out at 90° C. for 5 hours.

Studies of surface morphology, thickness and elemental composition of the samples were carried out on a scanning electron microscope (SEM) EVO MA10 (Carl Zeiss). The absorption spectra were studied using a Shimadzu UV 3600 spectrometer. The emission spectra of ZnO nanorods were obtained using a photoluminescent setup coupled to a 0.75 μm monochromator with a diffraction grating and highly sensitive photomultipliers. The excitation source was a longitudinally pumped nanosecond pulsed N_2 laser emitting at a wavelength of 337 nm (pulse duration ~6 ns, P ~15 kW, repetition rate 100 Hz). The emission spectra were recorded using a boxcar integrator with a gate width of 40 ns.

RESULTS AND THEIR DISCUSSION

As a result of SEM studies, images of the surface morphologies of grown samples of ZnO-LiNbO₃ structures were obtained, which are shown in Fig. 1. At high magnification, ZnO nanorods are clearly visible, with their sizes indicated. A similar picture is shown by the images of the ZnO-LiNbO₃:Fe surface, which we do not present.

Analysis of the SEM images of both samples shows that zinc oxide nanorods grow equally on both substrates. It can be seen that the average size of nanorods is 10–20 μm in length and 1–3 μm in diameter.

To measure the thickness of the nanorod layer in SEM, the sample was rotated through an angle of 90° to the surface grown from ZnO Fig. 2. It can be seen that the thicknesses in different parts of the applied layer are in the range of 2-12 μm. Note that, depending on the task, the layer thickness can be changed during its growth.
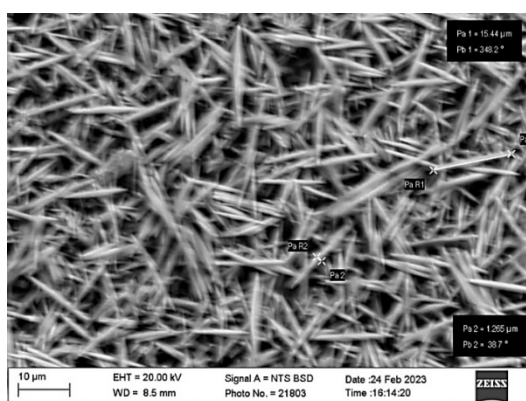

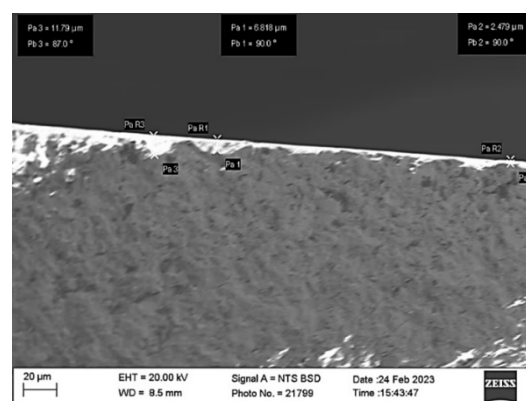**Figure 1.** Surface morphology of ZnO-LiNbO₃

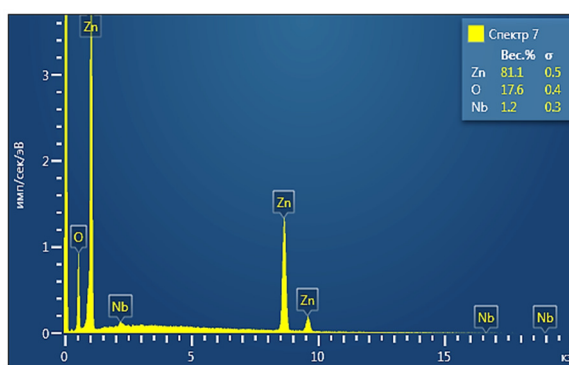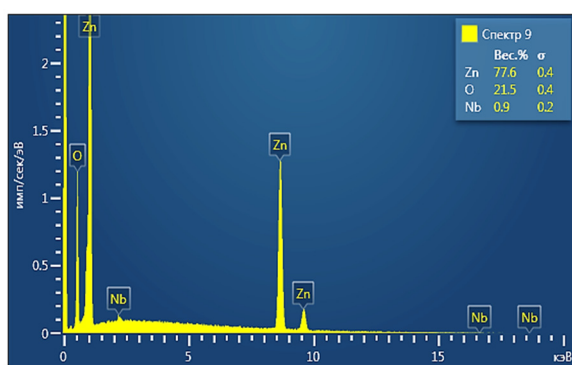**Figure 2.** Layer thicknesses of ZnO-LiNbO₃ nanorods

Figure 3. Elemental analysis a) ZnO-LiNbO₃ and b) ZnO-LiNbO₃:Fe

As can be seen from Fig. 3 elemental analysis of the spectra shows the presence and percentage of all components of the structures, the device does not see Fe, due to its low content, which goes beyond the measurement limits of the device.

The photoluminescence spectra of the structures under study are shown in Fig. 4. In both spectra of the structures under study, there is a narrow intense luminescence band located in the UV region, the maximum of which falls in the vicinity of the wavelength – 387 nm. The maximum of the luminescence band corresponding to the ZnO layer hydrothermally deposited on the LiNbO₃ surface (Figure 4, curve 1) is at a wavelength of 387 nm and has a half-width of 34 nm.

The maximum of the luminescence band corresponding to the ZnO layer hydrothermally deposited on the LiNbO₃:Fe surface (Figure 4, curve 2) is at a wavelength of 390 nm and has a half-width of 32 nm. The intensity of the band in the spectrum of ZnO nanorods grown on a LiNbO₃:Fe substrate is 12% less than the intensity of the analogous band in the photoluminescence spectrum for ZnO nanorods grown on a LiNbO₃ substrate. The position of the maxima of the narrow UV photoluminescence bands and their spectral half-width suggest that they are similar to the exciton

photoluminescence band [13]. Such a ratio between the intensities of the UV photoluminescence bands of the two samples under study can be explained as follows: the process responsible for intense photoluminescence in the UV spectral range is the recombination of excitons in the bulk of the ZnO layer [14]. The shift of the UV photoluminescence band by 3 nm toward longer wavelengths may be due to the fact that the observed photoluminescence in the zinc oxide layer of nanorods hydrothermally deposited on ferroelectric substrates is the total effect of luminescence from both exciton complexes and deep traps present in the bulk zinc oxide layer of nanorods.

For both structures under study, broad luminescence bands are observed, which lie in the blue-green spectral region of the visible range. These broad photoluminescence bands have similar half-widths and intensities (the spectra merge). The intensities of the broad photoluminescence band of the ZnO-LiNbO$_3$ and ZnO-LiNbO$_3$:Fe structures coincide. Its maximum is at a wavelength of 562 nm, and its half-width is 154 nm. The defects responsible for photoluminescence in this spectral range include oxygen vacancies, which are both electrically and optically active defects. Optically active defects and the spectral position of broad maxima correlate with the literature data [15].

We compared our results with the results obtained in the following works: [16] – ZnO films obtained by laser ablation; [1] – ZnO films obtained by vacuum deposition on LiNbO$_3$ ferroelectric substrates. The first exciton (in the UV spectral region) obtained peak is similar to the peak obtained in our studies from zinc oxide films grown by hydrothermal synthesis. But the peaks of vacancy oxygen in the second visible (blue-green spectral region) do not coincide. In our results, the symmetry of the spectral lines is practically preserved, and the intensities of both peaks are of the same order, no additional peaks are observed.

Studies have shown that grown ZnO nanorods are excited by ultraviolet light, the PL spectrum of ZnO nanorods consists of two peaks: a narrow one in the UV range and a broad emission band in the visible range. The UV peak was attributed to the near edge emission of the band or the free exciton of ZnO, and the blue-green emission to the far luminescence band and vacancy oxygen.
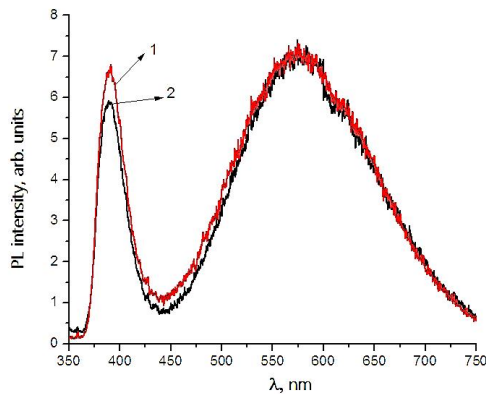
Figure 4. Photoluminescence spectra of structures: ZnO-LiNbO$_3$ (1), ZnO-LiNbO$_3$:Fe (2)
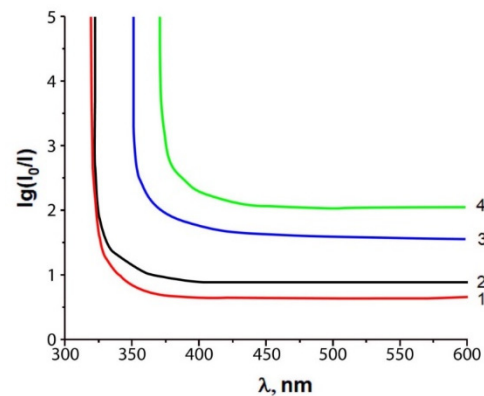
Figure 5. Absorption spectra of structures: ZnO-LiNbO$_3$ (1.2), ZnO-LiNbO$_3$:Fe (3.4)

To study the optical properties of the resulting semiconductor-ferroelectric structures in the UV and visible ranges of the spectrum, studies of the absorption spectra were carried out. The absorption spectra Fig. 5 were studied in the wavelength range from 200 to 900 nm. The parallelism of the spectral lines remains practically unchanged from 400 nm to the near infrared region. Absorption begins to increase rapidly from 400 nm. Therefore, in the figure, the range from the short-wavelength range to 600 nm is taken. absorption spectra were taken from both samples - from the side: ZnO (1.4) and substrates (2.3).

For comparison, the absorption spectra of the samples were measured on both sides. It can be seen from the spectra that in the ZnO-LiNbO$_3$ structure the spectrum taken from the side of the ZnO layer is lower than the spectrum taken from the side of the base (Fig. 5, curve 1). This indicates that the ZnO layer reflects light. But in the ZnO-LiNbO$_3$:Fe structure, on the contrary, the spectrum of the ZnO layer is higher (Fig. 5, curve 4). We can say that this is the effect of Fe ions participating in the structure. The obtained absorption spectrum in the decreasing linear part of the graph was approximated by a straight line up to the intersection with the abscissa axis. The point of intersection of this line with the abscissa axis is the wavelength corresponding to the absorption edge of the crystal. The band gap was determined by the formula:

$$E = \frac{hc}{\lambda} \tag{1}$$

where λ is the wavelength corresponding to the absorption edge, h is Planck's constant, c is the speed of light in vacuum.

The widths of the geometrically defined band gaps E$_g$ are 3.86, 3.85, 3.52, and 3.34 eV, respectively, according to the curves in Fig. 5. The refractive indices are determined by the following imperial formula, taking into account Eg, which is given in [17]:

$$n^2 - 1 = \frac{A}{(E_g + B)^2} \tag{2}$$

where A = 25E$_g$ + 212, B = 0.21E$_g$ + 4.25, while the changes in the refractive index look, respectively, as follows; 2.20, 2.21, 2.26, 2.30.

CONCLUSION

Thus, it can be said that for all methods of obtaining ZnO nanostructures on pure and iron-doped lithium niobate substrates, the surface morphology is the same, they are covered with ZnO nanoparticles or nanorods (clusters), and, in the elemental composition of nanoparticles, oxygen predominates, and vice versa in nanorods. The results of luminescence analysis show similarity of the spectra both in the UV region and in the blue-green part of the spectrum, but the spectra obtained by us are symmetrical and without additional "peaks", due to a larger amount of interstitial oxygen. In addition, it can be seen that the refractive indices calculated using the above empirical formula are very close to the experimental results of other authors.

ORCID IDs
Sharifa B. Utamuradova, https://orcid.org/0000-0002-1718-1122

REFERENCES
[1] N.M. Lyadov, A.I. Gumarov, R.N. Kashapov, A.I. Noskov, V.F. Valeev, V.I. Nuzhdin, V.V. Bazarov, et al., "Structure and optical properties of ZnO with silver nanoparticles," Physics and technology of semiconductors, **50**(1), (2016).
[2] A.B. Djurišić, and Y.H. Leung, Small **2**, 944-961 (2006). https://doi.org/10.1002/smll.200600134
[3] C.Y. Chen, M.W. Chen, J.J. Ke, C.A. Lin, J.R.D. Retamal, and J.H. He, "Surface effects on optical and electrical properties of ZnO nanostructures," Pure Appl. Chem. **82**, 2055 (2010). http://dx.doi.org/10.1351/PAC-CON-09-12-05
[4] A.K. Zeinidenov, A.K. Abisheva, B.R. Ilyassov, A.K. Aimukhanov, and S.E. Abilmazhinov, "Influence of structural features of zno films on optical and photoelectric characteristics of inverted polymer solar elements," Eurasian Physical Technical Journal, **18**(2), 40-46 2021, https://doi.org/10.31489/2021No2/40-46
[5] Ş. Kaya, "Effect of annealing temperature on structural, electrical, and UV sensingcharacteristics of n-ZnO/p-Si heterojunction photodiodes*,"* Turkish Journal of Physics, **43**(3), 4 2019). https://doi.org/10.3906/fiz-1812-16
[6] A.S. Bagdasarian, V.G. Dneprovski, G.Y. Karapetyan, S.A. Bagdasaryan, in: *Piezoelectric and Related Materials. Research and Applications*, edited by by I.A. Parinov, (Nova Science Publishers, New York, 2012), pp. 189.
[7] P. Sharma, S. Kumar, and K. Sreenivas, "Highly sensitive ultraviolet detector based on ZnO/LiNbO3 hybrid surface acoustic wave filter," Mater J. Res. **18**, 545 (2003). https://doi.org/10.1063/1.1622436
[8] A.A. Mohanan, R. Parthiban, and N. Ramakrishnan, "Shadow mask assisted direct growth of ZnO nanowires as a sensing medium for surface acoustic wave devices using a thermal evaporation method," J. Micromech, Microeng. **26**, 025017 (2016). https://doi.org/1088/0960-1317/26/2/025017
[9] Zh. Wen, Ch. Li, D. Wu, A. Li, and N. Ming, "Ferroelectric-field-effect-enhanced electroresistance in metal / ferroelectric / semiconductor tunnel junctions," Nature Materials. **12**, 617. (2013). https://doi.org/10.1038/nmat3649
[10] D.L. Cheng, K.S. Kao, C.H. Lo, C.H. Liang, L.P. Chan, C.W. Tsung, and Y.Y. Li, "Ultraviolet sensing system using ZnO based surface acoustic wave oscillator," in: *Proceedings of the 3rd International Conference on Industrial Application Engineering.* **435**, (2015), pp. 435-438. https://doi.org/10.12792/iciae2015.076
[11] Wa. Wen-Bo, G. Hang, H. Xing-Li, X. Wei-Peng, C. Jin-Kai, W. Xiao-Zhi, and L. Ji-Kui, "Transparent ZnO/glass surface acoustic wave based high performance ultraviolet light sensors," Chin. Phys. B, 24(5), 057701 (2015). https://doi.org/10.1088/16741056/24/5/057701
[12] R.R. Jalolov, B.N. Rustamova, Sh.Z. Urolov, and Z.Sh. Shaymardanov, "The influence of size on the photoluminescence properties of ZnO nanostructures," Uzbek Journal of Physics, **23**(2), 40-44 (2021). https://doi.org/10.52304/.v23i2.238
[13] B.D. Yao, V.F. Chang, and F. Wang, "Formation of ZnO nanostructures by a simple way of thermal evaporation," Appl. Phys. Lett. **81**, 757 (2002). https://doi.org/10.1063/1.1495878
[14] P. Narin, E. Kutlu, G. Atmaca, A. Atilgan, A. Yildiz, and S.B. Lisesivdin, "Structural and optical properties of hexagonal ZnO nanostructures grown by ultrasonic spray CVD," Optik, **168**, 86-91 (2018). https://doi.org/10.1016/j.ijleo.2018.04.089
[15] A.N. Gruzintsev, V.T. Volkov, "Modification of the electrical and optical properties of the ZnO thin films under the ultraviolet radiation", Physics and technology of semiconductors, **45(11)**, p.1476-1480 (2011). http://journals.ioffe.ru/articles/viewPDF/7556
[16] L.V. Grigoriev, I.S. Morozov, N.V. Zhuravlev, A.A. Semenov, and A.A. Nikitin, "Photoluminescent and photoelectric properties of the ZnO-LiNbO$_3$ thin-film structure in the ultraviolet and visible spectral ranges," Physics and technology of semiconductors, 54(3), (2020). https://www.springerprofessional.de/en/photoluminescence-and-photoelectric-properties-of-the-zno-linbo3/17934476
[17] Z.T. Azamatov, M.A.Yuldoshev, N.N. Bazarbayev, "Effect of gamma irradiation on optical properties of lithium niobate and LiNbO$_3$:Fe crystals," Izvestiya vuzov. Physics, **2**, 106-113 (2023).

ДЕЯКІ ВЛАСТИВОСТІ НАПІВПРОВІДНИКОВО-СЕГНЕТЕЛЕКТРИЧНИХ СТРУКТУР
Закір'ян Т. Азаматов, Шафіра Б. Утамурадова, Муроджон А. Юлдошев, Нурлан Н. Базарбаєв
Інститут фізики напівпровідників та мікроелектроніки Національного університету Узбекистану,
вул. Янги Алмазор, 20, Ташкент, Узбекистан

У статті представлені властивості напівпровідникових сегнетоелектричних структур, що складаються з наностержнів ZnO, вирощених при низьких температурах гідротермальним методом на підкладках LiNbO$_3$ та LiNbO$_3$:Fe. Отримані структури аналізували за допомогою скануючого електронного мікроскопа, фотолюмінесценції та спектрофотометрії. СЕМ зображення та спектри; спектри поглинання; спектри фотолюмінесценції в ультрафіолетовому і видимому діапазонах. Дослідження показали можливість використання поряд з іншими гідротермального методу синтезу Zn(NO$_3$)$_2$6H$_2$O та C$_6$H$_{12}$N$_4$ для отримання масивів наностержнів ZnO як чутливого елемента датчиків УФ-випромінювання на основі ПАР.
Ключові слова: *наностриж нії; фотолюмінесценція; скануючий електронний мікроскоп; спектр поглинання*

SIMULATION OF RADIONUCLIDE DISPERSION IN THE AIR AND ON THE SOIL SURFACE†

Maryna F. Kozhevnikova*, Volodymyr V. Levenets
NSC "Kharkiv Institute of Physics & Technology" NASU,
1, Academichna str., 61108, Kharkiv, Ukraine
Corresponding Author: marko@kipt.kharkov.ua
Received February 14, 2023; revised March 21, 2023; accepted April 7, 2023

Mathematical and numerical methods are used to simulate physical and chemical processes when building models of pollutants dispersion in the air and on the soil surface. Based on meteorological data and information on the source of emissions, these models characterize both the primary pollutants entering the atmosphere directly and the secondary ones formed as the result of complex chemical reactions. These models are important for the air quality management system, as they allow monitoring emissions into the atmosphere, predicting their distribution, as well as developing effective strategies intended for reducing harmful substances in the atmosphere. The article presents an overview of computational methods used to simulate the pollutants dispersion in atmospheric air and on the soil surface, such as the Gaussian torch model, the Lagrangian dispersion stochastic model, and the Eulerian model of atmospheric diffusion. The practical application of the considered models showed sufficient reliability and validity of the air and soil pollution levels forecast. The simulation uses computer programs that include algorithms for solving the mathematical equations that control pollutant dispersion. The dispersion models are used to estimate the concentration of air pollutants or toxins. They can also be used to predict future concentrations under certain scenarios. They are useful for studying the pollutants that disperse over long distances and can initiate reactions in the atmosphere. Such software products are as follows: AEROPOL, AERMOD, GRAL, TAPM CSIRO, CALPUFF, HYSPLIT, etc. A method of processing information about the pollution sources and the environmental parameters, based on the HYSPLIT program, is proposed to form maps of the volume and surface activity of radionuclides. This method was applied to analyze the process of the plutonium isotopes dispersion as a result of the movement of air masses in the places of fires in April 2020 in the exclusion zone of the Chornobyl NPP, as well as the associated hazard for the population health and the environment.
Keywords: *turbulent diffusion equation, impurity scattering in the atmosphere, point source, near-surface concentration level, atmospheric pollution, volumetric activity of radionuclides.*
PACS: 89.60.Gg, 89.60-k

Currently, the atmospheric pollution is increasing due to the anthropogenic influence of industrial enterprises, nuclear power plants, transport, industrial and household waste dumps, and urban construction. The problem of environmental protection requires a large amount of experimental research invested in monitoring of the environment state. Environmental monitoring systems, which include automatic (stationary) and mobile air pollution monitoring stations, have been created to effectively control the quality of the atmosphere. One of the main tasks of environmental monitoring is the collection of data on concentration of pollutants. This information is necessary for further analysis and forecasting of air and soil quality when making management decisions as to ensuring the environmental safety. Monitoring of the environment state allows analyzing data and determining the impact of atmospheric pollution on the quality of the environment and on the health of population.

Theoretical studies are needed to develop models that include identification of pollution sources, quantification of pollutant release rates, understanding of the process of the emission transportation from the source to the point of discharge, and knowledge of the physical and chemical transformation processes of the released substances, that may occur during this transportation.

The creation of models for the estimation of the concentration fields and source parameters using the observation data and model representations of the impurity dispersion processes allows more reliable control of the main parameters of the technogeneous pollution of the area. This approach makes it possible to determine the information capability of the observation systems and to optimize the position and the number of sampling points.

THE TECHNIQUES OF SIMULATION OF THE POLLUTANTS DISPERSION IN THE ATMOSPHERIC AIR

When building models of air quality, mathematical and numerical methods are used to simulate physical and chemical processes that affect the substances dispersion in the atmosphere. Based on meteorological data and information about the source of emissions (emission concentration, smokestack height, etc.), these models characterize both primary pollutants, which enter the atmosphere directly, and secondary pollutants, which are formed as a result of complex chemical reactions in the atmosphere. These models are of great importance for the creation of an atmospheric air quality management system, as they allow controlling emissions into the atmosphere, predicting their dispersion and developing effective strategies for reducing harmful substances in the atmosphere.

The development and improvement of new models is associated with the development of computer technology and the appearance of previously unavailable satellite meteorological data. This allows taking into account a large number of

pollutants and their interaction, a large number of emission sources of various configurations, and the influence of complex atmospheric processes.

The process of the dispersion of pollutants occurs due to their being transferred by air masses and the diffusion caused by turbulent air pulsations. Almost all the impurities sooner or later deposit on the Earth's surface, the heavy ones – under the influence of the gravitational field, the light ones – as a result of the diffusion process. The pollutants get into atmospheric air, water, soil, and later into the living organisms. The assessment of contamination of the atmosphere and the underlying surface with impurities is carried out using mathematical models built on the basis of partial differential aerodynamic equations, as well as their finite-difference approximations. These models are also known as atmospheric dispersion models.

Theoretical and experimental studies of processes of the impurities diffusion and features of their spatio-temporal dispersion are the basis for an objective assessment of the state and trends of changes in atmospheric air pollution of soil, vegetation, and water bodies.

The most significant amount of fundamental research in the field of the environment is performed in the USA and European countries. In many countries, the air quality is assessed using the AQI index (air quality index). This index is used by all the world environmental government bodies to inform the public about the level of air pollution, as well as to forecast air pollution [1, 2].

To obtain indicators of atmospheric air pollution, some up-to-date models for calculating the concentrations of pollutants in the atmosphere are needed.

The success of developing air pollution models depends on understanding the laws of pollutants dispersion. The main factors determining the dispersion of a pollutant are advection (horizontal transport) and vertical diffusion. The wind speed determines both the mechanism of transportation of impurities and atmospheric turbulence [3].

The input information that is required when building a model includes three main groups of parameters: source parameters, environment parameters, and boundary conditions.

The source parameters include the rate of the impurity release, the type of the source (point, linear, surface), the nature of the source functioning (instantaneous, continuous), the properties of the pollutant, and its chemical activity.

The group of environmental parameters includes: the temperature gradient (vertical, horizontal), wind direction and speed, cloud cover, radiation, precipitation, rate of temperature and pressure change, values of background concentrations of impurities in the air.

The group of boundary conditions is formed by the surface properties (roughness, topography), inversion height, surface temperature, and surface air currents.

The accuracy of the model depends on the completeness of accounting for the variables included in each group. The simulation allows obtaining the dispersion of impurity concentration in space and time, evaluating the processes of impurity deposition, washing-out, chemical interaction, and sorption [3].

There are four main approaches to solving the problem of the substance scattering of in a moving gaseous medium [4]:

1. Direct experimental research, which is related to the use of instrumental methods for determining the form of emissions, trajectory of the pollution spread, diffusion conditions. This approach is used to solve tasks of operational forecasting and management, but not long-term planning.

2. The theory of similarity is used in modeling in those cases when, it is impossible to correctly assess the boundary conditions and directions of air flows due to the complexity of the topography and buildings, and therefore the hydraulic models have to be used.

3. The theory of pollutant diffusion is based on the law of mass conservation. It assumes the uniformity of the main movement along the coordinate axes and the use of the common methods of averaging the turbulent characteristics consisting of average and pulsational components. The solution of the semi-empirical diffusion equation is widely used to calculate the dispersion of impurities in the atmosphere.

4. The classical statistical theory describes atmospheric turbulence in terms of its intensity, scale, and spectral properties. It allows studying the history of the movement of individual particles and determining the statistical characteristics necessary for the description of diffusion.

The type of random process, used in the study of turbulence and diffusion, can be characterized as stationary, homogeneous, isotropic, and Gaussian.

Since each approach has its advantages and disadvantages, the choice of any of the listed approaches depends on the fact how adequate the conditions of the pollution process under study are in this case. The progress in the development of atmospheric diffusion understanding is achieved by combining the use of the theory with carefully planned observations and experiments.

One of the last stages of simulation is related to the choice of the coordinate system. Some models use the moving Lagrangian coordinate system, some other ones use the fixed Euler coordinate system. The models using Lagrangian coordinates allow determining the substance concentration at any moment along the curvilinear trajectory of its dispersion, and here it is not necessary to integrate the model along all three spatial coordinates. The model with Euler coordinates allows obtaining a solution at any point in space and for any moment of time. Such a model turns to be convenient in the case of a large number of point sources.

The final stage in the process of the model building is the selection of its basic version, which is characteristic of the adopted approach to simulation. This basic model can be static or dynamic, deterministic or stochastic, linear or non-

linear, stationary or non-stationary by analogy with the models, which are used in chemical technology. Fig.1 presents the classification of mathematical models designed for the atmospheric pollution assessment and forecast.
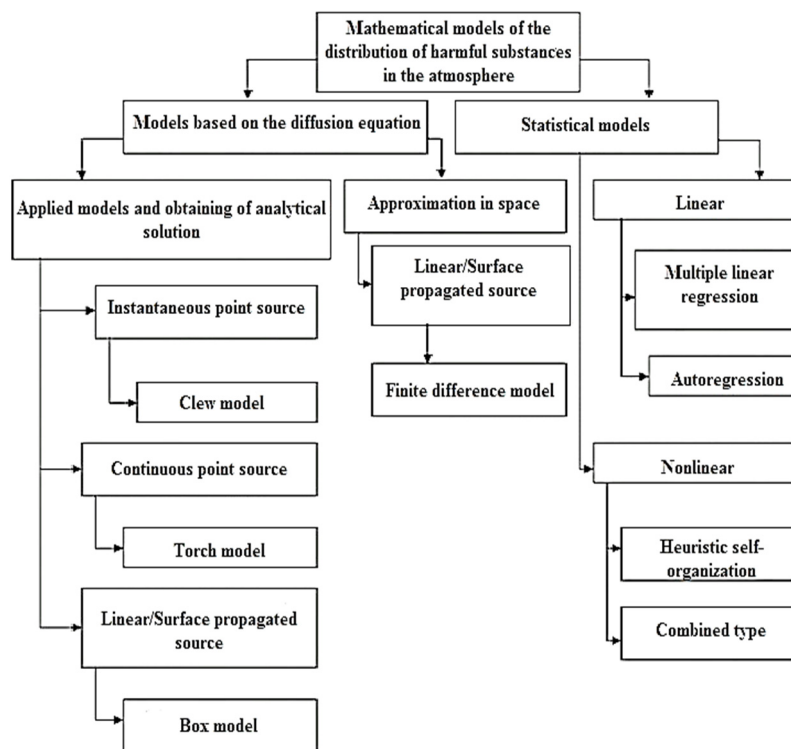
Figure 1. Block diagram of the mathematical models classification of the pollutants dispersion in the surface layer of the atmosphere

Forecasting models are used to simulate atmospheric air pollution processes. Long-term and operational forecasting models are distinguished. For long-term forecasting, the calculation (analytical, approximation) models, based on the solution of the turbulent diffusion equation, have become the most widespread. They are "torch", "clew", "box" models, and finite-difference ones. For operational forecasting, statistical models of linear and non-linear regression, as well as models of heuristic self-organization (method of group accounting of arguments) are widely used. For operational forecasting of air pollution in case of emergency and volley emissions, the calculation (analytical methods) " clew " models should be used, which are employed to forecast the spread of impurities from instantaneous point sources. The most common are forecasting models that are obtained with the solution of the turbulent diffusion equation taken into account. The phenomena of pollutant transfer and diffusion are described by the equation [2]:

$$\frac{dC}{dt} = div(K \cdot gradC) - grad(CU) \pm Q \tag{1}$$

$$\text{turbulent diffusion} \qquad \text{convection} \qquad \text{source}$$

where C is the concentration of the pollutant; $K = (k_x, k_y, k_z)$ is the vector of turbulent diffusion coefficients; $U = (u, v, w)$ is the vector of the averaged velocity field of the air medium; Q is the pollutant emission rate of the source.

The choice of the initial and boundary conditions, which are necessary to solve equation (1), depends on the operating conditions of the source and the properties of the underlying surface.

On the basis of equation (1), four main types of models are obtained: "clew", "torch", "box" and finite-difference ones. In general, solving equation (1) using analytical methods is impossible. This becomes possible either by simplifying the equation or by using numerical methods.

Thus, the presence in equation (1) of the assumptions about the absence of convective transfer, non-isotropy of the medium and the location of the source outside the analyzed area, leads to the equation:

$$\frac{\partial C}{\partial t} = k_x \frac{\partial^2 C}{\partial x^2} + k_y \frac{\partial^2 C}{\partial y^2} + k_z \frac{\partial^2 C}{\partial z^2}. \tag{2}$$

The fundamental solution of this equation has the form of Gaussian function. This solution is used in the models of "clew" and "torch" type.

The model of "clew" type assumes an instantaneous source of pollution. The process of transferring the forming cloud ("clew") from the source under the wind influence is considered in the moving coordinate system. The equation of the non-stationary Gaussian model has the form:

$$C(x, y, z, t) = \frac{Q}{(2\pi)^{\frac{3}{2}}\sigma_x\sigma_y\sigma_z} \cdot exp\left\{-\frac{1}{2}\left[\left(\frac{x-U_t}{\sigma_x}\right)^2 + \left(\frac{y-V_t}{\sigma_y}\right)^2 + \left(\frac{z-W_t}{\sigma_z}\right)^2\right]\right\} , \tag{3}$$

where C(x, y, z, t) is the concentration of the pollutant at the point with coordinates x, y, z at time t; U, V, W are the average values of wind speed in x, y, z directions at time t; σ_x, σ_y, σ_z are the standard deviations of "clew" dimensions in x, y, z directions, respectively; Q is the amount of the substance released by the pollution source at time t [4].

The model allows determining concentrations on the curved trajectory of the "clew" movement. In addition, it allows taking into account the change in atmospheric stability. Operating with the "clew" model involves real-time observation of the wind field. Integrating the model over space allows obtaining a solution for the instantaneous volumetric source.

The shortcomings of the model include: the requirement of a large amount of meteorological data (measurements of wind speeds along all three coordinates), the difficulty of determining the initial height of the gravity center of the "clew", the complexity of the calculation program.

The "torch" model (stationary Gaussian model) is based on the assumption of a continuously operating point source. It is obtained by integrating equation (1) over time. The equation of the "torch" model looks like this:

$$C(x, y, z, H) = \frac{Q}{2\pi\sigma_y\sigma_z U} exp\left[-\frac{1}{2}\left(\frac{y}{\sigma_y}\right)^2\right]\left\{exp\left[-\frac{1}{2}\left(\frac{z-H}{\sigma_z}\right)^2\right] + exp\left[-\frac{1}{2}\left(\frac{z+H}{\sigma_z}\right)^2\right]\right\}, \tag{4}$$

where C(x, y, z, H) is the concentration dispersion along the x, y, z coordinates; Q is the pollutant release rate; U is the average wind speed; σ_y , σ_z are standard deviations of the "torch" dimensions in the horizontal and vertical directions at the given x; H=h+Δh is the effective height of the "torch"; h is the pipe height; Δh is the rise of the "torch") due to its buoyancy [4].

The major advantage of the "torch" model is its simplicity and the possibility to calculate the concentration fields basing on a relatively small number of experimentally determined parameters.

The "box" model is used for the rough estimation of the pollutant released from large surface sources. In this model, it is assumed that inside the analyzed volume of air, the concentration does not depend on the coordinates y and z, and the particles of the substance do not move relative to the environment. The wind speed is assumed to be the same with height. Such an assumption is usually made in the absence of more precise meteorological data. Besides, it is necessary the diffusion of the jet in the transverse and vertical directions to be small. This assumption is valid if the source of pollution is limited by buildings, topographic irregularities (mountains, hills) and the inversion height.

In addition to the single "box" model, there are known options for building of the multi-box models intended to estimate the concentrations from the distributed emission sources. In these cases, the atmosphere is divided on the system of "boxes", and then the impurity fluxes between the boxes and the concentrations in each of them are calculated. The "boxes" are usually bounded below by the earth surface, and above by the height of the inversion or an arbitrarily chosen upper boundary.

Such a model is, in fact, a finite-difference analogue of the diffusion equation under the condition of vertical homogeneity of the medium, the absence of diffusive components, and the transfer occurring only due to advection being taken into account. Basing on such models, the impurity concentrations in the entire region are calculated for the same time.

The multi-box model has the following disadvantages: 1) the complete mixing is assumed to occur in the vertical direction; 2) the absence of diffusion between the "boxes" is assumed; 3) the accuracy of the model corresponds to the accuracy of the first-order differential equation.

Another broader class of models was obtained as a result of replacing the diffusion equation with simpler equations and using numerical methods for their solution, they are "finite-difference" models. These models are based on the approximation of the air basin by three-dimensional cells to obtain the numerical solution. The main problems here are due to the model stability and accuracy.

The practical application of the models considered above showed sufficient reliability and validity of the forecast of air pollution levels created by individual powerful point sources.

Subject to the implementation methodology, the known methods of forecasting atmospheric processes can be divided into numerical, statistical, and pattern recognition methods [4, 5].

The forecasting methods, being developed on the basis of mathematical description of the impurities dispersion, in which the turbulent diffusion equation is used, are numerical. Such methods are universal with respect to the source, medium characteristics, and boundary conditions and allow the use of turbulent exchange parameters. Numerical methods of forecasting are used to solve the following tasks:

1. Forecast of maximum impurity concentrations from the sources, that is, the calculation of maximum concentrations created at a certain distance from the source.

2. Forecast of integral characteristics of air pollution from the plane source.

3. Forecast of the highest concentration from dispersed sources.

For the forecast of air pollution from individual sources and from a group of sources, the methods of numerical integration of the atmospheric diffusion equation are used directly.

The forecast of air pollution in cities and industrial areas using the statistical models is carried out by statistical methods. The latter ones are based on statistical analysis of observations. It is assumed that during the analysis period, as well as during the forecast period, the emissions and location of the sources practically do not change. This is associated with certain errors and limitations of the results of analysis and forecasts, which are not characteristic of numerical methods, so the specified assumption is used for relatively short forecast periods, i.e. from a few hours to a few days. Besides, with a large number of sources and their insufficient power, it can be assumed that the increase in emissions from some of them is compensated by the decrease from the other ones. Therefore, the growth of average and total air pollution in the city is mainly associated with the changes in meteorological conditions or the synoptic situation.

The Important factors for ensuring the accuracy of the air pollution forecast are the choice of model parameters and the synoptic situation and sets of meteorological factors being taken into account.

To study the influence of meteorological conditions of air pollution, it is possible to apply the method of pattern recognition. The task of identifying the sources of air pollution can be considered as a typical task of pattern recognition. The image recognition is the classification of the initial data into a certain class using the choice of the existing features or properties, which characterize these data, from the total set of features. The subject of recognition combines a number of scientific disciplines. They are combined by the search for a solution to the common problem of distinguishing elements, which belong to a specific class among many different elements belonging to several classes.

ANALYSIS OF THE SOFTWARE DESIGNED FOR SIMULATION OF ATMOSPHERIC POLLUTION DISPERSION

The simulation of atmospheric dispersion is the mathematical simulation of the process of the pollutant's dispersion in the surrounding atmosphere. The simulation is carried out using computer programs that include algorithms to solve the mathematical equations, which govern the pollutant dispersion. The dispersion models are used to estimate concentrations of air pollutants or toxins emitted from the sources, such as industrial enterprises, motor traffic, or accidental emission of chemicals. They can also be used to predict future concentrations under certain scenarios. They are most useful for studying pollutants that disperse over long distances and can initiate reactions in the atmosphere.

Many up-to-date programs, designed to simulate dispersion, include a preprocessor module for inputting meteorological and other data, and a postprocessor module for graphical representation of the output data and mapping of the area exposed to the air pollutants. The diagram of the area under exposure may also include isopleths showing the areas having from minimum to high concentration, which represent the greatest risk for health.

In many countries of Europe and in the USA, currently, when numerically predicting the spread of impurities in the boundary layer of the atmosphere, the Gaussian "torch") model, or the dispersive Lagrangian stochastic model, or the Eulerian model of atmospheric diffusion is chosen.

The Gaussian model assumes that pollutant dispersion occurs in a Gaussian dispersion. Such models are usually used to predict the "torch") emitted by a stationary emission source. Gaussian-type models dominate in the majority of regulatory documents of many countries of the world, regulating the procedure and rules for calculating surface concentrations up to the distances of 50 km.

The Gaussian "torch" model functions in a stationary mode, the meteorological parameters do not change in time and space. This model is most often used to predict the spread of long-term atmospheric pollution from the sources located at the level of the earth surface or at some height. The application of the model is limited to the local scale. This technique is recommended by the United States Environmental Protection Agency (EPA) for calculations that are of a regulatory nature.

The Gaussian "torch" model is implemented in many software products. In fact, this is currently the most common method of atmospheric pollution simulation: CALINE4 [6], HIWAY2 [7], CAR-FMI [8], AEROPOL [9], ADMS5 [10], etc.

One of the most well-known systems for simulation of the pollutants spread in atmospheric air, which uses the Gaussian "torch" technique, is AERMOD [11].

AERMOD is the model developed by AERMIC (a joint working group of scientists from AMS (American Meteorological Society) and EPA) for regulation of atmospheric air pollutions. AERMOD is an up-to-date advanced "torch" model. This model uses the pollutant dispersion based on the atmospheric boundary layer turbulence structure and the scaling concept; it is capable of handling simple and complex terrain. AERMOD considers pollution from three types of "torches": main, indirect and penetrating (Fig. 2) [12].

For steady conditions, the expression for AERMOD concentration (C_s) has the Gaussian form and is similar to that used in many other steady-state "torch" models:

$$C_s(x, y, z) = \frac{Q}{u\sigma_{zs}\sqrt{2\pi}} F_y \sum_{m=-\infty}^{\infty} \left[exp\left(\frac{(z - h_{es} + 2mz_{ieff})^2}{2\sigma_{zs}^2}\right) + exp\left(\frac{(z + h_{es} + 2mz_{ieff})^2}{2\sigma_{zs}^2}\right)\right], \qquad (5)$$

$$F_y = \left(-\frac{1}{\sqrt{2\pi}\sigma_y} exp\left(-\frac{y^2}{2\sigma_y}\right)\right) \qquad (6)$$

where u is the wind speed; F_y is the lateral dispersion function; z_{ieff} is the effective mechanical height of the mixed layer; σ_{zs} is the total vertical dispersion; h_{es} is the height of the "torch") (the height of the emission source plus the height of the "torch" itself).
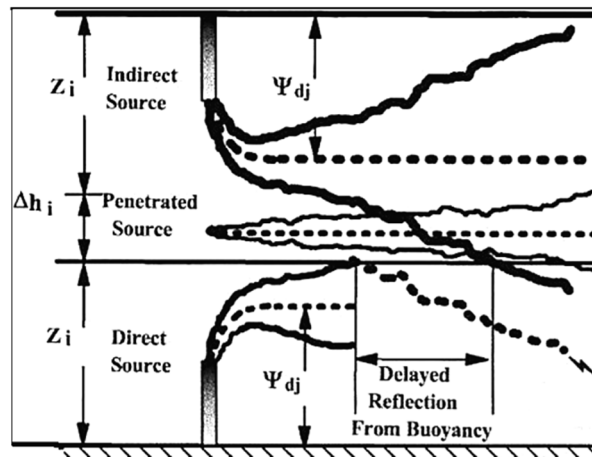
Figure 2. Schematic of the torch simulation in AERMOD [12]

In AERMOD, the total concentration (C) is calculated by formula (7) by summing the contribution from three sources:

$$C(x, y, z) = C_d(x, y, z) + C_p(x, y, z) + C_r(x, y, z). \tag{7}$$

The concentration from the main source is calculated by formula:

$$C_d = (x, y, z) = \frac{Qf_p}{\sqrt{2\pi}u} F_y \sum_{f=1}^{2} \sum_{m-0}^{\infty} \frac{\lambda_f}{\sigma_{zj}} \left[exp\left(-\frac{(z - \psi_{dj} - 2mz_j)^2}{2\sigma_{zj}^2} \right) + exp\left(-\frac{(z + \psi_{dj} + 2mz_j)^2}{2\sigma_{zj}^2} \right) \right], \tag{8}$$

$$\psi_{dj} = h_s + \Delta h_d \frac{xw_j}{u}, \tag{9}$$

where Δh_d is the plume height of the emission source; h_s is the plume height, with the height of the emission source taken into account; w_j is the vertical velocity for the upflow (j = 1) and dispersion of the downflow (j = 2); σ_{zj} and ψ_{dj} are the parameters of the emission source height and vertical dispersion. The subscript j=1 is used for the upflows and j=2 for the downflows.

The concentration from the indirect source is calculated according to the following formula:

$$C_r(x, y, z) = \frac{Qf_p}{\sqrt{2\pi}u} F_y \sum_{f=1}^{2} \sum_{m=0}^{\infty} \frac{\lambda_f}{\sigma_{zj}} \left[exp\left(-\frac{(z + \psi_{rj} - 2mz_j)^2}{2\sigma_{zj}^2} \right) + exp\left(-\frac{(z - \psi_{dj} + 2mz_j)^2}{2\sigma_{zj}^2} \right) \right], \tag{10}$$

where, $\psi_{rj} = \psi_{dj} - \Delta h_i$, and Δh_i is the plume from an indirect source.

For the penetrating source the expression for concentration (C_p) has Gaussian form in both vertical and transverse directions. The concentration caused by this source is determined by the formula:

$$C_p(x, y, z) = \frac{Q(1 - f_p)}{u\sigma_{zp}\sqrt{2\pi}} F_y \sum_{m=-\infty}^{\infty} \left[exp\left(-\frac{(z - h_{ep} + 2mz_{ieff})^2}{2\sigma_{zp}^2} \right) + exp\left(-\frac{(z + h_{ep} + 2mz_{ieff})^2}{2\sigma_{zp}^2} \right) \right], \tag{11}$$

where z_{ieff} is the height of the upper reflecting surface in the stable layer, and σ_{zp} is the total dispersion for the penetrating source.

The complete AERMOD simulation system consists of two processors: a meteorological preprocessor (AERMET) and a mapping program (AERMAP), as well as the dispersion model itself. The detailed information on the development of the model is described on the EPA resource [11].

The Lagrange's method and the Euler's method for describing turbulence are used when solving different problems, independently or mutually complementing each other.

The Euler's models are built on the solution of the semi-empirical equation of turbulent diffusion, which is integrated on a finite-difference Euler's grid. The representation of turbulence by Euler is related to the assignment of the field of random variables in space and time by means of an equation or a system of equations, such as the equations of hydrodynamics. By successively averaging these equations, a system of equations describing any processes in a turbulent environment is obtained. In this case, the argument is the set of coordinates of points in space, and the components of the velocity vector of the medium movement and the values of the impurity concentration at this point in space are functions of these coordinates and time [3, 13].

The Eulerian model of atmospheric diffusion rather easily solves the problems associated with predicting the mesoscale transfer of emissions. However, due to the use of a relatively coarse grid (horizontal linear size is several kilometers or more) there are difficulties in presenting concentration gradients from the point and line sources [3].

The Eulerian models differ among themselves subject to the method of obtaining the meteorological values, i.e. wind speed and turbulent diffusion coefficient. These models, unlike the Gaussian models, are rather complex and require significant software processing time. Currently, there are a large number of implemented Eulerian models of pollutant transport in the atmosphere. However, many of them are suitable only for the areas of about several tens of kilometers, what does not allow studying the long-range impurity transfer.

In the Lagrange method, an infinitesimal particle with coordinates at a fixed time is considered. And when it is moving, its coordinates are considered at the subsequent moments as functions of the time of the initial coordinates, with further averaging of the trajectory parameters or groups of trajectories according to the environment fluctuations. The particle velocities are derivatives of coordinates and time. The impurity from a point source is usually represented as an ensemble of discrete "balls" or particles. For each "ball" the trajectory of its movement in the time- and space-varying wind field is calculated and the diffusion transfer is also calculated. This is done, for example, using the stochastic models, and often the turbulent structure is assumed to be the Gaussian. Studying the transfer and scattering of a large number (several thousand) of tracer particles allows simulating the drift and dispersion of the impurity in the turbulent atmospheric boundary layer. The impurity concentration at any point in space is represented as the sum of contributions from each Lagrangian element.

The Lagrangian model of the atmospheric pollution spread is represented as a sequence of "torches", inside each of which the substance has a certain dispersion. This approach is more flexible than the principle of the Gaussian "torch", as it is closest to the physical essence of the matter scattering in the atmosphere. The Lagrange model allows simulating the process that is non-stationary in time and space, and quite correctly takes into account the changes in the direction of the wind, the complex topography of the area, and chemical transformations of the matter. This technique gives correct results when simulating both the instantaneous or short-term emission and the long-term emission, for example, for a seasonal or annual cycle. The Lagrange model is an effective tool in the study of atmospheric pollution propagation processes. The approach, in which the movement of individual particles is tracked, gives more opportunities to obtain qualitatively new results, as compared to the Euler approach. However, solving the problem of describing the matter movement by calculating the speed of its movement in the nodes of the coordinate grid imposes a number of restrictions. For example, if the substance is a certain amount of radionuclides, then the process of describing the decay and/or transformation into other types of radioactive particles with this approach is difficult. On the contrary, the Lagrangian approach offers a simple solution to this problem.

A few decades ago, the use of Lagrange models was practically impossible due to the large volume of necessary calculations, but now, with the growth of up-to-date computing power, it is quite possible.

The application of the Lagrangian model is justified, when it is important to take into account temporal and spatial changes in meteorological conditions. Also, the model makes it possible to estimate the pollutant spread in calm weather much better.

This class of models is relatively young, as compared to the Gaussian "torch" model. There are several software implementations of this approach: GRAL [14], TAPM CSIRO [15], CALPUFF [16], HYSPLIT [17].

One of the examples of the Lagrangian cloud model implementation is HYSPLIT [18]. More precisely, HYSPLIT uses a combined Lagrangian-Eulerian model, which is widely used in the up-to-date pollutant dispersion modeling systems.

In order to take into account the shortcomings of the analyzed approaches, some hybrid models of impurity propagation in the atmosphere were proposed, in which the Lagrangian dispersive stochastic approach is used at the initial stage of emission propagation, and the Eulerian model of atmospheric diffusion is used to predict the further transfer and transformation of pollution over long distances. Nevertheless, when using this method, there are still problems associated with the combination of two different approaches for the description of the impurity.

To obtain the pollutant concentration cards, the task of selecting the necessary software product arises. Installing and running all the pollutant propagation modeling systems is a time-consuming task: for each software product, it is necessary to find the raw data in a certain format, learn the architecture and startup procedure, and install certain software and hardware. Therefore, the choice of the most effective system is based on the study of domestic and foreign research.

As a result of the up-to-date models analysis, the HYSPLIT (HYbrid Single-Particle Lagrangian Integrated Trajectory), was chosen, which had been developed at the NOAA Air Mass Laboratory (USA) and the Australian Bureau of Meteorology [19].

The HYSPLIT model allows for three-dimensional modeling of the process of formation and spread of an air pollution cloud from the given source. The HYSPLIT model combines two classical approaches: Lagrangian and Euler, the advection and diffusion equations are solved independently in the Lagrangian formulation, and the concentration calculations are performed within the framework of the Euler approach on the fixed spatial grid. The input meteorological information that is required for HYSPLIT is borrowed from the calculation data of the meteorological models, which are based on the results of the in-situ measurements. Generally, this information is presented on the regular spatial grid and includes the data on the vertical dispersion of horizontal and vertical wind components, temperature and pressure, as well as the surface pressure, and some other parameters.

HYSPLIT functions in the dialog mode and has a detailed user manual; it can be operated online from the NOAA page or via an executive program.

The user kit contains a library of programs for each specific application. There is a need to have a grid of weather data in one of several geographic projections at certain intervals. This data, in the form of the archival materials or the results of weather forecast models, are available on the Internet in the form of the already formatted data for input into HYSPLIT.

In addition, there are programs intended to convert NOAA output information, The National Center for Atmospheric Research (NCAR), or European Center for Medium-Range Weather Forecasts (ECMWF) source data into the format, which is suitable for the HYSPLIT model.

The impurities concentration in the air is calculated at the points of intersection of the grid coordinates (in latitude and longitude) for the air flows, and for the individual particles – in the form of cell-averaged concentrations. The model contains a ground coordinate grid, the sizes of bumps, and the terrain information at 1° resolution in the Northern Hemisphere. The model allows consideration of dry and wet deposition of impurities, radioactive decay and restoration of the suspension state.

The main initial parameters for the simulation are as follows:
• The initial time (year, month, day, hour);
• The position (initial values of latitude, longitude and altitude);
• The initial time and duration of dispersion (i.e. run duration);
• The impurity characteristics (number of types, speed and duration of the radiation);
• The size of the calculation grid (including the mixing height and the height of each vertical level on the concentration grid);
• The particle properties (diameter, density and shape, deposition rate, molecular weight, coefficient of chemical interaction with the surface, diffusion rate, half-life, suspension rate, etc.) and sampling time.

Currently, in some Eastern European countries, all the calculations of atmospheric pollution are carried out applying special software tools, i.e. the unified programs for calculating atmospheric pollution, which are an appendix to "Methods for calculation of the harmful substances concentration in the atmospheric air" [20]. In 2018, its new edition came into force, but the approach to simulation had not changed significantly ("Methods for calculating the dispersion of emissions of harmful (polluting) substances in the atmospheric air" [21]).

The unified program for the calculation of atmospheric pollution allows determining the concentrations of pollutants in atmospheric air by calculation. The program can be applied to any sources of emissions of polluting substances, regardless of which branch of the national economy they belong to.
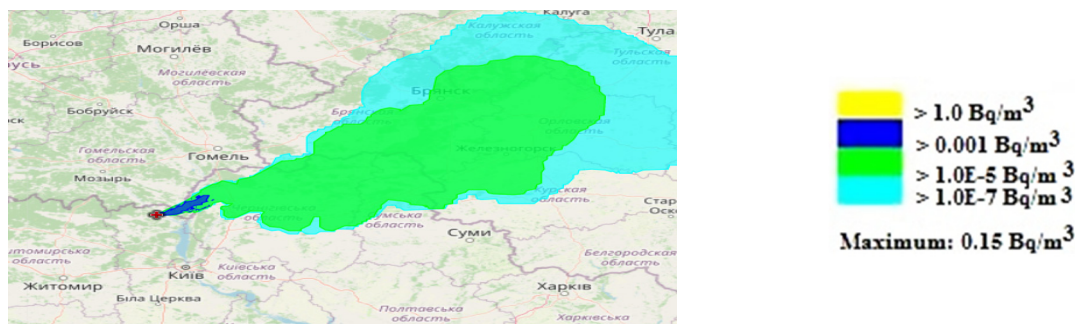
A number of software products are based on this approach: the "Ecolog" program series of the "Integral" company [22], the Unified Program for the Calculation of Atmospheric Pollution "ECOcenter-Standard" [23], and others.

METHODOLOGY OF PROCESSING THE INFORMATION ON THE RADIONUCLIDES DISPERSION IN THE AIR AND ON THE SOIL SURFACE

Adaptation of the modeling system to a specific region or a specific task is a separate complex task [24, 25]. The method of processing information about pollution sources and environmental parameters for the formation of pollutant concentration maps consists of the following stages: analysis of the parameters required for processing; simulation of the pollution dispersion; visualization of simulation results (both archival and predictive).

This method was applied to analyze the process of Pu isotopes dispersion due to the movement of air masses in the places where fires occurred in April 2020 in the exclusion zone of the Chernobyl NPP and the associated dangers for the population and the environment [25]. The HYSPLIT program was used to study the pollutants spatial dispersion.

The maps of volumetric and surface activity of radionuclides in the air and in the process of their falling on the ground in the period of April 8-13, 2020 were constructed. Fig. 3 presents the map of Pu radionuclides volumetric activity in the air on April 9, 2020, due to the fire in the area of Kopachi village to Chistogalivka village.

Figure 3. Volumetric activity of Pu isotopes in the air on April 9, 2020 due to the fire in the area of Kopachi village to Chystohalivka village (per day), the source height being 20 m [25]

Fig. 4 presents the map of the surface activity of Pu isotopes in the process of their falling on the soil on April 9, 2020 in this area.

As a result of the analysis of the dispersion of Pu radionuclides in the territory under consideration, it was established that due to the presence of this element, the radioactivity in the air and in the process of radioactive particles falling on the ground was low. Despite the high radio toxicity of Pu isotopes, the contribution of their radioactivity to the radiation effect on the population during inspiration or consumption of food products will be insignificant.

The risk of fires in the exclusion zone of Chernobyl increases with the climate change, and the measures to prevent them should be considered in some emergency programs. This information will allow to gain some important insights about the dynamics of accumulation, transformation and migration of Pu and [241]Am isotopes. There is also an opportunity to study the impact of ionizing radiation from the fires in the exclusion zone of the Chernobyl NPP on the environment.

Figure 4. Surface activity of Pu isotopes in the process of their falling on the ground on April 9, 2020 due to the fire in the area of Kopachi village to Chistohalivka village (per day), the source height being 20 m [25]

CONCLUSIONS

An analysis of the up-to-date methods of simulation of the pollutants dispersion in atmospheric air, as well as the software complexes, which are based on them, has been carried out.

A method of processing the information about the pollution sources and environmental parameters for the formation of pollutant concentration maps, based on the HYSPLIT software complex has been proposed.

The expediency of using the HYSPLIT pollutant dispersion model for the analysis of Pu isotopes dispersion due to the movement of air masses in the places, where fires occurred in April 2020 in the exclusion zone of the Chornobyl NPP, is shown.

ORCID Ids
Maryna F. Kozhevnikova, https://orcid.org/0000-0003-2464-3847; **Volodymyr V. Levenets,** https://orcid.org/0000-0002-6439-0576

REFERENCES
[1] AirNow, U.S. Environmental Protection Agency, Office of Air Quality Planning and Standards (OAQPS), Information Transfer Group, Research Triangle Park, NC 27711, https://www.airnow.gov/international/us-embassies-and-consulates
[2] S. Åström, L. Källmark, K. Yaramenka, and P. Grennfelt, *Доклад C598-R. Меры по обеспечению качества воздуха в Европе и Центральной Азии* [*Report C598-R. Air quality measures in Europe and Central Asia*], (IVL Swedish Environmental Research Institute, 2021), pp. 47. https://www.diva-portal.org/smash/get/diva2:1590828/FULLTEXT02 (in Russian)
[3] V.M. Gulyaev, and L.V. Dranishnikov, *Мониторинг окружающей среды* [*Environmental monitoring*], (Publishing house DSTU, 2005), pp. 354. (in Russian)
[4] M.E. Berlyand, *Прогноз и регулирование загрязнения атмосферы* [*Forecast and regulation of atmospheric pollution*], (Gidrometeoizdat, Leningrad, 1985), pp. 271. (in Russian)
[5] I.I. Marchuk, *Математическое моделирование в проблеме окружающей среды* [*Mathematical modeling in the problem of the environment*], (Nauka, Moscow, 1982), pp. 320. (in Russian)
[6] P.E. Benson, *Caline4 – A dispersion model for predicting air pollutant concentrations near roadways*, (Division of new technology and research, California, 1984), pp. 205.
[7] W.B. Petersen, *User's guide for HIWAY-2. A highway air pollution model. EPA600/8-80-018* (Research Triangle Park, N.C., U.S. EPA, 1980), pp. 83. https://nepis.epa.gov/
[8] Finnish meteorological institute, Dynamicum, FI-00560 Helsinki, Atmospheric dispersion models at the Finnish Meteorological Institute, CAR-FMI, https://en.ilmatieteenlaitos.fi/air-quality-models
[9] M. Kaasik, and V. Kimmel, International Journal of Environment and Pollution, **20(1-6),** 114-120 (2004). http://dx.doi.org/10.1504/IJEP.2003.004256
[10] Cambridge Environmental Research Consultants Ltd, Cardiff, Cambridge, CB2 1SJ, https://www.cerc.co.uk/environmental-software/ADMS-model.html
[11] *Aermod implementation guide*, (U.S. Environmental Protection Agency, 2022), pp. 37. https://gaftp.epa.gov/Air/aqmg/SCRAM/models/preferred/aermod/aermod_implementation_guide.pdf
[12] A. Melo, J. Santos, I. Mavroidis, and N. Reis Junior, Building and environment, **56,** 8-20 (2012). https://doi.org/10.1016/J.BUILDENV.2012.02.017
[13] M.E. Berlyand, *Современные проблемы атмосферной диффузии и загрязнения атмосферы* [*Modern problems of atmospheric diffusion and atmospheric pollution*], (Gidrometeoizdat, Leningrad, 1975), pp. 448. (in Russian)
[14] GralDispersionModel, Graz University of Technology, Institute of Thermodynamics and Sustainable Propulsion Systems, Inffeldgasse 25C, 8010 Graz, Austria, https://github.com/GralDispersionModel/GRAMM

[15] P. Hurley, *CSIRO Marine and Atmospheric Research Paper No.25*, (CSIRO, 2008), pp. 59. https://www.cmar.csiro.au/research/tapm/docs/tapm_v4_technical_paper_part1.pdf

[16] SRC, CALPUFF Modeling System, http://www.src.com/.

[17] National Oceanic and Atmospheric Administration, Air Resources Laboratory, NCWCP, R/ARL, Rm. 4204, 5830 University Research Court, College Park, Maryland 2074, HYSPLIT, ARL NOAA, https://www.arl.noaa.gov/hysplit/

[18] R.R. Draxler, and G.D. Hess, *Description of the HYSPLIT-4 Modeling System*, (Silver Spring: Air resources Laboratory, NOAA Technical Memorandum ERL ARL-224, 1997), pp. 22. https://www.arl.noaa.gov/documents/reports/arl-224.pdf

[19] R.R. Draxler, and G.D. Hess, Australian Meteorological Magazine, **47**(4), 295-308 (1998).

[20] *Методика расчета концентраций в атмосферном воздухе вредных веществ, содержащихся в выбросах предприятий (ОНД-86)* [*Methodology for calculating the concentrations in the atmospheric air of harmful substances contained in the emissions of enterprises (OND-86)*], (Leningrad: Gidrometeoizdat, 1987), pp. 94. (in Russian) http://www.sfund.kiev.ua/down/ond86.pdf

[21] *Методы расчетов рассеивания выбросов вредных (загрязняющих) веществ в атмосферном воздухе* [*Methods for calculating the dispersion of emissions of harmful (polluting) substances into the atmospheric air*], http://www.consultant.ru/document/cons_doc_LAW_222765/0fdf0dd96d8d3a3c60e96b9afe38abfccd1cfe96/

[22] *УПРЗА "Эколог" вер. 4.х Программа расчета рассеивания* [*Unified Atmospheric Pollution Calculation Program "Ecologist" version 4.x Scattering program*], https://forum.integral.ru/viewtopic.php?f=29&t=19176

[23] *УПРЗА «ЭКОцентр – Стандарт»* [*Unified Atmospheric Pollution Calculation Program "ECOcenter – Standard"*], https://eco-c.ru/ecology/программы-для-экологов/упрза-экоцентр-стандарт/

[24] M. Kozhevnikova, and V. Levenets, Radiation Science and Technology, **5**(3), 20-26 (2019). http://dx.doi.org/10.11648/j.rst.20190503.11

[25] M.F. Kozhevnikova, and V.V. Levenets, East Eur. J. Phys. **2,** 161 (2021). https://doi.org/10.26565/2312-4334-2021-2-14

МОДЕЛЮВАННЯ ПОШИРЕННЯ РАДІОНУКЛІДІВ У ПОВІТРІ ТА НА ПОВЕРХНІ ҐРУНТУ

Марина Ф. Кожевнікова, Володимир В. Левенець
Національний науковий центр «Харківський фізико-технічний інститут», НАНУ
вул. Академічна, 1, 61108, Харків, Україна

При побудові моделей поширення забруднюючих речовин у повітрі та на поверхні ґрунту використовуються математичні та чисельні методи для моделювання фізичних та хімічних процесів. На основі метеорологічних даних та інформації про джерело викидів, ці моделі характеризують як первинні забруднюючі речовини, що потрапляють безпосередньо в атмосферу, так і вторинні забруднювачі, що утворюються внаслідок складних хімічних реакцій. Ці моделі мають значення для системи управління якістю атмосферного повітря, оскільки дозволяють контролювати викиди в атмосферу, прогнозувати їх поширення та розробляти ефективні стратегії щодо скорочення шкідливих речовин в атмосфері. У статті наведено огляд обчислювальних методів, які застосовуються при моделюванні поширення забруднюючих речовин в атмосферному повітрі та на поверхні ґрунту, такі як модель гаусового факела, лагранжева дисперсійна стохастична модель, ейлерова модель атмосферної дифузії. Практичне застосування розглянутих моделей показало достатню надійність та достовірність прогнозу рівнів забруднення повітря та ґрунту. Моделювання виконується за допомогою комп'ютерних програм, що включають алгоритми для вирішення математичних рівнянь, які керують дисперсією забруднювача. Моделі розсіювання використовуються з метою оцінки концентрації забруднювачів повітря чи токсинів. Їх також можна використовувати для прогнозування майбутніх концентрацій за певних сценаріїв. Вони корисні для вивчення забруднюючих речовин, які розсіюються на великі відстані і можуть розпочинати реакцію у атмосфері. До таких програмних продуктів належать: AEROPOL, AERMOD, GRAL, TAPM CSIRO, CALPUFF, HYSPLIT тощо. Запропоновано метод обробки інформації про джерела забруднення та параметри навколишнього середовища для формування карт об'ємної та поверхневої активності радіонуклідів на основі програми HYSPLIT. Цей метод був застосований для аналізу процесу поширення ізотопів плутонію внаслідок руху повітряних мас у місцях виникнення пожеж у квітні 2020 р. у зоні відчуження Чорнобильської АЕС та пов'язані з цим небезпеки для населення та навколишнього середовища.

Ключові слова: *рівняння турбулентної дифузії; розсіювання домішки в атмосфері; точкове джерело; рівень приземної концентрації; забруднення атмосфери; об'ємна активність радіонуклідів*

X-RAY STRUCTURAL INVESTIGATIONS OF n-Si<Pt> IRRADIATED WITH PROTONS†

Sharifa B. Utamuradova[a,#], Aliona V. Stanchik[b,#], Dilmurod A. Rakhmanov[a,*]

aInstitute of Semiconductor Physics and Microelectronics at the National University of Uzbekistan
20 Yangi Almazar st., Tashkent, 100057, Uzbekistan
bScientific-Practical Materials Research Centre NAS of Belarus, Minsk, Belarus
Corresponding Author e-mail: dilmurod-1991@bk.ru; #e-mail: sh-utamuradova@yandex.ru; #e-mail: alena.stanchik@bk.ru

In this work, the effect of proton irradiation on the change in the structure of silicon samples doped with platinum was studied. The samples were irradiated with protons at a dose of 9×10^{14} cm^{-2} with an energy of 600 keV and a current of 1÷1.5 µA. To determine the change in the structure after irradiation, the methods of X-ray diffraction and atomic force microscopy were used. The obtained results indicate that doping with platinum does not lead to a modification of the cubic crystal structure of silicon, but only to minor changes in the structural characteristics and surface morphology. In this case, proton irradiation of a silicon single crystal with a dose of 9.0×10^{14} cm^{-2} with an energy of 600 keV leads to the formation of defects without the formation of an amorphous near-surface layer.
Keywords: *Silicon; platinum; diffusion; doping; irradiation; proton; X-ray diffraction*
PACS: 78.30.Am

INTRODUCTION

Today in the world, much attention is paid to the development of microelectronics and semiconductor materials science. The influence of various types of radiation on semiconductor materials is being intensively studied, the defects created in semiconductors under the action of radiation, as well as their effect on the electrical conductivity of semiconductor materials and structures based on them, are being studied, ways are being sought to eliminate the influence of radiation-induced defects caused by radiation. All this is considered one of the urgent tasks of our time.

The formation of radiation defects affects the physical processes in semiconductor materials and changes the parameters of devices based on them. Irradiation of semiconductor structures with low-energy protons changes their physical properties in the near-surface region, the depth of which can reach from 0.1 µm to 1 mm. The study of the formation of radiation defects upon irradiation with low-energy protons has both scientific and practical significance [1-3].

The interest in protons is due to the wide range of processed material depths and the absence of complex radiation complexes of defects with a high annealing temperature after proton irradiation. The main factors affecting the change in the properties of semiconductors after proton irradiation are the formation of new impurities as a result of nuclear reactions, radiation defect formation, and the accumulation of hydrogen atoms [4].

The aim of this work is to study the changes in the crystal structure and morphology of the near-surface region of n-Si silicon single crystals after doping with platinum and irradiation with protons using X-ray diffraction and atomic force microscopy.

MATERIALS AND METHODS

For the experiments, we used n-type silicon grown by the Czochralski method with a resistivity of 40 Ω×cm. The phosphorus dopant concentration in the initial n-Si single crystals was $7.3\times10^{13}÷7.1\times10^{15}$ cm^{-3}. Doping of silicon with platinum was carried out by the diffusion method with deposition of platinum atoms on the silicon surface in evacuated quartz ampoules at temperatures T = 900÷1250 °C for 2÷10 hours. Subsequent cooling of the samples occurred at different rates [5–7].

Samples of n-Si were polished and then irradiated with protons with an energy of 600 keV at a current of 1-1.5 µA and a dose of 9×10^{14} cm^{-2}. The samples were irradiated at the SOKOL EG-2 electrostatic accelerator at the Research Institute of Semiconductor Physics and Microelectronics.

Doped and irradiated silicon samples were studied on an X-ray spectrometer with a Miniflex 300/600 goniometer and a D/teX Ultra2 detector. Cukα1 radiation (λ= 1.541 Å) was used at an accelerating voltage of 40 keV and a current of 15 mA on an X-ray tube. The measurements were carried out in the Bragg–Brentano beam geometry in the range 2θ = from 5° to 60° continuously at a scan rate of 10 deg/min and an angular step of 0.02°.

To study the surface morphology of silicon single crystals, an NT-MDT atomic force microscope was used.

RESULTS AND DISCUSSION

Figure 1 shows experimental X-ray diffraction patterns of single-crystal n-type Si before and after doping with Pt and irradiation with protons. As can be seen, in all cases, there is an intense peak in the X-ray patterns in the range

$2\theta \approx 28.5$–$29.5°$. According to the Crystallography Open Database (COD), this diffraction peak corresponds to the (111) peak of cubic silicon space group F-43m (COD#00-080-0018).

In the case of irradiation of samples with protons, the (111) peak shifts from silicon in X-ray patterns towards larger angles (from 28.80° to 29.25°), as well as an increase in its intensity by almost one and a half times and a decrease in its full width at half maximum (FWHM) (from 0.091° to 0.052°). Whereas doping with platinum leads to only minor changes in this peak. In this case, the increase in the intensity of the diffraction peak is probably associated with an improvement in the degree of crystallinity of the samples due to recrystallization of the near-surface region during the doping process at high temperature [6] or with a change in the atomic scattering coefficient due to the presence of Pt [8, 9]. Diffraction peaks from other phases in the obtained X-ray patterns of Si<Pt> samples, for example, Pt, Pt-Si, are not observed. The results obtained indicate that the cubic structure of the silicon single crystal is not modified by doping with Pt, and irradiation does not lead to the formation of an amorphous silicon layer.
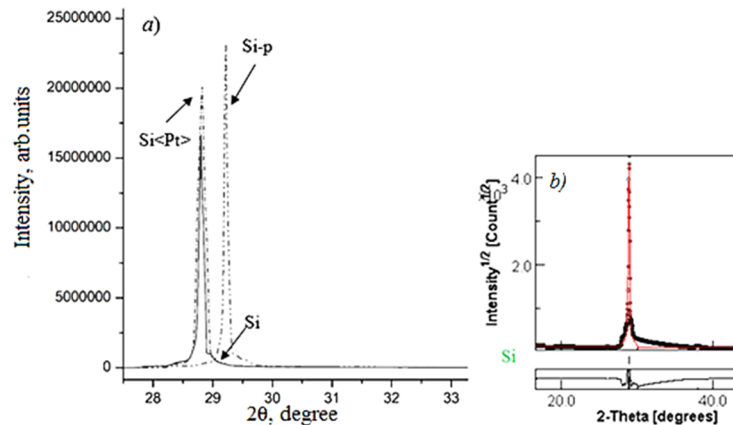
Figure 1. (a) - X-ray diffraction patterns of an n-type Si single crystal before and after doping with Pt and irradiation with protons
(b) - Typical X-ray diffraction pattern Si refined by Rietveld using the MAUD program

Table 1 shows the calculated values of the structural characteristics for the samples under study using the Material Analysis Using Diffraction (MAUD) program, which is based on the full-profile analysis of X-ray diffraction patterns using the Rietveld method. The table shows that the unit cell constant a for initial Si is less than the theoretical value (a = 5.392 Å, V = 156.770 Å^3; COD#00-080-0018). The refined X-ray diffraction pattern of silicon by the Rietveld method presented in Figure 1b clearly shows a good fit of the curve to the experimental line, which confirms the data obtained. Doping of silicon with Pt leads to a further slight decrease in the constant a and, accordingly, to volume compression. In this case, the size of crystallites and microstress increase.

Table 1. Parameter (a) and unit cell volume (V), crystallite size (D), microstress (ε) for n-type Si single crystal before and after Pt doping and proton irradiation

| Samples	a, Å	V, Å^3	D, нм	ε,
Si	5,360	153,991	288	5×10^{-9}
Si<Pt>	5,342	152,444	619	3×10^{-5}
Si irradiated with proton	5,486	165,108	147	5×10^{-5}

Irradiation of a single crystal of Si with protons leads to an increase in the parameter a of the unit cell, while the main peak from silicon, as noted earlier, undergoes a shift towards larger angles (up to 29.3°) and, accordingly, there is a decrease in the interplanar distance (up to 3.056 Å). The size of the crystallites decreases by half, and the microstress increases and is almost the same as for doped silicon. The dislocation density calculated by Equation (1) for a silicon single crystal increase from 0.49×10^{-9} nm^{-2} to 0.99×10^{-5} nm^{-2} as a result of irradiation. An increase in the dislocation density is associated with a decrease in the crystallite size.

$$\rho = 15\varepsilon / a \, D. \qquad (1)$$

In [10], the transformation of radiation defects in proton-irradiated n-type silicon crystals were studied using high-resolution X-ray diffraction analysis. It was shown that successive implantation of protons into silicon with an energy of 100, 200, or 300 keV at a dose of 2×10^{16} cm^{-2} causes the formation of a damaged layer 2.4 μm thick with a large crystal lattice parameter. The layer is formed simultaneously with the accumulation of intrinsic radiation defects, such as vacancies and interstitials. It was noted in [9,10] that when silicon crystals are irradiated with protons at room temperature, most of the formed Frenkel pairs disappear as a result of mutual annihilation, and the separated pair components create more complex and stable secondary radiation defects. The results obtained in this work are consistent with the results of [10-12], and it can be assumed that proton irradiation of a silicon single crystal at a dose of 9.0×10^{14} cm^{-2} with an energy of 600 keV leads to the formation of defects.

Figures 2 and 3 show AFM images with a scanning area of 10×10 μm² of the initial silicon single crystal and after its doping with platinum, respectively. Silicon single crystal samples (Fig. 2a) are characterized by a smooth and uniform surface in different scanning areas. On the surface of the samples, there are depressions up to 1 μm wide in the form of grooves, the appearance of which is due to mechanical processing. Small rounded protrusions are observed on the surface of the single crystal, which is confirmed by the cross-section profile (Fig. 2b), the height of which varies in the range from 2 to 7 nm in diameter. The difference in height of the silicon surface relief is 39.3 nm.
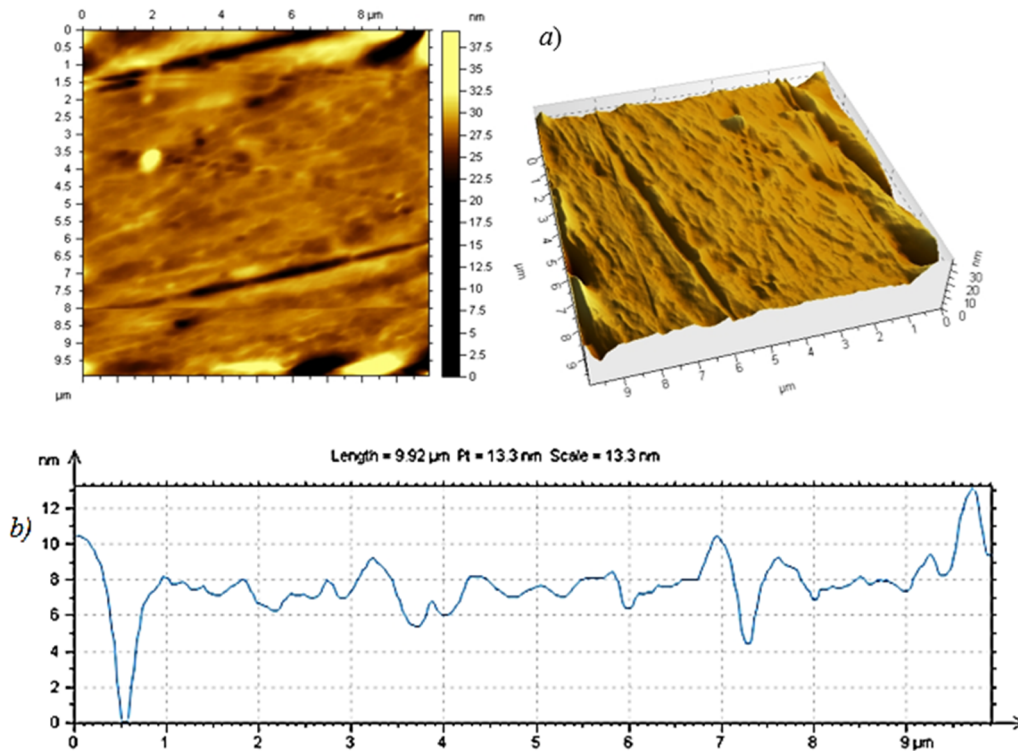
Figure 2. Typical 2D and 3D AFM images of the surface (a), section profile along the main irregularities (b) of an n-type silicon single crystal.
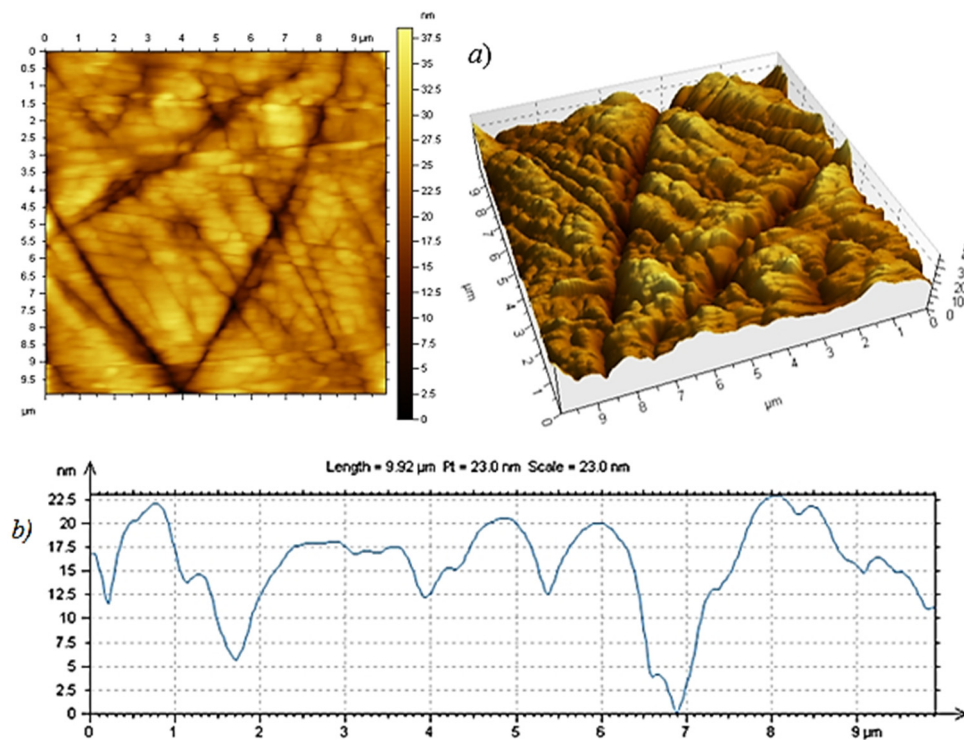
Figure 3. Typical 2D and 3D AFM images of the surface (a), cross-sectional profile (b) of an n-type silicon single crystal doped with platinum

Doping silicon single crystals with platinum leads to significant changes in their surface morphology (Fig. 3a). But at the same time, the height difference of the relief is 38.5 nm, which practically does not change as a result of the diffusion process. Similarly, to the original silicon sample, scratches are observed on the surface of doped samples, which remain after polishing. Large structural elements of different sizes are formed on the surface. According to the profile curve shown in Figure 3b, their sizes range from several hundreds of nanometers to several microns in diameter. Analysis of the 3D image showed that large structural elements are composed of smaller ones. However, this is not visible on the cross-sectional profile of the AFM image of the surface (Fig. 3b), which may be due to the difficulties in visualizing the interfaces due to the nanosize and shape of these structural elements. The observed change in the silicon surface morphology as a result of diffusion by platinum is probably due to the fact that during diffusion at 1200 °C, the collision of platinum ions with the crystal surface leads to structural surface defects of the material, which in turn contributes to the growth of material islands on the surface, their growth and agglomeration [13-15].

CONCLUSION

This paper presents the results of studying the effect of platinum doping and proton irradiation on the crystal structure and surface morphology of an n-type Si single crystal obtained by the Czochralski method. It has been found that the X-ray diffraction patterns of a Si single crystal before and after doping with Pt and irradiation with protons contain an intense peak at $2\theta = 28.5–29.5°$, corresponding to cubic silicon of space group F-43m. It was found that irradiation of samples with protons leads to a shift of the (111) peak from silicon towards larger angles, as well as an increase in its intensity and a decrease in its full width at half maximum, while doping does not lead to significant changes in this peak. The presence of phases associated with Pt, Pt-Si, etc. was not found in the Si<Pt> samples. The unit cell constant calculated for the initial Si single crystal using the MAUD program is 5.360 Å, which is slightly less than the theoretical value. Subsequent doping and irradiation lead to a decrease to 5.342 Å and an increase to 5.486 Å, respectively, of the unit cell constant, which is associated with a change in the size of crystallites and microstress. The revealed change in the morphology of the silicon surface after doping is probably due to the fact that during diffusion at a high temperature, the collision of platinum ions with the crystal surface leads to the formation of structural surface defects, which contributes to the growth of material islands on the surface, their growth and agglomeration. Thus, the obtained results indicate that doping with platinum does not lead to modification of the cubic crystal structure of silicon, but only to minor changes in the structural characteristics and surface morphology. In this case, proton irradiation of a silicon single crystal with a dose of 9.0×10^{14} cm^{-2} with an energy of 600 keV leads to the formation of defects without the formation of an amorphous near-surface layer.

Conflict of Interest
The authors declare that there is no conflict of interest regarding the publication of this paper.

ORCID IDs
Sharifa B. Utamuradova, https://orcid.org/0000-0002-1718-1122; **Aliona V. Stanchik,** https://orcid.org/0000-0001-8222-8030
Dilmurod A. Rakhmanov, https://orcid.org/0000-0003-1275-5999

REFERENCES
[1] N.M. Bogatov, L.R. Grigorian, A.I. Kovalenko, et al. Influence of Radiation Defects Induced by Low-Energy Protons at a Temperature of 83 K on the Characteristics of Silicon Photoelectric Structures. Semiconductors, 54, 196 (2020). https://doi.org/10.1134/S1063782620020062

[2] Sh.B. Utamuradova, Sh.Kh.Daliev, K.M. Fayzullaev , D.A. Rakhmanov, and J.Sh. Zarifbayev. , "New materials, compounds and applications," **7**(1), 37-43 (2023). http://jomardpublishing.com/UploadFiles/Files/journals/NMCA/V7N1/Utamuradova_et_al.pdf

[3] Sh.B. Utamuradova, D.A. Rakhmanov, A.S. Doroshkevich, I.G. Genov, Z. Slavkova, and M.N. Ilyina, Advanced Physical research, **5**(1), 5 (2023). http://jomardpublishing.com/UploadFiles/Files/journals/APR/V5N1/Utamuradova_et_al.pdf

[4] V.V. Kozlovsky, V.A. Kozlov, and V.N. Lomasov, FTP, **34**(2), 129 (2000). http://journals.ioffe.ru/articles/viewPDF/37060

[5] B.I. Boltaks, *Diffusion in semiconductors*, (State publishing house of physical and mathematical literature, Moscow, 1971).

[6] Sh.B. Utamuradova, A.V. Stanchik, D.A. Rakhmanov, A.S. Doroshkevich, and K.M. Fayzullaev, "New materials, compounds and applications," **6**(3), 214 (2022). http://jomardpublishing.com/UploadFiles/Files/journals/NMCA/V6N3/Utamuradova_et_al.pdf

[7] Sh.B. Utamuradova, S.A. Muzafarova, A.M. Abdugofurov, K.M. Fayzullaev, E.M. Naurzalieva, and D.A. Rakhmanov, Applied Physics, **4**, 90 (2021). https://applphys.orion-ir.ru/appl-21/21-4/PF-21-4-81.pdf (in Russian)

[8] Sh.B. Utamuradova, and D.A. Rakhmanov, Annals of University of Craiova, Physics, **32**, 132 (2022). https://cis01.central.ucv.ro/pauc/vol/2022_32/15_PAUC_2022_132_136.pdf

[9] Y.S. Katharria, S. Kumar, F. Singh, J.C. Pivin, and D. Kanjilal, J. Phys. D: Appl. Phys. **39**, 3969 (2006). https://dx.doi.org/10.1088/0022-3727/39/18/007

[10] https://www.xtal.iqfr.csic.es/Cristalografia/parte_05-en.html

[11] S.A. Speakman, *Fundamentals of Rietveld Refinement*. http://prism.mit.edu/xray/oldsite/6a%20Fundamentals%20of%20Rietveld%20Refinement%20XRD%20Simulation.pdf

[12] I.S. Smirnovn, I.G. Dyachkovan, E.G. Novoselova, Modern Electronic Materials, **2**, 29 (2016). http://dx.doi.org/10.1016/j.moem.2016.08.005

[13] O.V. Skaliaukh, "Defect formation in silicon upon irradiation with alpha particles with an energy of 5.4 MeV", Ph.D. Thesis, Ulyanovsk, 2005.

[14] V.A. Zinoviev, "Processes on the silicon surface under low-energy ion exposure under conditions of molecular-beam epitaxy," Thesis, Siberian Branch of the Russian Academy of Sciences, Institute of Semiconductor Physics. Novosibirsk, 2004.

[15] S.M. Osadchii, A.A. Petukhov, and V.B. Dunin, J. Surf. Investig. **13**, 690 (2019). https://doi.org/10.1134/S1027451019040311

РЕНТГЕНО-СТРУКТУРНІ ДОСЛІДЖЕННЯ n-Si<Pt>, ОПРОМІНЕНОГО ПРОТОНАМИ

Шаріфа Б. Утамурадова[a], Альона В. Станчик[b], Ділмурод А. Рахманов[a]

[a]Інститут фізики напівпровідників та мікроелектроніки Національного університету Узбекистану
100057, Ташкент, Узбекистан, вул. Янги Алмазар, 20
[b]Науково-практичний матеріалознавчий центр НАН Білорусі, Мінськ, Білорусь

У даній роботі досліджено вплив протонного опромінення на зміну структури зразків кремнію, легованого платиною. Зразки опромінювали протонами в дозі 9×10^{14} см$^{-2}$ з енергією 600 кеВ і силою струму $1 \div 1,5$ мкА. Для визначення зміни структури після опромінення використовували методи рентгенівської дифракції та атомно-силової мікроскопії. Отримані результати свідчать про те, що легування платиною не призводить до модифікації кубічної кристалічної структури кремнію, а лише до незначних змін структурних характеристик і морфології поверхні. У цьому випадку протонне опромінення монокристала кремнію дозою $9,0 \times 10^{14}$ см$^{-2}$ з енергією 600 кеВ призводить до утворення дефектів без утворення аморфного приповерхневого шару.

Ключові слова: *кремній; платина; дифузія; допінг; опромінення; протон; рентгенівська дифракція*

IMPROVEMENT OF THE SHIELDING EFFECTIVENESS OF PMMA/MWCNTS/Ag HYBRID COMPOSITE FOR X-BAND APPLICATION[†]

Badiaa Ismal Alawi, ⬤Nadia Abbas Ali*

Department of Physics, College of Science, University of Baghdad, Baghdad, Iraq
*Corresponding author: nadia.ali@sc.uobaghdad.edu.iq
Received March 10, 2023; revised March 21, 2023; accepted March 27, 2023

Herein, the Polymethyl Methacrylate/Mutiwalled Carbon Nanotube/Silver (PMMA/MWCNT/Ag) hybrid composite films are prepared by solvent casting method to be used in an electrical application. The AC conductivity and dielectric characteristics have been investigated at room temperature. The electrical conductivity of the hybrid composite reaches a percolation critical concentration of 2.14×10^{-4} S/cm by Ag doping. For all PMMA/MWCNT/Ag hybrid composites, the frequency-dependent dielectric constant decreases as the frequency area widens. As the concentrations of MWCNT and Ag increase, the AC conductivity exhibits an increasing trend. The MWCNT and Ag content was found to significantly affect the SE of the given composites. A high electromagnetic (EM) shielding efficiency (SE) was achieved between 8.2 and 12.4 GHz (X-band). The highest EM attenuation of 18 dB at 12 GHz was achieved using 0.5 wt% MWCNT and Ag. The thermal analysis of the formed PMMA/MWCNT/Ag hybrid composites showed that exothermic reactions with the greatest weight loss took place between 200°C and 300°C. Field emission scanning electron microscope (FESEM) show that PMMA/MWCNT/Ag hybrid composites had uniform dispersion of the carbon nano tube and silver particles within the PMMA matrix.

Keywords: *Electromagnetic interference shielding; X-band; Electrical conductivity; Dielectric constant; Dielectric loss; Thermal analysis*
PACS: 72.15.Cz; 77.22.Gm, 73.22.f

INTRODUCTION

An electromagnetic interference (EMI) barrier, preventing the radiation from flowing through it, is formed when electromagnetic radiation is reflected or absorbed by a substance [1]. Nowadays, protecting against EMI is essential in the world of electronic systems and components. In the 8.2 to 12.4 GHz (X-band) range, the EMI shielding is very important for both industrial and military applications, systems for Doppler, weather radar, TV picture transmission, and telephone microwave [2,3]. Thermoplastics like polycarbonate (PC), polypropylene (PP), polyethylene (PE), polystyrene (PS), polylactide (PLA), polymethylmethacrylate (PMMA), acrylonitrile butadiene styrene (ABS), or polyvinylidene fluoride (PVDF) and thermosets like epoxy resins, polydimethylsiloxane (PDMS), or polyurethane (PU) are two types of polymer matrices that are frequently utilized for EMI shielding materials [4]. There are a variety of conductive fillers that can be used for functionalizing cork-polymer composites (CPC) such as metal fillers like steel fibers, copper, and silver nanowires, or metal oxide fillers like magnetite ferrite which can be easily spread in various polymer matrices. Amongst, the carbon-based fillers, graphite and carbon black are most typically utilized because of their small weight and strong conductivity [5].

Recently, more research is being done on polymer composites with metallic additives as possible electromagnetic field shielding materials. The metal-filled polymer composites are beneficial because of their low specific weight, good corrosion resistance, plasticity, and straightforward, inexpensive production techniques [6]. A wide range of alterations to polymer composites (in terms of filler type, structure, and content, as well as matrix polymer selection) enables the control of their electromagnetic characteristics for a given application. Polymer composites with metal fillers remain one of the most crucial materials to take into account for EMI shielding applications. In addition, metals like silver, copper, gold, and aluminum are ideal for reflecting light due to their high conductivity [7].

A new type of pollution known as noise, radio frequency interference, electromagnetic radiation, or EMI, which causes equipment to malfunction, has been produced by the expansion of the use of electronic gadgets [8]. The development of polymer composites has revealed a novel carbon-based polymer composite. The carbon nanotubes (CNTs) have demonstrated potential as reinforcement fillers in polymers to improve an EMI shielding material due to their substantial specific surface area, distinct 3D networking structure, and distinctive electrical structure [9]. Silver nanoparticles (Ag-NPs) have a significant impact on the field of nanotechnology and are significant due to their unique optical, electrical, and magnetic properties depending on their particle size [10]. It was also used in electronics, optics, and other fields due to its high conductivity, antibacterial properties, and chemical stability.

The CNTs and Ag-NPs have recently been able to play a significant role in the creation of nano EMI shielding materials thanks to their distinctive electrical, mechanical, and magnetic properties [11]. Research on next-generation EMI shielding materials is now heavily focused on EMI shielding hybrid composites made by combining CNTs and Ag with organic polymers [12]. MWCNT-PMMA composite films have been reported to have up to 27 dB SE for high CNT loadings of around 40 wt% by Kim et al. [13] who researched the EMI shielding capabilities of MWCNT-PMMA

films in the range (50 MHz–13.5 GHz). In situ polymerization and ex-situ manufacturing procedures were used to prepare MWCNT-PMMA composites. Yuen et al. [14] investigated the impact of processing variables on the EMI shielding capabilities of these composites. It was reported that the shielding efficiency of EMI of composites prepared by stacking 10 layers of 0.1-mm MWCNT-PMMA films was higher than a single 1-mm thick piece of bulk 4.76 wt% MWCNT-PMMA composite, confirming the composite stacking process as a better fabrication method. In addition, it was deduced that the SE was higher for in situ fabricated composites. Liu et al. [15] showed that PU/SWCNT composites with a 20 wt% SWCNT loading may produce an EMI SE of up to 17 dB in the 8.2-12.4 GHz range. It was deduced that the EMI shielding levels for SWCNT- or MWCNT-polymer composites reported up to this point typically vary between 20 and 30 dB only in the X-band frequency range. Higher values have been seen in the X-band, although at frequencies other than that. Yuan et al. [16] generated electromagnetic absorbent materials based on the PMMA/CNT nanocomposite. The dielectric loss of PMMA/CNT nanocomposite foams rose, with a CNT loading of 4–8 wt %, from 2.1 to 10.8 (X-band). This demonstrates that a conducting network of nanotubes formed in the PMMA matrix as a result of the nanofiller loading. The electrical conductivity of the nanocomposite foam increased as a result, resulting in a dielectric loss. The layered structure is meant to increase the absorption bandwidth of the PMMA/CNT nanocomposite foams. The layered nanocomposite foam's absorption bandwidth was 3.5 GHz. The top layer of the foam had a low dielectric constant due to lower CNT content than the bottom layers, which had higher concentrations of nanofiller. PMMA and single-walled carbon nanotube (SWCNT) nanocomposites were primed by Das et al. [17]. The percolation threshold was increased from 10^{-15} to 10^{-2} by the SWCNT loading. The PMMA/SWCNT percolation threshold was 3 wt%. An improvement in the EMI shielding of 40 dB was seen at 200 MHz in the X-band (8-12 GHz) for 20 wt% SWCNT.

The objective of this study is to investigate the role of MWCNT and Ag as fillers in intrinsically conducting PMMA polymer in altering the EMI shielding performance of polymer hybrids. For this purpose, various ratios of MWCNT and Ag are incorporated into the PMMA to obtain the optimum doping ratio. The chemical structure, electrical conductivity measurement, frequency-dependent dielectric constant, electromagnetic shielding efficiency as well as thermal analysis of the formed polymer hybrids were investigated and discussed.

1. EXPERIMENTAL DETAILS
1.1. Sample preparation

The MWCNT filler, in this work, had a diameter of 20–40 nm and a length of 10–30 μm. The PMMA/MWCNT/Ag hybrid composite films were synthesized by the solvent casting method. In this method, the MWCNT and Ag were ultrasonically dispersed in chloroform for 2 h to form a stable suspension. Then, the suspension was combined with a solution of 3 g PMMA in chloroform to form a combination of PMMA/MWCNT/Ag including 0.1, 0.2, 0.3, 0.4, and 0.5 wt% MWCNT and utilizing a constant ratio of Ag at 0.5 wt%. The mixture was once more ultrasonically processed for 2 h to achieve a consistent dispersion of MWCNTs and Ag in PMMA. Finally, the thin polymer film was cast from this solution by pouring it into a Petri dish covered with Teflon spray (diameter ~ 4 cm). After the solvent had evaporated, the nanocomposite films were allowed to dry at room temperature for a day before being removed from the glass dishes and cut into pieces for characterization and structural analysis. The thicknesses of the formed PMMA/MWCNT/Ag nanocomposite film were measured to be around 0.25 mm.

1.2. Sample characterizations

The chemical bonds in the formed samples were analyzed using the Infrared Fourier Transform (FTIR) Analysis. For this purpose, the FTIR spectroscopy model Shimadzu type FTIR-7600 was used to record the infrared spectra in the wavenumber range from 400 to 4000 cm^{-1}. The electrical characteristics were carried out by evaluating the resistivity (ρ) of the films. The electrical resistance has been measured as a function of temperature (T) in the temperature range of 303-393 K using the following equation [18]: $\rho = RAL$, where R is the electric resistance of the sample, A is the film's cross-sectional area and L is the sample's thickness. From the relationship, the conductivity (σ_{dc}) of the films was calculated: $\sigma_{dc} = \frac{1}{RAL}$. The electrical conductivity, which is determined by the Arrhenius equation and varies exponentially with temperature and is derived by: $\sigma_{dc} = \sigma_0 e^{\frac{-E_a}{k_B T}}$. The total conductivity was calculated from the following equation: $\sigma_t(\omega) = \frac{L}{RA}$. The AC conductivity $\sigma_{ac}(\omega)$ was calculated by using the relation: $\sigma_{tot}(\omega) = \sigma_{ac}(\omega) + \sigma_{dc}$ and $\sigma_{ac}(\omega) = \sigma_t - \sigma_{dc} = A\omega^s$, where σ_{dc} is the DC conductivity, A is a constant independent of temperature, ($\omega = 2\pi f$), and s is the frequency exponent.

The dielectric permittivity of a material (ε) is considered a complex quantity with a real part (ε_r) and imaginary part (ε_i) and is given by [17]: $\varepsilon = \varepsilon_r + \varepsilon_i$. The values of the parallel mode capacitance (C_p) and the loss tangent (tan (δ)) are used to determine the real and imaginary components of the dielectric permittivity or ε_r and ε_i, respectively. For the frequency range of 10 kHz–100 MHz and room temperature, the values of Cp and tan are calculated. The values of r and I are determined using the following equations: $\varepsilon' = C_p d\varepsilon_o A$; $\varepsilon'' = \varepsilon' \tan(\delta)$ and $\tan(\delta) = \varepsilon''/\varepsilon'$ where $\delta = 90 - \varphi$, d and A are the thickness and cross-sectional area of the sample, respectively, and ε_o is the permittivity of free space.
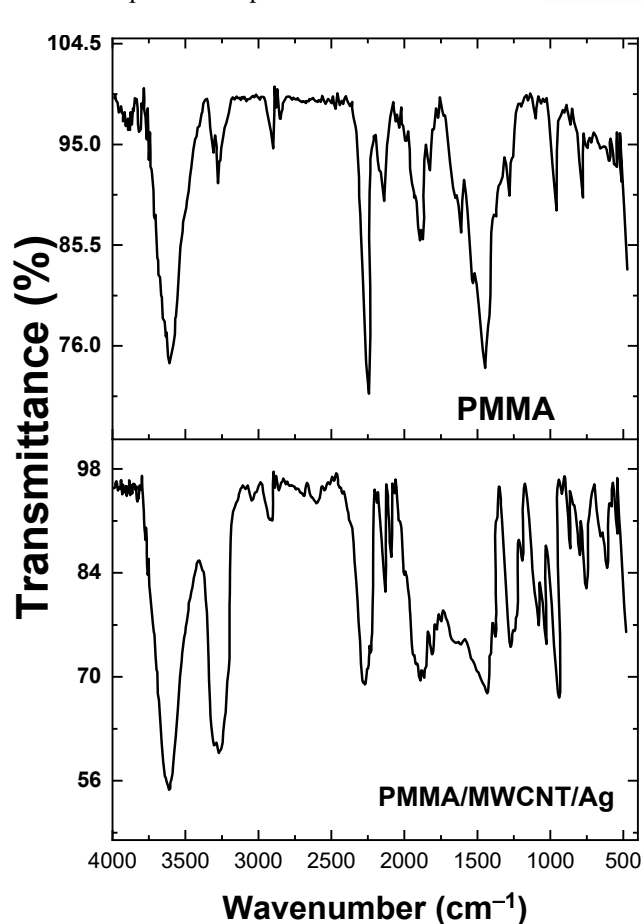
The electromagnetic properties of the samples are evaluated by the waveguide technique at X-band frequency (closed system). The about 1.3 cm thick preparation samples are cut to fit in the cross-section of the rectangular

waveguide (2.29×1.02 cm^2). The sample is positioned inside the waveguide (sample holder) so that it completely encloses the cross-section to prevent any EM radiation leakage. The incident and transmission energy between 8.2-12.4 GHz is utilized to determine the shielding effectiveness. The SE of the PMMA/MWCNT/Ag hybrid composite was measured using a network analyzer and the coaxial line technique following ASTM D4935-99 [19] in the frequency range of 8.2 to 12.4 GHz (X-band). The sum of the contributions from absorption loss (SE$_A$), reflection loss (SE$_R$), and multiple reflections (SE$_M$) may be used to describe SE (SE$_{total}$) [20]. The value of SE was determined and represented in decibels (dB) using the following equation: SE$_{total}$ = SE$_A$ + SE$_R$ + SE$_M$.

There are descriptions of measuring the glass and various polymer transitions. A hypothesis explaining how a glass transition appears in a Differential Thermal Analysis device (DTA) thermogram and how to extract the thermogram's true value is provided. The thermal analysis and thermal stability of the investigated samples were carried out using the DTA model a TG-209F with a heating rate of 10 °C/min under nitrogen flowing at a rate of 50 ml/min. For this purpose, around 10–19 mg of the samples were provided at thermal degradation temperatures of 25–400°C. Field emission scanning electron microscopy (FESEM) provides topographical and elemental information at magnifications of 10× to 300,000×.

2. RESULTS AND DISSECTION

The FTIR spectra provide information on the functional groups and chemical structure of the investigated materials. The FTIR spectrum of pure PMMA film as well as PMMA/MWCNT/Ag nanocomposites are shown in **Fig. 1**.

Figure 1. FTIR spectra for pure PMMA and PMMA/MWCNT/Ag hybrid composites.

For pure PMMA, the left region, between 1500 and 4000 cm^{-1}, is referred to as the diagnostic region, and the second, between 400 and 1500 cm^{-1}, is referred to as the fingerprint region that points to the functional group region. The left region is particularly close to 4000 cm^{-1} because it is for the high energy bonds. The O-H stretching vibration is represented by the peak at 3414 cm^{-1}, while the C=O stretching vibration from PMMA is characterized by the absorption band at 1732 cm^{-1}. The C-O stretching vibration in PMMA is shown by the absorption band at 1147 cm^{-1}. The absorption band at 1242 cm^{-1} indicates C-C from PMMA, while the absorption band at 2951 cm^{-1} corresponds to C-H stretching in that area. A strong peak at 1736 cm^{-1} was seen belonging to the ester carbonyl group's (C=O) stretching vibration. The large peak between 1260 and 1000 cm^{-1} can be attributed to the stretching vibration of the C-O (ester bond). The bending of C-H is what causes the broadband from 950-481 cm^{-1}. It is possible to attribute the peak at 2935 cm^{-1} to -CH stretching, which is consistent with other work [17].

The FTIR spectrum for PMMA/MWCNT/Ag hybrid composite exhibits three distinct peaks, C=O, O-H, and C-O. These peaks are the result of oxidation forming the COOH groups on the surface of MWCNTs, which demonstrated an aromatic skeletal vibration (C=C stretching) at 1615 cm^{-1}. The absorption band observed at 1540 cm^{-1} is more likely from the C=C stretching mode of CNTs. The C=O stretch of the -COOH group is responsible for the peak that was seen at 1731 cm^{-1}. Stretching vibrations are responsible for the wide peak between 4000 and 2900 cm^{-1}, while the peak at 1195 cm^{-1} is due to -O-CH$_3$ stretching vibrations. Peaks for C=C stretching and O-H broadening stretching are located at 1660 and 3307 cm^{-1}, respectively. Due to the existence of ester carbonyl group stretching vibration, or C=O stretching, a peak was visible at 1872 cm^{-1}. The stretching vibration of the C-O (ester bond) can be used to explain the wide peak spanning from 1260 to 1000 cm^{-1}. The peak for N-H stretching is at 3394 cm^{-1}, followed by C-O stretching at 1731 cm^{-1}, C-H bending at 1057 cm^{-1}, and C-O stretching at 3433 cm^{-1}. The absorption bands for O-H bending and C-O stretching are at 1410 cm^{-1} and 1090 cm^{-1}, respectively. The peaks at 2920 and 2850 cm^{-1} are connected to the C-H stretching mode, whereas the strong peak at 3440 cm^{-1} is related to the O-H stretching of the hydroxyl group. The principal silver peaks were seen at 2927, 1631, and 1383 cm^{-1}. A distinct and powerful absorption band at 1631 cm^{-1} was visible in the spectra and was identified as the

stretching vibration of the (NH) C=O group. A band at 1383 cm^{-1} was created for the stretching of C-C and C-N; while a strong peak at 2927 cm^{-1} was attributed to the stretching vibrations of C-H and C-H (methoxy compounds).

The DC electrical conductivity (σ) for PMMA/MWCNT/Ag hybrid composite films for various ratios of MWCNT and Ag at a temperature range of 30-120 °C is shown in **Fig. 2**. The findings indicate that the value of for PMMA was around 1.1×10^{-9} (S·cm^{-1}) and the value of for PMMA/MWCNT/Ag is shown in **Table 1**.
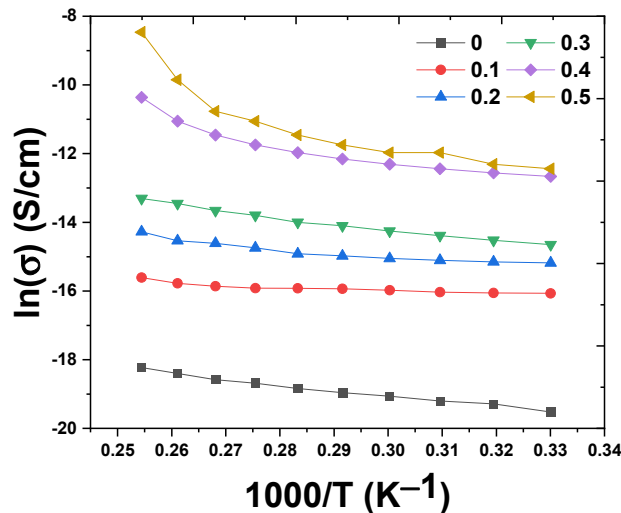
Figure 2. Electrical conductivity (σ) versus ($\frac{10^3}{T}$) for pure PMMA and PMMA/MWCNT/Ag
hybrid composites with ratios of MWCNTs of 0.1, 0.2, 0.3, 0.4, and 0.5 wt%.

Table 1. Electrical conductivity (σ) and activation energy (E_a) for electrical transition, the exponential factor (s) for PMMA/MWCNT/Ag hybrid composites.

MWCNT ratio (wt%)	0	0.1	0.2	0.3	0.4	0.5
σ (S/cm)	3.21×10^{-9}	1.05×10^{-7}	2.54×10^{-7}	1.01×10^{-6}	1.57×10^{-5}	2.15×10^{-4}
E_a (eV)	2.36	2.1	2.09	1.96	1.88	1.52
S	0.94	0.66	0.64	0.63	0.55	0.39

The following may be used to explain why PMMA/MWCNT/Ag hybrid composite films have increased d.c electrical conductivity: The presence of MWCNTs and Ag as filler in the PMMA matrix aids in the creation of broad conductive networks that enable the movement of electrons inside the composite and that MWCNTs induce the current to flow even if there are no direct connections between MWCNTs. The electrons can travel through the insulator with a certain probability between conductive components (MWCNTs) in a process known as "quantum mechanical tunneling". In addition, electrons can go between conductors by "tunneling" through the insulating layer to put it another way. A low percolation threshold and conventional percolating network characteristics were displayed by the carbon nanotube network. Although silver has high conductivity qualities, metal is costly and bulky [6]. With a high aspect ratio and distinctive conductivity, MWCNTs have mostly been utilized as conductive fillers up until this point due to their low density.

The insulating PMMA matrix becomes conductive plastic when MWCNT is added, as seen in **Fig. 2**. The loading of MWCNT from 0.1 to 0.5 wt%, and 0.5 wt% Ag increased the electrical conductivity of the PMMA. Only 0.5% of MWCNT/Ag added to PMMA produced conductivities as high as 2.15×10^{-4} S/cm. The conductivity was enhanced in a traditional percolating manner with a percolation threshold of roughly 0.5 wt% due to the widespread usage of used Ag as a conductor wire in circuits that call for high conductivity. Although individual MWCNTs have great characteristics, their microscale length necessitates electron percolation from one CNT to another, often thousands of times. The greater resistance of the MWCNT-MWCNT junction significantly lowers the electron mean free path, lowering the electrode's conductivity. The Ag-NPs are the most well-known choices for enhancing MWCNT network conductivities due to their high conductivity, chemical stability, and compatibility with sintering even at low temperatures.

The table illustrates the link between ln(σ$_{dc}$) and the inverse absolute temperature of nanocomposites. From the fitted lines the slope can be used to characterize the activation energy (E_a), and the findings revealed that the PMMA-/MWCNT/Ag hybrid composite reduced the activation energy values of samples owing to the effect of the space charge, with high values E_a ranging from 2.36 eV to 1.52 eV. In the prohibited energy gap, it also generates local energy levels that interact to trap charge carriers that jump between levels, and the conduction process lowers the concentration of hopping. The activation energy is low for PMMA/MWCNT/Ag at (0.5 wt%) due to the formation of a continuous network of carbon nanotubes and silver inside the hybrid composite that contains routes that aid charge carriers in passing through, and it decreases as the loading ratio of MWCNT and Ag increases. The voids in the carbon nanotube network must be bridged with another conductive material, such as silver, which has no voids, or at least with

a much smaller scale void pattern that has high transparency, high conductivity, and solution processability [15]. This will also result in low sheet resistance and a uniform conductive film.

<div align="center">AC Conductivity</div>

Figure 3 shows the AC electrical conductivity of PMMA for 10 kHz to 10 MHz at room temperature along with different amounts of MWCNT and Ag integrated. The MWCNT and Ag network's connection and electron transport mechanism in the polymeric matrix is revealed by the hybrid composites' AC conductivity. It has been shown that all samples' conductivities rise with frequency, however, PMMA's conductivity is lower than that of its MWCNT, Ag. This may be explained by dipoles' propensity to point in the direction of the applied field in polymeric materials [11,12].

The AC conductivity is derived by subtracting the AC conductivity from the total conductivity. **Figure 3** depicts the frequency dependence of AC conductivity. The graph clearly shows that as frequency increases, a.c. increases. One may determine the frequency exponent (s), which is less than one, by computing the slope of the straight lines in **Fig. 3**. The average values of (s) appear to be consistent with protons acting as charge carriers that hop across polymer chains.
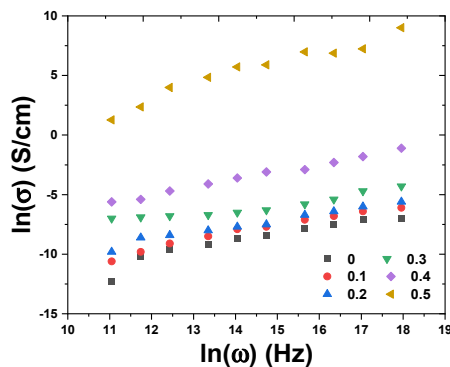
Figure 3. ln(σ) versus ln (ω) for pure PMMA and PMMA/MWCNT/Ag hybrid composites with ratios of MWCNTs of 0.1, 0.2, 0.3, 0.4, and 0.5 wt%.

The hybrid composite including MWCNT/Ag (0.1-0.4/0.5 wt%) demonstrates frequency-dependent conductance and is within the percolation threshold, except for its conductance being an order of magnitude larger. At low filler loading, there is not enough filler to form a conductive network; hence, AC conduction occurred via the tunneling current. The percolation threshold was likely created by the interaction of the nanotubes and silver to create conductive pathways, and the increase in AC conductance is attributed to the leakage current, according to a significant rise in conductance at MWCNT/Ag (0.5/0.5 wt%) [16].

PMMA/MWCNT/Ag hybrid composites plotted against each other at different ratios showed the exponential factor (s). As seen in **Table 1**, the values of s for all composite samples are quite small. As a result, it can be concluded that conductivity occurs during hopping. However, the exponents fluctuate as the filler content varies, and increases in exponents are attributed to the increase in charge carriers caused by the addition of MWCNT and Ag. The results showed that between 10 kHz and 10 MHz, the "total" climbs as frequency increases.

All of the PMMA/MWCNT/Ag hybrid composites have had their dielectric characteristics examined. For all of the composites, **Figs. 4a** and **4b** depict the frequency-dependent fluctuation in dielectric constant and dielectric loss. Ag at an increase in frequency with a drop of and" at high concentrations, and the higher frequency loss becomes virtually constant at lower MWCNT concentrations. Because there are two types of dielectric losses, this suggests that dipoles organize themselves along field direction at low frequencies to increase overall polarization. The first is known as conduction loss and is caused by the actual charge flowing into the dielectric. The second is known as dielectric loss and is caused by molecules' or atoms' spins in an alternating current field [21, 22].

Figure 4c illustrates how the value of the loss tangent rises with frequency, reaches a maximum at a certain frequency, and then falls at higher frequencies. The lack of dielectric materials to follow the applied electric field causes a loss tangent to arise, which is characterized by the generation of heat.
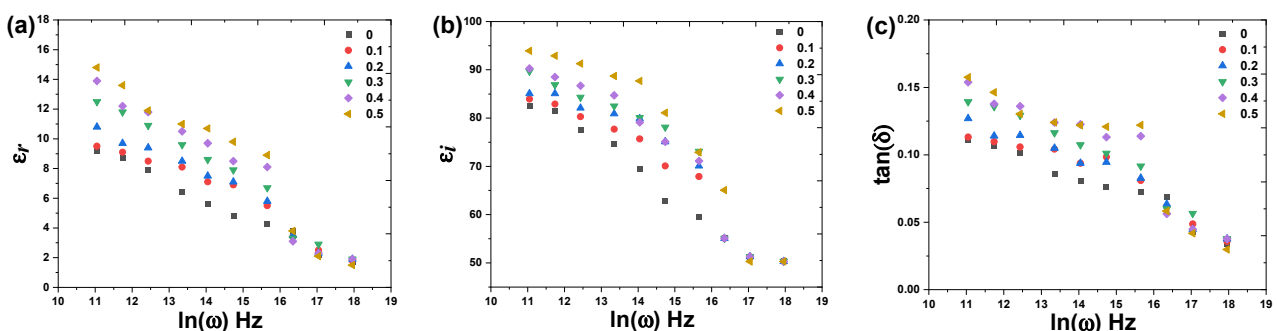

Figure 4. **(a)** real (ε_r), **(b)** imaginary (ε_i) parts of dielectric constant, and **(c)** loss tangent (tan(δ) versus ln(ω) at the temperature of 323 K for pure PMMA and PMMA/MWCNT/Ag hybrid composites with ratios of MWCNTs of 0.1, 0.2, 0.3, 0.4, and 0.5 wt%.

<div align="center">Electromagnetic Interference shielding (EMI)</div>

High reflection and low absorption should generally define the EMI shielding material. The best course of action in this situation is to apply a few layers of the copper-filled composite material that reflects light, as illustrated in **Fig. 5** The SE of EMI of PMMA/MWCNT/Ag hybrid composites increased with MWCNT and Ag content because carbon nanotubes (CNTs) comprise electrically conducting organic nanomaterials, and their composite displays significant

EMI shielding capabilities. By layering 0.1 mm thick MWCNT/Ag/PMMA composite films, it was feasible to achieve EMI shielding effectiveness of up to 19 dB in the frequency range of 8.2-12.4 GHz (X-band).

The different carbonaceous fillers' EMI shielding capabilities are in-depth studied. In the live broadcasting, entertainment, aviation, and defense industries, electromagnetic interference (EMI) has been a major source of worry since it can worsen while critical radio signals are present. Due to their flexibility, low density, high mechanical strength, high thermo-stability, high electrical and thermal conductivity, outstanding fracture toughness, and high friction/wear resistance, organic polymeric composites containing carbonaceous fillers are frequently employed to lessen the impact of EMI. Many carbon-based materials, both in mono and compound form, are employed as EMI shielding materials. Although increasing the number of MWCNT would increase the shielding capacity, doing so would make it more difficult to produce composites with large MWCNT volume fractions. By including 0.5 wt% of Ag in all composites, these flaws may be fixed, and the superior conductivity of silver is retained while still enhancing the interfacial contact of MWCNT, which agrees with other works [16,17].
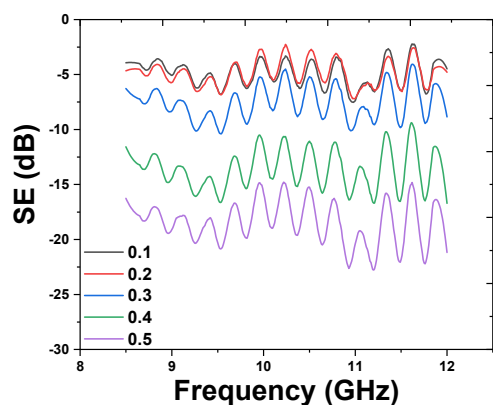
Figure 5. Electromagnetic interference (EMI) shielding (SE) versus frequency for PMMA/MWCNT/Ag hybrid composites with ratios of MWCNTs of 0.1, 0.2, 0.3, 0.4, and 0.5 wt%.

Hybrid particles, which were created by fusing metal and polymer, have shown advantageous qualities including conductive composite, EMI shielding, electromagnetic wave absorption, catalysts, batteries, and sensors. The metal with specified electrical conductivity properties can be used in a variety of industrial applications, including shielding against radio frequency interference (RFI), electrostatic discharge (ESD), electrically conductive adhesives, and circuit components in microelectronics. Silver is the single metal with the highest electrical conductivity, and unlike other metals, its oxide form is also electrically conductive. These benefits have led to silver's predominant use in a variety of sectors as a polymer/silver composite. However, the volume proportion of silver was spread in the polymer matrix to achieve excellent electrical conductivity.

One of the practical approaches favored for material characterization is TGA-DTA. Using this method, changes brought about by breakdown, transformation, and formation processes during a controlled heating process may be examined. Samples were heated at a rate of 5C/min from ambient temperature to 350°C. The endothermic action shows the elimination of the chemically bonded water at higher temperatures of 200–300°C. The exothermic effect discovered in the temperature range of 200 to 350°C was attributed to the combustion of organic materials that weren't completely burned during firing in reducing conditions and transformed into carbonaceous particles, which are believed to have been purposefully added into the PMMA. The thermal degradation of PMMA in an oxygen-containing environment (O_2, Air) initially results in an increase in the PMMA thermal stability as the temperature for the commencement of mass loss rises by 50°C and 70°C. A gas-containing atmosphere (Air) destabilizes the PMMA at about 230–250°C, accelerating the thermal breakdown process.
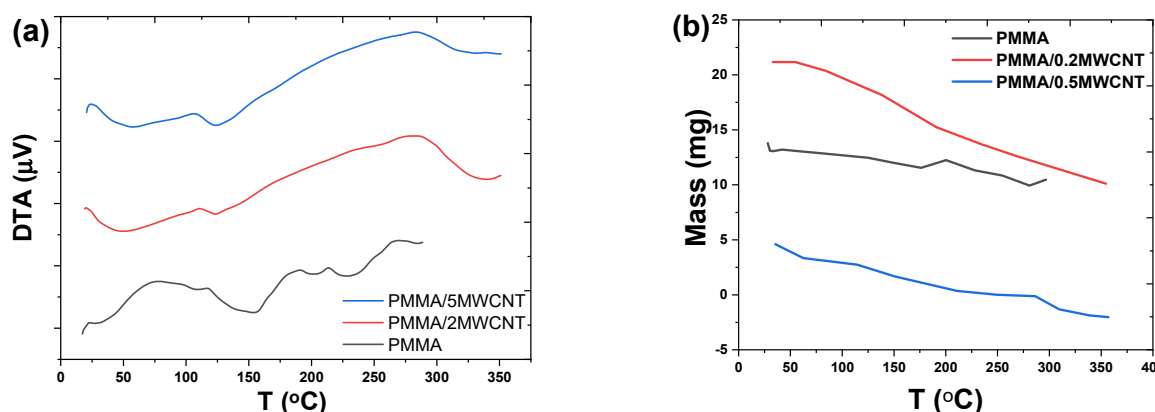
Figure 6. (a) Differential Thermal Analysis (DTA) and **(b)** mass versus temperature (T) for pure PMMA and PMMA/MWCNT/Ag hybrid composites

The melting peak changes to lower temperatures emerge at (153.84°C, 121.45°C, and 125.67°C) in **Figs. 6a** and 6**b** DTA and TGA curves of pure PMMA and PMMA/MWCNT/Ag. These curves exhibit one mass endothermic peak that represented the melting point of the raw materials (PMMA, MWCNT, and Ag). The curve also demonstrates a significant endothermic reaction beginning at 114°C and continuing to 140°C. The level of adsorption is typically higher than the molar mass of the PMMA. This is predicted because just a portion of the polymer chain was adsorbed,

whereas the remaining chain is more likely to bind to the MWCNT surface by CH interactions. The MWCNTs exhibit minimal mass loss owing to the presence of amorphous carbon and other impurities and are thermally stable across the whole temperature range investigated (up to 600°C) [20]. Additionally, when the accessible MWCNT surface area increases, more polymer may adsorb, which leads to PMMA adsorption when the number of MWCNTs is increased. The PMMA/MWCNT/Ag sample's TGA/DTA diagrams show a weight loss as a result of the carbon layer's thermal degradation, which begins at 279–309°C and 278–305°C, respectively. The DTA diagram's exothermic peak, which is located at 288°C and 290°C, respectively, denotes the exothermic curves caused by the crystalline phase of composites and thermal breakdown. The DTA plot shows a large endothermic peak between 200 and 300°C, which is mostly due to the crystallization of additional silver nanoparticles to hybrid PMMA/MWCNT. The DTA profiles show that the material completely cooled and crystallized at the same time.

The properties associated with polymer matrix composites are the functions of the filler size, shape, dispersion and the matrix and filler interactions. In this work the filler shape and size is same throughout the experiments. The main purpose of FESEM is to check the degree of dispersion and filler matrix interaction. The FESEM analysis surface morphology of the samples shows the micrographs of pure PMMA and PMMA/MWCNT/Ag at 0.1/0.5 concentration is showing good dispersion into the matrix dispersed in PMMA. From the Figures it is observed that dispersed MWCNT, Ag filler particle creates considerable change in the morphology of the pure PMMA film. The SEM images of the pure PMMA shows a pores and granular structure while the MWCNT, Ag dispersed PMMA matrix exhibits a smoother and more compact amorphous surface morphology, i.e., no major cracks were obtained. It is important to mention that the PMMA particles retained their exhibit spherical morphology after being deposited and cured because they weren't fully melted during the heating process for the film formation. the good dispersion of Ag-NPs results in an essential enhancement in the properties of the fabricated PMMA/Ag nanocomposites. The FESEM image of the hybrid composite fi lm shows a homogeneous dispersion of MWCNTs, Ag in PMMA (Fig. 7) with no aggregation of nanotubes even with 0.5/0.5% loading which suggests that ultra-sonication is quite useful in dispersion of the tubes in PMMA that enhanced electrical properties and showed high electrical conductivity and EMI shielding properties.
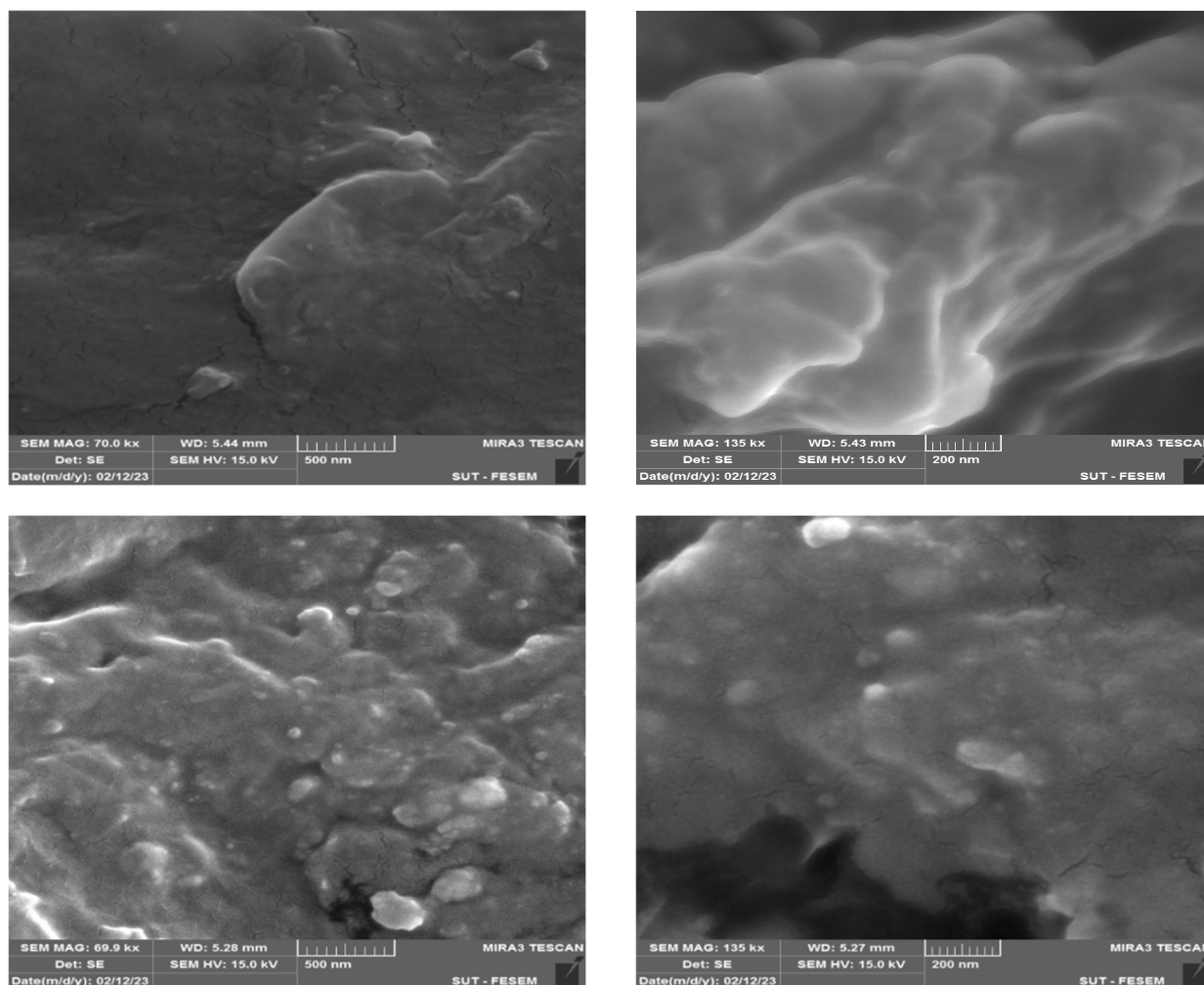
Figure 7. Field Emission Scanning Electron Microscope (FESEM) for pure PMMA and PMMA/MWCNT/Ag hybrid composites

Figure 7 showed that the fabricated Ag-materials were of a mean size of about 30 nm i.e. Ag-NPs were dispersed in PMMA/MWCNT/Ag nanocomposites and led to well significant results on the various characteristics of PMMA//MWCNT/Ag nanocomposites such as electrical, thermal, shielding properties. Homogeneous dispersion of Ag-NPs is preferred to avoid the formation of crack creativities in the PMMA/MWCNT nanocomposites loaded (0.5%wt) on the distribution and the dispersion of the Ag-NPs as nanofiller in the PMMA/MWNT/Ag nanocomposites matrix.

3. CONCLUSION

PMMA/MWCNT/Ag hybrid composite display electrical conductivity of around 2.14×10^{-4} S/cm as a percolation critical concentration is obtained at 0.5 wt% for MWCNT and 0.5 wt% for Ag. Dielectric properties have been tested across a wide frequency range. The AC conductivity varies with variations in MWCNT and Ag concentrations, as well as with applied field frequency and dielectric constant, illustrative of the significantly improved permittivity of these hybrid composites. Increased frequency causes a reduction in the dielectric constant, dielectric loss, loss of tangent, and dielectric loss. The PMMA/MWCNT/Ag hybrid composite's shielding performance is significantly influenced by the weight proportion (0.5 wt%/0.5 wt%) of MWCNT and Ag, which increases the X-band shielding efficiency. According to TGA/DTA research, exothermic reactions cause the majority of weight loss between 200 and 300°C. FESEM show that PMMA/MWCNT/Ag hybrid composites had uniform dispersion of the carbon nano tube and silver particles within the PMMA matrix that due to filler presents large surface area for better interfacial bonding between the matrix and particles.

• **Author Contribution**
Nadia Abbas Ali wrote the main manuscript text and Badiaa Alaw prepared figures and Tables and collected the data
• **Conflict of Interest**
   o All authors have participated in (a) conception and design, or analysis and interpretation of the data; (b) drafting the article or revising it critically for important intellectual content; and (c) approval of the final version.
   o This manuscript has not been submitted to, nor is under review at, another journal or other publishing venue.
   o The authors have no affiliation with any organization with a direct or indirect financial interest in the subject matter discussed in the manuscript
• **Data Availability Statement**
   o Deposit your research data in a relevant data repository

ORCID IDs

◉**Nadia Abbas Ali,** https://orcid.org/0000-0002-3996-112X

REFERENCES

[1]   R.S. Yadav, I. Kuritka, and J. Vilcakova, *Advanced Spinel Ferrite Nanocomposites for Electromagnetic Interference Shielding Applications*, (Elsevier, 2020).
[2]   A. Sami, and M.E. Abdulmunem, "Synthetic Aperture Radar Image Classification: a Survey," Iraqi Journal of Science, **61**(5), 1223-1232 (2020). https://doi.org/10.24996/ijs.2020.61.5.29
[3]   A.A. Kareem, and H.Kh. Rasheed, "Electrical and thermal characteristics of MWCNTs modified carbon fiber/epoxy composite films,," Materials Science Poland, **37**(4), (2019). https://doi.org/10.2478/msp-2019-0081
[4]   H. Lecocq, N. Garois, O. Lhost, P.-F. Girard, P. Cassagnau, and A. Serghei, "Polypropylene/carbon nanotubes composite materials with enhanced electromagnetic interference shielding performance: Properties and modeling," Composites Part B: Engineering, **189**, 107866 (2020). https://doi.org/10.1016/j.compositesb.2020.107866
[5]   H. Wang, K. Zheng, X. Zhang, X. Ding, Z. Zhang, C. Bao, L. Guo, et al., "3D network porous polymeric composites with outstanding electromagnetic interference shielding," Composites Science and Technology, **125**, 22-29 (2016). http://dx.doi.org/10.1016%2Fj.compscitech.2016.01.007
[6]   A.N. Abd, A.H. Al-Agha, and M.A. Alheety, "Addition of Some Primary and Secondary Amines to Graphene Oxide, and Studying Their Effect on Increasing its Electrical Properties," Baghdad Science Journal, **13**(1), (2016). https://doi.org/10.21123/bsj.2016.13.1.0097
[7]   A.M. Abd-Elnaiem, S.I. Hussein, H.S. Assaedi, and A.M. Mebed, "Fabrication and evaluation of structural, thermal, mechanical and optical behavior of epoxy–TEOS/MWCNTs composites for solar cell covering," Polym. Bull. **78**(7), 3995-4017 (2021). https://doi.org/10.1007/s00289-020-03301-5
[8]   D. Yuan, H. Guo, K. Ke, and I. Manas-Zloczower, "Recyclable conductive epoxy composites with segregated filler network structure for EMI shielding and strain sensing," Composites Part A: Applied Science and Manufacturing, **132**, 105837 (2020). https://doi.org/10.1016/j.compositesa.2020.105837
[9]   Z. Zeng, W. Li, N. Wu, S. Zhao, and Xuehong Lu, "Polymer-assisted fabrication of silver nanowire cellular monoliths: toward hydrophobic and ultraflexible high-performance electromagnetic interference shielding materials," ACS applied materials & interfaces, **12**(34), 38584-38592 (2020). https://doi.org/10.1021/acsami.0c10492
[10] S. Ghosh, S. Ganguly, P. Das, T.K. Das, M. Bose, N.K. Singha, A.K. Das, and N.C. Das, "Fabrication of reduced graphene oxide/silver nanoparticles decorated conductive cotton fabric for high performing electromagnetic interference shielding and antibacterial application," Fibers and Polymers, **20**, 1161-1171 (2019). https://doi.org/10.1007/s12221-019-1001-7
[11] F. Ren, Z. Li, L. Xu, Z. Sun, P. Ren, D. Yan, and Z. Li, "Large-scale preparation of segregated PLA/carbon nanotube composite with high efficient electromagnetic interference shielding and favourable mechanical properties," Composites Part B: Engineering, **155**, 405-413 (2018). https://doi.org/10.1016/j.compositesb.2018.09.030

[12] H. Gargama, A.K. Thakur, and S.K. Chaturvedi, "Polyvinylidene fluoride/nanocrystalline iron composite materials for EMI shielding and absorption applications," Journal of Alloys and Compounds, **654**, 209-215 (2016). https://doi.org/10.1016/j.jallcom.2015.09.059

[13] H.M. Kim, K. Kim, C.Y. Lee, J. Joo, S.J. Cho, H.S. Yoon, D.A. Pejaković, et al., "Electrical conductivity and electromagnetic interference shielding of multiwalled carbon nanotube composites containing Fe catalyst," Applied physics letters, **84**(4), 589-591 (2004). https://doi.org/10.1063/1.1641167

[14] S.-M. Yuen, C.-C.M. Ma, C.-Y. Chuang, K.-C. Yu, S.-Y. Wu, C.-C. Yang, and M.-H. Wie, "Effect of processing method on the shielding effectiveness of electromagnetic interference of MWCNT/PMMA composites," Composites Science and Technology, **68**(3-4), 963-968 (2008). https://doi.org/10.1016/j.compscitech.2007.08.004

[15] Y. Liu, D. Song, C. Wu, and J. Leng, "EMI shielding performance of nanocomposites with MWCNTs, nanosized Fe3O4 and Fe," Composites Part B: Engineering, **63**, 34-40 (2014). http://dx.doi.org/10.1016/j.compositesb.2014.03.014

[16] H. Yuan, Y. Xiong, Q. Shen, G. Luo, D. Zhou, and L. Liu, "Synthesis and electromagnetic absorbing performances of CNTs/PMMA laminated nanocomposite foams in X-band," Composites Part A: Applied Science and Manufacturing, **107**, 334-341 (2018). https://doi.org/10.1016/j.compositesa.2018.01.024

[17] N.C. Das, Y. Liu, K. Yang, W. Peng, S. Maiti, and H. Wang, "Single-walled carbon nanotube/poly (methyl methacrylate) composites for electromagnetic interference shielding," Polymer Engineering & Science **49**(8), 1627-1634 (2009). https://doi.org/10.1002/pen.21384

[18] H.K. Al-Lamy, E.M. Nasir, H.J. Abdul-Ameer, "Electrical properties of Cdxse1-x films at different thickness and annealing temperatures," Digest Journal of Nanomaterials and Biostructures, **15**(1), 143-156 (2020). https://chalcogen.ro/143_LamyHK.pdf

[19] A.H. Mohammed, A.N. Naje, and R.K. Ibrahim, "Photoconductive Detector Based on Graphene Doping with Silver Nanoparticles," Iraqi Journal of Science, **63**(12), 5218-5231 (2022). https://doi.org/10.24996/ijs.2022.63.12.12

[20] ASTM D4935-10, *Standard Test Method for Measuring the Electromagnetic Shielding Effectiveness of Planar Materials*, (2010).

[21] A.F. Ahmad, S.A. Aziz, S.J. Obaiys, M.H.M. Zaid, K.A. Matori, K. Samikannu, and U.S. Aliyu, "Biodegradable poly (lactic acid)/poly (ethylene glycol) reinforced multi-walled carbon nanotube nanocomposite fabrication, characterization, properties, and applications," Polymers, **12**(2), 427 (2020). https://doi.org/10.3390/polym12020427

[22] A.S. Abd-Alsada, and M.F.A. Alias, "Impact of CNT Concentrations on Structural, Morphological and Optical Properties of ZnO: CNT Nano composite Films," Journal of Physics: Conference Series, **2114**(1), 012020 (2021). https://doi.org/10.1088/1742-6596/2114/1/012020

[23] I.M. Ali, A.A. Mohammed, and A.H. Ajil, "A study of the characterization of CdS/PMMA nanocomposite thin film," Iraqi Journal of Physics, **14**(29), 191-197 (2016). https://www.iasj.net/iasj/pdf/c3192b6d984e4477

ПІДВИЩЕННЯ ЕКРАНУЮЧОЇ ЕФЕКТИВНОСТІ ГІБРИДНОГО КОМПОЗИТУ PMMA/MWCNTS/Ag ДЛЯ ЗАСТОСУВАННЯ В Х-ДІАПАЗОНІ

Бадіа Ісмал Алаві, Надя Аббас Алі
Факультет фізики, Науковий коледж, Багдадський університет, Багдад, Ірак

Гібридні композитні плівки багатошарові поліметилметакрилат/вуглецеві нанотрубки зі сріблом (PMMA/MWCNT/Ag) одержані методом лиття з розчинника для використання в електротехніці. Провідність змінного струму і діелектричні характеристики були досліджені при кімнатній температурі. Електропровідність гібридного композиту досягає критичної концентрації перколяції 2,14×10⁻⁴ см/см за рахунок легування Ag. Для всіх гібридних композитів PMMA/MWCNT/Ag частотно-залежна діелектрична проникність зменшується з розширенням діапазону частот. Зі збільшенням концентрації MWCNT та Ag провідність змінного струму має тенденцію до збільшення. Встановлено, що зміст MWCNT та Ag істотно впливає на SE даних композитів. Високу ефективність електромагнітного (EM) екранування (SE) було досягнуто в діапазоні частот від 8,2 до 12,4 ГГц (Х-діапазон). Максимальне EM згасання у 18 дБ на частоті 12 ГГц було досягнуто при використанні 0,5 мас.% MWCNT та Ag. Термічний аналіз сформованих гібридних композитів PMMA/MWCNT/Ag показав, що екзотермічні реакції з найбільшою втратою маси протікають в інтервалі температур від 200°C до 300°C. Скануючий електронний мікроскоп з польовою емісією (FESEM) показує, що гібридні композити PMMA/MWCNT/Ag мають однорідну дисперсію вуглецевих нанотрубок та частинок срібла у матриці PMMA.

Ключові слова: *екранування електромагнітних перешкод; Х-діапазон; електрична провідність; діелектрична постійна; діелектричні втрати; термічний аналіз*

STUDY OF MgO UNDER PRESSURE STRUCTURAL AND ELECTRONIC PROPERTIES[†]

**Yamina Benkrima[a],*, Abderrahim Achouri[b], Djamel Belfennache[c], Radhia Yekhlef[c],
Naim Hocine[d]**

[a]Ecole Normale Supérieure de Ouargla, 30000 Ouargla, Algeria
*[b]Université de Ouargla, Faculté des Mathématiques et des Sciences de la Matière, Lab. Développement des énergies nouvelles
et renouvelables dans les zones arides et sahariennes, Ouargla 30000, Algeria*
[c]Research Center in Industrial Technologies CRTI, P.O. Box 64, Cheraga, 16014 Algiers, Algeria
[d]University of Science and Technology Oran, 31024 Oran, Algeria
Corresponding author: b-amina1@hotmail.fr

In this study, the Density Function Theory (DFT), Generalized Gradient Approximation (GGA) and Local Density Approximation (LDA) were used, based on the Siesta code, in order to study the magnesium oxide compound (MgO) and focus on the (B4) Wurtzite phase. This is to find the primary cell constants and energy gap at 0 pressure, which are consistent with previous results. The effect of pressure on the energy gap and the size of the primary cell as well as the dielectric constant were studied. The study also revealed that the (B4) phase can move to the (B2) phase at the pressure of 45.86 GPa and from the h-MgO phase to the (B2) phase at 70 GPa.
Keywords: *MgO; Siesta; Structural Properties; Electronic Properties; Pressure*
PACS: 71.15.Mb, 73.61.Cw

1. INTRODUCTION

In recent years, the compound MgO has emerged as one of the most intriguing oxides.1Several theoretical and practical studies have been conducted on it. The majority of phases on which it crystallizes are eitherB1, B3 or B4. Many researchers have attempted to conduct several laboratories experiments whose goal was to search for the formed crystal structures of MgO, resulting from their deposition on metal substrates [2–5]. The B1 phase is called the rocky structure; the B3 and B4 phases are called Zinc blend and Wurtzite respectively. MgO is a solid, white mineral that is found in the earth's crust. It belongs to group (II-VI), meaning that it consists of an oxygen atom with an ionic bond. It is one of a large group of industrially important materials due to its energy gap of 7.833 eV [6].

In the ordinary case, we find that MgO crystallizes in the B1 phase, with a space group (Fm3m), under ordinary conditions. Under the influence of pressure, we find that the phase (B1) moves to (B2), but experimentally speaking, the researchers were unable to confirm such a transition. MgO compound has been studied theoretically and experimentally in order to know its electronic structure and properties. This is what was highlighted by the works [7-12]. H. Abu-Farsakh et al. [7] investigated the structural and electrical characteristics of MgO in the B1 and B2 phases, using the DFT and the LDA and Jaffe et al. [8] using both LDA and GGA in studying the two compounds MgO and ZnO under high pressure, which results in a phase transition. Through the use of the linearized augmented plane wave (FP-LAPW) approach, Zhu et al [10], also discovered the general characteristics of MgO at the B1 phase.

The structure and optoelectronic properties of MgO were also researched and verified by Liu et al. [11]. Besides, to determine the characteristics of the MgO structure, Anderson and Andreatch [12] carried out experimental research, as it is one of the prominent components of the earth's layers, so its electronic structure will inevitably and significantly change under the earth, compared to its state under high pressure. Our study theoretically explains how these transitions occur, which in turn stresses the importance of knowing the way and conditions of the occurrence of transitions between some phases of MgO compound subject to different pressure values. In fact, we will focus on Wurtzite (B4), how is it transited and how does its energy gap change along with the pressure changing.

2. THEORETICAL CALCULATION METHOD

We have concentrated on magnesium oxide in the Wurtzite structure, which is an appropriate host for weaken attractive semiconductors. A Wurtzite structure has two zinc particles and two oxygen iotas in its unit cell, and it has P63mc space bunch evenness. We utilized test esteems for our three gem boundaries, in particular a = b = 3.283 Å, c = 5.095 Å and u = 0.388 Å [13]. To profit from Bloch's hypothesis in intermittent designs, we made a 2×2×2 super-cell of the unit cell that contains 24 particles. The estimations were acted in the structure of thickness utilitarian hypothesis in the free molecule guess utilizing Kohn and Sham [14,15] eigen states and eigen values. Was used the Generalized Gradient Approximation by Perdew-Burke-Ernzerh (PBE-GGA) [16] and of Local Density Approximation (LDA) by Ceperley and Alder [17] are employed in the exchange correlation effect calculation. The summed-up inclination estimate and the nearby thickness guess were utilized for the trade connection energy. Likewise, we utilized an equal simultaneous molecule approach in our computations, as executed in the Rest code. Central electrons that do not have a significant

---

effect on chemical and electronic properties are replaced by effective Troullier-Martins pseudo-potentials in their fully separable form in the SIESTA code [18]. In this code, a set of pseudo-atomic orbitals (PAO's) for valence electrons has been used for wave function expansion. These orbitals are built by multiplying an angular function with defined quantum values m and l, which are used to indicate the size of the orbitals, by a numerical radius function. Among the three basic set types of the code, DZP was chosen. There are two parameters of the SIESAT that need to be optimized [19]. These parameters, which correspond to the Kgrid-cutoff and Mesh-cutoff energy values, were optimized by bringing the total energy to 20, and 350 eV respectively. The convergence criterion – the total energy – is set at 10^{-4}.

3. RESULTS AND DISCUSSION
3.1. Structural Properties

Over a decade of research, the lattice constants of MgO have been confirmed numerous times [20]. The P63mc group and the lattice constants estimated to be: a=b=3.283Å, c=5.095Å, α = 90.03°, β = 90.037°, and γ = 119.90° [13] characterize the stable main cell structure of MgO, which is (B4) Würtzite. Each primary cell of MgO consists of four atoms, each two atoms of Mg occupy the following positions (0, 0, 0), (1/3.2/3.1/2). As far as O atoms are concerned, they occupy the following implantation positions (0, 0, μ), (1/3.2/3.μ), whereas μ is the internal variable of the Wurtzite structure, which determines the length of the bonds between Mg and O atoms. The variable μ is given as the following: μ = (1/4 + (c2/(3.a2))).The Siesta software, which was used to determine the primary cell constant constants of MgO, is a factor in the computations in this paper. The primary cell constants of MgO were calculated using the following results. The Table 1 contains the results.

Table 1. Comparison of primary cell constants of MgO with theoretical and practical results

	a (Å)	c (Å)	μ (Å)	c/a
Present work GGA LDA	3.327 3.288	5.025 5.004	1.0117 1.2205	1.5103 1.5219
Theoretical works GGA	3.281 [21] 3.3105 [22] /	5.1360 [21] 5.12363 [22] /	0.3930 [21] 0.3915 [22] /	/ / 1.547 [21] 1.530 [13]
Theoretical works LDA	3.322 [20] 3.249 [22] 3.320 [13] 3.322 [23] 3.169 [24] / [26] 3.278	/ 5.277 [22] 5.056 [13] / 5.175 [24] / 5.062 [26]	0.3916 [20] 0.3917 [22] 0.386 [13] 0.392 [23] 0.3750 [24] 0.3935 [25]	/ 1.546 [20] 1.547 [22] 1.565 [13] / 1.536 [24] 1.506 [25] /
Experimental work	3.283 [13]	5.095 [13]	0.388 [13]	1.552 [13]

We were able to compute the primary cell constants using the Density Function Theory (DFT) and the Siesta software, and we subsequently discovered the values of 3.327Å for constant a and 5.025Å for constant c. It should be noticed that these findings substantially agree with the conclusions of applied theory included in Table 1 results of previous theoretical and experimental work [13, 21-26]. Additionally, the percentage of error in the obtained values has been calculated. Assuming that they are compared to the experimental values that were used as a reference, we discovered that the error value was estimated at 1.34 percent for the constant a and 1.37 percent for the constant c with GGA. With LDA, it was calculated to be 0.15% for constant a and 1.79% for constant c. This suggests that the determined error results are likely to be minor and that the calculation's procedure was logical and reasonable.

The selected Brillion region is the primary structure to study electronic properties of the matter. The Figure 1 shows the Brillion region related to the hexagon.
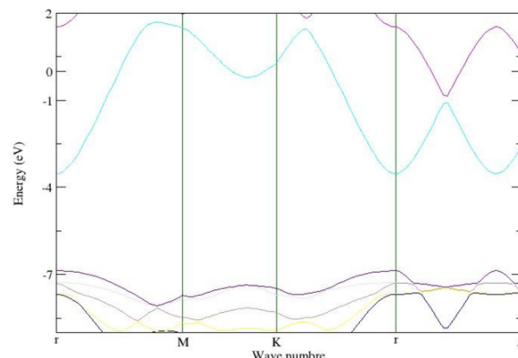
Figure 1. Energy band structure of the Wurtzite phase MgO

It is worth noting that the study of properties on this region can be generalized later to MgO. DFT and GGA were used to determine the energy gap of MgO. This method has also been relied upon because it is among the best suitable methods for studying the electronic structures of materials. The energy bands structure of MgO was calculated for the previously obtained lattice constants (a = 3.327Å, c = 5.025Å, β = 90.037°, α = 90.03°, γ = 119.90°). The structure of energy bands of MgO was calculated as shown in Figure 1.

It is noticeable in the previous figure that the highest peak of the valence band and the lowest peak of the conduction band are on the same line, passing through the point. This explains that MgO has a direct gap estimated at: 3.27 eV. The following values concern the energy gap, calculated with GGA and LDA and compared to other theoretical results, as shown in Table 2.

Table 2. The energy gap Eg (eV)

| Used method	Energy gap Eg(eV)	
	GGA	LDA
Our results	3.27	/
Otherresults	4.408 [27] 4.431 [28] 4.450 [29] EV-GGA 5.419 [28] MBJ–GGA 7.2 [28]	/ 968.4 [28] 5.05 [30]
Experimentalresults	7.833 [6] 3.48 [21]	
Proportionalerror (%)	15.96	

We note that the value of the energy gap obtained by this theory was close to the theoretical results listed in Table 2. Our calculated results for the structure of the energy bands by GGA method are smaller than the experimental ones. This indicates that it does not provide very precise results. Unfortunately, we found that the value of the energy gap calculated by GGA is smaller compared to the experimental results. Even if we use LDA, the value of the energy band will also be less than the experimental value as well. It is well known that the GGA reduces the calculated forbidden band value compared to the experimental value, so the calculated values remain as a lower estimate of the true values of the energy gap [31].

3.3. Characteristics of MgO by changing the pressure
In a previous study, we fixed the pressure value at 0 GPa, now we will change it from 0 GPa to 100 GPa, then we study the new structural and electronic properties.

a) Variation of the dielectric constant
The value of the dielectric constant of MgO is calculated by GGA and LDA. The results are shown in Figure 2.
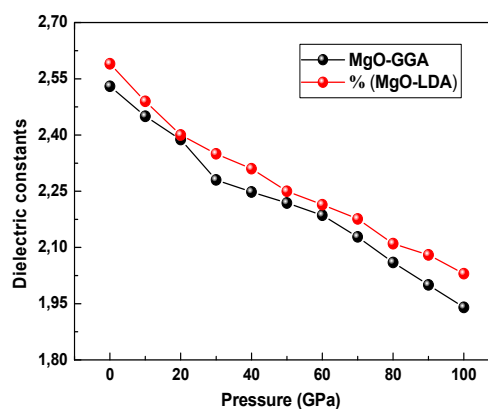
Figure 2. Variations of the dielectric constant with GGA and LDA in terms of pressure

Figure 2 displays the changes of the dielectric constant values in terms of the change of the pressure value exerted on MgO compound using GGA and LDA. We notice that the values of the dielectric constant are decreasing the more the value of the pressure exerted on the primary cell is increasing. Besides, the two curves of variations of the dielectric constant value with GGA and LDA are the same. This is consistent with the work of S. Labidi et al. [28]. The results of the values of the dielectric constant at a 0 GPa pressure value with GGA and LDA, are shown in the Table 3.

Table 3. Values of the dielectric constant at 0 GP pressure

	Our results	Theoretical results	Experimental results
Value of the dielectric constant at0 GP (pressure)	GGA (2.53) LDA (2.59)	2.840 [28] 3.12 [29]	2.95 [32]

The table shows that the values of the dielectric constant with GGA and LDA are close. Actually, the value of the dielectric constant at 0 GPa is very close to the theoretical work [28,29], and to the practical one [32].

b)   Energy Gap Variation

The energy gap was calculated in terms of the pressure change of MgO by GGA and LDA, as shown in the Figure 3.
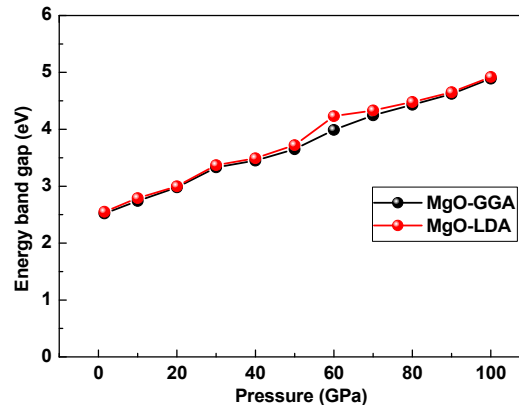

Figure 3. Energy gap by GGA and LDA in terms of pressure

The diagram shows that the greater the value of the pressure exerted on the primary cell, the higher the value of the energy gap for both curves by GGA and LDA. This is consistent with the work of S. Labidi et al [28].

c)   Change in Enthalpy Energy

The changes in enthalpy energy value of MgO were calculated for the transition from B4 to B2 phase and from h-MgO phase to B2 using GGA. In order to study the possibility of structural optimization and to know the value of the pressure transition Pt of MgO from B4 to B2 phase and from h-MgO to B2 phase, we used the GGA, where an increasing pressure was applied to the MgO compound to study the phase transition from B4 to B2 structure, as well as from h-MgO to B2 structure. We performed the enthalpy calculations in the case of B2 and B4 phases, we got the curve of the Figure 4a, and in the case of B2 and h-MgO phases, we got the curve of the Figure 4b.
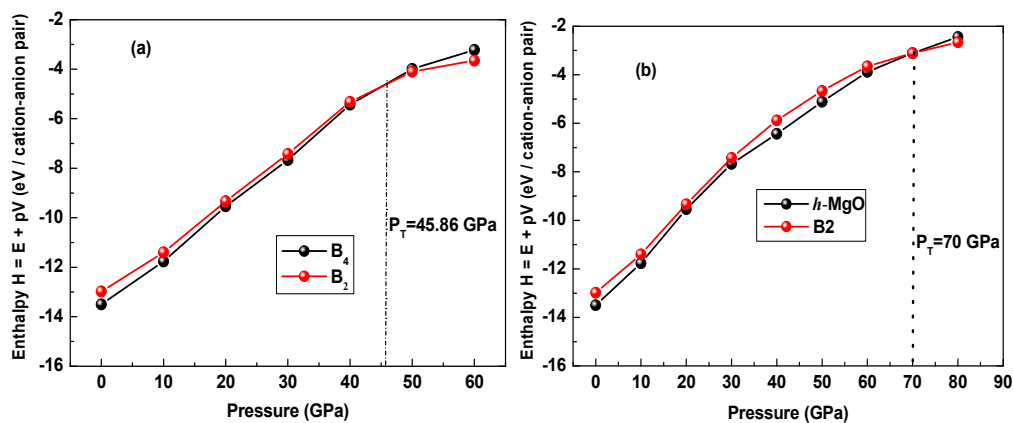

Figure 4. Enthalpy H as a function of transition pressure from: (a) – B4 to B2 phase, (b) – h-MgO to B2 phase

Studying the curves, we notice that the Figure 4. Enthalpy H as a function of transition pressure from: (a) B4 to B2 phase, (b) h-MgO to B2 phase enthalpy value of B4 phase is the lowest compared to B2 phase. In Figure b, the enthalpy value of h-MgO phase is the lowest compared to B2 phase, considering the pressure value applied to this phase from (0 GPa to 44 GPa), (0 GPa to 70 GPa), respectively. This area was characterized by the fact that each of the phases B4, h-MgO is the most stable compared to B2 phase for both curves, at the pressure value 45.86 GPa, it was observed that the enthalpy value of the phases B4 and h-MgO is exactly equal to the enthalpy value of B2 phase. For both curves, respectively, this point is the value between the phase transition from B4 or h-MgO to B2 phase. For the values from 46 GPa to 60 GPa and from 70 GPa to 80 GPa, we see that B2 structure has become the one having lower enthalpy in both Figures 4a and 4b, respectively, and therefore higher stability. This is largely consistent with the results of K.B. Joshi et al [33].

d)   Size Changes

Changes in the values of the size of MgO in terms of pressure have been recorded using both GGA and LDA. Figure 5 shows those findings.
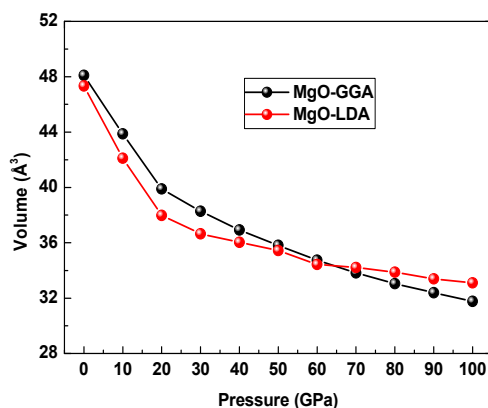
Figure 5. The size of MgO in terms of pressure using GGA and LDA

Through the curve of Figure 5, we see that whenever the value of the pressure exerted on the primary cell of the compound MgO is raised by GGA and LDA, the cell size decreases. It was also observed that the cell size in (0-62) GPa scope calculated by the GGA is larger than in the LDA, while the opposite is recorded after the pressure value reaching 63 GPa. Our results are consistent with the work of Jackson et al. [34], the Figure 3 shows that.

4. CONCLUSION

In this paper, we searched for the structural and electronic properties of the compound MgO with phase (B4) Wurtzite. The primary cell constants and the energy gap value were calculated by DFT, using GGA and LDA, with the help of Siesta program. Our results were very close with the available theoretical and experimental results. The calculations were carried out under the ordinary pressure value and other different values. The conclusions reached as summarized as follows:

• The ground state properties of the wurtzite structure such as the primary cell constants and the energy gap were found under ordinary conditions of temperature and pressure, which are consistent with previous theoretical and experimental results.

• The study also showed that the increase in the pressure value increases the energy gap value.

• The size of the primary cell is subject to change. If the structure is subjected to the influence of increasing pressure, there will be a decrease in its size.

• Calculations of the aliasing values predict the phase transition from: B4 → B2 and from: h-Mgo→B2. This is at the following pressure values: 45.86 GPa and 70 GPa, respectively.

ORCID IDs
Yamina Benkrima, https://orcid.org/0000-0001-8005-4065; **Djamel Belfennache,** https://orcid.org/0000-0002-4908-6058

REFERENCES
[1] C. Zhang, Y. Li, J. Zhao, and Z. He, "Sulfidation performance of MgO-modified calcium-based waste from calcium looping: Experimental and density functional theory study," J. Environ. Chem. Eng. **10(3)**, 108039 (2022). https://doi.org/10.1016/j.jece.2022.108039

[2] H. Liu, T. Han, Q. Li, B. Sun, and C. Wang, "Novel microstructures inducing an excellent combination of strength and elongation in in-situ MgO/AZ31 composites," Compos. Struct. **294**, 115770 (2022). https://doi.org/10.1016/j.compstruct.2022.115770

[3] Y. Wang, K. Huo, X. Meng, D. Cai, B. Wang, and J. Liu. "MgO recycling in l-lactic acid fermentation and effects of the reusable alkaline neutralizer on Lactobacillus rhamnosus: From process integration to transcriptome analysis," LWT, **163**, 113616 (2022). https://doi.org/10.1016/j.lwt.2022.113616.

[4] A. Taşer, M.E. Güldüren, and H. Güney, "Fe doping effects in MgO thin films grown with SILAR technique," Mater. Chem. Phys. **272**, 124993 (2021). https://doi.org/10.1016/j.matchemphys.2021.124993

[5] Z. Song, B. Zhao, Q. Wang, and P. Cheng, "Steering reduction and decomposition of peroxide compounds by interface interactions between MgO thin film and transition-metal support," Appl. Surf. Sci. **459**, 812-821 2018). https://doi.org/10.1016/j.apsusc.2018.08.071.

[6] R.C. Whited, C.J. Flaten, and W.C. Walker, "Excitonthermoreflectance of MgO and CaO," Solid. State. Commun. **13**, 1903-1905 (1973). https://doi.org/10.1016/0038-1098(73)90754-0

[7] H. Abu-Farsakh, I. Al- Qasir, and A. Qteish, "Fundamental properties and phase stability of B1 and B2 phases of MgO over a wide range of pressures and temperatures: A first-principles study," Comput. Mater. Sci. **154**, 159-168 (2018). https://doi.org/10.1016/j.commatsci.2018.07.035.

[8] J.E. Jaffe, J.A. Snyder, Z. Lin, and A.C. Hess, "LDA and GGA calculations for high-pressure phase transitions in ZnO and MgO," Phys. Rev. B. **62**, 1660 (2000). https://doi.org/10.1103/PhysRevB.62.1660

[9] S. Ritterbex, T. Harada, and T. Tsuchiya. "Vacancies in MgO at ultrahigh pressure: About mantle rheology of super-Earths," Icarus, **305**, 350-357 (2018). https://doi.org/10.1016/j.icarus.2017.12.020

[10] Y.Z. Zhu, G.D. Chen, H. Ye, A. Walsh, C.Y. Moon, and S.H. Wei, "Electronic structure and phase stability of MgO, ZnO, CdO, and related ternary alloys," Phys. Rev. B, **77**, 245209 (2008). https://doi.org/10.1103/PhysRevB.77.245209

Yamina Benkrima, Abderrahim Achouri, et al.

[11] Z.J. Liu, Y.X. Du, X.L. Zhang, J.H. Qi, L.N. Tian, and Y. Guo. "Density functional calculations of the electronic structure and optical properties of magnesium oxide," Solar Energy Phys. Status Solidi B, **247(1)**, 157-162 (2010). https://doi.org/10.1002/pssb.200945276

[12] O.L. Andreson, and P.J. Andreatch, "Pressure Derivatives of Elastic Constants of Single-Crystal MgO at 23° and -195.8°C," J. Am. Ceram. Soc. **49**(8), 404-409 (1966). https://doi.org/10.1111/j.11512916.1966.tb15405.x

[13] M. Toporkov, D.O. Demchenko, Z. Zolnai, J. Volk, V. Avrutin, H. Morkoc, and U. Ozgür, "Lattice parameters and electronic structure of BeMgZnO quaternary solid solutions: Experiment and theory," J. Appl. Phys. **119**, 095311 (2016). https://doi.org/10.1063/1.4942835

[14] P. Hohenberg, and W. Kohn, "Inhomogeneous Electron Gas," Phys. Rev. B, **136**, 864-871 (1964). http://dx.doi.org/10.1103/PhysRev.136.B864

[15] W. Kohn, and L.J. Sham, "Self-Consistent Equations Including Exchange and Correlation Effects," Phys. Rev. **140**, A1133 (1965). https://doi.org/10.1103/PhysRev.140.A1133

[16] J.P. Perdew, K. Perdew, and M. Ernzerhof, "Generalized Gradient Approximation Made Simple," Phys. Rev. Lett. **77**, 3865 (1996). https://doi.org/10.1103/PhysRevLett.77.3865.

[17] D.M. Ceperley, and B.J. Alder, "Ground State of the Electron Gas by a Stochastic Method," Phys. Rev. Lett. **45**, 566 (1980). https://doi.org/10.1103/PhysRevLett.45.566

[18] P. Ordejon, E. Artacho, and J.M. Soler, "Self-consistent order- N density-functional calculations for very large systems," Phys. Rev. B. **53**, R10441(R) (1996). https://doi.org/10.1103/PhysRevB.53.R10441

[19] N. Troullier, and J.L. Martins, "Efficient pseudopotentials for plane-wave calculations," Phys. Rev. B. Condens. Matter. **43(3)**, 1993-2006 (1991). https://doi.org/10.1103/physrevb.43.1993

[20] A. Schleife, F. Fuchs, J. Furthmuller, and F. Bechstedt, "First-principles study of ground- and excited-state properties of MgO, ZnO, and CdO polymorphs," Phys. Rev. B. **73**, 245212 (2006). https://doi.org/10.1103/PhysRevB.73.245212

[21] Y.Z. Zhu, G.D. Chen, Y. Honggang, W. Aron, C.Y. Moon, and S.H. Wei, "Electronic structure and phase stability of MgO, ZnO, CdO, and related ternary alloys," Phys. Rev. B. **77**, 245209 (2008). https://doi.org/10.1103/PhysRevB.77.245209

[22] A. Djelal, k. Chaibi, N. Tari, K. Zitouni, and A. Kadri, "Ab-initio DFT-FP-LAPW/TB-mBJ/LDA-GGA investigation of structural and electronic properties of $Mg_xZn_{1-x}O$ alloys in Würtzite, Rocksalt and Zinc-Blende phases," Superlattices and Microstructures, **109**, 81-97 (2017). https://doi.org/10.1016/j.spmi.2017.04.041

[23] Y. Duan, L. Qin, G. Tang, and L. Shi, "First-principles study of ground- and metastable-state properties of XO (X = Be, Mg, Ca, Sr, Ba, Zn and Cd)," Eur. Phys. J. B. **66**, 201-209 (2008). https://doi.org/10.1140/epjb/e2008-00415-3

[24] W.R.L. Lambrecht, and S. Limpijumnong, "Theoretical study of the relative stability of wurtzite and rocksalt phases in MgO and GaN," Phys. Rev. B. **63**, 104103 (2001). https://doi.org/10.1103/PhysRevB.63.104103

[25] M. Heinemann, M. Giar, and C. Heiliger, Mater. Alloys. Res. Soc. Symp. Proc. **1201**, 533 (2010). https://doi.org/10.1557/PROC-1201-H05-33

[26] Q. Yan, P. Rinke, M. Winkelnkemper, A. Qteish, D. Bimberg, M. Scheffler, and C.G. Van de Walle, "Strain effects and band parameters in MgO, ZnO, and CdO," Appl. Phys. Lett. **101,** 152105 (2012). https://doi.org/10.1063/1.4759107

[27] F. Daniel, B.J. Morgan, and W. Aron, "Self-Consistent Hybrid Functional Calculations: Implications for Structural, Electronic, and Optical Properties of Oxide Semiconductors," Nanoscale. Research. Letters, **12**(1), 19 (2017). https://doi.org/10.1186/s11671-016-1779-9

[28] S. Labidi, J. Zeroual, M. Labidi, K. Klaa, and R. Bensalem, "Structural Electronic and Optical Properties of MgO, CaO and SrO Binary Compounds: Comparison Study," Solid State Phenomena, **257**, 123-126 (2016). https://doi.org/10.4028/www.scientific.net/SSP.257.123

[29] M. Dadsetani, and R. Beiranvand, "Optical properties of alkaline-earth metal oxides from first principles," J. Solid. State. Sci. **11**, 2099-2105 (2009). https://doi.org/10.1016/j.solidstatesciences.2009.08.018

[30] H. Baltache, R. Khenata, M. Sahnoun, M. Driz, B. Abbar, and B. Bouhafs, "Full potential calculation of structural, electronic and elastic properties of alkaline earth oxides MgO, CaO and SrO," Physica B: Condensed Matter. **344**, 334-342 (2004). https://doi.org/10.1016/j.physb.2003.09.274

[31] M. Brik, "First-principles calculations of the structural, electronic, optical and elastic properties of the $CuYS_2$ semiconductor," J. of Phys. Cond. Matt. **25**(34), 345802 (2013). https://doi.org/10.1088/0953-8984/25/34/345802

[32] M.E. Lines, "Bond-orbital theory of linear and nonlinear electronic response in ionic crystals. I. Linear response," Phys. Rev. B. **41**, 3372 (1990). https://doi.org/10.1103/PhysRevB.41.3372

[33] K.B. Joshi, B.K. Sharma, U. Paliwal, and B. Barbiellini, "Pressure-dependent electronic properties of MgO polymorphs: a first-principles study of Compton profiles and autocorrelation functions," J. Mater Sci. **47**, 7549 (2012). https://doi.org/10.1007/s10853-012-6521-0

[34] I. Jackson, and H. Niesler, in: *High-Pressure Research in Geophysics*, editors S. Akimoto, and M.H. Manghnani (Center for Academic Publication, Tokyo, 1982). pp. 93-113.

ДОСЛІДЖЕННЯ СТРУКТУРНИХ ТА ЕЛЕКТРОННИХ ВЛАСТИВОСТЕЙ MgO ПІД ТИСКОМ

Яміна Бенкріма[a], Абдеррахім Ачурі[b], Джамель Бельфеннаше[c], Радхіа Єхлеф[c], Наїм Хосін[d]
[a]Вища нормальна школа Уаргла, 30000 Уаргла, Алжир
[b]Університет Уаргла, факультет математики та матеріалознавства, лабораторія розвитку нових і відновлюваних джерел енергії в посушливих зонах і зонах Сахари, Уаргла 30000, Алжир
[c]Дослідницький центр промислових технологій CRTI, P.O. Box 64, Черага, 16014, Алжир
[d]Університет науки і технологій Оран, 31024 Оран, Алжир

У цьому дослідженні використовувалися теорія функції густини (DFT), узагальнена градієнтна апроксимація (GGA) і локальна апроксимація густини (LDA) на основі коду Siesta для вивчення сполуки оксиду магнію (MgO) і зосередження на (B4) фазі Вюрцита. Це зроблено для визначення констант первинної комірки та енергетичного розриву при тиску 0, що відповідає попереднім результатам. Досліджено вплив тиску на ширину забороненої зони, розмір первинної комірки та діелектричну проникність. Дослідження також показало, що фаза (B4) може переходити у фазу (B2) при тиску 45,86 ГПа та з фази h-MgO у фазу (B2) при 70 ГПа.

Ключові слова: *MgO; Siesta; структурні властивості; електронні властивості; тиск*

CALCULATION OF THE TOTAL CURRENT GENERATED IN A TUNNEL DIODE UNDER THE ACTION OF MICROWAVE AND MAGNETIC FIELDS[†]

Gafur Gulyamov[a], Sharifa B. Utamuradova[b], Mukhamadjon G. Dadamirzaev[a],
Nozimjon A. Turgunov[b], Munira K. Uktamova[b,§], Kakhramon M. Fayzullaev[b,*],
Arofat I. Khudayberdiyeva[c], Alisher I. Tursunov[d]

ᵃNamangan Engineering Construction Institute, Namangan, Uzbekistan
ᵇInstitute of Semiconductor Physics and Microelectronics at the National University of Uzbekistan, Tashkent, Uzbekistan
ᶜTashkent Institute of Chemical Technology, ᵈTermiz State University, Termiz, Uzbekistan
*Corresponding Author e-mail: qahramonfayzullayev8@gmail.com, §e-mail: umk9391@gmail.com

In this paper, a formula was derived for calculating the total current generated in a tunnel diode under the action of a microwave field and a magnetic field. In addition, the dependence of the total current of the tunnel diode on the total power induced by the microwave field is theoretically presented and compared with experimental data. For the total current in the tunnel diode, without taking into account the excess current, volt-ampere characteristics was obtained for cases with and without the influence of a microwave field.
Keywords: *Chynowet model; Tsu-Esaki model; microwave field; magnetic field; barrier transparency coefficient; excess current*
PACS: 71.20. – b, 71.28. + d

INTRODUCTION

At present, the study of semiconductor-based nanostructures is a very topical direction in both fundamental and applied aspects [1–5].

The tunneling effect was experimentally discovered by Yajima and Esaki in a highly doped germanium-based diode [6]. A model was proposed by Leo Esaki in 1958 to explain this effect. In 1960, Evan O [7] developed a comprehensive theory of experience. Shortly thereafter, Karlovsky [8] proposed a simpler version of Esaki's model. In the Karlovsky model, the Fermi levels were sufficiently small. I. Shalish [9] and Kane, who worked independently, proposed the same model of the tunnel effect mechanism without knowing each other. In 1969, Duke presented a more advanced version of tunnel models [10]. As research on the properties of semiconductor materials and devices based on them continues, various tunneling models for p-n junction diodes have been presented. Since the electrical properties of semiconductor materials mainly depend on the state of impurity atoms in their volume, when choosing an alloying element, one should pay attention to their physicochemical parameters [11–14]. At a conference in Berlin in 1989, Herks presented a new model that related the rate of Shockley-Reed-Hall (SRH) recombination and zone-tunneling in the opposite direction [10]. In his work, Herks calculated the contribution of the tunneling effect as the recombination rate of the flux density. In the same direction, in 1991, Claassen [10] presented his model for the case of direct tunneling. The tunneling probability can also be calculated using the Wenzel-Kramers formula, but it is more convenient to calculate the tunneling probability using the transfer matrix method. Currently, the calculation of the tunnel current for diodes with a p-n junction using the Tsu-Esaki model [15] gives good results. This model was developed taking into account the possibility of tunneling mentioned above. Today, scientists are proposing new models, as silicon-based diodes are used in many experimental works.

Tunnel diodes are widely used in the manufacture of various modern devices, such as nuclear weapons guiding installations, the creation of aerospace equipment, microwave ovens, etc. This indicates that the study of the properties of tunnel diodes and their wide application has great scientific and practical meaning. From the works presented above and from the available literature data, it can be seen that the effect of a magnetic field and an electromagnetic field with an ultrahigh frequency on a tunnel diode has not been studied enough. Based on this, the purpose of this work is to develop a new model for calculating the total current for a tunnel diode, taking into account the impact on the tunnel diode of a magnetic field and a microwave electromagnetic field [12–14].

A NEW MODEL FOR CALCULATING THE TOTAL CURRENT IN A TUNNEL DIODE

According to the Tsu-Esaki theory, the direct current flowing through a tunnel diode is determined by the product of the $N(E_X)$- distribution function and the $T_C(E_X)$- transfer coefficient [10, 15, 16]:

$$I_T = \frac{4\pi m_{ef}q}{\hbar^3} \int_{min}^{max\int} T_C(E_X)N(E_X)dE_X. \tag{1}$$

The values of tunnel currents passing from region p to region n and from region n to region p are determined by the following expressions [15]:

$$I_{p \to n} = A \int_{\varepsilon_n}^{\varepsilon_p} f_p(\varepsilon) \, \rho_p(\varepsilon) P[1 - f_n(\varepsilon)] \rho_n(\varepsilon) d\varepsilon. \tag{2}$$

$$I_{n \to p} = A \int_{\varepsilon_n}^{\varepsilon_p} P \, f_n(\varepsilon) \rho_n(\varepsilon) [1 - f_p(\varepsilon)] \rho_p(\varepsilon) d\varepsilon. \tag{3}$$

The total tunnel current in the p-n junction is equal to the difference between expressions (2) and (3):

$$I = A \int_{\varepsilon_n}^{\varepsilon_p} \rho_p(\varepsilon) \rho_n(\varepsilon) P[f_n(\varepsilon) - f_p(\varepsilon)] d\varepsilon. \tag{4}$$

The $T_C(E_X)$-transfer coefficient and $N(E_X)$-distribution functions can be specified as follows [16]:

$$N(E_X) = \int_0^\infty [f_n(\varepsilon) - f_p(\varepsilon)] \, dE_P, \tag{5}$$

$$T_C(E_X) = \int P \rho_P(\varepsilon) \, \rho_n(\varepsilon) d\varepsilon. \tag{6}$$

where ε_n and ε_p - are the minimum energy that electrons can accept in the conduction band of an n-semiconductor and the maximum energy that electrons can accept in the valence band of a p-semiconductor.

If we take the lower part of the conduction band as the beginning of the energy axis, that is, if we take $\varepsilon_n = 0$ (Fig. 1), and, based on this figure, we have the following expression for the energy (ε_P):

$$\varepsilon_P = qV_K - E_g = \mu_n + \mu_P. \tag{7}$$

where μ_n and μ_P are the chemical potentials (Fermi level) for the regions n and p, respectively.
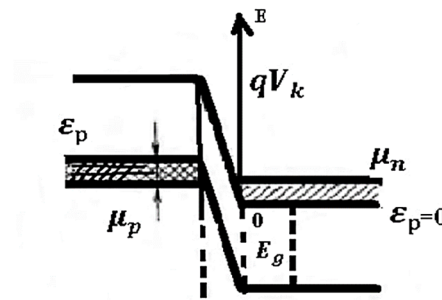
Figure 1. Scheme of forming the current-voltage characteristic of a tunnel diode

Also, when an external voltage is applied, we have:

$$\varepsilon_P = \mu_n + \mu_P - qV. \tag{8}$$

And the distribution function is determined by the expressions:

$$f_n(\varepsilon) = \frac{1}{exp\left(\frac{\varepsilon - \mu_n}{kT}\right) + 1}, \tag{9}$$

$$f_P(\varepsilon) = \frac{1}{exp\left(\frac{\varepsilon + \mu_P - qV_K + E_g + qV}{kT}\right) + 1}. \tag{10}$$

The density of states of electrons and holes is $\rho_n(\varepsilon) = C\sqrt{\varepsilon}$, $\rho_P(\varepsilon) = C'\sqrt{qV_K - E_g - qV - \varepsilon}$, where C and C' - are constant numbers. Taking into account the above, using expression (10), we obtain the following expression for the tunnel current [15]:

$$I_T = PTA \left(\int_0^{qV_K - E_g - qV} \left(\frac{1}{exp\left(\frac{\varepsilon - \mu_n}{kT}\right) + 1} - \frac{1}{exp\left(\frac{\varepsilon + \mu_P - qV_K + E_g + qV}{kT}\right) + 1} \right) \sqrt{\varepsilon(qV_K - E_g - qV - \varepsilon)} \right) d\varepsilon. \tag{11}$$

Using expressions (9) and (10), finding qV_k and substituting expression (11), we obtain the following expression for the tunnel current:

$$I_t = APT \int_0^{\mu_n + \mu_p - qV} \sqrt{\varepsilon(\mu_n + \mu_p - \varepsilon - qV)} \left(\frac{1}{exp\left(\frac{\varepsilon - \mu_n}{kT}\right) + 1} - \frac{1}{exp\left(\frac{\varepsilon - \mu_n + qV}{kT}\right) + 1} \right) d\varepsilon. \tag{12}$$

where: $A = C'C\frac{4\pi m_{eff}q}{\hbar^3}$. For the transparency coefficient, we use the following formula [10, 17]:

$$P = exp\left(-\frac{\alpha E_g^{\frac{3}{2}}}{F}\right). \tag{13}$$

where: E-field strength, $\alpha = \theta\frac{4\sqrt{2m_e}}{3q\hbar}$; $\theta \approx 1$ (θ is a constant parameter of the Chynoweth model). In many models [10, 17, 18], the barrier transparency coefficient was not taken into account, since E=const. Taking the value for the drift velocity of an electron at a p-n junction:

$$\vartheta = \mu E_x. \tag{14}$$

(Where, m_{eff} is the mobility of the electron, E_x is the intensity of the microwave field), the expression of the power generated by the microwave field:

$$F = qE_x. \tag{15}$$

as well as the value for the total power induced by the microwave field:

$$P_1 = F\vartheta. \tag{16}$$

we have the following expression for the power under the action of a microwave field at a p-n tunnel junction:

$$\frac{P_1-P_0}{N} = F\vartheta. \tag{17}$$

where N is the number of electrons, is the difference between the total powers of the microwave field applied to the diode and the sample. If we generalize the above expressions, then the expression for the power spent on an electron under the action of a microwave field in a p-n tunnel junction can be written as follows.

$$\frac{P_1-P_0}{N} = q\mu E_x^2. \tag{18}$$

from this expression we have the following formula for the Ex-strength of the field under action:

$$E_x = \sqrt{\frac{P_1-P_0}{Nq\mu}}. \tag{19}$$

And the expression for the transparency coefficient of the barrier under the action of the microwave field will have the form:

$$P = exp\left(-\frac{\alpha E_g^{\frac{3}{2}}}{E+E_x}\right) = exp\left(-\frac{\alpha E_g^{\frac{3}{2}}}{E+\sqrt{\frac{P_1-P_0}{Nq\mu}}}\right). \tag{20}$$

The expression for the diffusion current for a heated electron is given by the following formula [19, 20]:

$$I_d = \left(I_0 \cdot \left(\frac{T}{T_0}\right)^3\right) \cdot exp\left(\frac{E_g \cdot q}{k \cdot T_0}\left(1-\frac{T_0}{T}\right)\right) \cdot \left(e^{\frac{q\cdot\phi}{k\cdot T}-\frac{q\cdot(\phi-V)}{k\cdot Te}}-1\right). \tag{21}$$

It is known that the total current I generated in a tunnel diode is the sum of the tunnel current, I_{Ch} excess current, and I_d diffusion currents in the tunnel diode [20].

If the excess current in the tunnel diode is affected by the microwave field, then we have the following expression for volt-ampere characteristics:

$$I_{Ch} = DP = \int_{\mu_n+\mu_p}^{0}\left(\sqrt{\varepsilon(\mu_n+\mu_p-\varepsilon-qV)}\left(\frac{1}{exp\left(\frac{\varepsilon-\mu_n}{kT}\right)+1}-\frac{1}{exp\left(\frac{\varepsilon-\mu_n+qV}{kT}\right)+1}\right)\right)d\varepsilon \times exp\left(-\frac{\alpha E_g^{\frac{3}{2}}}{E+E_x}\right) \tag{22}$$

Here we have obtained the electric field strength as $E_X = \frac{V_K-V+V_m}{d}$, V - external voltage, V_k - contact potential difference, d - potential barrier width, V_m- voltage applied by the microwave field). Also, here we assumed that the density of states formed by impurities in the band gap in a p-n tunnel diode is constant. Now, summing all the current expressions, we obtain the following expression for the resulting total current for the tunnel diode:

$$I = TA\,exp\left(-\frac{\alpha E_g^{\frac{3}{2}}}{E+\sqrt{\frac{P_1-P_0}{Nq\mu}}}\right) \times$$

$$\times \int_0^{\mu_n+\mu_p-qV}\left(\sqrt{\varepsilon(\mu_n+\mu_p-\varepsilon-qV)}\left(\frac{1}{exp\left(\frac{\varepsilon-\mu_n}{kT}\right)+1}-\frac{1}{exp\left(\frac{\varepsilon-\mu_n+qV}{kT}\right)+1}\right)\right)d\varepsilon +$$

$$+I_0\left(\frac{T}{T_0}\right)^3 exp\left(\frac{E_g q}{kT_0}\left(1-\frac{T_0}{T}\right)\right)\left(exp\left(\frac{q\phi}{kT}-\frac{q(\phi-V)}{kT_e}\right)-1\right)$$

$$\int_{\mu_n+\mu_p}^{0}\left(\sqrt{\varepsilon(\mu_n+\mu_p-\varepsilon-qV)}\left(\frac{1}{exp\left(\frac{\varepsilon-\mu_n}{kT}\right)+1}-\frac{1}{exp\left(\frac{\varepsilon-\mu_n+qV}{kT}\right)+1}\right)\right)d\varepsilon\; exp\left(-\frac{\alpha E_g^{\frac{3}{2}}}{E+E_x}\right) \quad (23)$$

Let us compare the graph of the dependence of the total current of the tunnel diode on the total power of the acting microwave field, calculated using the above theoretical expression (Fig. 2), with the experimental graph (Fig. 3) shown in [21].
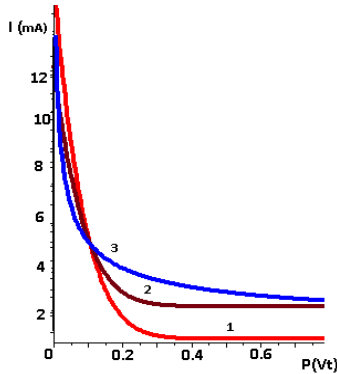

Figure 2. Graph of the dependence of the total current of the tunnel diode on the total power of the microwave field, calculated by expression (23).
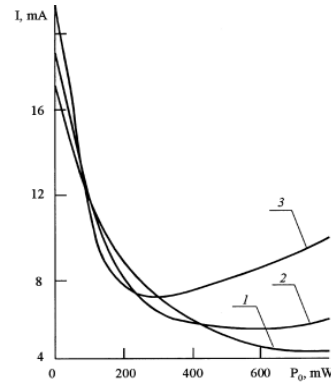

Figure. 3. Graph of the dependence of the total current of the tunnel diode on the total power of the microwave field [21] (experimental result).

It can be seen from these compared graphs that the theoretical and experimental results are qualitatively compatible. If we express the density of states of electrons in the conduction band of the n-region and in the valence band of the p-region given in expression (23) in terms of the Landau levels [22] under the action of a magnetic field, we obtain the following:

$$\rho_C(\varepsilon) = \frac{1}{4\pi^2}\left(\frac{2m}{\hbar^2}\right)^{\frac{3}{2}}\hbar\omega_H^C\sum_0^{N_C}\frac{1}{\sqrt{\varepsilon-\varepsilon_C-\left(n+\frac{1}{2}\right)\hbar\omega_H^{N_C}}}d\varepsilon;$$

$$\rho_V(\varepsilon) = \frac{1}{4\pi^2}\left(\frac{2m}{\hbar^2}\right)^{\frac{3}{2}}\hbar\omega_H^{N_V}\sum_0^{N_V}\frac{1}{\sqrt{\varepsilon-\varepsilon_V-\left(n+\frac{1}{2}\right)\hbar\omega_H^{N_V}}}d\varepsilon. \quad (24)$$

We can get the Hall voltage arising from the action of a magnetic field on the diffusion current in terms of the total current in the tunnel diode by adding it to the field voltage U_{xx}-microwave field. The Hall voltage is defined as [23]:

$$U_{XX} = \frac{IdB}{qn}. \quad (25)$$

Let us use the expression for the dependence of the Hall coefficient on the mobility of electrons and holes $R_{XX} = \frac{-A(nu_n^2-pu_P^2)}{q(nu_n+pu_P)^2}$. If we take the concentrations of electrons and holes equal, then for the Hall coefficient we get the following:

$$R_{XX} = \frac{-A(u_n-u_P)}{qn(u_n+u_P)}. \quad (26)$$

where, we use the expression $n = \int_0^\infty \rho(\varepsilon)f(\varepsilon)d\varepsilon$ for the electron concentration, for $\rho(\varepsilon)=\rho_c(\varepsilon)\rho_V(\varepsilon)$ equals and $f(\varepsilon)$ we give the following:

$$\rho(\varepsilon) = \rho_C(\varepsilon) = \frac{1}{4\pi^2}\left(\frac{2m}{\hbar^2}\right)^{\frac{3}{2}} \hbar\omega_H^C \sum_0^{N_C} \frac{1}{\sqrt{\varepsilon - \varepsilon_C - \left(n+\frac{1}{2}\right)\hbar\omega_H^{N_C}}} d\varepsilon \times$$

$$\times \frac{1}{4\pi^2}\left(\frac{2m}{\hbar^2}\right)^{\frac{3}{2}} \hbar\omega_H^{N_V} \sum_0^{N_V} \frac{1}{\sqrt{\varepsilon - \varepsilon_V - \left(n+\frac{1}{2}\right)\hbar\omega_H^{N_V}}} d\varepsilon$$

$$f(\varepsilon)d\varepsilon = \left(\frac{1}{exp\left(\frac{\varepsilon-\mu_n}{kT}\right)+1} - \frac{1}{exp\left(\frac{\varepsilon-\mu_n+qV}{kT}\right)+1}\right)d\varepsilon \tag{27}$$

In this case, expression (23) for the tunneling current under the action of a microwave field and a magnetic field will have the following form:

$$I = I_t(E_X, B) + I_{Ch}(E_X, B) + I_d(E_X, B), \tag{28}$$

$$I_T(E_X,B) = AT \, exp\left(-\frac{\alpha E_g^{\frac{3}{2}}}{E + \sqrt{\frac{P_1 - P_0}{Nq\mu}}}\right) \int_0^{\mu_n+\mu_p-qV} \frac{1}{4\pi^2}\left(\frac{2m}{\hbar^2}\right)^{\frac{3}{2}} \hbar\omega_H^{N_V} \sum_0^{N_C} \frac{1}{\sqrt{\varepsilon - \varepsilon_C - \left(n+\frac{1}{2}\right)\hbar\omega_H^{N_C}}} d\varepsilon \times$$

$$\times \frac{1}{4\pi^2}\left(\frac{2m}{\hbar^2}\right)^{\frac{3}{2}} \hbar\omega_H^{N_V} \sum_0^{N_V} \frac{1}{\sqrt{\varepsilon - \varepsilon_V - \left(n+\frac{1}{2}\right)\hbar\omega_H^{N_V}}} d\varepsilon \left(\frac{1}{exp\left(\frac{\varepsilon-\mu_n}{kT}\right)+1} - \frac{1}{exp\left(\frac{\varepsilon-\mu_n+qV}{kT}\right)+1}\right) d\varepsilon$$

$$I_X(E_X,B) = exp\left(-\frac{\alpha E_g^{\frac{3}{2}}}{E + \sqrt{\frac{P_1 - P_0}{Nq\mu}}}\right) \int_0^{\mu_n+\mu_p} \left(\begin{array}{l} \frac{1}{4\pi^2}\left(\frac{2m}{\hbar^2}\right)^{\frac{3}{2}} \hbar\omega_H^{N_V} \sum_0^{N_C} \frac{1}{\sqrt{\varepsilon - \varepsilon_C - \left(n+\frac{1}{2}\right)\hbar\omega_H^{N_C}}} d\varepsilon \times \\ \times \frac{1}{4\pi^2}\left(\frac{2m}{\hbar^2}\right)^{\frac{3}{2}} \hbar\omega_H^{N_V} \sum_0^{N_V} \frac{1}{\sqrt{\varepsilon - \varepsilon_V - \left(n+\frac{1}{2}\right)\hbar\omega_H^{N_V}}} d\varepsilon \times \\ \times \left(\frac{1}{exp\left(\frac{\varepsilon-\mu_n}{kT}\right)+1} - \frac{1}{exp\left(\frac{\varepsilon-\mu_n+qV}{kT}\right)+1}\right) \end{array} \right) d\varepsilon$$

$$I_d(E_X,B) = I_0 \left(\frac{T}{T_0}\right)^3 exp\left(\frac{E_g q}{kT_0}\left(1 - \frac{T_0}{T}\right)\right)\left(exp\left(\frac{q\phi}{kT} - \frac{q(\phi - V + U_{XX})}{kT_e}\right) - 1\right)$$

In a tunnel diode, the total current consists of the tunnel current according to the Tsu-Esaki model, as well as diffusion and excess currents. If we do not take into account the excess current here, then the total current consists of tunneling and diffusion currents. For this case, the volt-ampere characteristics graph was shown with and without the influence of the magnetic field and without the influence of the tunnel diode (Fig. 4 and 5).
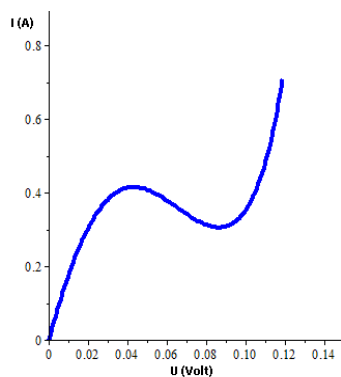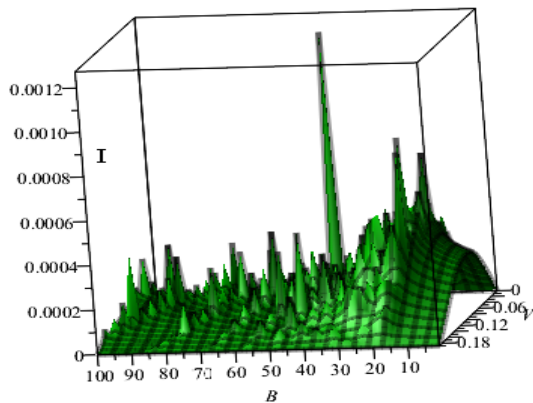

Figure 4. Volt-Ampere characteristics of total current without the influence of the microwave field and magnetic field and without taking into account excess current
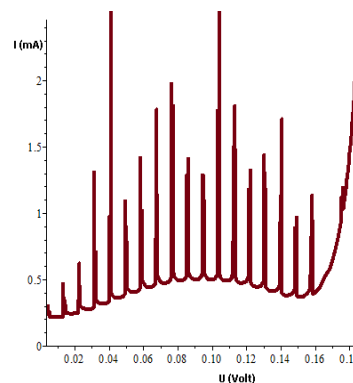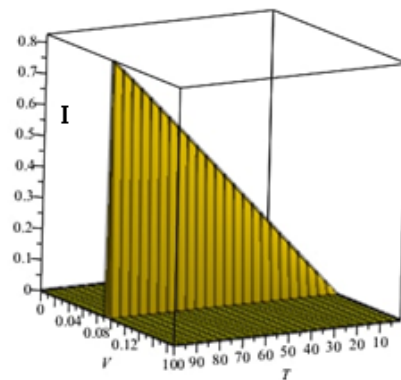
Figure. 5. Volt-Ampere characteristics of the total current taking into account the microwave field and magnetic field and without taking into account the excess current

A three-dimensional spatial view of the CVC of the above tunnel diode under the action of a magnetic field is presented in two forms - in fig. 6 on the change in the magnetic field induction, in fig. 7 - by temperature change.

Figure 6. Three-dimensional view of the volt-ampere characteristics of a tunnel diode under the influence of various magnetic fields

Figure 7. Three-dimensional spatial representation of the change in the volt-ampere characteristics at different temperatures for a tunnel diode under the influence of a magnetic field.

CONCLUSION

An expression volt-ampere characteristics for the excess current of a tunnel diode under the action of a microwave field is obtained, as well as a formula for calculating the total current generated in a tunnel diode under the action of a microwave field and a magnetic field. In addition, the dependence of the total current of the tunnel diode on the total power induced by the microwave field is theoretically presented and compared with experiments in the available literature. For the total current in the tunnel diode, without taking into account the excess current, the volt-ampere characteristics were obtained for the affected and unaffected states, respectively.

ORCID IDs
Gafur Gulyamov, https://orcid.org/0000-0001-9879-3165
Sharifa B. Utamuradova, https://orcid.org/0000-0002-1718-1122
Mukhamadjon G. Dadamirzaev, https://orcid.org/0000-0001-8258-4617
Nozimjon A. Turgunov, https://orcid.org/0000-0003-3481-5622
Kakhramon M. Fayzullaev, https://orcid.org/0000-0001-7362-1439

REFERENCES

[1] K.P. Abdurakhmanov, Sh.B. Utamuradova, Kh.S. Daliev, S.G. Tadjy-Aglaeva, and R.M. Ergashev, Semiconductors, **32**(6), 606 (1998). https://doi.org/10.1134/1.1187448

[2] Sh.B. Utamuradova, A.V. Stanchik, D.A. Rakhmanov, A.S.Doroshkevich, and K.M.Fayzullaev, New Materials, Compounds and Applications, **6**(3), 214 (2022). http://jomardpublishing.com/UploadFiles/Files/journals/NMCA/V6N3/Utamuradova_et_al.pdf

[3] Sh.B. Utamuradova, Kh.S. Daliev, Sh.Kh. Daliev, and K.M. Fayzullaev, Applied Physics, **6**, 90 (2019). https://applphys.orion-ir.ru/appl-19/19-6/PF-19-6-90.pdf

[4] S.A.Muzafarova, Sh.B.Utamuradova, A.M.Abdugafurov, K.M.Fayzullaev, E.M.Naurzalieva and D.A. Rakhmanov, Applied Physics, **4,** 81 (2021). https://applphys.orion-ir.ru/appl-21/21-4/PF-21-4-81.pdf

[5] Sh.B.Utamuradova, A.V.Stanchik, K.M.Fayzullaev, B.A.Bakirov, Applied Physics, **2**, 33 (2022). https://applphys.orion-ir.ru/appl-22/22-2/PF-22-2-33_EN.pdf

[6] P.R. Berger, Comprehensive Semiconductor Science and Technology, 176 (2011). https://doi.org/10.1016/B978-0-44-453153-7.00013-4

[7] E.O. Kane, Journal of Applied Physics, **32,** 83 (1961). https://doi.org/10.1063/1.1735965

[8] J.S. Karlovsky, Phys. Rev. **127,** 419 (1962). https://doi.org/10.1103/PhysRev.127.419

[9] I. Shalish, Journal of applied physics, **124,** 075102 (2018). https://aip.scitation.org/doi/10.1063/1.5038800

[10] N. Moulin, A. Mohamed, F. Mandorlo, and M. Lemiti, Journal of Applied Physics, American Institute of Physics, **126(3),** 033105 (2019). http://dx.doi.org/10.1063/1.5104314

[11] N.A. Turgunov, E.H. Berkinov, and D.X. Mamazhonova, Applied Physics, **3,** 40 (2020). https://applphys.orion-ir.ru/appl-20/20-3/PF-20-3-40.pdf

[12] N.A. Turgunov, Inorganic Materials, **12**(54), 1183 (2018). https://link.springer.com/article/10.1134/S0020168518120178

[13] N.A. Turgunov, D.Kh. Mamajonova, and E.Kh. Berkinov, Journal of nano- and electronic physics. **5(13),** 05006 (2021). https://jnep.sumdu.edu.ua/download/numbers/2021/5/articles/jnep_13_5_05006.pdf

[14] S.V. Syrotyuk, East. Eur. J. Phys. **4**, 31 (2021), https://doi.org/10.26565/2312-4334-2021-4-03

[15] S.M. Sze, and K.K. Ng, *Physics of Semiconductor Devices*, (John Wiley & Sons, Inc., Hoboken, New Jersey, (2007). **3,** 418 https://onlinelibrary.wiley.com/doi/pdf/10.1002/9780470068328.fmatter

[16] T.A. Growden, Zh. Weidong, E.R. Brown, D.F. Storm, K. Hansen, P. Fakhimi, D.J. Meyer, and P.R. Berger, Applied physics letters, **112**, 033508 (2018). https://doi.org/10.1063/1.5010794

[17] G. Gulyamov, M.G. Dadamirzaev, and M.K. Uktamova, Guangdianzi Jiguang/Journal of Optoelectronics Laser. **9**(41), 419 (2022). http://gdzjg.org/index.php/JOL/article/view/1144

[18] A.G. Chynoweth, W.L. Feldman, and R.A. Logan, Phys. Rev. **121,** 684 (1961). https://doi.org/10.1103/PhysRev.121.684

[19] M.K. Uktamova, and Sh. Nazarov, Web of scientist: International scientific research journal, **10**(3), 800 (2022). https://wos.academiascience.org/index.php/wos/article/view/2601/2475

[20] G. Gulyamov, M.G. Dadamirzaev, M.K. Uktamova, and B.Z. Mislidinov, AIP Conference Proceedings, **2700,** 050007(2023). https://aip.scitation.org/doi/abs/10.1063/5.0126516

[21] I.K. Kamilov, K.M. Aliev, Kh.O. Ibragimov, and N.S. Abakarova, J. Phys. Condens. Matter. **148,** 171 (2008). https://doi.org/10.1016/j.ssc.2008.06.017

[22] G. Gulyamov, U.I. Erkaboev, and N.Yu. Sharibaev, Semiconductors, **48,** 1287 (2014). http://dx.doi.org/10.4236/ojapps.2015.512073

[23] G. Gulyamov, G. Majidova, and F. Muxitdinova, AIP Conference Proceedings. **2700,** 050008 (2023). https://doi.org/10.1063/5.0126385

[24] G. Gulyamov, M.G. Dadamirzayev and M.O. Qosimova, AIP Conference Proceedings, **2700,** 050013 (2023). https://doi.org/10.1063/5.0124926

РОЗРАХУНОК ПОВНОГО СТРУМУ, ЩО ГЕНЕРУЄТЬСЯ В ТУНЕЛЬНОМУ ДІОДІ ПІД ДІЄЮ МІКРОХВИЛЬОВОГО ТА МАГНІТНОГО ПОЛІВ

Гафур Гулямов[a], Шаріфа Б. Утамурадова[b], Мухамаджон Г. Дадамірзаев[a], Нозімджон А. Тургунов[b],
Муніра К. Уктамова[b], Кахрамон М. Файзуллаев[b], Арофат І. Худайбердієва, Алішер І. Турсунов
[a]Наманганський інженерно-будівельний інститут, Наманган, Узбекистан
[b]Інститут фізики напівпровідників та мікроелектроніки Національного університету Узбекистану, Ташкент, Узбекистан,
[c]Ташкентський хіміко-технологічний інститут, [d]Термізький державний університетт, Терміз, Узбекистан

У цій роботі була виведена формула для розрахунку повного струму, який утворюється в тунельному діоді під дією мікрохвильового та магнітного полів. Крім того, теоретично подано та порівняно з експериментальними даними залежність повного струму тунельного діода від повної потужності, індукованої НВЧ полем. Для повного струму в тунельному діоді без урахування надлишкового струму отримано вольт-амперну характеристику для випадків з і без впливу НВЧ поля.

Ключові слова: *модель Чиновета; модель Цу-Есакі; мікрохвильове поле; магнітне поле; бар'єрний коефіцієнт прозорості; надлишковий струм*

SYNTHESIS AND CHARACTERIZATION OF (PVA-CoO-ZrO2) NANOSTRUCTURES FOR NANOOPTOELECTRONIC FIELDS[†]

Zainab Sabry Jaber[a,§], Majeed Ali Habeeb[b,*], Waleed Hadi Radi[a]

[a]Directorate of Education Babylon, Ministry of Education, Iraq
[b]University of Babylon, College of Education for Pure Sciences, Department of Physics, Iraq
[*]Corresponding Author e-mail: pure.majeed.ali@uobabylon.edu.iq, [§]E-mail: zainab.sabri.jaber@babylon.moedu.iq

Nanocomposites have a wide range of applications, including optical integrated circuits, sensors, coatings, and medical devices. As a result, the purpose of this paper is to prepare a new type of nanocomposites made of polyvinyl alcohol (PVA) with different concentrations (0, 1, 2 and 3) wt% of cobalt oxide and zirconium dioxide (CoO-ZrO2) nanoparticles by using casting method. Microscopic photographs demonstrate the fact that the additive distribution amount of NPs in the polymer was uniform, and (CoO-ZrO2) NPs formed a continuous network within the polymer when the concentration reached 3wt.%. The outcomes of optical properties indicate that the absorbance of nanocomposites improves as the concentrations of cobalt oxide and zirconium dioxide nanoparticles increase while transmittance and the optical energy gap decrease. On the other hand, optical constants of nanocomposites (refractive index, absorption coefficient, extinction coefficient, real and imaginary the dielectric constants) and optical conductivity are increase with increases in the weight percentages of (CoO-ZrO2) nanoparticles. These outcomes demonstrate the (PVA-CoO -ZrO2) NCs use for various optical devices.
Keywords: *Nanocomposites; Optical properties; Cobalt oxide; Zirconium dioxide*
PACS: 77.84.Jd, 78.20.-e, 78.40.Me

INTRODUCTION

Metallic nanoparticles differ from bulk metals in their physical and chemical properties (lower melting points, higher specific surface area, specific optical properties, mechanical strength, and specific magnetization). These properties are appealing in a variety of industrial applications thus, nanoparticles are the most fundamental component in nanostructure fabrication. Nanoparticles are intriguing and unique because of their optical properties [1,2]. Nanocomposites have shown great promise in many industries, including microelectronics, Automobiles, drug delivery, sensors, injection moulded products, membranes, packaging materials, aerospace, coatings, adhesives, fire retardants, medical devices, consumer goods and many more [3,4]. Polymer matrices can be tailored to meet not only specific technological requirements, but also size and shape nanostructures dependant features that can be exploited, opening up exciting prospects for the creation of polymer-based nanocomposites with antimicrobial activity. The physical properties of polymer nanocomposites, which are polymer matrices doped with nanosized phases such as nanoparticles, nanofibers, nanosheets, and nanotubes, etc., depend largely on the interaction between polymer molecules and nanofillers [5,6]. Polyvinyl alcohol (PVA) is a type of polymer that has excellent Optical, mechanical, physical, and electrical characteristics are examples of properties. The best way to incorporate metal oxides is as Al_2O_3, CoO, TiO_2, ZnO, and ZrO_2 greatly improves its characteristics. In particular, ZrO_2 possesses excellent wear and chemical resistance, exceptional mechanical strength, fracture toughness, and hardness, as well as decent ionic characteristics [7,8]. Cobalt nanoparticle powders (CoO) have been discussed of intensive studies and development recently because of their promising applications in fields as diverse as rechargeable batteries, ceramic pigments, catalysts, magnetic materials, gas sensors, and solar energy absorbers [9,10] . Nanocomposites are an emerging class of materials that incorporate nanoscale fillers. The term "organic/inorganic hybrid" refers to the combination of inorganic nanoparticles with organic (polymer) materials, because of the strong interfacial connection between organic and inorganic materials that occurs when CoO is incorporated into a polymer, the latter takes on improved optical and mechanical properties. Polyvinyl alcohol (PVA) occurs naturally as a biodegradable and water-soluble substance, making it a model example of a green material. It is possible that oxide can be used to make thin films with a useful natural functionality [11].

EXPERIMENTAL PART

In this analysis, samples create from polyvinyl alcohol and (cobalt oxide- zirconium oxide) NPs with different concentrations (0, 1, 2 and 3) wt% using the casting technique, which involved dissolving polyvinyl alcohol in (40 ml) of distilled water for 45 minutes while stirring with a magnetic stirrer at temperature 70 ^{0}C to achieve a more homogeneous solution. In a petri dish, the solution was kept. After three days of progressive drying at room temperature, polymer mix nanocomposites were formed. The NCs from the petri dish (PVA-CoO-ZrO2) were cut out and measured. Nanocomposites were tested in various concentrations utilizing a light microscopy of the kind Nikon-73346 made by Olympus a magnification of (10×) and a microscopic photography camera. The UV-1800 from Shimadzu was used to assess the optical properties of (PVA-CoO-ZrO2) NCs in the range 220 to 1100 nm. The formula below is used to calculate absorbance [12]

$$A = \frac{I_A}{I_O} \tag{1}$$

(I_A) is the amount of the substance's absorption of light, and (I_O) is the magnitude of the incident light.
The formula is utilized transmittance [13]

$$T = I_T/I_O \tag{2}$$

(I_T) the amount of beam transmitted through a substance, and(I_O) the brightness of the light that is incident
We can measure the absorption coefficient (α) from these equation [14]

$$\alpha = 2.303 \, A/d \tag{3}$$

Absorbance is represented by (A), and film thickness is represented by d
The energy gap was formed by applying the connection [15]

$$\alpha \, h\upsilon = B \, (h\upsilon - E_g)r \tag{4}$$

(r = 2) for allowed indirect transitions and (r = 3) for forbidden indirect transitions. ($h\upsilon$) incidental photon energy,
(B) constant, and optical energy band gap (E_g)
Relation can be used to determine the refractive index (n) [16]

$$n = (1+R^{1/2})/ (1-R^{1/2}) \tag{5}$$

R is reflectance. Equation below can be used to determine the extinction coefficient (k) [17]

$$k = \alpha \, \lambda/4\pi \tag{6}$$

The incident light's wavelength is (λ).
The real (ε_1) and the imaginary (ε_2) components of the dielectric constant are determined by the subsequent mathematical calculations [18]

$$\varepsilon_1 = n^2 - k^2 \tag{7}$$
$$\varepsilon_2 = 2nk \tag{8}$$

The following equation is used to determine the optical conductivity (σ) [19]

$$\sigma = \alpha \, n \, C \, /4\pi \tag{9}$$

Light velocity is denoted by (C)

RESULTS AND DISCUSSION

Figure (1) shows optical microscope images of (PVA-CoO- ZrO$_2$) nanocomposites taken at a magnification power of 10× at various concentrations of nanoparticles. From this figure we can see that the images (A, B, C, D) when the combination of (CoO-ZrO$_2$) When nanostructures reach 3 wt.%, Inside the polymer, they form a unified network. the nanoparticles are linked in this network includes routes for charge carriers to travel through, causing a shift in the material properties [20,21].
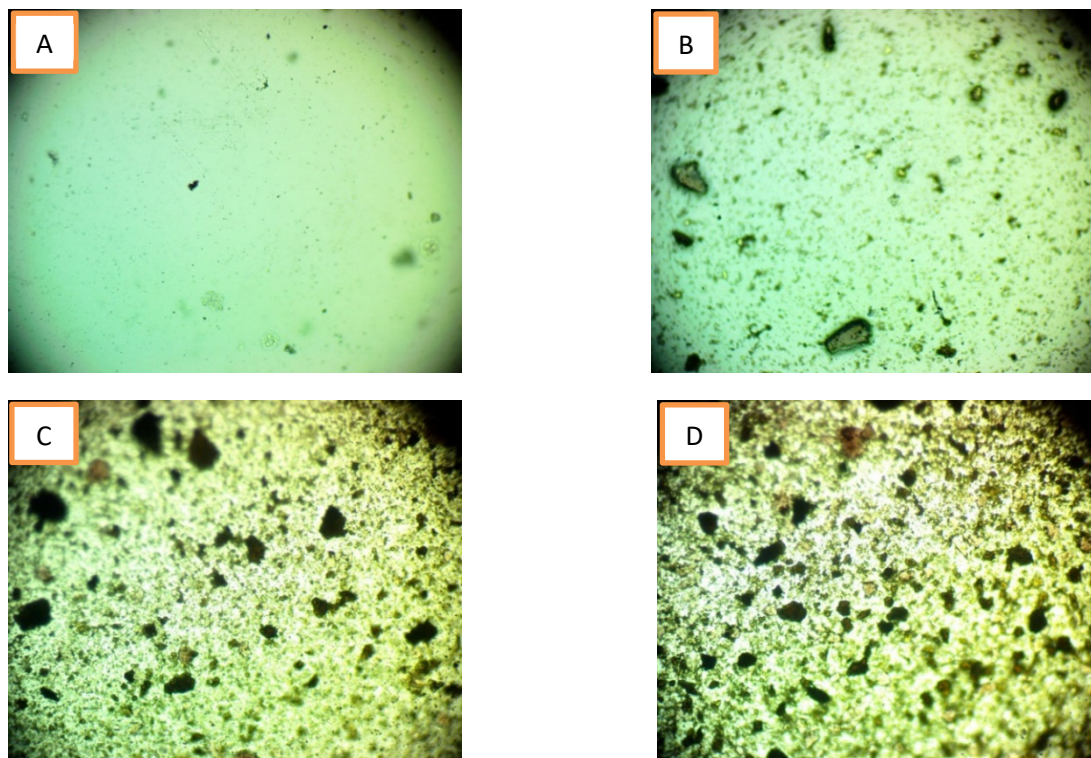
Figure 1. Photomicrographs (×10) for (PVA-CoO-ZrO$_2$) nanocomposites
(A) PVA, (B) 1wt.% CoO-ZrO$_2$ nanoparticles, (C) 2 wt.% CoO-ZrO$_2$ nanoparticles, (D) 3 wt.% CoO-ZrO$_2$ nanoparticles

Figure (2) shows the optical absorbance of (PVA-CoO-ZrO₂) nanocomposites varies with wavelength. from this figure, absorption has increased in the ultraviolet region while decreasing in the visible and infrared regions. the incident photon has a high wavelength and the photon is not transmitted because there is not enough energy to communicate with atoms. The photon-material interaction occurs and the photon absorbs as the wavelength decreases. The absorbance increases as the concentration of CoO-ZrO₂ NPs increases. This is due to free electrons absorbing incident light [22,23].

The relationship between transmittance and wavelength for (PVA-CoO-ZrO₂) nanocomposites is shown in Fig. 3. The transmittance decrease with increase of added concentration of (CoO-ZrO₂) nanoparticles. The method is not followed by emission from the radiation because the transferred electrons in its outer orbits have occupied vacancy positions of the energy bands, absorb part of the light incident that does not exceed a material dosage which is induced by (CoO-ZrO₂) electrons on their outer orbs and transmits them to higher energy levels [24,25].
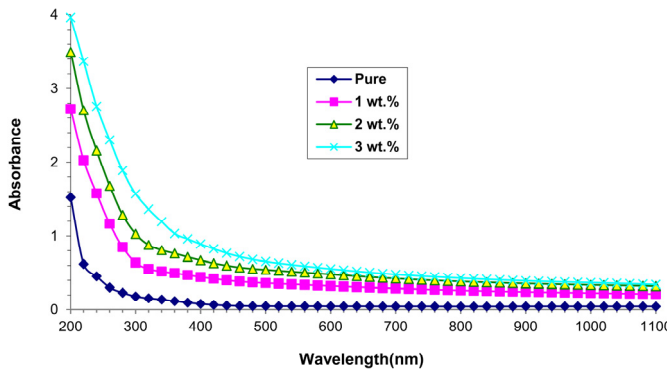

Figure 2. Absorbance spectra with photon wavelength of (PVA-CoO-ZrO₂) nanocomposites
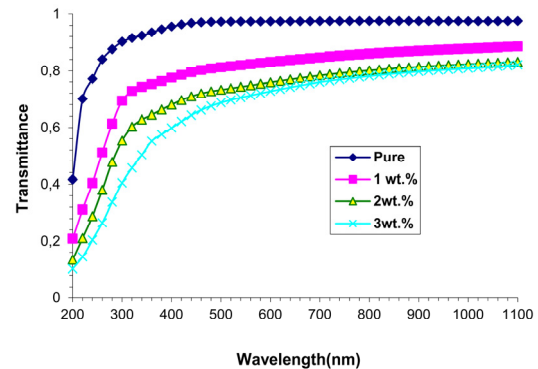

Figure 3. Transmittance spectra of (PVA-CoO-ZrO₂) NCs as a function of wavelength

Fig. 4 shows the connection between incident radiation and absorption coefficients for (PVA-CoO-ZrO2) nanostructures. As in our view, this absorption coefficient is lowest at wavelength with energy high, indicating there being isn't much possible electron transition because the force of the input photon is insufficient for the electron to be able to move from the V.B. to the C.B. ($hv > Eg$). This shows how the absorption coefficient influences the type of electron transfer that takes place. When the absorption coefficient is extremely high ($>10^4$ cm^{-1} at high speeds), an electron is expected to undergo a direct transition, and the electrons and photons retain this same energy and moment. However, because absorption coefficients at low energies are small, (10^4cm^{-1}) This is anticipated in which an electron will undergo a deceptive transition, so that its electronic traction shall be preserved through to the adsorption process. The coefficient of absorption intensity of PVA-CoO-ZrO₂ nanocomposites is less than ($>10^4$ cm^{-1}), indicating that the transition of the electron in these nanocomposites is indirect [26,27].
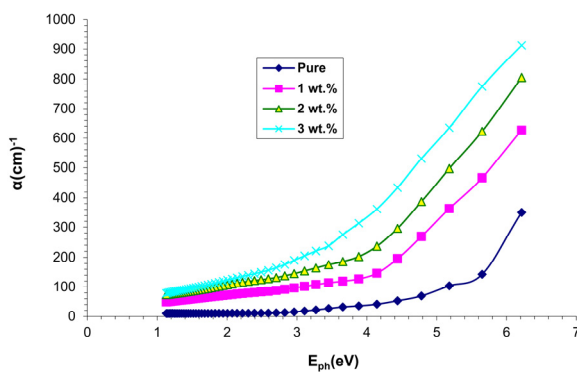

Figure 4. Variation of absorption coefficient with photon energy for (PVA-CoO-ZrO₂) nanocomposites
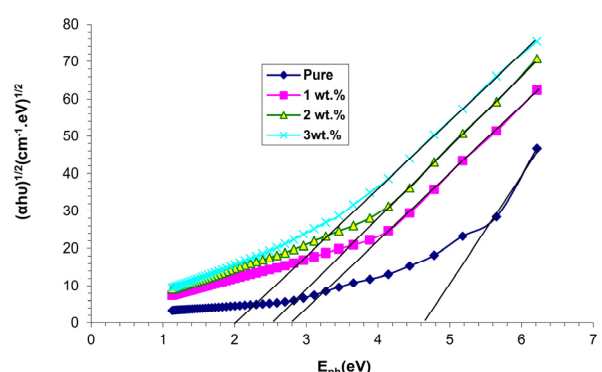

Figure 5. The connection between $(\alpha hv)^{1/2}$ (cm^{-1}·eV)$^{1/2}$ and photon energy of (PVA-CoO-ZrO₂) NCs

Figure (5) demonstrates the relationship between $(\alpha hv)^{1/2}$ and photon energy. This figure indicates energy gap decreased by an increase in (CoO-ZrO₂) concentration for (PVA-CoO-ZrO₂) nanocomposites, this is because the material has risen in disruption, which means that the secondary excitation within the band can be made possible and the width of these levels increases with increasing concentrations of CoO-ZrO₂) NPs, that minimize the energy gap [28,29]. Figure 6 illustrates the relationship between $(\alpha hv)^{1/3}$(cm^{-1}·eV)$^{1/3}$ and photon energy of (PVA-CoO-ZrO₂) nanocomposite. This graph clearly shows the energy gap values for forbidden transition.

The change in the coefficient of attenuation is shown in Figure (7) as a function of wavelength. With an increase in (CoO-ZrO₂) nanoparticles we have noticed that the coefficient of attenuation increases. This is because the absorption value is enhanced and the (CoO-ZrO₂) nanoparticles weight percentage is increased[30,31]. The extinction coefficient varies with wavelength (PVA-CoO-ZrO₂) nanocomposites there is an effect of the geometric structure of the material on the tops extinction coefficient, when the percentage of nanomaterial increases, the proportion of geometric deformation increases in the crystal lattice [32,33].
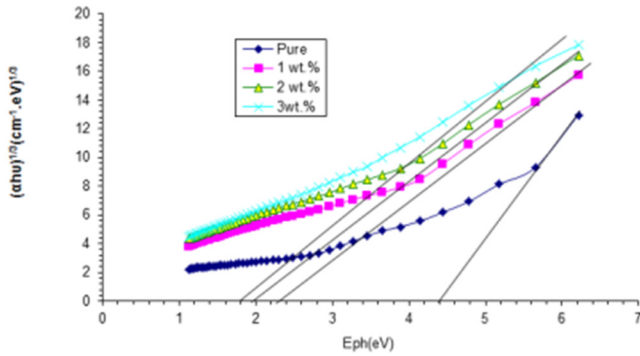

Figure 6. The relationship between $(\alpha h\nu)^{1/3}(cm^{-1} \cdot eV)^{1/3}$ and photon energy of (PVA-CoO-ZrO₂) nanocomposites
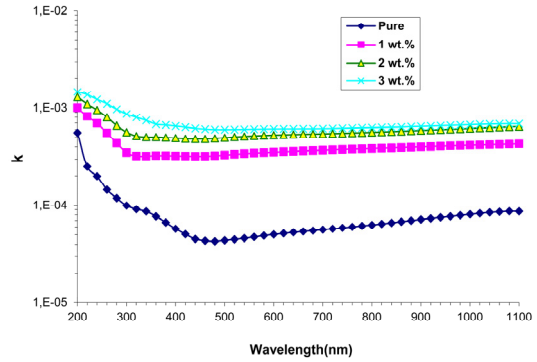

Figure 7. Deference of extinction coefficient of (PVA-CoO-ZrO₂) nanocomposites with wavelength

Figure (8) demonstrates the relationship between refractive index and wavelength for (PVA-CoO-ZrO₂) nanocomposites. The graph demonstrates that as density increases, (CoO-ZrO₂) nanoparticle concentration to (PVA) nanocomposites' refractive index increases. Due to its low transmittance, the UV region has high refractive index values, while the visible range has little values because of its high transmittance [34,35].
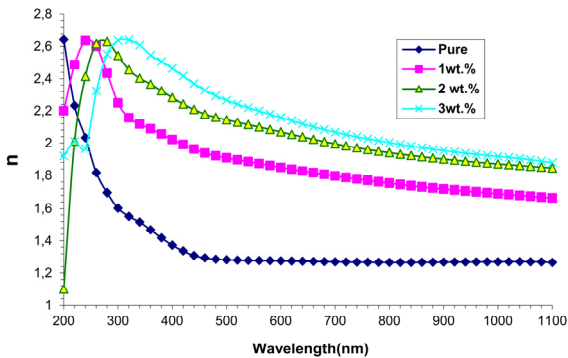
Figure 8. Refractive index (n) for (PVA-CoO-ZrO₂) nanocomposites as a function of wavelength
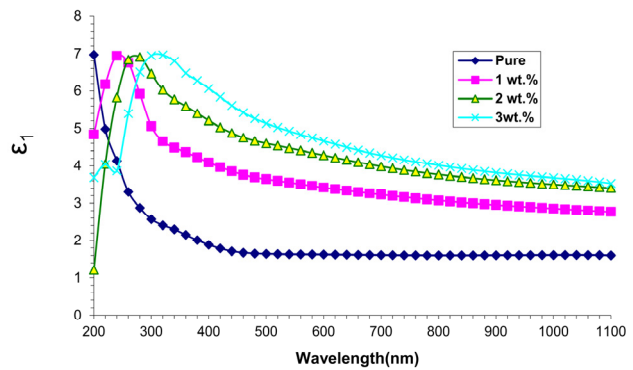
Figure 9. Actual dielectric constant (ε_1) as a function of incident wavelength for (PVA-CoO-ZrO₂) nanocomposites

Figure (9) the difference between ε_1 and wavelength. It is concluded that there is a variation of ε_1 is primarily, depends on the n^2 because of little k^2 values. The relationship amid the imaginary part of the dielectric constant and wavelength of PVA-CoO-ZrO₂ nanocomposites as shown in fig. (10). We can see the (ε_2) values that vary due to the absorption coefficient are dependent on (k) because of their relationship between (ε_2) with (k) [36,37,38]
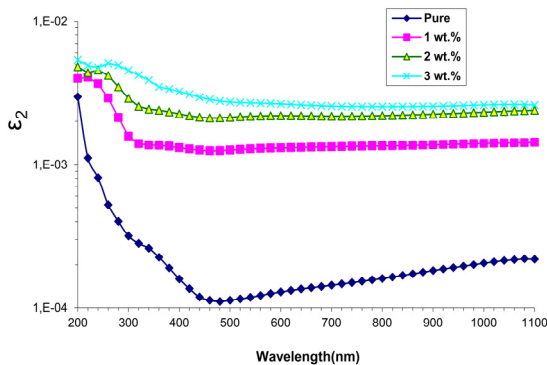
Figure 10. Imaginary dielectric constant (ε_2) as a function of wavelength of (PVA-CoO-ZrO₂) nanocomposites
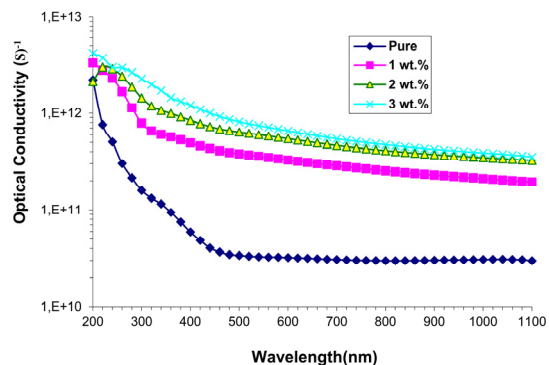
Figure 11. Optical conductivity of (PVA-CoO-ZrO2) nanocomposites as a function of wavelength

Difference of optical conductivity with wavelength for (PVA-CoO-ZrO$_2$) nanocomposites is shown in fig. (11). As the proportion of CoO-ZrO$_2$ NPs reached to the (3wt%), the optical conductivity of (PVA) rises. Because of the new levels in this band gap, electrons can move more easily the V.B., followed by the municipal and state levels, and then the C.B. The band gap closes as a consequence, and conductivity rises [39,40,41].

CONCLUSION

1- Optical microscope images show that the additive distribution of nanoparticles in the polymer was homogeneous and (CoO-ZrO$_2$) nanoparticles form a continuous network inside the polymer

2- The absorbance of (PVA-CoO-ZrO$_2$) nanocomposites increases with increasing CoO-ZrO$_2$ nanoparticle concentrations, whereas the transmittance and energy gap of (PVA-CoO-ZrO$_2$) nanocomposites decreases with increasing CoO-ZrO$_2$ nanoparticle concentrations.

3- With increasing (CoO-ZrO$_2$) weight percentage, the absorption coefficient, extinction coefficient, refractive index, real and imaginary parts of dielectric constant, and optical conductivity increase.

ORCID IDs

Majeed Ali Habeeb, https://orcid.org/0000-0001-5064-2835

REFERENCES

[1] M. Khairy, and M.E. Gouda, "Electrical and optical properties of nickel ferrite/polyaniline nanocomposite," J. Adv. Res. **6**(4), 555-562 (2015). https://doi.org/10.1016/j.jare.2014.01.009

[2] A.H. Hadi, and M.A. Habeeb, "The dielectric properties of (PVA-PVP-CdS) nanocomposites for gamma shielding applications," Journal of Physics: Conference Series, **1973**(1), 012063 (2021). https://doi.org/10.1088/1742-6596/1973/1/012063

[3] S.K. Sharma, J. Prakash, K. Sudarshan, D. Sen, S. Mazumder, and P. K. Pujari, "Structure at interphase of poly (vinyl alcohol)– SiC nanofiber composite and its impact on mechanical properties: positron annihilation and small-angle X-ray scattering studies," Macromolecules, **48** (16), 5706–5713 (2015). https://doi.org/10.1021/acs.macromol.5b01095

[4] S.M. Mahdi , and M.A. Habeeb, "Fabrication and Tailored Structural and Dielectric characteristics of (SrTiO$_3$/NiO) Nanostructure Doped (PEO/PVA) polymeric Blend for Electronics Fields," Physics and Chemistry of Solid State, 23 (4), 785-792 (2022) . https://doi.org/10.15330/pcss.23.4.785-792

[5] H.J. Zhou, M.Z. Rong, M.Q. Zhang, and K. Friedrich, "Effects of reactive compatibilization on the performance of nano-silica filled polypropylene composites," J. Mater. Sci. **41**(17), 5767–5770 (2006). https://doi.org/10.1007/s10853-006-0112-x

[6] S.M. Mahdi, and M.A. Habeeb, "Low-cost piezoelectric sensors and gamma ray attenuation fabricated from novel polymeric nanocomposites," AIMS Materials Science, **10**(2), 288–300 (2023). https://doi.org/10.3934/matersci.2023015

[7] W.J. Qi, R. Nieh, B.H. Lee, L. Kang, Y. Jeon, and J.C. Lee, "Electrical and reliability characteristics of ZrO 2 deposited directly on Si for gate dielectric application," Appl. Phys. Lett. **77**(20), 3269–3271 (2000). https://doi.org/10.1063/1.1326482

[8] S.M. Mahdi, and M.A. Habeeb, "Evaluation of the influence of SrTiO3 and CoO nanofillers on the structural and electrical polymer blend characteristics for electronic devices," Digest Journal of Nanomaterials and Biostructures, **17**(3), 941-948 (2022). https://doi.org/10.15251/DJNB.2022.173.941

[9] J.C. Toniolo, A.S. Takimi, and C.P. Bergmann, "Nanostructured cobalt oxides (Co3O4 and CoO) and metallic Co powders synthesized by the solution combustion method," Mater. Res. Bull. **45**(6), 672–676 (2010). https://doi.org/10.1016/j.materresbull.2010.03.001

[10] M.A. Habeeb, "Effect of rate of deposition on the optical parameters of GaAs films," European Journal of Scientific Research, **57**(3), 478-484 (2011).

[11] J. Hoffmann, I. Řezníčková, J. Kozáková, J. Růžička, P. Alexy, D. Bakoš, and L. Precnerová, "Assessing biodegradability of plastics based on poly (vinyl alcohol) and protein wastes," Polym. Degrad. Stab. **79**(3), 511–519 (2003). https://doi.org/10.1016/S0141-3910(02)00367-1

[12] N. Hayder, M.A. Habeeb, and A. Hashim, "Structural, optical and dielectric properties of (PS-In$_2$O$_3$/ZnCoFe$_2$O$_4$) nanocomposites," Egyptian Journal of Chemistry, **63**, 577-592 (2020). https://dx.doi.org/10.21608/ejchem.2019.14646.1887

[13] Q.M. Jebur, A. Hashim, and M.A. Habeeb, "Structural, A.C electrical and optical properties of (polyvinyl alcohol-polyethylene oxide-aluminum oxide) nanocomposites for piezoelectric devices," Egyptian Journal of Chemistry, **63**, 719-734 (2020). https://dx.doi.org/10.21608/ejchem.2019.14847.1900

[14] J. Lee, D. Bhattacharyya, A.J. Easteal, and J.B. Metson, "Properties of nano-ZnO/poly (vinyl alcohol)/poly (ethylene oxide) composite thin films," Curr. Appl. Phys., **8**(1), 42–47 (2008).

[15] M.A. Habeeb, A. Hashim, and N. Hayder, "Fabrication of (PS-Cr$_2$O$_3$/ZnCoFe$_2$O$_4$) nanocomposites and studying their dielectric and fluorescence properties for IR sensors," Egyptian Journal of Chemistry, **63**, 709-717 (2020). https://dx.doi.org/10.21608/ejchem.2019.13333.1832

[16] A. Hashim, M.A. Habeeb, and Q.M. Jebur, "Structural, dielectric and optical properties for (Polyvinyl alcohol-polyethylene oxide manganese oxide) nanocomposites," Egyptian Journal of Chemistry, **63**, 735-749 (2020). https://dx.doi.org/10.21608/ejchem.2019.14849.1901

[17] E. Randjbaran, R. Zahari, and R. Vaghei, "Scanning Electron Microscopy Interpretation In Carbon Nanotubes Composite Materials After Postbuckling-Review Paper," MATRIX Acad. Int. Online J. Eng. Technol. **2**(2), 1–6 (2014).

[18] Q.M. Jebur, A. Hashim, and M.A. Habeeb, "Fabrication, structural and optical properties for (Polyvinyl alcohol-polyethylene oxide iron oxide) nanocomposites," Egyptian Jour of Chemistry, **63** (2), 611-623 (2020). https://dx.doi.org/10.21608/ejchem.2019.10197.1669

[19] M.A. Habeeb, and W.S. Mahdi, "Characterization of (CMC-PVP-Fe$_2$O$_3$) nanocomposites for gamma shielding application," International Journal of Emerging Trends in Engineering Research, **7** (9), 247-255 (2019). https://dx.doi.org/10.30534/ijeter/2019/06792019

[20] R. Tintu, K. Saurav, K. Sulakshna, V.P.N. Nampoori, P. Radhakrishnan, and S. Thomas, "Ge28Se60Sb12/PVA composite films for photonic applications," J. Non-Oxide Glas. **2**(4), 167–174 (2010).

[21] M.A. Habeeb, and R.S.A. Hamza, "Synthesis of (polymer blend –MgO) nanocomposites and studying electrical properties for piezoelectric application," Indonesian Journal of Electrical Engineering and Informatics, **6**(4), 428-435 (2018). https://dx.doi.org/10.11591/ijeei.v6i1.511

[22] M.A. Habeeb, and R.S. Abdul Hamza, "Novel of (biopolymer blend-MgO) nanocomposites: Fabrication and characterization for humidity sensors," Journal of Bionanoscience, **12** (3), 328-335 (2018). https://doi.org/10.1166/jbns.2018.1535

[23] J. Selvi, S. Mahalakshmi, and V. Parthasarathy, "Synthesis, structural, optical, electrical and thermal studies of polyvinyl alcohol/CdO nanocomposite films," Journal of Inorganic and Organometallic Polymers and Materials, **27**, 1918-1926 (2017).

[24] M.A. Habeeb, A. Hashim, and N. Hayder, "Structural and optical properties of novel (PS-Cr₂O₃/ZnCoFe₂O₄) nanocomposites for UV and microwave shielding," Egyptian Journal of Chemistry, **63**, 697-708 (2020). https://dx.doi.org/10.21608/ejchem.2019.12439.1774

[25] M.A. Habeeb, W.K. Kadhim, "Study the optical properties of (PVA-PVAC-Ti) nanocomposites," Journal of Engineering and Applied Sciences, **9** (4), 109-113(2014). https://doi.org/10.36478/jeasci.2014.109.113

[26] R. Tintu, K. Saurav, K. Sulakshna, V.P.N. Nampoori, P. Radhakrishnan, and S. Thomas, "Ge28Se60Sb12/PVA composite films for photonic applications," J. Non-Oxide Glas. **2**, (4), 167–174 (2010)

[27] A.H. Hadi, and M.A. Habeeb, "Effect of CdS nanoparticles on the optical properties of (PVA-PVP) blends," Journal of Mechanical Engineering Research and Developments, **44**(3), 265 – 274 (2021). https://jmerd.net/03-2021-265-274/

[28] D.S. McLachlan, C. Chiteme, C. Park, K.E. Wise, Sh.E. Lowther, P.T. Lillehei, E.J. Siochi, and J.S. Harrison, "AC and DC percolative conductivity of single wall carbon nanotube polymer composites," Journal of Polymer Sciences Part B, **43**(22) 3273-3287 (2005).

[29] S.M. Mahdi, and M.A. Habeeb, "Synthesis and augmented optical characteristics of PEO–PVA–SrTiO3–NiO hybrid nanocomposites for optoelectronics and antibacterial applications," Optical and Quantum Electronics, **54**(12), 854 (2022). https://doi.org/10.1007/s11082-022-04267-6

[30] M.A. Habeeb, "Dielectric and optical properties of (PVAc-PEG-Ber) biocomposites," Journal of Engineering and Applied Sciences, **9** (4), 102-108 (2014). https://doi.org/10.36478/jeasci.2014.102.108

[31] G. Shui, J. Hu, M. Qiu, M. Wei, D. Xiao, "Study of Dielectric Properties For (Calcium Oxide-poly-vinyl alcohol) Composites," Chinese Chem. letters, **15**(12), 1501-1504 (2004).

[32] M.A. Habeeb, and W.H. Rahdi, "Titanium carbide nanoparticles filled PVA‑PAAm nanocomposites, structural and electrical characteristicsfor application in energy storage," Optical and Quantum Electronics, **55** (4), 334 (2023). https://doi.org/10.1007/s11082-023-04639-6

[33] V.M. Bhargav, P.B. Mohan, V. Raja, A.K. Sharma, and V.V.R.N. Rao, "Optical and Electrical Properties of Pure and Doped PEO Polymer Electrolyte Films," Soft Mater, **5**, 33–46 (2007). https://dx.doi.org/10.1080/15394450701405291

[34] M.A. Habeeb, and Z.S. Jaber, "Enhancement of Structural and Optical Properties of CMC/PAA Blend by Addition of Zirconium Carbide Nanoparticles for Optics and Photonics Applications," East European Journal of Physics, **4**, 176-182 (2022). https://doi.org/10.26565/2312-4334-2022-4-18

[35] S.M. Mahdi, M.A. Habeeb, "Tailoring the structural and optical features of (PEO–PVA)/(SrTiO3–CoO) polymeric nanocomposites for optical and biological applications," Polymer Bulletin, (2023). https://doi.org/10.1007/s00289-023-04676-x

[36] K.R. Nemade, S.A. Waghuley, "Synthesis of MgO nanoparticles by solvent mixed spraypyrolysis technique for optical investigation," Int. J. Metals, **2014** (4), (2014), Article ID 389416, http://dx.doi.org/10.1155/2014/389416

[37] M.H. Dwech, M.A. Habeeb, and A.H. Mohammed, "Fabrication and Evaluation of Optical Characterstic of (PVA-MnO2–ZrO₂) Nanocomposites for Nanodevices in Optics and Photonics," Ukr. J. Phys. **67**(10), 757-762 (2022). https://doi.org/10.15407/ujpe67.10.757

[38] A.A. Mohammed, and M.A. Habeeb, "Modification and Development of the Structural, Optical and Antibacterial Characteristics of PMMA/Si3N4/TaC Nanostructures," Silicon, (2023), https://doi.org/10.1007/s12633-023-02426-2

[39] A. Gautam, and S. Ram, "Preparation and Thermomechanical Properties of Ag-PVA Nanocomposite Films," Mater. Chem. Phys. **119** (2), 266-271 (2010)

[40] N.K. Al‑Sharifi, and M.A. Habeeb, "Synthesis and Exploring Structural and Optical Properties of Ternary PS/SiC/Sb2O3 Nanocomposites for Optoelectronic and Antimicrobial Applications," Silicon, (2023), https://doi.org/10.1007/s12633-023-02418-2

[41] N.B.V. Crasta, R. Kumar, and B.M. Praveen, "Advancement in Microstructural, Optical, and Mechanical Properties of PVA (Mowiol 10-98) Doped by ZnO Nanoparticles," Physics Research International, **9**(3), (2014), https://doi.org/10.1155/2014/742378

СИНТЕЗ ТА ХАРАКТЕРИСТИКА НАНОСТРУКТУР (PVA-CoO-ZrO₂)
ДЛЯ НАНООПТОЕЛЕКТРОННИХ ЗАСТОСУВАНЬ

Зейнаб Сабрі Джаберᵃ, Маджід Алі Хабібᵇ, Валід Хаді Радіᵃ
ᵃДиректорат освіти Вавилона, Міністерство освіти, Ірак
ᵇВавилонський університет, Коледж освіти для чистих наук, Фізичний факультет, Ірак

Нанокомпозити мають багато застосувань, включаючи оптичні інтегральні схеми, датчики, покриття та медичні пристрої. У зв'язку з цим метою цієї роботи є отримання нового типу нанокомпозитів з полівінілового спирту (ПВС) з різними концентраціями (0, 1, 2 і 3) мас.% оксиду кобальту та діоксиду цирконію (CoO-ZrO₂) наночастинок методом лиття. Мікроскопічні фотографії демонструють, що додаткова кількість наночастинок у полімері була рівномірною, і наночастинок (CoO ZrO₂) утворювали безперервну мережу в полімері, коли концентрація досягала 3 мас.%. Крім того, результати оптичних властивостей вказують на те, що поглинання нанокомпозитів покращується, оскільки концентрація наночастинок оксиду кобальту та діоксиду цирконію збільшується під час пропускання та зменшується розрив візуальної енергії. З іншого боку, оптичні константи нанокомпозитів (показник заломлення, коефіцієнт поглинання, коефіцієнт екстинкції, дійсна та уявна діелектричні константи) і оптична провідність зростають зі збільшенням масових часток (CoO-ZrO₂) наночастинок. Ці результати демонструють використання наночастинок PVA-CoO-ZrO₂ для різних оптичних пристроїв.
Ключові слова: *нанокомпозити; оптичні властивості; оксид кобальту; діоксид цирконію*

THERMOELECTRIC PROPERTIES INVESTIGATION OF Ni/Co DOPED ZrCoBi HALF-HEUSLER ALLOY[†]

Mahmoud Al-Elaimi*

Department of Basic Sciences, Preparatory Year Deanship, University of Ha'il, Ha'il, Saudi Arabia
E-mail: m.alelaimi@gmail.com
Received March 26, 2023; revised March 30, 2023; accepted March 31, 2023

Half-Heusler (HH) thermoelectric (TE) composites have been intensively inspected due to their excellent TE properties in the medium-to high-temperature range. First-principle calculations make it easier to discover or improve more HH compounds. This article presents an ab initio theoretical evaluation of TE properties of $ZrCoBi$ Half-Heusler alloy, when doped with Nickel (Ni), using FP-LAPW and the semi classic Boltzmann theory. Thermoelectric parameters were calculated using BoltzTraP code, like Seebeck coefficient (S), electrical conductivity to relaxation time ratio (σ/τ), electronic thermal conductivity to relaxation time ratio (κ_e/τ), thermoelectric power factor to relaxation time ratio ($S^2\sigma/\tau$), and the dimensionless figure-of-merit (ZT) in a temperature range of 0 – 500 K. Calculated Seebeck coefficient reveals that the studied alloys show a tendency to conduct as p-type with balanced TE performance between both charge carriers (holes and electrons). A high electronic thermal conductivity value is found, which predicts a potential use in heat sink applications for the investigated alloys. Obtained results, such as a high thermoelectric power factor and ZT $\cong$ 1, postulate that $ZrCo_{1-x}Ni_xBi$ alloys could have potential thermoelectric applications.
Key words: *ab initio calculations; Half-Heusler alloys; $ZrCoBi$; Ni/Co doping; Thermoelectric properties; Transport properties*
PACS: 72.80.Tm, 72.15.Jf, 74.25.Fy, 85.80.Fi, 73.50.Lw

INTRODUCTION

Since humans have started depending on fossil fuel energy, many environmental issues appeared. Climate change and global warming are of the most serious problems humans have to face. Recently, a decline rate of environmental issues was noticed due to COVID-19 breakout. However, these issues began to increase gradually after recovering from this pandemic [1]. Developing new renewable and sustainable energy technologies has become a vital choice for mankind in 21st century to confront such threats. Finding new and reliable metamaterials with desired thermoelectric (TE) characteristics has attracted more ambitious researchers and manufacturers as well. The new metamaterials with enhanced properties are utilized in many practical applications.

Generally, the performance of TE metamaterials is estimated by the thermoelectric figure-of-merit (ZT) that is described by the following formula:

$$ZT = \frac{\sigma S^2}{\kappa} T$$

here S, σ, σS^2, κ, T are Seebeck coefficient, electrical conductivity, thermoelectric power factor, thermal conductivity and absolute temperature, respectively [2-4].

The thermal conductivity (κ) has electronic and lattice contributions:

$$\kappa = \kappa_e + \kappa_l$$

Where κ_e is the electronic thermal conductivity and κ_l is the lattice thermal conductivity. The ZT of a TE metamaterial can be enhanced by increasing the σS^2 and/or by decreasing κ. But the close interdependent relations among S, σ, and κ_e via the carrier concentration leads to a real challenge in optimizing the TE transport properties while κ_l is considered relatively independent [5].

Generally, in order to produce promising TE metamaterials, a high ZT must be achieved [6-8], which can be fulfilled by optimizing σS^2 through tuning the carrier concentration. Usually, tuning carrier concentration can be obtained either by doping or by band engineering [9, 10], and reducing the thermal conductivity κ [11-13].

Among all TE materials, Half-Heusler (HH) compounds are excellent candidates for TE applications, such as spintronics [14], thermoelectric [15], optoelectronic [16], piezoelectric [17], shape memory alloys [18], and solar cell applications [19]. HH compounds have been intensively investigating since their discovery in 1903 by Friedrich Heusler [20] for their promising characteristics, such as thermoelectricity [15], high thermoelectric power factor σS^2 [21], tunable band gap [22], magnetism [23], durable mechanical properties [24], semi-metallicity [25], notable thermal stabilities [26], etc. HH compounds typically exhibit a valence electron count (VEC) of 18 per unit cell and have cubic MgAgAs structure ($F\bar{4}3m$). They are ternary intermetallic with a general formula of XYZ, where X is usually the d-electron transition metal, Y is a f-electron transition metal and Z is a p-electron element [27].

However, the main issue with HH compounds is their relatively high thermal conductivity that reduces ZT value and, accordingly, limits their TE performance. For that reason, many researchers have recently spent many efforts in

searching for enhanced HH thermoelectric materials. That enhancement can be attained through reducing the lattice thermal conductivity via optimizing nanoparticle phonon scattering centers [28], point defects [29], and grain size reduction [30].

Since experimental improving the TE materials is sometimes time consuming and/or costs a lot, many researchers prefer ab initio calculations. This procedure allows screening bigger sets of compounds along with shorter time using efficient codes and modern computers [31]. Hence, new high performance TE compounds might be identified. For example, Qureshi, M.T. et al. studied the Cu_2O based semiconductor materials and observed an elevation in the Seebeck coefficient consequent of Ag doping. They stated that these materials are promising candidates for modern electric devices. [32]. Huang et al. found interstitial Sn atoms in substitution leads to increase S and decrease the κ_e of n-type NbCoSb; thus, an enhanced figure-of-merit of ~ 0.56 is acquired [33]. Nenuwe et al. announced figure-of-merit values of (ZT = 3.27 and 1.43), suggesting that FeCrSb, and RuCrSb are potential materials for TE applications [34]. Dhakshayani et al. found that XCaB (X = Na, K and Rb) compounds have desired ferromagnetic and half-metallic behaviors with ZT of 1.00, and can be used for TE and spintronics applications [35].

One of the recently studied HH compounds with interesting TE properties is ZrCoBi. Nura Ibrahim et al. studied the TE properties of the heavily doped ZrCoBi. The results revealed desired TE properties, such as a high σS^2 at high-temperature region, and a high ZT of ~ 0.35 for $ZrCo_{0.75}Ni_{0.25}Bi$ at 900 K [36]. Zhu et al. announced the discovery the Half-Heusler of ZrCoBi with a huge TE conversion efficiency of $\sim 9\%$, which is computed at a wide temperature variation of about 500 K, and reached a good ZT amount of about 1.42 at 973 K [37]. Yazdani-Kachoei, M. et al. studied the electronic and structural characteristics of ZrRhBi and ZrCoBi. They showed that those compounds have high Seebeck value and low electrical conductivity [38]. Hangtian Zhu et al. have studied the TE characteristics of ZrCoBi-based Half-Heuslers. They showed that those compounds can be used as mid- and high-temperature TE power generators [39].

In this research, the ab-initio calculations are used to investigate the TE properties of Ni-doped Half-Heusler ZrCoBi compounds. In the following section, the computational details are briefly summarized. The effects of Ni doping into Co site on the thermoelectric behavior of ZrCoBi were demonstrated and discussed in section 3. The conclusion is given in section 4.

COMPUTATIONAL DETAILS

Half-Heusler $ZrCo_{1-x}Ni_xBi$ compounds have a cubic lattice structure with space group of $F\bar{4}3m$. The Ni concentrations (x) are chosen to be (0, 0.25, 0.75 and 1) such that an optimal structural stability is achieved. Their structural, thermal, and electronic properties were discussed in details in a previous study [40]. Where the Full-Potential Wien2k package [41], the Linearized Augmented Plane Wave (FP-LAPW) method [42], the generalized gradient approximation (PBE-GGA) [43] were used. The convergence test limits of the self-consistent calculations were chosen to be 0.1×10^{-3} Ry for the determined total energy and 0.1×10^{-3} e for crystal charge. In this work, the thermoelectric transport coefficients were calculated using BoltzTraP code, which is interfaced within Wien2k. The calculations are based on DFT and Boltzmann theory [44].

RESULTS AND DISCUSSION

In this section, the thermoelectric behavior of Ni-doped ZrCoBi alloys are presented and discussed. Seebeck coefficient (S), electrical conductivity to relaxation time ratio (σ/τ), electronic thermal conductivity to relaxation time ratio (κ_e/τ) were calculated in the temperature range 0 – 500 K. Then the thermoelectric power factor to relaxation time ratio ($S^2\sigma/\tau$), and the dimensionless figure-of-merit (ZT) were worked out. The temperature (T) dependence of the Seebeck coefficient (S) is plotted in Fig. 1, where S behavior for both charge carriers is illustrated. It is noticed that Seebeck coefficient reaches its optimal value in the low-temperature region then decreases exponentially with increase in temperature.
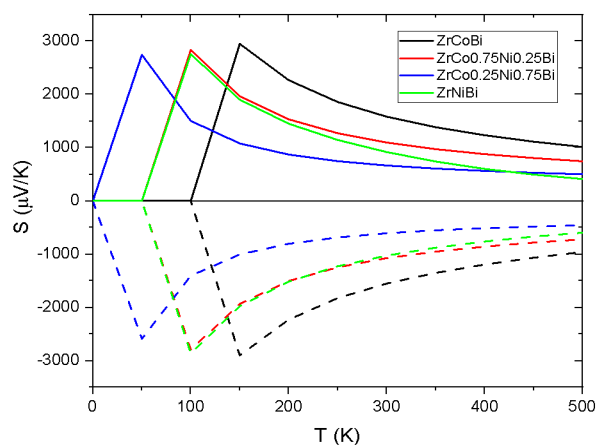
Figure 1. Temperature dependence of Seebeck coefficient of $ZrCo_{1-x}Ni_xBi$. Solid (dashed) lines denote hole (electron) charge carriers.

The S_{max} values for hole (electron) charge carrier are found to be $2.95 \times 10^3 \mu V/K$ at 150 K ($-2.90 \times 10^3 \mu V/K$ at 150 K) for ZrCoBi, $2.83 \times 10^3 \mu V/K$ at 100 K ($-2.79 \times 10^3 \mu V/K$ at 100 K) for $ZrCo_{0.75}Ni_{0.25}Bi$, $2.74 \times 10^3 \mu V/K$ at 50 K ($-2.59 \times 10^3 \mu V/K$ at 50 K) for $ZrCo_{0.25}Ni_{0.75}Bi$, and $2.76 \times 10^3 \mu V/K$ at 100 K ($-2.86 \times 10^3 \mu V/K$ at 100 K) for ZrNiBi. Ni substitution in Co site shifts the S curves to a lower temperature region, especially the $ZrCo_{0.25}Ni_{0.75}Bi$. A rapprochement of S_{max} values for both hole and electron charge carrier is noticed for all doping cases. From these values, it is expected that $ZrCo_{1-x}Ni_xBi$ can split between both charge carriers (holes and electrons) quasi-Fermi levels at donor/acceptor interface.

The dependence of Seebeck coefficient on charge carrier concentration (n) of $ZrCo_{1-x}Ni_xBi$ alloys are plotted in Fig. 2. The S_{max} values relative to n are located at 0, 1, 1, and 3 for ZrCoBi, ZrNiBi, $ZrCo_{0.75}Ni_{0.25}Bi$, and $ZrCo_{0.25}Ni_{0.75}Bi$, respectively. It is obviously noticed that the change of temperature does not influence S values for both charge carriers. However, Ni-doping shifts the curves to the higher positive (hole) concentration region, especially the $ZrCo_{0.25}Ni_{0.75}Bi$. According to the obtained S_{max} and n values, it is found that $ZrCo_{1-x}Ni_xBi$ can alter between both charge carriers (holes and electrons) with the same thermoelectric efficiency and work as p-type alloys.
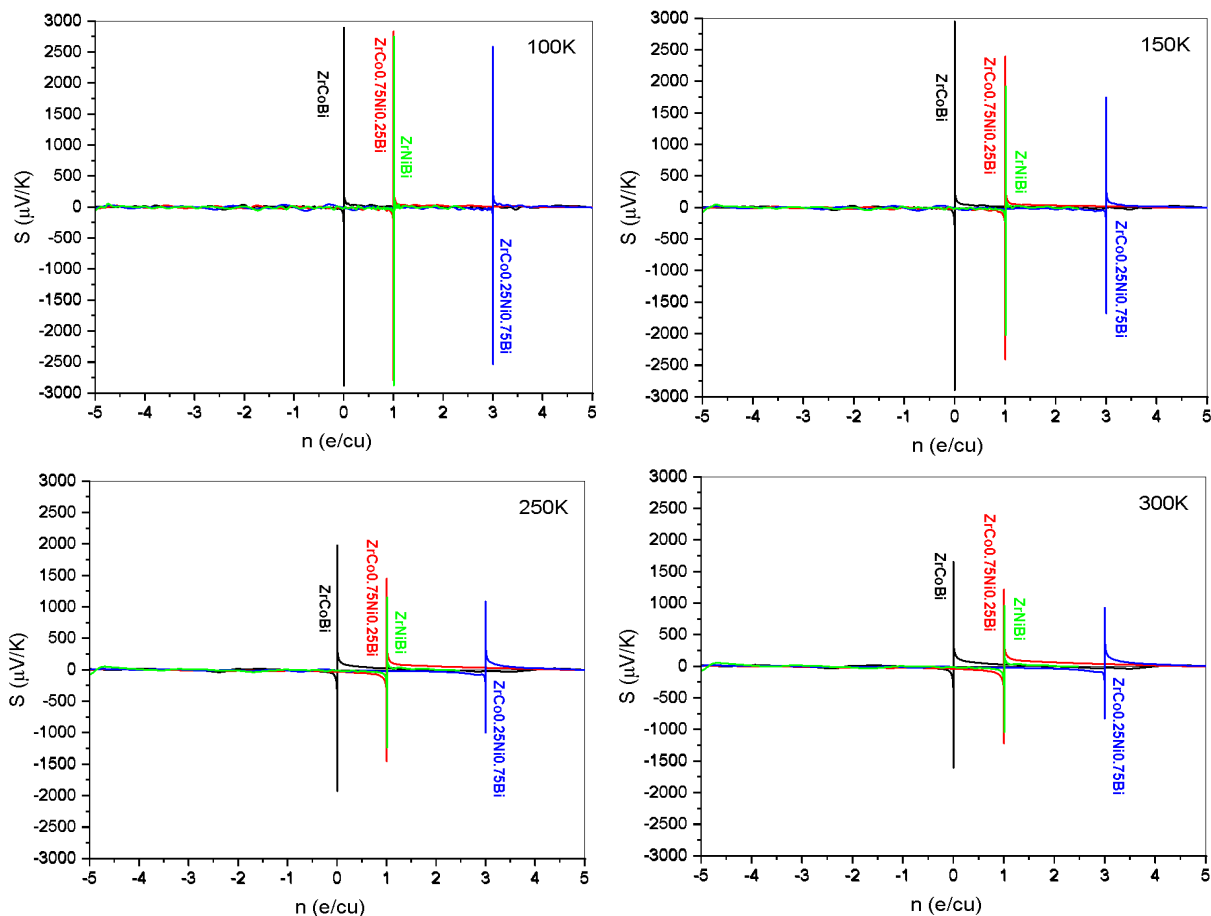
Figure 2. The charge carrier concentration dependence of Seebeck coefficient of $ZrCo_{1-x}Ni_xBi$ at 100, 150, 250, and 300 K.

The potential applicability of $ZrCo_{1-x}Ni_xBi$ as a thermoelectric material not only depends on the thermoelectric power, but also on the most important charge transport properties, namely the electrical and thermal conductivities. The temperature dependence of electrical conductivity to relaxation time ratio (σ/τ) is calculated. σ/τ is found directly (inversely) proportional to T (S) satisfying the Mott formula [45]. A remarkable preference of $ZrCo_{0.25}Ni_{0.75}Bi$ is noticed, as shown in Fig. 3.

The desired response of σ/τ implies a growing of n that elevates holes to the conduction band. The highest σ/τ value is found to be for $ZrCo_{0.25}Ni_{0.75}Bi$ for all chosen temperatures. By comparison to the other studied compounds, the elevated σ/τ amount of $ZrCo_{0.25}Ni_{0.75}Bi$ for both charge carrier concentrations exhibits significantly large band dispersion at the band edges, and hence a small effective mass. Moreover, the computed σ/τ values are found nearly the same for both charge carriers, which is in agreement with the previous conclusion about the ability of all Ni-doped compounds to exchange between charge carriers (holes and electrons).

Fig. 4 illustrates that σ/τ is directly proportional to n at 300 K. The computed $(\sigma/\tau)_{max}$ amounts of the p-type (n-type) doping regime are $3.06 \times 10^{20} (\Omega ms)^{-1}$ at $1.76 \, e(c.u)^{-1}$ ($3.81 \times 10^{20} (\Omega ms)^{-1}$ at $-3.49 \, e(c.u)^{-1}$) for ZrCoBi, $1.71 \times 10^{20} (\Omega ms)^{-1}$ at $4.90 \, e(c.u)^{-1}$ ($2.30 \times 10^{20} (\Omega ms)^{-1}$ at $-3.34 \, e(c.u)^{-1}$) for $ZrCo_{0.75}Ni_{0.25}Bi$,

1.06×10^{20} $(\Omega ms)^{-1}$ at 5.53 $e(c.u)^{-1}$ $(2.79 \times 10^{20}$ $(\Omega ms)^{-1}$ at -2.88 $e(c.u)^{-1})$ for $ZrCo_{0.25}Ni_{0.75}Bi$, and 2.52×10^{20} $(\Omega ms)^{-1}$ at 2.46 $e(c.u)^{-1}$ $(4.16 \times 10^{20}$ $(\Omega ms)^{-1}$ at -2.47 $e(c.u)^{-1})$ for $ZrNiBi$. A preference of σ/τ is clearly noticed for n-type doping regime over p-type at 300 K.
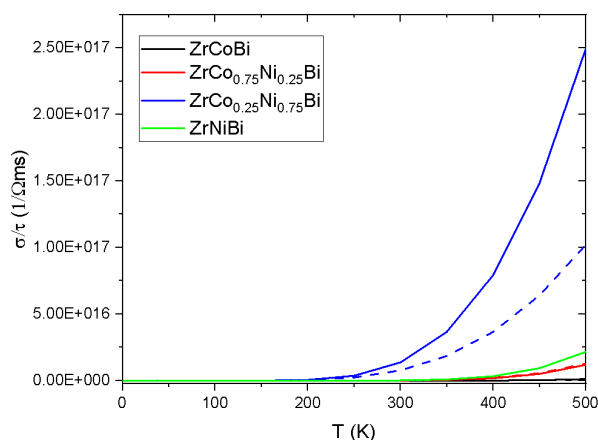
Figure 3. The temperature dependence of electrical conductivity to relaxation time ratio (σ/τ) of $ZrCo_{1-x}Ni_xBi$. Solid (dashed) lines denote hole (electron) charge carriers
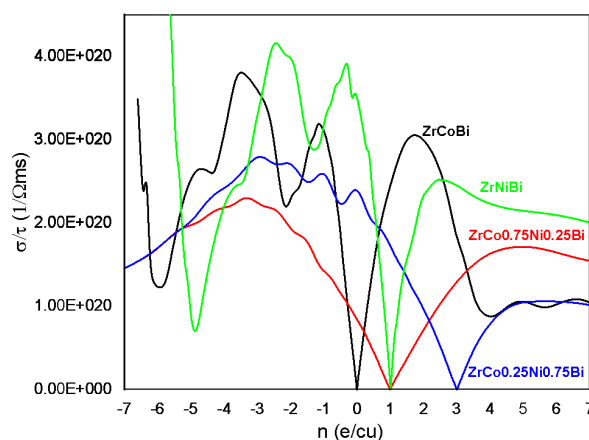
Figure 4. The charge carrier concentration dependence of electrical conductivity to relaxation time ratio (σ/τ) of $ZrCo_{1-x}Ni_xBi$ at 300 K

The variation of the electronic thermal conductivity to relaxation time ratio (κ_e/τ) with temperature is demonstrated in Fig. 5. It is found that κ_e/τ vs T and σ/τ vs T curves have a comparable behavior. They are directly (inversely) proportional to T (S) that satisfies the Mott formula. Below room temperature, there is a monotonic variation in κ_e/τ. While, beyond room temperature, the $\kappa_e/\tau$ shows strong temperature dependence. This implies a stoichiometric composition of the alloys, and an increasing charge carrier flow with the raising temperature. In addition, Wiedemann–Franz law, which describes the κ_e and σ relationship, is also verified as κ_e/σ is found to be constant. The high electronic thermal conductivity values, especially for $ZrCo_{0.25}Ni_{0.75}Bi$, suggests a use in heat sink applications for studied compounds.

Besides S, the thermoelectric power factor to relaxation time ratio ($S^2\sigma/\tau$) is an excellent measure that grants credibility to $ZrCo_{1-x}Ni_xBi$ to be used in thermoelectric applications. Fig. 6 presents the temperature dependence of the thermoelectric power factor to relaxation time ratio for both charge carriers. It is found that $S^2\sigma/\tau$ raises as the temperature elevates for both doping systems. A clear preference of $ZrCo_{0.25}Ni_{0.75}Bi$ is noticed, which exhibits a sharp elevation above ambient temperature region. This behavior indicates that $ZrCo_{0.25}Ni_{0.75}Bi$ has promising thermoelectric properties, like waste heat usage in power generators.
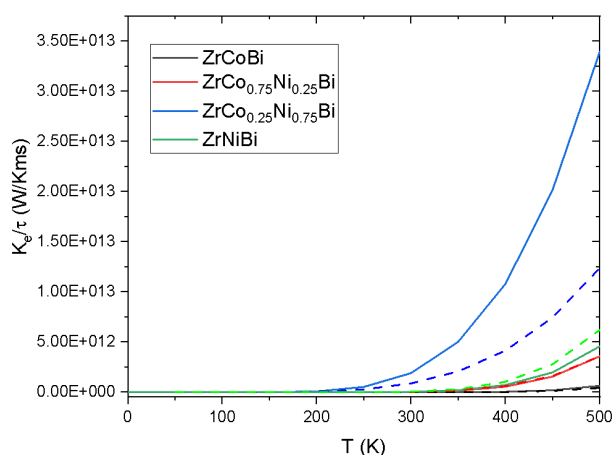
Figure 5. The temperature dependence of the electronic thermal conductivity to relaxation time ratio (κ_e/τ) of $ZrCo_{1-x}Ni_xBi$. Solid (dashed) lines denote hole (electron) charge carriers
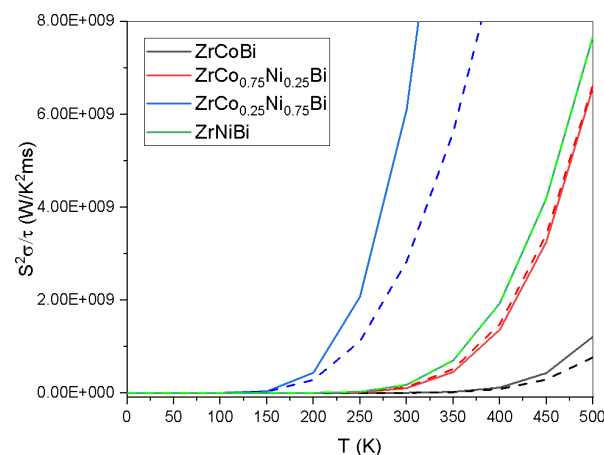
Figure 6. The temperature dependence of the thermoelectric power factor to relaxation time ratio ($S^2\sigma/\tau$) of $ZrCo_{1-x}Ni_xBi$. Solid (dashed) lines denote hole (electron) charge carriers

Fig. 7 demonstrates the charge carrier concentration dependence of $S^2\sigma/\tau$ at 300 K. The evaluated maximum $S^2\sigma/\tau$ values at 300K are found 6.33×10^{11}, 3.23×10^{11}, 3.90×10^{11}, and 6.87×10^{11} W/K^2ms for $ZrCoBi$, $ZrCo_{0.75}Ni_{0.25}Bi$, $ZrCo_{0.25}Ni_{0.75}Bi$, and $ZrNiBi$, respectively. The elevated $S^2\sigma/\tau$ values foresee that $ZrCo_{1-x}Ni_xBi$ are good future candidates for thermoelectric device applications.

The results of electrical conductivity, electronic thermal conductivity, and Seebeck coefficient were used to calculate the figure-of-merit (ZT). The variation of the ZT with temperature corresponding to the hole and electron charge carrier of the present alloys are shown in Fig. 8. The obtained ZT values are nearly equal to 1 for all compounds up to 150K. At higher temperatures, ZT drops marginally, but remain in the high ZT region for all compounds except ZrNiBi. ZrNiBi shows a strong temperature dependence as its ZT value drops more promptly in the high temperature region. Being ZT is equal to 1 up to 150K and about 0.90 till 500K predicts beneficial thermoelectric properties of $ZrCo_{1-x}Ni_xBi$ alloys. Experimental values of figure-of-merit for Ni-doped ZrCoBi are not available for comparison.
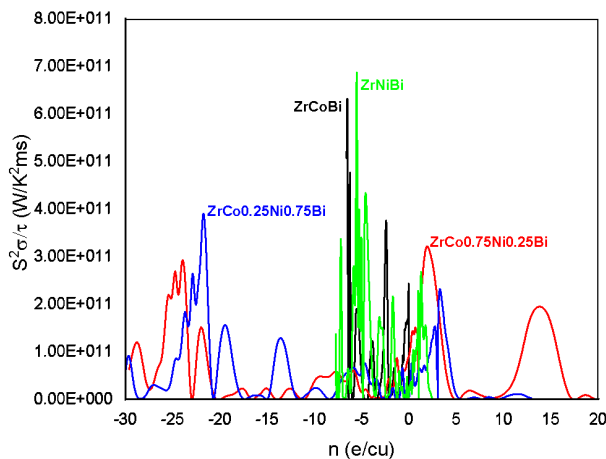
Figure 7. The charge carrier concentration dependence of thermoelectric power factor to relaxation time ratio ($S^2\sigma/\tau$) of $ZrCo_{1-x}Ni_xBi$ at 300 K
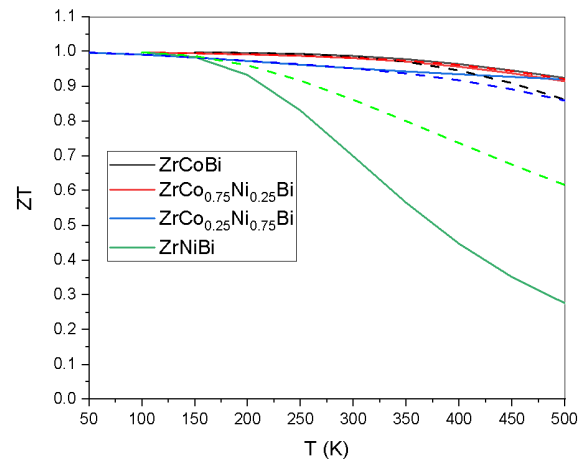
Figure 8. Figure-of-merit (ZT) of $ZrCo_{1-x}Ni_xBi$. Solid (dashed) lines denote hole (electron) charge carriers

Based on Seebeck coefficient, electronic conductivity, electronic thermal conductivity, thermoelectric power factor, and relatively high ZT value, $ZrCo_{1-x}Ni_xBi$ are predicted to be good TE materials. These compounds might be used in TE applications, such as thermoelectric power generator from waste heat and sustainable energy systems. Moreover, the current findings may inspire experimentalists to explore these compounds at wider doping concentration and temperature ranges.

CONCLUSION

In this paper, the transport parameters of the cubic ternary $ZrCo_{1-x}Ni_xBi$ half-Heusler alloys have been computed using FP-LAPW and Boltzmann theory. The transport parameters, calculated by using BoltzTraP code, are Seebeck coefficient (S), electrical conductivity to relaxation time ratio (σ/τ), electronic thermal conductivity to relaxation time ratio (κ_e/τ), thermoelectric power factor to relaxation time ratio ($S^2\sigma/\tau$), and the dimensionless figure-of-merit (ZT) in the temperature range 0 – 500 K. Findings show that $ZrCo_{1-x}Ni_xBi$ have a p-type doping character with ability to alter between hole and electron charge carrier. The high value of S at low temperature range proposes favorable thermoelectric applications of the studied compounds. A remarkable high σ/τ value of $ZrCo_{0.25}Ni_{0.75}Bi$ is noticed. The high electronic thermal conductivity value especially for $ZrCo_{0.25}Ni_{0.75}Bi$ suggests that these compounds can be used in the heat sink applications. Due to the high values of thermoelectric power factor and figure-of-merit (ZT $\cong$ 1), potential thermoelectric device applications are predicted, such as sustainable energy systems.

ORCID ID

Mahmoud Al-Elaimi, https://orcid.org/0000-0001-6985-1012

REFERENCES

[1] M.M. Alam, M.A. Aktar, N.D.M. Idris, and A.Q. Al-Amin, J World Development Sustainability, **2**, 100048 (2023), https://doi.org/10.1016/j.wds.2023.100048

[2] C. Gayner, and K. K. Kar, J. Progress in Materials Science, **83**, 330-382 (2016), https://doi.org/10.1016/j.pmatsci.2016.07.002

[3] R. Liu, H. Chen, K. Zhao, Y. Qin, B. Jiang, T. Zhang, G. Sha, X. Shi, C. Uher and W. Zhang, J. Advanced Materials, **29**(38), 1702712 (2017), https://doi.org/10.1002/adma.201702712

[4] T. Zhu, C. Fu, H. Xie, Y. Liu and X. Zhao, Advanced Energy Materials, **5**(19), 1500588 (2015), https://doi.org/10.1002/aenm.201500588

[5] A. Mubarak, S. Saad, F. Hamioud and M. Al-Elaimi, J. Solid State Sciences, **111**, 106397 (2021), https://doi.org/10.1016/j.solidstatesciences.2020.106397

[6] J. Wei, L. Yang, Z. Ma, P. Song, M. Zhang, J. Ma, F. Yang and X. Wang, J. Journal of Materials Science, **55**, 12642-12704 (2020), https://doi.org/10.1007/s10853-020-04949-0

[7]   D. Li, Y. Gong, Y. Chen, J. Lin, Q. Khan, Y. Zhang, Y. Li, H. Zhang and H. Xie, J. Nano-Micro Letters, **12**, 1-40 (2020), https://doi.org/10.1007/s40820-020-0374-x

[8]   P.A. Finn, C. Asker, K. Wan, E. Bilotti, O. Fenwick, and C.B. Nielsen, J. Frontiers in Electronic Materials, **1**, 677845 (2021), https://doi.org/10.3389/femat.2021.677845

[9]   Y. Zheng, T.J. Slade, L. Hu, X.Y. Tan, Y. Luo, Z.-Z. Luo, J. Xu, Q. Yan and M. G. Kanatzidis, J. Chemical Society Reviews, **50** (16), 9022-9054 (2021), https://doi.org/10.1039/D1CS00347J

[10] A. Kumar, S. Bano, B. Govind, A. Bhardwaj, K. Bhatt and D. Misra, J. of Electronic Materials **50**, 6037-6059 (2021), https://doi.org/10.1007/s11664-021-09153-7

[11] Z. Bu, W. Li, J. Li, X. Zhang, J. Mao, Y. Chen, and Y. Pei, J. Materials Today Physics, **9**, 100096 (2019), https://doi.org/10.1016/j.mtphys.2019.100096

[12] S. Roychowdhury, R.K. Biswas, M. Dutta, S.K. Pati, and K. Biswas, J. ACS Energy Letters, **4** (7), 1658-1662 (2019), https://doi.org/10.1021/acsenergylett.9b01093

[13] S. Li, J. Yang, J. Xin, Q. Jiang, Z. Zhou, H. Hu, B. Sun, A. Basit, and X. Li, J. ACS Applied Energy Materials, **2** (3), 1997-2003 (2019), https://doi.org/10.1021/acsaem.8b02096

[14] K. Elphick, W. Frost, M. Samiepour, T. Kubota, K. Takanashi, H. Sukegawa, S. Mitani and A. Hirohata, J. Science technology of advanced materials, **22** (1), 235-271 (2021), https://doi.org/10.1080/14686996.2020.1812364

[15] K. Xia, C. Hu, C. Fu, X. Zhao and T. Zhu, J. Applied Physics Letters, **118** (14), 140503 (2021), https://doi.org/10.1063/5.0043552

[16] F. Parvin, M. Hossain, I. Ahmed, K. Akter, and A. Islam, J. Results in Physics, **23**, 104068 (2021), https://doi.org/10.1016/j.rinp.2021.104068

[17] Z. Almaghbash, O. Arbouche, A. Dahani, A. Cherifi, M. Belabbas, A. Zenati, H. Mebarki, and A. Hussain, J. International Journal of Thermophysics, **42**, 1-19 (2021), https://doi.org/10.1007/s10765-020-02755-z

[18] S. Dhanal, A. Ghaste, V. Akkimardi, S. Kori, and C. Bhosale, AIP Conference Proceedings, **2162**(1), 020002 (2019), https://doi.org/10.1063/1.5130212

[19] V.K. Solet, S. Sk, and S.K. Pandey, J. Physica Scripta, **97**(10), 105711 (2022), https://doi.org/10.1088/1402-4896/ac93c1

[20] T. Graf, C. Felser and S.S. Parkin, J. Progress in solid state chemistry, **39**(1), 1-50 (2011), https://doi.org/10.1016/j.progsolidstchem.2011.02.001

[21] G.A. Naydenov, P.J. Hasnip, V. Lazarov, and M. Probert, J. Journal of physics: Materials, **2**(3), 035002 (2019), https://doi.org/10.1088/2515-7639/ab16fb

[22] M.K. Bamgbose, J. Applied Physics A, **126**(564), 1-8 (2020), https://doi.org/10.1007/s00339-020-03691-3

[23] D. Vishali, and R. John, J. Journal of Crystal Growth, **583**, 126556 (2022), https://doi.org/10.1016/j.jcrysgro.2022.126556

[24] W.Y.S. Lim, D. Zhang, S.S.F. Duran, X.Y. Tan, C.K.I. Tan, J. Xu, and A. Suwardi, J. Frontiers in Materials, **8**, 745698 (2021), https://doi.org/10.3389/fmats.2021.745698

[25] R. Majumder, M.M. Hossain, and D. Shen, J. Modern Physics Letters B, **33**(30), 1950378 (2019), https://doi.org/10.1142/S0217984919503780

[26] E. Rausch, B. Balke, S. Ouardi and C. Felser, J. Energy Technology, **3** (12), 1217-1224 (2015), https://doi.org/10.1002/ente.201500183

[27] A.S. Gzyl, A.O. Oliynyk, and A. Mar, J. Crystal Growth Design, **20**(10), 6469-6477 (2020), https://doi.org/10.1021/acs.cgd.0c00646

[28] M. Sato, Y.W. Chai, and Y. Kimura, ACS Appl. Mater. Interfaces, **13**(21), 25503-25512 (2021), https://doi.org/10.1021/acsami.1c03525

[29] T. Chibueze, A. Raji, and C. Okoye, J. Phys. Chem. Solids, **139**, 109328 (2020), https://doi.org/10.1016/j.jpcs.2019.109328

[30] X. Zhang, S. Li, B. Zou, P. Xu, Y. Song, B. Xu, Y. Wang, G. Tang, and S. Yang, J. of Alloys and Compounds, **901**, 163686 (2022), https://doi.org/10.1016/j.jallcom.2022.163686

[31] A. Mubarak, S. Tariq, F. Hamioud, and B. Alsobhi, Journal of Physics: Condensed Matter, **31**(50), 505705 (2019), https://doi.org/10.1088/1361-648X/ab3140

[32] M.T. Qureshi, F. Ullah, R.S.A. Hameed, M. Al-Elimi, J. Humadi, A. Nassar, M. Badr, K.A. Halim, and M. Saleem, J. Ceramics International, (2023), https://doi.org/10.1016/j.ceramint.2023.03.103

[33] L. Huang, Q. Zhang, Y. Wang, R. He, J. Shuai, J. Zhang, C. Wang, and Z. Ren, J. Physical Chemistry Chemical Physics, **19**(37), 25683-25690 (2017), https://doi.org/10.1039/C7CP04801G

[34] N. Nenuwe, and E. Omugbe, J. Current Applied Physics, **49**, 70-77 (2023), https://doi.org/10.1016/j.cap.2023.02.013

[35] Y. Dhakshayani, G. Suganya, and G. Kalpana, Journal of Crystal Growth, **583**, 126550 (2022), https://doi.org/10.1016/j.jcrysgro.2022.126550

[36] N. Ibrahim, R.A. Ahmed, H. Adri, and I. Reisya, J. Materials Today Communications, **32**, 103908 (2022), https://doi.org/10.1016/j.mtcomm.2022.103908

[37] H. Zhu, R. He, J. Mao, Q. Zhu, C. Li, J. Sun, W. Ren, Y. Wang, Z. Liu and Z. Tang, J. Nature communications, **9**(1), 1-9 (2018), https://doi.org/10.1038/s41467-018-04958-3

[38] M. Yazdani-Kachoei, and S. Jalali-Asadabadi, Journal of alloys compounds, **828**, 154287 (2020), https://doi.org/10.1016/j.jallcom.2020.154287

[39] H. Zhu, J. Mao, Z. Feng, J. Sun, Q. Zhu, Z. Liu, D.J. Singh, Y. Wang, and Z. Ren, J .Science advances, **5**(6), eaav5813 (2019), https://doi.org/10.1126/sciadv.aav5813

[40] M. Al-Elaimi, East Eur. J. Phys. (2), 103-111 (2022), https://doi.org/10.26565/2312-4334-2022-2-13

[41] P. Blaha, K. Schwarz, P. Sorantin, and S. Trickey, J. Computer physics communications, **59**(2), 399-415 (1990), https://doi.org/10.1016/0010-4655(90)90187-6

[42] P. Hohenberg, and W. Kohn, J. Physical Review, **136**(3B), B864 (1964), https://doi.org/10.1103/PhysRev.136.B864

[43] J.P. Perdew, K. Burke, and M. Ernzerhof, J. Physical review letters, **77**(18), 3865 (1996), https://doi.org/10.1103/PhysRevLett.77.3865

[44] G.K. Madsen, and D.J. Singh, J, Computer physics communications, **175**(1), 67-71 (2006), https://doi.org/10.1016/j.cpc.2006.03.007

[45] M. Cutler, and N. F. Mott, J. Physical Review, **181**(3), 1336 (1969), https://doi.org/10.1103/PhysRev.181.1336

ДОСЛІДЖЕННЯ ТЕРМОЕЛЕКТРИЧНИХ ВЛАСТИВОСТЕЙ СПЛАВУ НАПІВГЕЙСЛЕРА ZrCoBi, ЛЕГОВАНОГО Ni/Co

Махмуд Аль Елаймі

Факультет фундаментальних наук, деканат підготовчого року, Університет Хаїль, Хаїль, Саудівська Аравія

Термоелектричні (ТЕ) композити Half-Heusler (HH) були перевірені через їхні відмінні ТЕ властивості в діапазоні середніх і високих температур. Розрахунки на основі першопринципів полегшують відкриття або покращення більшої кількості сполук HH. У статті представлено теоретичну оцінку ТЕ властивостей сплаву Half-Heusler ZrCoBi, легованого нікелем (Ni), з використанням FP-LAPW і напівкласичної теорії Больцмана. Термоелектричні параметри розраховувалися за допомогою коду BoltzTraP, наприклад, коефіцієнт Зеєбека (S), відношення електропровідності до часу релаксації (σ/τ), відношення електронної теплопровідності до часу релаксації (κ_e/τ), відношення коефіцієнта термоелектричної потужності до часу релаксації ($S^2\sigma/\tau$), а також безрозмірну добротність (ZT) в діапазоні температур 0-500 К. Розрахований коефіцієнт Зеєбека показує, що досліджувані сплави демонструють тенденцію до провідності р-типу зі збалансованою ТЕ характеристикою між обома носіями заряду (дірки та електрони). Знайдено високе значення електронної теплопровідності, що передбачає потенційне використання досліджуваних сплавів у тепловідвідних програмах. Отримані результати, такі як високий коефіцієнт термоелектричної потужності та $ZT \cong 1$, припускають, що сплави $ZrCo_{1-x}Ni_xBi$ можуть мати потенційне термоелектричне застосування.

Ключові слова: *ab initio розрахунки; сплави напівгейслера; ZrCoBi; легування Ni/Co; термоелектричні властивості; транспортні властивості*

STUDY OF FUSION REACTIONS OF LIGHT PROJECTILES ON LIGHT AND MEDIUM TARGETS[†]

Malik S. Mehemed

Education Directorate Babylon, Ministry of Education, Babil, Iraq
E-mail: malikmehemed9@gmail.com
Received April 6, 2023; revised April 26, 2023; accepted April 29, 2023

The fusion and breakup reactions of some light projectiles on light and medium targets using semi-classical and full quantum mechanical approaches were adopted to calculate the total cross section σ_{fus} and the distribution of the fusion barrier D_{fus} for the systems $^{12}C + ^{48}Ti$, $^{16}O + ^{63}Cu$, $^{35}Cl + ^{25}Mg$ and $^{35}Cl + ^{27}Al$. The coupling between the channel's contribution from elastic and breakup channels were considered to show their importance in the calculations. The results compared with the measured data and shows reasonable matching, and it is shown that the coupling considered is very essential to be considered, especially below the Coulomb barrier V_b.

Keywords: *Coupled-channels; Fusion cross section; Fusion barrier distribution*
PACS: 34. 85. +x, 24.10.-i, 25.70.Jj

1. INTRODUCTION

One of the most important modern researches fields in nuclear physics is studying the collision of weakly bound stable and radioactive nuclei, around the potential barrier [1]. The understanding of the processes associated with these reactions can be achieved throw adopting both theoretical and experimental offers in order to obtain the best agreement between them. many researches during the last years supported the strong relation between the different nuclear reaction modes starting by the elastic scattering and ending with the fusion reaction, so that will provide the researchers with a wide field of reaction modes to collect more information about the secrets of the nuclear structure and properties of our universe ingredients. The weakly bound systems collisions are very influenced by both transfer and breakup channels which have a very large cross-section according to their low breakup threshold. The projectile mass is one of the most effective factors on the reaction strength, so it is very important to study the reactions with medium mass projectile to examine the relationship between reaction modes and bombarding energy and nucleon number. The fusion of weakly bound colliding projectiles was very effected statically by their fusion barrier characteristics such as its long tail energy which cause a lower barrier and by the way will give an enhancement to the cross section of the fusion at the energies at the sub-barrier [2, 3]. Dynamically, fusion was affected by the different channels coupling, including the elastic, breakup, inelastic and transfer ones [4]. The kinetic energy of the projectile should exceed the corresponding Coulomb barrier for producing nuclear reaction [5].

All of the energy, mass number, momentum, charge, spin and parity are conserved during the nuclear reaction. The Q-value have a great effect on the fusion calculations because it represents the amount of energy emitted or absorbed during the reaction [6]. The two colliding nuclei in the fusion reaction are considered as objects with rigid spherical shape that interact with the potential barrier so the probability of nuclear fusion to accurse represents the ability of the system to penetrate the potential barrier [7], 8]. There are many important factors that have a major role in the experimental determination of the fusion cross section such as the colliding nuclei internal degrees of freedom relative motion, the particles transfer and the nuclear deformation [9, 10]. The collision process is very complex at low temperature, so to be understood it need to unify the description for the different reaction mechanism with a unique nuclear potential [11]. The fusion is very complex reaction because of the combination between the coulomb and nuclear interactions in addition to the effect of the flexible intrinsic synthesis during the reaction and the different reaction channels [12].

This study aims to study the fusion reaction of light projectiles on light targets for the systems $^{12}C + ^{48}Ti$, $^{16}O + ^{63}Cu$, $^{35}Cl + ^{25}Mg$ and $^{35}Cl + ^{27}Al$ by using semi-classically and full quantum mechanically methods where the coupling between the elastic and breakup channels will be considered.

2. THE SEMI-CLASSICAL TREATMENT
2.1. The single channel theory

In one-dimensional potential model, we need to use the semiclassical approach for the fusion cross-section determination by eliminating the degree of freedom by the relative motion between the colliding heavy ion only. [13,14,15]. Semi-classically, this can be treated by the assumption of energy and momentum independent Schrödinger equation;

$$[-\hbar^2\nabla^2/2\mu + V(r) - E]\psi(r) = 0, \tag{1}$$

where μ and $V(r)$ are the reduced mass and total energy potential of the system respectively. The time dependence function can be used to determine the semiclassical amplitudes by evaluating the particle trajectory using classical dynamics, including all the potential types, as;

$$V(r) = V_C(r) + V_N(r) + V_l(r). \tag{2}$$

In addition, the complex potential which represents the imaginary part of the nuclear potential, should be contained.

$$V_N(r) = U_N(r) - iW(r). \tag{3}$$

The above method can be used to study the effect of the nuclear potential with its real and imaginary parts on the interacting l waves [13,16,17]. According to the semi-classical theory, the fusion takes place when the nuclei be closer to the barrier, and the WKB approximation can be used to determine the penetration probability below the barrier [13,18,19,20].

$$P_{fus}^{WKB}(\ell, E) = \frac{1}{1 + e^{\left[2\int_{r_b^{(l)}}^{r_a^{(l)}} k_l(r)dr\right]}}. \tag{4}$$

Then it can be simplified as:

$$P_{fus}^{WKB}(l, E) = \frac{1}{1 + e^{\left[\frac{2\pi}{\hbar\Omega_l}(V_b(l) - E)\right]}}. \tag{5}$$

Where $r_b^{(l)}$ and $r_a^{(l)}$ represent the turning points of the fusion barrier potential for its inner and outer and $\kappa_l(r)$ is the wave number. If a parabolic function used as an approximation for the fusion barrier, then the Hill–Wheeler formula can be used to find the penetration probability above the barrier [13].

$$P_{fus}^{WH}(l, E) = \frac{1}{1 + e^{\left[\frac{2\pi}{\hbar\Omega_l}(E - V_b(l))\right]}}. \tag{6}$$

E is the bombarding energy and $V_b(l)$ is the height parameter of the partial wave fusion barrier with curvature parameter Ω_l. The fusion cross-section can be determined by using the WKB approximations as [17, 21]:

$$\sigma_{fus}(E) = \frac{\pi}{k^2} \sum (2l + 1) P_{fus}^{WKB}(\ell, E), \tag{7}$$

$$P_{fus}^{\gamma}(\ell, E) = \frac{4k}{E} \int dr |u_{\gamma l}(k_{\gamma}, r)|^2 W_{fus}^{\gamma}(r). \tag{8}$$

In the above equation, $u_{\gamma l}(k_{\gamma}, r)$ refers to the wave function of the radial part in γ channel, and the potential imaginary part denoted by $W_{fus}^{\gamma}(r)$.

The using of semiclassical theory to compute heavy ions fusion cross section by approximating the trajectory r, and the projectile intrinsic states (ξ) using the Coupled-Channel Continuum Discretized (CCCD) method with the helpful of Winther and Alder (AW) theory [21,22,23,24,25]. The Hamiltonian of the projectile is,

$$h = h_0(\xi) + V(\xi, r), \tag{9}$$

where $h_0(\xi)$ is the Hamiltonian fundamental states and $V(\xi, r)$ is the interaction potential that determine as;

$$V(\xi, r) = V_N(\xi, r) + V_C(\xi, r).$$

The path of Rutherford transmits on the reaction energy, E, and the momentum, l. Classically, the potential can be solved as;

$$V(r) = \langle \psi_0 | V(r, \xi) | \psi_0 \rangle,$$

where Ψ_0 refers to the bounded state of the projectile. Therefore, time dependence Schrödinger equation have been satisfied inn both ξ-space $V_l(\xi, t) = V(r_{l(t)}, \xi)$ and Hamiltonian for intrinsic eigenstates $|\psi_{\gamma}\rangle$ [26, 27],

$$h|\psi_{\gamma}\rangle = \varepsilon|\psi_{\gamma}\rangle. \tag{10}$$

The wavefunction expansion as a function of the intrinsic ground sate is,

$$\psi(\xi, t) = \sum a_{\gamma}(l, t)\psi_{\gamma}(\xi)e^{-i\varepsilon_{\gamma}t/\hbar}. \tag{11}$$

Then the AW equation can be written as;

$$i\hbar \, \dot{a}_{\gamma}(l, t) = \sum_{\epsilon} \langle \psi_{\gamma} | V(\xi, t) | \psi_{\gamma} \rangle e^{i(\varepsilon_{\gamma} - \varepsilon_{\epsilon})t/\hbar} \gamma\epsilon(l, t). \tag{12}$$

The AW equations can be computed by the assumption of the ground state at initial conditions $a_{\gamma}(l, t \to -\infty) = \delta_{\gamma 0}$. The final population of γ-channel final population of the collision is $P_{fus}^{\gamma}(l, E) = |a_{\gamma}(l, t \to -\infty)|^2$, where l is the angular momentum [17].

2.2. The Coupled Channel Description

The dynamics of the projectile-target can be described by using $\vec{r}$ and ξ in the projectile intrinsic Hamiltonian $H_0(\xi)$ and the interaction of the projectile-target $V(\vec{r}, \xi)$ as; [28],

$$H = H_0(\xi) + V(\text{r}, \xi). \tag{13}$$

The eigenstates of $H_0(\xi)$ is [28],

$$H_0|\varphi_\beta\rangle = \varepsilon_\beta|\varphi_\beta\rangle, \tag{14}$$

ε_β is the internal motion energy.

There are two steps to consider the AW method. First, the evolution of time of the variable $\vec{r}$ has been considered classically. The energy E, and the momentum $\hbar\ell$ are the two effected parameters on the path with $V(\vec{r}) = \langle\varphi_0|V(\vec{r}, \xi)|\varphi_0\rangle$, where $|\varphi_0\rangle$ represents the ground level. The coupling will be a time dependence and $V_\ell(\xi, t) \equiv V(\vec{r}_\ell(t), \xi)$. Second, the quantum mechanical time-dependent problem has been used to treat the dynamics in the intrinsic apace. Throw expanding the wavefunction as [29],

$$\psi(\xi, t) = \sum_\beta a_\beta(\ell, t)\varphi_\beta(\xi)e^{-i\varepsilon_\beta t/\hbar}, \tag{15}$$

the AW equations can be evaluated by substituting the above expansion into Schrodinger equation, we get [32],

$$i\hbar\dot{a}_\beta(\ell, t) = \sum_\alpha a_\gamma(\ell, t)\langle\varphi_\beta|V_\ell(\xi, t)|\varphi_\beta\rangle e^{-i(\varepsilon_\beta - \varepsilon_\gamma)t/\hbar}. \tag{16}$$

Under the initial conditions at the ground state the solution of the coupled differential equations can to be obtained by assuming $a_\beta(\ell, t \to -\infty) = \delta_{\beta 0}$, at $(t \to -\infty)$. The final population is $P_\ell^{(\beta)} = \left|a_\beta(\ell, t \to +\infty)\right|^2$, where ℓ is the angular momentum at β channel. the integration of the cross section gives [29,30],

$$\sigma_\beta = \frac{\pi}{k^2}\sum_\ell(2\ell + 1)P_\ell^{(\beta)}. \tag{17}$$

For a simple determination of the fusion reaction cross section, the whole contribution channels can be assumed to be bound to zero spin. Using the expansion of the wave function for all contributions, leads to [18],

$$\sigma_F = \sum_\beta\left[\frac{\pi}{k^2}\sum_\ell(2\ell + 1)P_\ell^F(\beta)\right], \tag{18}$$

with,

$$P_\ell^F(\beta) = \frac{4k}{E}\int W_\beta^F(r)\left|u_{\beta\ell}(k_\beta, r)\right|^2 dr. \tag{19}$$

Where W_β^F is the imaginary part of the optical potential in the channel β and $u_{\beta\ell}(k_\beta, r)$ its ℓth-partial wavefunction. The approximated formula can be adopted to find the cross section with the help full of AW, as [28],

$$P_\ell^F(\beta) \simeq \overline{P}_\ell^{(\beta)} T_\ell^{(\beta)}(E_\beta). \tag{20}$$

above, $\overline{P}_\ell^{(\beta)}$ represents the probability of β -channel for the system to be at classical trajectory, and $T_\ell^{(\beta)}(E_\beta)$ is the probability for the particle at $E_\beta = E - \varepsilon_\beta$ and reduced mass $\mu = M_P M_T/(M_P + M_T)$, referring to the masses of the projectile and target by M_P, M_T, respectively, [28].

By using loosely bound projectiles, the CF for some systems will be studied. For simplicity, the projectile ground state is considered to be the only bound one in which the breakup reaction achieved in two parts, F$_1$ and F$_2$. therefore, it will be referred to the ground and breakup states by the labels $\beta = 0$ and $\beta \neq 0$, respectively. If the sequential contribution has been neglected, the CF can only contribute from the elastic channel. So, σ_{CF} is determined as,

$$\sigma_{CF} = \frac{\pi}{k^2}\sum_\ell(2\ell + 1)P_\ell^{Surv}T_\ell^{(0)}(E). \tag{21}$$

P_ℓ^{Surv} is the survival probability, which is given by; [18].

$$P_\ell^{Surv} \equiv \overline{P}_\ell^{(0)} = |a_0(\ell, t_{ca})|^2. \tag{22}$$

2.3. Quantum Mechanical Approximation

The relative motion between the colliding nuclei in addition to the nuclear intrinsic degrees of freedom need to be studied quantum mechanically by assuming $\Psi(\mathbf{r}, \xi)$ to be the entire wave function for the reaction with r represents the separation vector of the projectile and target while ξ refers to their intrinsic coordinates set. By the Hamiltonian, the reaction dynamics can be determined as [18],

$$H = H_0 + T + U(23).$$

In which H_0 represents the inherent Hamiltonian, T is the operator of the energy associated with the collide nuclei movement which given as $T \equiv -\hbar^2 \boldsymbol{\nabla}^2/2\mu$, and the potential of the interaction $U \equiv U(\mathbf{r}, \xi)$. an intrinsic Hamiltonian with eigenstates $|\alpha\rangle$ can satisfy the Schrödinger equation as [13],

$$(e_\eta - H_0)|\alpha\rangle = 0. \tag{24}$$

With

$$\langle \alpha'|\alpha\rangle = \int d\xi \, \varphi_{\alpha'}^*(\xi) \, \varphi_\alpha(\xi) = \delta_{\eta\eta'}, \tag{25}$$

where the wave function $\varphi_\alpha(\xi) \left(\varphi_{\alpha'}(\xi) \right)$ is corresponding to $|\alpha\rangle$ $(|\alpha\rangle)$ state in the ξ- space. The potential represented as,

$$U = U' + U'', \tag{26}$$

where U' is the channel space diagonal, such that [13],

$$U(\mathrm{r}) = \int d\xi \, |\varphi_\alpha(\xi)|^2 \, U'(\mathrm{r}, \xi), \tag{27}$$

$$U''_{\alpha,\alpha'}(\mathrm{r}) = \int d\xi \, \varphi_{\alpha'}^*(\xi) \, U''(\mathrm{r}, \xi) \, \varphi_\alpha(\xi). \tag{28}$$

The potential U' is not random for the diagonal in channel space. It is appropriate to take U' in the case of U'' is not diagonal and $U'' = U - U'$ with [13],

$$U''_{\alpha,\alpha'}(\mathbf{r}) = \int d\xi \, \varphi_{\alpha'}^*(\xi) \, U''(\mathbf{r}, \xi) \, \varphi_\alpha(\xi) - \delta_{\alpha\alpha'} \, U'_\alpha(\mathbf{r}), \tag{29}$$

from the Schrödinger equation, the equation of the coupling is,

$$(E - H) \, |\Psi_\alpha(\alpha_0 \, \mathbf{k}_0)\rangle = 0, \tag{30}$$

and the expansion,

$$|\Psi_\alpha(\alpha_0 \, \mathbf{k}_0)\rangle = \sum_\alpha |\psi_\alpha(\alpha_0 \, \mathbf{k}_0)\rangle \, |\alpha\rangle, \tag{31}$$

where $|\Psi(\alpha_0 \, \mathbf{k}_0)\rangle$ represents the collision initiating in channel α_0, $\mathbf{k}_0$ is the wave vector, the energy scale was chosen to be $e_{\alpha_0} = 0$. The Schrödinger equation solution components according to the off-diagonal part of the reaction are $|\Psi_\alpha(\alpha_0 \, \mathbf{k}_0)\rangle$ for $\alpha = \alpha_0$ and $\alpha \neq \alpha_0$. The Hamiltonian written as [13],

$$H = H_0 + H' + U''. \tag{32}$$

We can get the coupled channel equations from Eqs. (24), (25) and (23) as, [13],

$$(E_\alpha - H'_\alpha)|\psi_\alpha(\alpha_0 \, \mathbf{k}_0)\rangle = \sum_{\beta'} U''_{\alpha,\alpha'}(\mathbf{r}) \, |\psi_{\alpha'}(\alpha_0 \, \mathbf{k}_0)\rangle. \tag{33}$$

With using $|\psi_\alpha(\alpha_0 \, \mathbf{k}_0)\rangle \longrightarrow \psi_\alpha(\mathbf{r})$ in Eq. (25), we get,

$$U'_\alpha = V_\alpha + iW_\alpha. \tag{34}$$

The imaginary part W_α refers to the flux gain by the other channels from channel α. The non-Hermitian nature of H leads to break down of the continuity equation, while for the Hermitian U''_α in the coupled channel interaction, the continuity equation has the form [30].

$$\boldsymbol{\nabla} \cdot \sum_\alpha \mathbf{J}_\alpha = \frac{2}{\hbar} \sum_\alpha W_\alpha(\mathbf{r}) \, |\psi_\alpha(\mathbf{r})|^2 \neq 0. \tag{35}$$

$\mathbf{J}_\alpha$ represents the probability density. By taking the integration of Eq. (39) in spherical region covering the interaction area and with the helpful of σ_α definition, we get [22],

$$\sigma_\alpha = \frac{k}{E} \sum_\alpha \langle \psi_\alpha | W_\alpha | \psi_\alpha \rangle, \tag{36}$$

the potential absorption is given as;

$$W_\alpha = W_\alpha^D + W_\alpha^F, \tag{37}$$

where W_α^D refers to the lost flux and W_α^F refers to the fusion absorption in channel α, the total cross section represented as [22],

$$\sigma_F = \frac{k}{E} \sum_\alpha \langle \psi_\alpha | W_\alpha^F | \psi_\alpha \rangle. \tag{38}$$

3. FUSION BARRIER DISTRIBUTION

The ability of the wave to cross a barrier is influenced by the fusion due to the opposite nuclear and Coulomb forces. One of the most important factors that should be taken into account is the fusion barrier distribution D_{fus} that can be divided into several to describe the coupling effect as [13, 18],

$$D_{fus}(E) = \frac{d^2 F(E)}{dE^2}. \tag{39}$$

$F(E)$ in the above equation is given by;

$$F(E) = E\sigma_{fus}(E). \tag{40}$$

It is very important to understand the fusion reaction through collecting information on the collision coupling channels from the distribution of the fusion barrier, the most important progress of that understanding can be achieved from the experimental data of the reaction. From the above equation we have numerical uncertainties that appears from the barrier distribution data extraction [28, 29].

$$D_{fus}(E) \approx \frac{F(E+\Delta E)+F(E-\Delta E)-2F(E)}{\Delta E^2}, \tag{41}$$

where ΔE is the energy value between the measured total fusion reaction cross sections. There is a statistical error associated to the fusion barrier distribution that can be determined from Eqn. 24, as [30],

$$\delta D_{fus}^{stat}(E) \approx \frac{\sqrt{[\delta F(E+\Delta E)]^2+[\delta F(E-\Delta E)]^2+4[\delta F(E)]^2}}{(\Delta E)^2}, \tag{42}$$

where $\delta F(E)$ refers to the confidence ($E\sigma_f$) product at a certain energy of the reaction. The uncertainty can be given as [18],

$$\delta D_{fus}^{stat}(E) \approx \frac{\sqrt{6}\delta F(E)}{(\Delta E)^2} \tag{43}$$

4. RESULT AND DISCUSSION

The effect of the breakup channel on fusion reaction have been studied by adopting the semi-classical theory performed using code SCF and the coupled channel with continuum discretized (CCCD) conducted by the code CC to obtain the fusion cross section (σ_{fus}) and the fusion barrier distribution (D_{fus}) for the systems $^{12}C + ^{48}Ti$, $^{16}O + ^{63}Cu$, $^{35}Cl + ^{25}Mg$ and $^{35}Cl + ^{27}Al$. The WS potential parameters are tabularized in Table 1.

Table 1. The WS potential parameters for the studied systems

| Systems | Real parts | | | imaginary parts | | | L_{min} | L_{max} | V_b (MeV) |
	V_0 (MeV)	r_0 (fm)	a_0 (fm)	W_0 (MeV)	r_i (fm)	a_i (fm)			
$^{12}C + ^{48}Ti$	-33.9	0.99	0.52	-10.5	0.923	0.777	0	21	24.68
$^{16}O + ^{63}Cu$	-91.9	1	0.9	-27.6	0.931	0.769	0	39	32.72
$^{35}Cl + ^{25}Mg$	-100	1	0.8	-29.6	0.935	0.765	0	45	30.4
$^{35}Cl + ^{27}Al$	-63.8	1.18	0.74	-18.8	0.937	0.763	0	44	30.7

4.1 $^{12}C + ^{48}Ti$ System

The obtained σ_{fus} and D_{fus} for $^{12}C + ^{48}Ti$ are drown in Figure 1 with its labels (a) and (b), respectively.
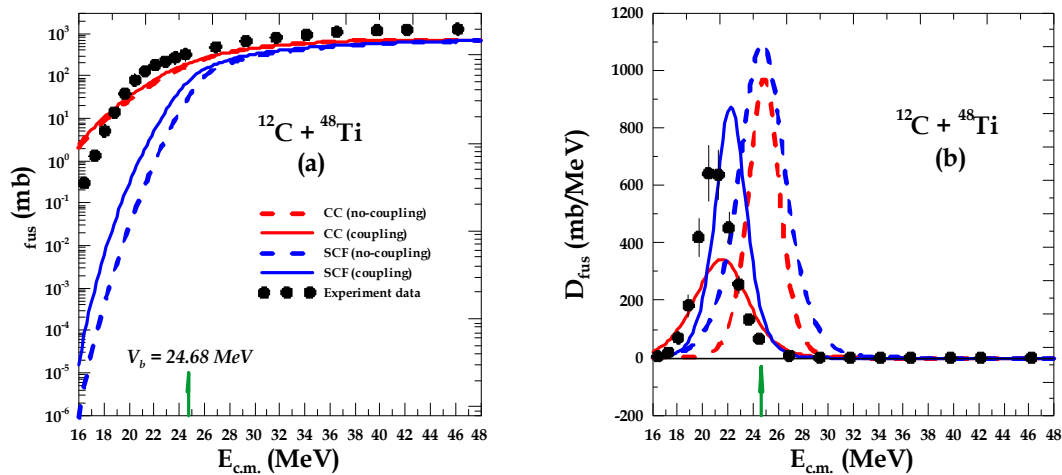
Figure 1. The semiclassical calculations with the blue colour and quantum mechanical calculations with the red colour for both σ_{fus} and D_{fus} in panels (a) and (b) respectively for the system $^{12}C + ^{48}Ti$

The semiclassical calculations are represented in blue colour curves, while quantum mechanical calculations are represented in red colour curves. The solid and dashed curves represent the calculations with and without the channel coupling respectively. Figure 1 show that the best obtained calculations for both σ_{fus} and D_{fus} under and above the Coulomb barrier V_b are those including the channel coupling in the quantum mechanical calculations.

4.2 $^{16}O+^{63}Cu$ System

The calculations for σ_{fus} are more accurate for those treated using the similclassical treatment with channel coupling as shown in panel (a) of Figure 2, while the best calculations for D_{fus} are those treated using the quantum mechanical treatment with channel coupling as shown in panel (b) of Figure 2.

Figure 2. The semiclassical and quantum mechanical calculations for both σ_{fus} and D_{fus}
in panels (a) and (b) respectively for the system $^{16}O+^{63}Cu$

4.3 $^{35}Cl+^{25}Mg$ System

The calculations for σ_{fus} are in more agreement with the experimental data for those treated using the semi-classical approach with channel coupling as shown in panel (a) of figure 3, while the best D_{fus} calculations are those treated using the channel coupling in quantum mechanical treatment as shown in panel (b) of the figure.

Figure 3. The semiclassical and quantum mechanical calculations for both σ_{fus} and D_{fus}
in panels (a) and (b) respectively for the system $^{35}Cl+^{25}Mg$

4.4 $^{35}Cl+^{27}Al$ System

Panel (a) in figure 4 show in panel (a) that the best obtained calculations for σ_{fus} under and above the Coulomb barrier V_b are those calculated using semi-classical treatment with effect of coupled channel included, while the panel (b) show that the best calculations for D_{fus} are those obtained using the quantum mechanical treatment with the effect of channel coupling.
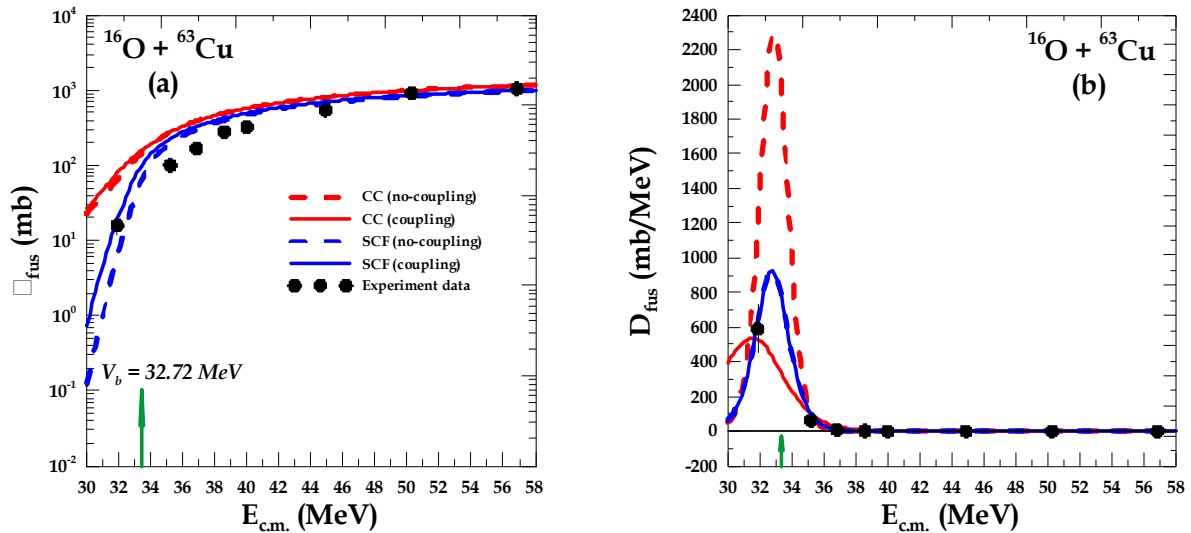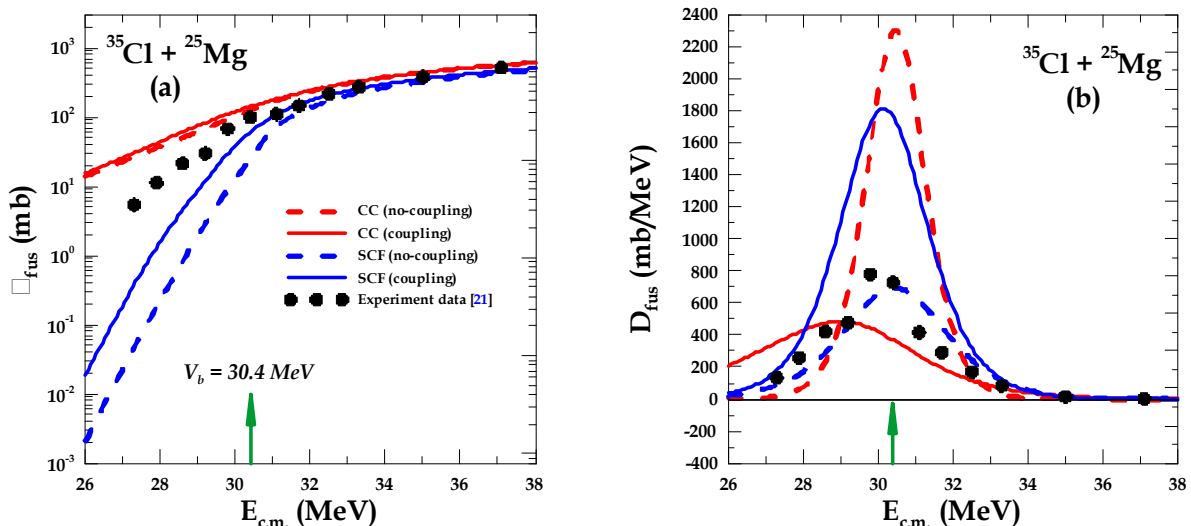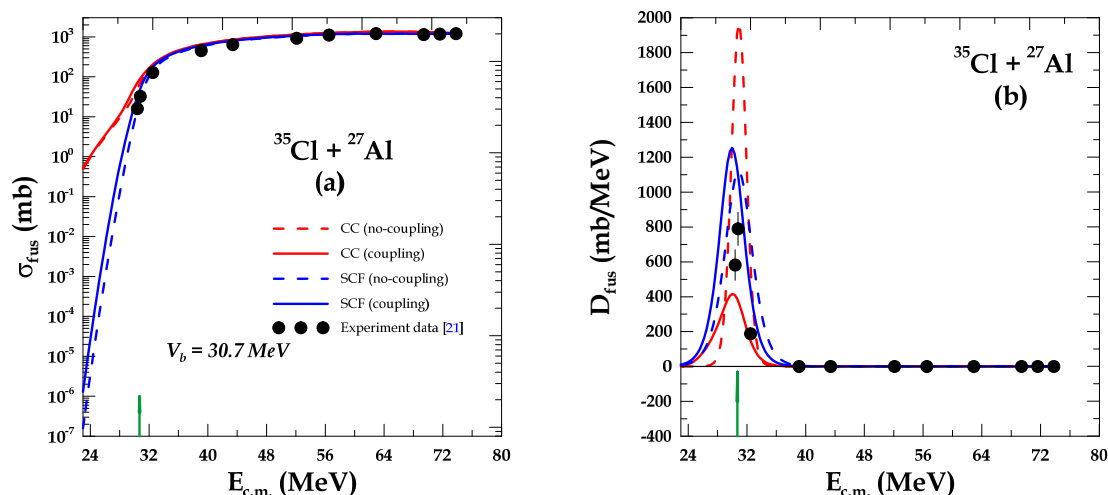
Figure 4. The semiclassical and quantum mechanical calculations for both σ_{fus} and D_{fus}
in panels (a) and (b) respectively for the system ^{35}Cl $+^{27}$Al

5. CONCLUSION

The results for all the studied systems show a remarkable influence for the channel coupling on the calculations of σ_{fus} and D_{fus} for ^{12}C $^{+48}$Ti, ^{16}O+^{63}Cu, ^{35}Cl+^{25}Mg and ^{35}Cl $+$ ^{27}Al systems, also we conclude that quantum mechanical treatment was proved to be successful for the total cross section determination while the fusion barrier distribution. The semi-classical calculations succeeded in describing the measured data especially above the Coulomb barrier V_b.

ORCID ID

Malik S. Mehemed, https://orcid.org/0009-0002-7892-2032

REFERENCES

[1]   R. Fereidonnejad, H. Sadeghi, and M. Ghambari, Astrophys. Space Sci. **363**(3), 50 (2018). https://doi.org/10.1007/s10509-018-3272-7
[2]   P.R.S. Gomes, J. Lubian, L.F. Canto, D.R. Otomar, D.R.M. Junior, P.N. de Faria, R. Linares, et al., "Reactions with Weakly Bound Nuclei, at near Barrier Energies, and the Breakup and Transfer influences on the Fusion and Elastic Scattering", Few-Body Syst. **57**, 165-176, (2016). https://doi.org/10.1007/s00601-015-1036-2
[3]   K.S. Choi, M.K. Cheoun, W.Y. So, K. Hagino, and K.S. Kim, "Coupled-channels analyses for ^{9,11}Li + ^{208}Pb fusion reactions with multi-neutron transfer couplings", Physical Letters B, **780**, 455–460, (2018). https://doi.org/10.1016/j.physletb.2018.03.049
[4]   L.F. Canto, P.R.S. Gomes, J. Lubian, L.C. Chamon, and E. Crema, Journal of Physics G: Nuclear and Particle Physics, **36**, 015109 (2009). https://doi.org/10.1016/j.physletb.2018.03.049
[5]   M. Veselský, "Nuclear reactions with heavy ion beams", Act. Phys. Slo. **63**, 1 (2013). https://doi.org/10.2478/apsrt-2013-0001
[6]   P.J. Siemens, "Liquid–gas phase transition in nuclear matter", Lett. Nat. **305**, 410 (1983). https://doi.org/10.1038/305410a0
[7]   L.C. Vaz, J.M. Alexander, and G.R. Satchler, "Fusion barriers, empirical and theoretical: Evidence for dynamic deformation in subbarrier fusion", Phys. Rep. **69**, 373-339 (1981). https://doi.org/10.1016/0370-1573(81)90094-6
[8]   G. Pollarolo, and A. Winther, "Fusion excitation functions and barrier distributions: A semiclassical approach", Phys. Rev. C, **62**, 054611 (2000). https://doi.org/10.1103/PhysRevC.62.054611
[9]   M. Beckerman, "Subbarrier fusion of atomic nuclei", Phys. Rep. **129**, 145 (1985). https://doi.org/10.1016/0370-1573(85)90058-4
[10] H. Esbensen, "Fusion and zero-point motions", Nucl. Phys. A, **352**, 147 (1981). https://doi.org/10.1016/0375-9474(81)90565-0
[11] A.B. Balantekin, and N. Takigawa, "Quantum tunnelling in nuclear fusion", Rev. Mod. Phys. **70**, 77 (1998). https://doi.org/10.1103/RevModPhys.70.77
[12] N. Keeley, R. Raabe, N. Alamanos, and J.L Sida, "Fusion and direct reactions of halo nuclei at energies around the Coulomb barrier", Prog. Part. Nucl. Phys. **59**, 579 (2007). https://doi.org/10.1016/j.ppnp.2007.02.002
[13] L.F. Canto, P.R.S. Gomes, R. Donangelo, and M.S. Hussein, "Fusion and breakup of weakly bound nuclei", Phys. Rep. 424, 1-111 (2006). https://doi.org/10.1016/j.physrep.2005.10.006
[14] K. Alder, and A. Winther, *Electromagnetic Excitations*, (North- Holland, Amsterdam, 1975).
[15] M.S. Mehemed, S.M. Obaid, and F.A. Majeed, "Coupled channels calculation of fusion reaction for selected medium systems," Int. J. Nucl. Energy Sci. Technol. **14**(2), 165-180 (2020). https://doi.org/10.1504/IJNEST.2020.112162
[16] P.R.S. Gomes, M.D. Rodríguez, G.V. Martí, I. Padron, and L.C. Chamon, "Effect of the breakup on the fusion and elastic scattering of weakly bound projectiles on ^{64}Zn", Phys. Rev. C, **71**, 034608 (2005). https://doi.org/10.1103/PhysRevC.71.034608
[17] L.F. Canto, P.R.S. Gomes, R. Donangelo, and M.S. Hussein, "Recent developments in fusion and direct reactions with weakly bound nuclei", Phys. Rep. **596**, 1-86 (2015). https://doi.org/10.1016/j.physrep.2015.08.001
[18] C.A. Bertulani, and L.F. Canto, "Semiclassical calculation of Coulomb break-up of weakly-bound nuclei", Nucl. Phys. A, **539**, 163-176 (1992). https://doi.org/10.1016/0375-9474(92)90240-K
[19] P. Gomes, T. Penna, E. Chagas, R.L. Neto, J. Acquadro, P. Pascholati, E. Crema, et al., "Fusion of ^{59}Co with light projectiles at near barrier energies", Nucl. Phys. A, **534**, 429 (1991). https://doi.org/10.1016/0375-9474(91)90510-D
[20] D.J. Griffiths, and D.F. Schroeter, *Introduction to quantum mechanics*, (University Printing House, Cambridge, United Kingdom, 2018). https://doi.org/10.1017/9781316995433

[21] M.S. Hussein, M.P. Pato, L.F. Canto, and R. Donangelo, "Real part of the polarization potential for [11]Li-induced fusion reactions", Phys.Rev. C, **47**, 2398-2400 (1992). https://doi.org/10.1103/physrevc.47.2398

[22] W.H.Z. Cárdenas, L.F. Canto, R. Donangelo, M.S. Hussein, J. Lubian, and A. Romanelli, "Approximations in fusion and breakup reactions induced by radioactive beams", Nucl. Phys. A, **703**, 633-648, (2002). https://doi.org/10.1016/S0375-9474(01)01672-4

[23] F.M. Hussain, F.A. Majeed, and Y.A. Abdul-Hussien, "Description of coupled-channel in Semiclassical treatment of heavy ion fusion reactions", IOP Conference Series: Materials Science and Engineering, **571**, 12113, (2019). https://doi.org/10.1088/1757-899X/571/1/012113

[24] F.A. Majeed, F.M. Hussain, and Y.A. Abdul-Hussien, "Enhanced calculations of fusion barrier distribution for heavy-ion fusion reactions using Wong formula", Int. J. Nucl. Energy Sci. Technol. **13**, 226-267, (2019). http://dx.doi.org/10.1504/IJNEST.2019.103237

[25] F.M. Hussain, F.A. Majeed, and Y.A. Abdul-Hussien, "Coupling channels mechanism of complete fusion reactions in some light stable nuclei", AIP Conference Proceedings, **2144**, 30003 (2019). https://doi.org/10.1063/1.5123073

[26] A.A. Ibraheem, and A. Bonaccors, "Coulomb breakup effects on the optical potentials of weakly bound nuclei", Nucl. Phys. A, **748**, 414-432 (2005). https://doi.org/10.1016/j.nuclphysa.2004.12.036

[27] J.F. Liang, and C. Signorini, "Fusion induced by radioactive ion beams", Int. J. Mod. Phys. E, **14**, 1121-1150 (2005). https://doi.org/10.1142/S021830130500382X

[28] M. Abramowitz, and I. Stegun, editors, *Handbook of Mathematical Functions*, (US Gov. Printing House, Washington, 1972).

[29] N. Rowley, G.R. Satchler, and P.H. Stelson, "On the "distribution of barriers" interpretation of heavy-ion fusion", Phys. Lett. B, **254**, 25 (1991). https://doi.org/10.1016/0370-2693(91)90389-8

[30] A.J. Najim, F.A. Majeed, and K.H. Al-Attiyah, "Improved calculation of fusion barrier distribution", IOP Conference Series: Materials Science and Engineering, **571**, 012124 (2019). http://dx.doi.org/10.1088/1757-899X/571/1/012124

ДОСЛІДЖЕННЯ РЕАКЦІЙ ЗЛІТТЯ ЛЕГКИХ ЯДЕР ІЗ ЛЕГКИМИ І СЕРЕДНІМИ ЯДРАМИ
Малік С. Мехемед

Управління освіти Вавілон, Міністерство освіти, Бабіль, Ірак

Для розрахунку повного перерізу σ_{fus} та розподілу бар'єру синтезу D_{fus} для систем $^{12}C + ^{48}Ti$, $^{16}O + ^{63}Cu$, $^{35}Cl + ^{25}Mg$ і $^{35}Cl + ^{27}Al$ були використані реакції синтезу та розпаду деяких легких ядер на легких та середніх мішенях з використанням напівкласичного та повного квантово-механічного підходів. Було розглянуто зв'язок між вкладом каналу від пружних каналів та каналів розпаду, щоб показати їх важливість у розрахунках. Результати порівнюються з виміряними даними і показують розумний збіг, також показано, що зв'язок, що розглядається, дуже важливий, особливо нижче кулонівського бар'єру V_b.

Ключові слова: *пов'язані канали; переріз реакцій синтезу; розподіл бар'єру синтезу*

CZTS THIN FILMS GROWN BY SULFURIZATION OF ELECTRODEPOSITED METALLIC PRECURSORS: THE EFFECT OF INCREASING TIN CONTENT OF THE METALLIC PRECURSORS ON THE STRUCTURE, MORPHOLOGY AND OPTICAL PROPERTIES OF THE THIN FILMS†

E.A. Botchway, ⓘFrancis Kofi Ampong, ⓘIsaac Nkrumah*, D.B. Puzer, ⓘRobert Kwame Nkum, Francis Boakye

Department of Physics, Kwame Nkrumah University of Science and Technology, Kumasi, Ghana
*Corresponding Author e-mail: inkrumah.sci@knust.edu.gh
Received April 2, 2023; revised April 26, 2023; accepted May 4, 2023

A study has been carried out to investigate the influence of the amount of Sn in the precursor solution, on some physical properties of CZTS films grown by sulfurization of electrodeposited metallic precursors. The growth of the CZTS samples was achieved by sequential electrodepositon of constituent metallic layers on ITO glass substrates using a 3-electrode electrochemical cell with graphite as a counter electrode and Ag/AgCl as the reference electrode. The Sn-content in the metallic precursor was varied by varying the deposition time of Sn. The stacked elemental layer was then soft annealed in Argon at 350 °C, and subsequently sulfurized at 550° C to grow the CZTS thin films. The structure, morphology and optical properties were investigated. X-ray diffraction studies revealed that, irrespective of the Sn content all the films were polycrystalline and exhibited the Kesterite CZTS structure with preferred orientation along the (112) plane. However, there was an increase in the amount of peaks indexed to the undesirable secondary phases, as the Sn content in metallic precursor was increased. Optical absorption measurements revealed the existence of a direct transition with band gap values decreasing from 1.74 eV to 1.25 eV with increasing amounts of Sn. The lower value for the band gap was attributed to the presence of secondary phases formed in addition to the CZTS film. Morphology of the sulfurized films showed a compact and rocky texture with good coverage across the entire substrate. However, CZTS films with a higher Sn content appeared to have a molten metallic surface with deep cracks which could have adverse effects on the electrical properties of the film. EDAX analysis showed all the films were consistent with the formation of CZTS. It is evident from all the characterization techniques that increasing the Sn content of the stacked metallic precursors beyond stoichiometric amounts had an adverse effect on the structural and optical properties of CZTS films grown by this technique.
Keywords: *CZTS thin films; electrodeposition, sulfurization; characterization*
PACS: 81.15.-z, 68.55.-a, 78.20.-e

INTRODUCTION

New types of thin film solar cells made from earth-abundant, and environmentally benign materials with adequate physical properties such as energy band-gap, large absorption coefficient and p-type conductivity are needed in order to replace the current technology based on $CuInGaSe_2$ and CdTe absorber materials, which contain scarce and toxic elements. One material which has been largely explored because of its suitability as a solar cell absorber layer, is Cu_2ZnSnS_4 (CZTS). This material is one of the ideal candidates for the production of thin film solar cells at large scale due to the natural abundance of all the constituent elements [1, 2]. CZTS has a direct band gap of ~ 1.5 eV, a large absorption coefficient greater than 10^{-4} cm^{-1} and low thermal conductivity [3]. It is a p-type semiconductor that matches well with the solar spectrum, and it has achieved a benchmark power conversion efficiency of more than 10% [4].

The need for synthesis of new materials for industrial applications has resulted in a tremendous increase of innovative thin film processing technologies [5]. CZTS thin films, have been synthesized by various techniques. These include: Rf sputtering, co-evaporation, hybrid sputtering, photochemical deposition, sulfurization of electrochemically deposited metallic precursors among others. However, electrodeposition has emerged as one of the versatile and cost-effective growth technique of metal, metalloid and semiconductor materials [6, 7]. Production of thin film semiconductors for photovoltaics using electrodeposition gives several advantages when compared to other methods of deposition: the technique is simple and is carried out using low cost apparatus, low operating temperature, and economical due to its low material wastage. Depending on the electrical parameters such as electrode potential and current density, the thin film thickness can be controlled in a precise manner. Electrodeposition method has been used for the preparation of thin and thick films of metals, magnetic materials, super capacitive materials and chalcogenides [8].

Available literature indicates that the production of CZTS thin films by a two-step process involving the sulfurization of electrochemically deposited metallic precursors, has been reported as producing some of the best CZTS thin films. This has prompted several research groups to investigate various aspects needed to improve this synthesis route such as; techniques to address the volatility of certain elements, especially Sn at elevated temperatures [9, 10]. Others like Borate et al. [11], have examined the effect of deposition potential on the composition and morphology of CZTS thin films, whilst Mahjoubi et al. [12] reported on the influence of the concentration of Cu in the precursor solution, on some

properties of the films. Payno et al. [13] published an article on the effect of sulfurization temperature on a CZTS solar cell. These investigations are needed to determine the right synthesis conditions needed for optimum device performance. In spite of all these efforts, Sn loss always occurs during the sulfurization process [14], therefore, fabrication of high quality CZTS thin films is of great challenge [15]. Larramona et al. [16], have confirmed that controlling Sn losses in the annealing environment could improve the efficiency of CZTS solar cells, significantly and reproducibly.

In this paper, we report on the effect of increasing the amount of Sn in the precursor solution, on the structure, morphology and optical band gap of CZTS films grown by sulfurization of electrochemically deposited metallic precursors. The choice of electrode materials, was based on Botchway et al. [17]. To the best of our knowledge, such an investigation has rarely been sighted in literature.

METHODOLOGY
Substrate preparation

Indium-doped tin oxide (ITO) glass substrates were used. The substrates were cleaned by first dipping them into a beaker containing acetone and placed on an ultrasonic cleaner for a few minutes and then rinsed with deionized water. They were then transferred into a beaker containing ethanol and sonicated for another 5 minutes. After rinsing again with deionized water, the substrates were kept in dilute nitric acid for 5 minutes and rinsed with copious amounts of de-ionized water. After the cleaning process was complete, the substrates were left to dry in a desiccator

Preparation of the electrolyte solutions

Copper electrolyte was prepared by mixing together aqueous solutions of 0.24 M $CuSO_4.5H_2O$ (source of Cu^{2+} ions) and 1.36 M $C_6H_5Na_3O_7.2H_2O$ (complexant) in a 100 ml beaker. The pH of resulting solution was adjusted to 3.00 by the dropwise addition of 1.00 M $C_4H_6O_6$ (tartaric acid). An acidic medium was used because Cu^{2+} ions are thermodynamically more stable in acidic electrolytes than in an alkaline one [18].

The tin electrolyte was prepared by mixing together aqueous solutions of 0.55 M of $SnCl_2.2H_2O$ (source of Sn (II) ions) and 1.00 M $C_6H_{14}O_6$ in a 100 ml beaker. Sorbitol ($C_6H_{14}O_6$) serves as a complexing agent and improves stability of Sn (II) and also adhesion of Sn [19]. The pH of the resulting solution was adjusted to 12.16 by adding a few drops of 2.25 M NaOH. An alkaline Sn electrolyte was chosen, because for the stacking sequence adopted for the deposition, copper was to be deposited first followed by Sn, an acid Sn electrolyte will dissolve the Cu layer already deposited on the substrate [20]. Secondly NaOH also serves to stabilize Sn (II) and prevent it from oxidizing to Sn (IV) which forms colloids and precipitate [21].

Zinc electrolyte was prepared from an aqueous solution of 0.10 M of $ZnSO_4.7H_2O$ (source of Zn^{2+} ions), pH was adjusted to 6.26 by adding a few drops of 35 % ammonia solution. Aqueous ammonia, acts as a buffer to prevent large changes in pH at the electrode surface. Electrolyte volumes of ~75 ml ensured that concentration of metal cations was virtually constant during electrodeposition. All chemicals used were of Analytical reagent grade.

Electrodeposition of the metallic precursors

The deposition of the metallic precursors was carried out sequentially from different batch solutions in the order, Cu/Sn/Zn. This technique was used to deposit the metallic precursors because it is easier to control the composition of the CZTS film and secondly, the highest efficiency CZTS solar cells have been fabricated via the SEL approach [22].

Prior to electrodeposition of the metal precursors, an ER 466 EDAQ computerized Potentiostat system was used to perform cyclic voltammetry (CV) on the individual electrolyte solutions to determine deposition potentials for the metallic elements of interest. Electrodeposition of each metal layer was carried out at these predetermined potentials.

High quality films of Cu, Sn and Zn were then deposited at -0.6 V, -1.10 V and -1.30 vs Ag/AgCl respectively. All depositions were at room temperature (30 ± 2 °C).

The thickness of the stacked elemental layers was well controlled by controlling the deposition time to achieve the desired composition. Each deposited film was tested for adhesion by placing it in a steady flow of distilled water before the subsequent deposition. To produce films with the required stoichiometry, the electrodeposition time reached for Cu, Sn and Zn was 10, 10 and 15 min. These deposition times were employed to achieve an optimum component atom ratio of Cu:Sn:Zn = 2:1:1. Which is the right stoichiometric ratio for the CZTS films.

To vary the Sn-content in the metallic precursors, different samples (metallic stacks) were prepared with the deposition time of Sn controlled for 1, 5, 10 and 15 minutes respectively, keeping all other deposition parameters constant.

Table 1 shows how the thickness of the Sn layer varied with deposition time. The thicknesses were measured by the gravimetric technique explained in Mondal et al. [23].

Table 1. Variation of the thickness of the Sn layer with deposition time

Time/minutes	1	5	10	15
thickness/μm	1.243626	1.4020705	1.559188	1.863976

Table 1 confirms an increase in Sn content with deposition time. It should be mentioned that these figures only reflect the Sn content in the metallic precursors and not in the CZTS film formed after sulfurization. As mentioned earlier, Sn loss always occurs during the sulfurization process [14].

Post Deposition Treatment

The stacked metallic precursor were first soft annealed in argon at a temperature of ~ 350 °C to improve intermixing of the elements Cu-Sn-Zn and subsequently sulfurized at 550 °C to obtain the CZTS thin films. The techniques employed for the soft annealing and sulfurization process are as described by Botchway et al [17] and Puzer et al. [24].

Thin Film Characterization

All XRD data were obtained using a PANalytical Empyrean Series 2 powder X-ray diffractometer with a Cu-kα radiation (1.5406 Å) in the 2θ range 10 to 90. The machine was operated at 40 mA and 45 kV for phase analysis using the Bragg-Brentano geometry. Total analysis time per samples was around 35 minutes for a 2θ scan step of 0.06°. XRD data treatment and analysis were carried out using high score plus software packages. A Cecil CE7500 series double beam UV-Visible spectrometer operating in the wavelength range of 190 nm to 1100 nm, a step height of 0.3 nm and a scan rate of 5 nm per second was used for optical absorbance measurements on thin films. Scanning electron microscopy (SEM) images and energy dispersive X-ray (EDX) analyses were obtained using a Phenom instrument with nominal electron beam voltages of 15 kV respectively.

RESULTS AND DISCUSSION
X-Ray Diffraction Studies

The X-ray diffraction (XRD) patterns for various stages of the synthesis process, of the CZTS films deposited with the right stoichiometric ratios, are shown in Figure 1.
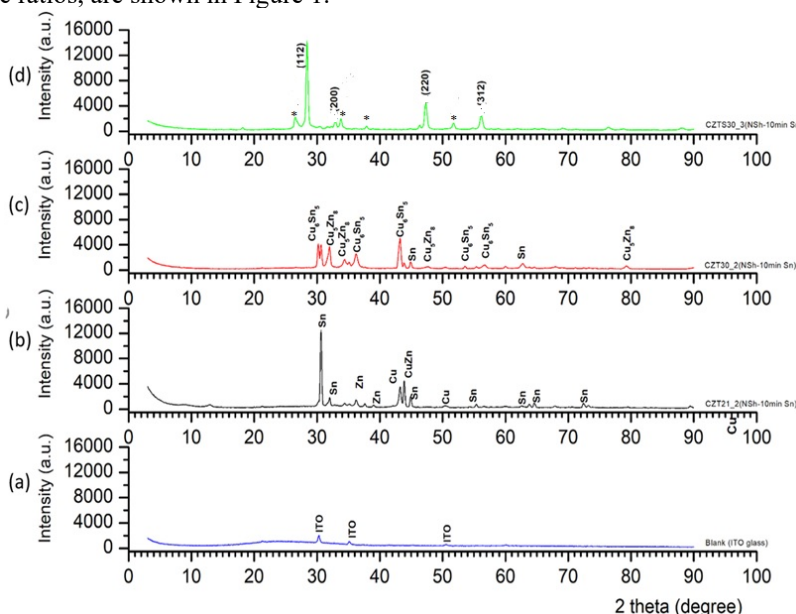
Figure 1. XRD pattern of (a) ITO glass substrate (b) as-deposited elemental stacks (c) metallic precursors, soft annealed at 350°C in Argon and (d) CZTS films formed after sulfurizing the metallic precursors at 550°C

Figure 1 shows the diffraction patterns of the film at various stages of the synthesis process for growing CZTS films with the right stoichiometry. The deposition time was 10 minutes for Cu and Sn, and 15 minutes for Zn.

Figure 1(b) is the diffractogram of the as-deposited stacked metallic layers. The assignments of peaks confirm the presence of Cu, Sn, and Zn. The peak at 2θ position 44 was indexed to the binary compound Cu_1Zn_1.

Figure 1 (c) shows the diffractogram after soft annealing the metallic precursors in Argon at 350 °C. Indexing the peaks revealed that at this stage the film was composed of the following binary compounds: Cu_5Zn_8 and Cu_6Sn_5. A few low intensity peaks were assigned to Sn.

The diffractogram in Figure 1 (d) confirms the formation of the kesterite CZTS phase after sulphurizing the films at 550°C. The prominent peaks observed at 2θ position 28.4446°, 32.8765°, 47.3409° and 56.1703° were indexed to reflections from the (112), (200), (220) and (312) planes of the kesterite structure Cu_2ZnSnS_4. A few impurity peaks labelled with asterisks are also observed in the diffractogram of Figure 1d. These impurity peaks are referenced to Cu_2S_1 (PDF card # 98-002-0560), Cu_2SnS_3 (PDF card # 00-027-0198) and SnS_2.

Figure 2 compares the diffraction patterns of the Kesterite CZTS thin films obtained after sulfurizing the electrodeposited metallic precursors containing different amounts of Sn. In other the precursor solutions used for these films do not contain right stoichiometric amount of Sn.

From Figure 2, it is evident that as the deposition time of Sn, and thus the amount of Sn in the metallic precursor is increased, the resulting CZTS film formed after sulfurization has an increasing number of peaks associated with impurities. These impurities, called secondary phases are due to the presence of compounds such as Cu_2S_1, Cu_2SnS_3 and SnS_2 which are formed in addition to the CZTS compound.
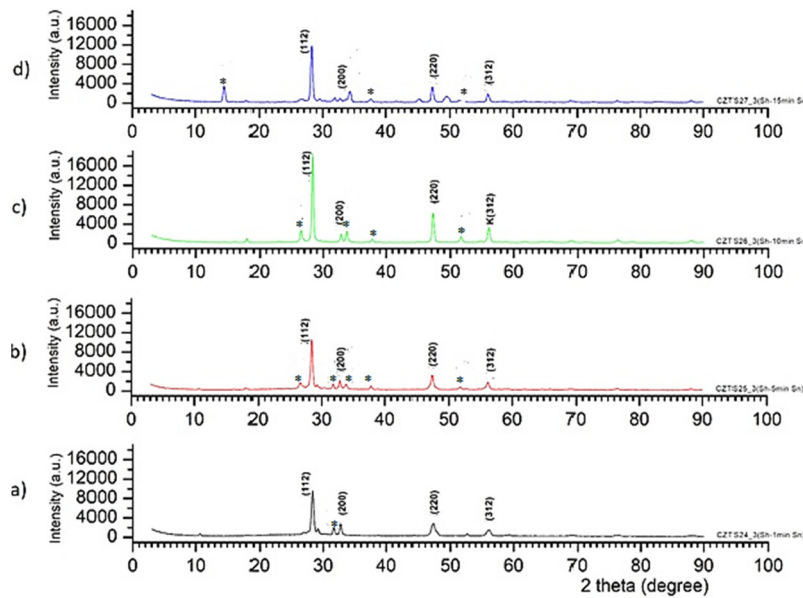
Figure 2. XRD patterns of the Kesterite CZTS obtained after sulfurizing the metallic precursors for the different deposition times of Sn: (a) 1 minute (b) 5 minutes (c) 10 minutes (d) 15 minutes

The formation of secondary phases, is due to the volatile nature of certain key elements such as Zn, and SnS under certain reaction conditions [9]. The loss of Sn through desorption of SnS from CZTS during annealing/sulfurization at elevated temperatures (400°C) is well documented by many researchers [10]. These have an adverse effect on some electrical, optical, and structural properties. From figure 2a, the precursor solution with the 1-minute deposition time for Sn, had the least number of impurities/secondary phases. A publication by Scragg *et al.* [25], offers some explanation for this observation. According to the authors, a stoichiometry of Zn/Sn =1 produces the best quality films. In this work, the conditions used, produced a very thin layer of Zn, thus, the one-minute deposition time of Sn might just be enough to create a stoichiometry close to Zn/Sn =1, thus producing the best films. However, this observation would have to be probed further. It is also important to note that, most of the impurities/secondary phases such as; cubic Cu_2SnS_3 and cubic ZnS have peak positions which are very similar to that of CZTS, due to similar crystal structure [21]. This makes it difficult to distinguish CZTS from these secondary phases in a diffractogram. However, some of the other secondary phases such as; Cu_2S and SnS can be identified due to the peak positions which are entirely different from CZTS.

Scanning electron microscopy

Figures 3 to 6 show the SEM images of the CZTS thin films grown at different deposition times of Sn. Figure 3 shows a non-uniform particle size with clearly defined large grains, formed from aggregation of small particles, spread non-uniformly among smaller grains on the surface of the substrate. The morphology is compact without any clear voids.

Figure 4 shows an increase in surface roughness with a larger number of grains with well-defined edges and shapes. This also shows a compact morphology without any clear voids.
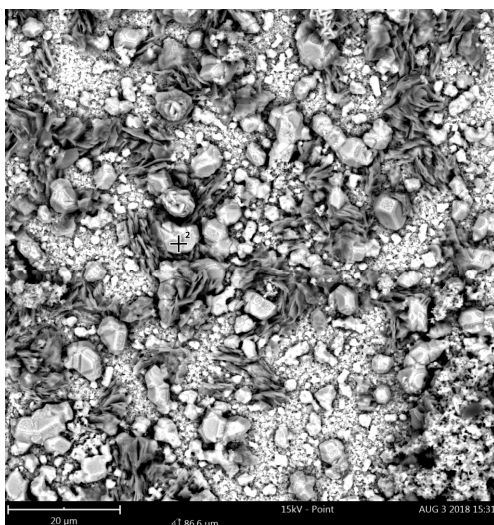
Figure 3. SEM image of CZTS thin film (deposition time of Sn is 1 minute)

Figure 4. SEM image of CZTS thin film (deposition time of Sn is 5 minute)

The film in Figure 5, appears compact with a relatively smoother texture and good coverage across the entire area of the substrate. Some areas look like a molten matrix composed of smaller grains. In Figure.6, the grains are no longer clearly defined and distinct. Instead, the surface appears to be disfigured with large sheets of a molten matrix which appears to have several cracks and voids. This type of morphology is not favorable for photovoltaic applications.
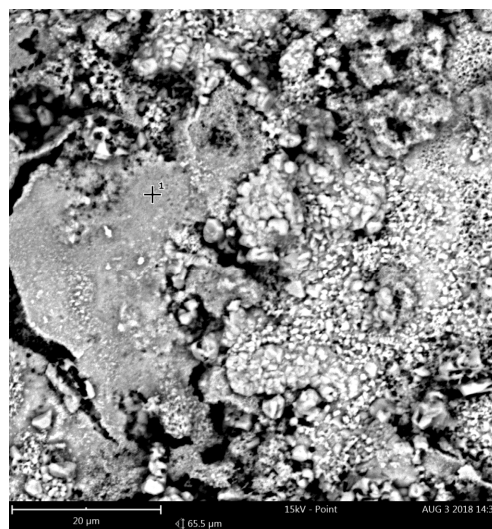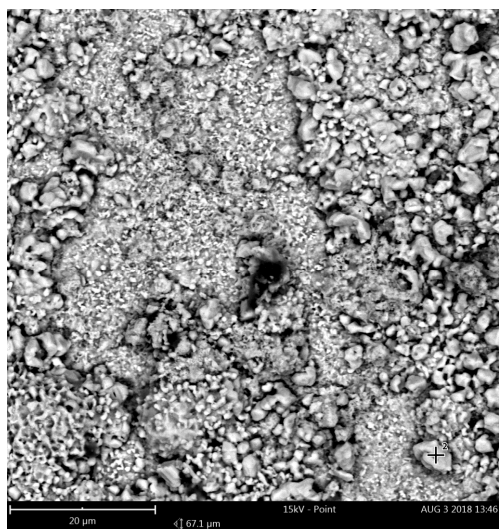
Figure 5. SEM image of CZTS thin film (deposition time of Sn is 10 minute)

Figure 6. SEM image of CZTS thin film (deposition time of Sn is 15 minute)

ENERGY DISPERSIVE X-RAY SPECTROSCOPY (EDAX)

The EDAX spectra of some of the CZTS films are shown in Figures 7 and 8.

Element Symbol	Atomic Conc.	Weight Conc.	Oxide Symbol	Stoich. wt Conc.
Zn	24.44	30.47	Zn	31.33
Sn	11.86	26.85	Sn	27.60
S	42.17	25.79	S	26.52
Cu	10.26	12.43	Cu	12.78
O	8.97	2.74		
K	2.31	1.72	K	1.77
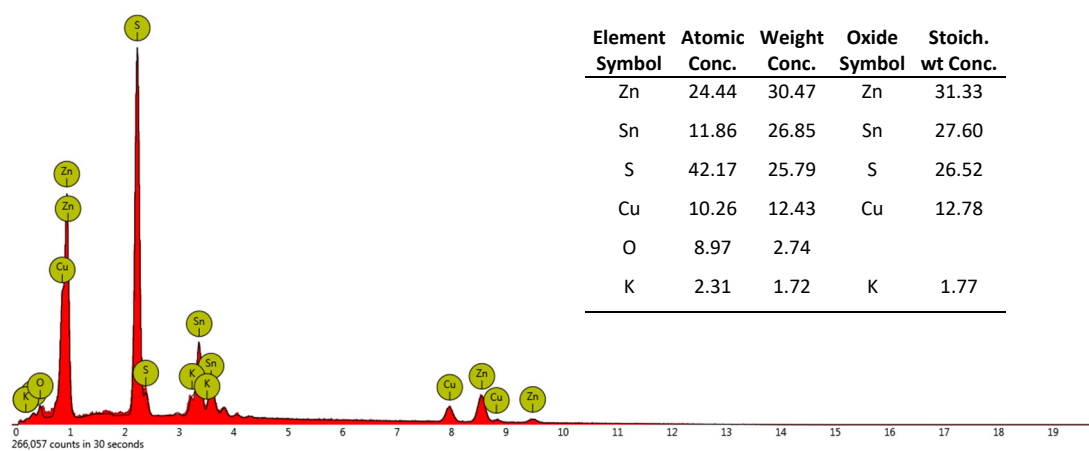
Figure 7. EDX spectrum of the CZTS thin film shown in Figure 3

Element Symbol	Atomic Conc.	Weight Conc.	Oxide Symbol	Stoich. wt Conc.
S	49.88	28.32	S	28.32
Sn	11.03	23.18	Sn	23.18
Zn	18.01	20.85	Zn	20.85
Cu	16.72	18.80	Cu	18.80
In	4.36	8.86	In	8.86
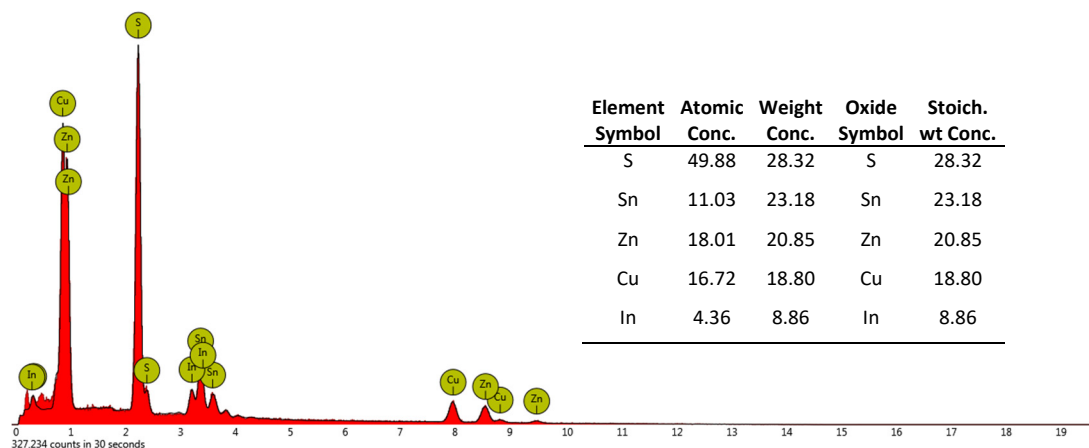
Figure 8. EDX spectrum of the CZTS thin film shown in Figure 5

Figures 7 and 8 show the EDAX spectrum and elemental composition of some of the CZTS thin films. The EDAX analyses of the films are consistent with the formation of CZTS. Other elements such as O, K, and In may emanate from the substrate.

Results of the optical absorption spectroscopy

The optical properties, like other properties of thin films, show profound sensitivity on the film microstructure. Any changes in the electronic structure of the material would be reflected in its optical behavior [26].
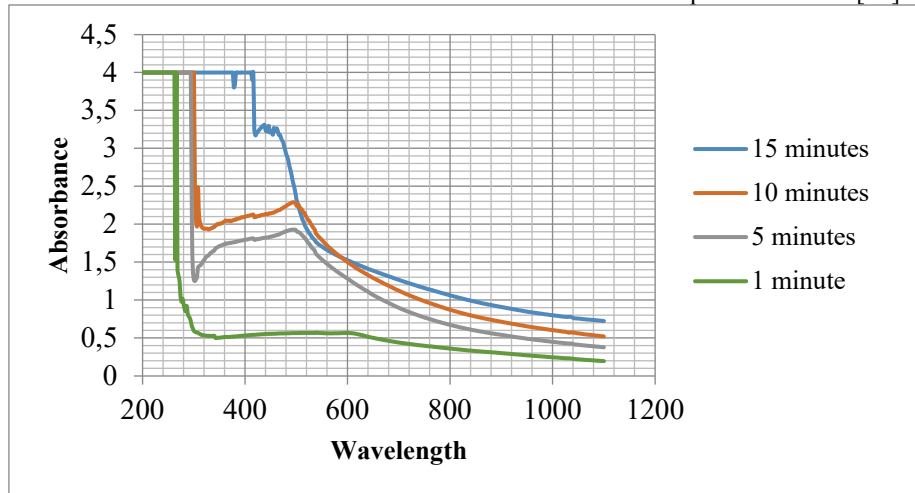
Figure 9. A plot of absorbance against wavelength for CZTS films prepared at different deposition times of Sn.

Figure 9 shows the absorbance for the CZTS samples prepared at different deposition times of Sn in the precursor solution. It can be observed that the absorbance increases with increasing deposition times of Sn. This behavior could be attributed to the formation of photon absorption sites caused by the presence of secondary phases. This view is supported by results from the XRD analysis which shows an increase in impurity peaks/secondary phases with increasing deposition time of Sn.

Determination of the optical band gap

The energy band gap and type of electron transition were determined by the Stern relationship [27, 28] which is given by the expression:

$$A = \frac{[k(h\nu - E_g)]^{n/2}}{h\nu}$$

where A is the absorbance, E_g is the band gap, ν is the frequency, h is the Planck's constant, k is a constant. The value of n is 1 and 4 for the direct transition and indirect transition respectively.

CuS, ZnS and SnS are all direct band gap materials. Thus, we assume that their mixed compositions would also have a direct band gap and hence, n is taken as 1. The energy band gap is obtained by plotting a line of best fit to the linear portion of the graph and extrapolating it to the point where it intersects the $h\nu$ axis as shown in Figures 10 and 11.
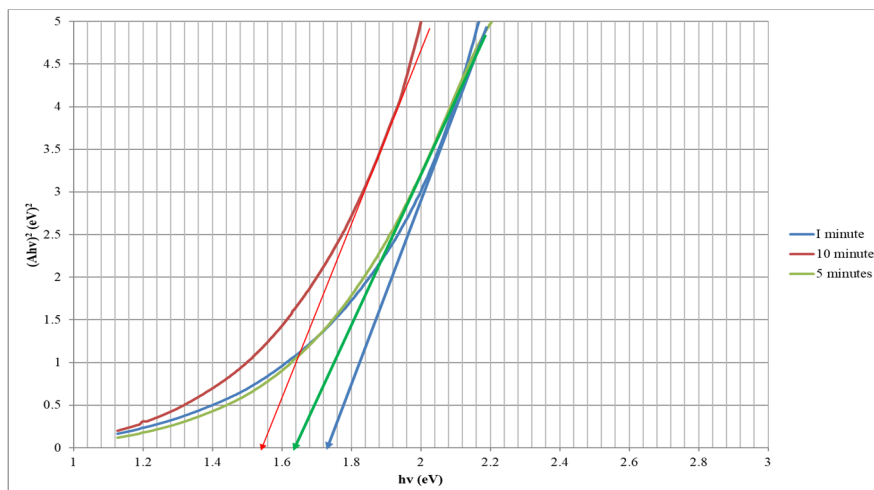
Figure 10. Plot of $(Ah\nu)^2$ versus $h\nu$ for the CZTS films grown with a 1, 5 and 10-minute deposition time of Sn

From Figures 10 and 11, the estimated band gaps are 1.74 eV, 1.62 eV, 1.54 eV and 1.25 eV for the 1, 5, 10- and 15-minutes deposition time of Sn. These values compare well with the values obtained by Khammar et al. [29]. The lower values for the higher deposition times may be attributed to the presence of secondary phases such as Cu_2S, SnS, and Cu_2SnS_3 formed in addition to the CZTS film.
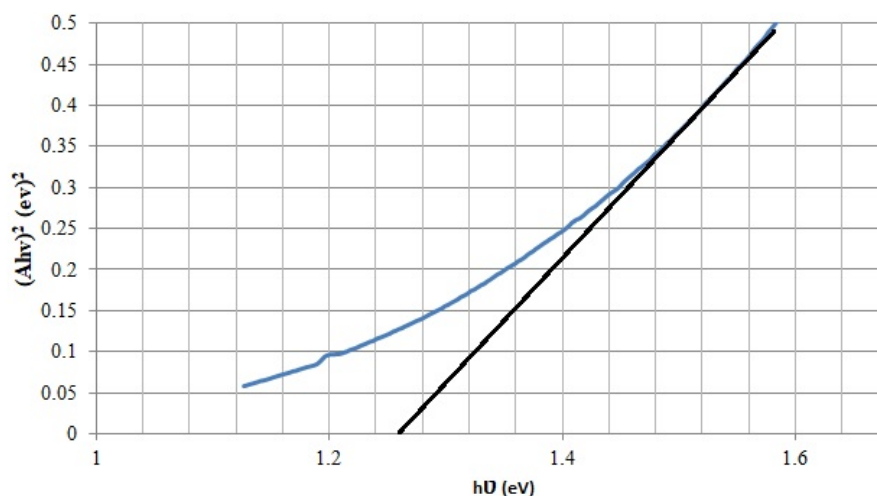
Figure 11. Plot of $(Ah\upsilon)^2$ versus $h\upsilon$ for the CZTS films grown with a 15-minute deposition time of Sn

CONCLUSION

The effect of increasing Sn-content on the structure and optical properties of CZTS films grown by sulfurization of electrodeposited metallic precursors, has been studied. X-ray diffraction measurements showed that the kesterite CZTS structure was not altered by increasing the Sn content in the metallic precursor, however, there was an increase in the number of impurity peaks which were indexed to the presence of compounds such as Cu_2S_1, Cu_2SnS_3 and SnS_2 which are formed in addition to the CZTS compound. Optical absorption measurements revealed an increase in absorbance due to the presence of secondary phases. All the films showed direct transition with an estimated band gap which decreased from 1.74 eV to 1.25 eV with increasing Sn content. The lower value for the band gap was attributed to the presence of secondary phases formed in addition to the CZTS film. Morphology of the sulfurized films showed a compact and rocky texture with good coverage across the entire substrate. However, films with a higher Sn content appeared to have a molten metallic surface with deep cracks after sulfurization, making it unfavorable for photovoltaic applications. EDAX analysis confirmed the formation of CZTS. In conclusion, results of all the characterization techniques indicate that although the synthesis technique used in this work produced kesterite CZTS films with good crystallinity and favorable optical properties, increasing the Sn content of the metallic precursors beyond stoichiometric amounts had an adverse effect on all the physical properties investigated.

ORCID IDs
Isaac Nkrumah, https://orcid.org/0000-0003-4030-7931; **Francis Kofi Ampong**, https://orcid.org/0000-0003-3562-8183
Robert Kwame Nkum, https://orcid.org/0000-0003-0404-760X

REFERENCES
[1] S.D. Sharma, K. Bayikadi, S. Raman, and S. Neeleshwar, Nanotechnology, **31**, (36), 365402 (2020). https://doi.org/10.1088/1361-6528/ab9393
[2] S. Prabhu, S.K. Pandey, and S. Chakrabarti, International Journal of Energy Research, **46**(11), 15300 (2022). https://doi.org/10.1002/er.8232
[3] K. Diwate, K. Mohite, M. Shinde, S. Rondiya, A. Pawbake, A. Date, H. Pathan, and S. Jadkar, Energy Procedia, **110**, 180 (2017). https://doi.org/10.1016/j.egypro.2017.03.125
[4] D.B. Mitzi, O. Gunawan, T.K. Todorov, K. Wang, and S. Guha, Solar Energy Materials and Solar Cells, **95**(6), 1421 (2011). https://doi.org/10.1016/j.solmat.2010.11.028
[5] S. Giraldo, Z. Jehl, M. Placidi, V. Izquierdo-Roca, A. Pérez-Rodríguez, and E. Saucedo, Advanced Materials, **32**, 1806692 (2019). https://doi.org/10.1002/adma.201806692
[6] C. Gougaud, D. Rai, S. Delbos, E. Chassaing, and D. Lincot, Journal of The Electrochemical Society, **160**(10), 485 (2013). https://doi.org/10.1149/2.105310jes
[7] I. Nkrumah, F.K. Ampong, A. Britwum, M. Paal, B. Kwakye-Awuah, R.K. Nkum, and F. Boakye, Chalcogenide Letters, **20**(3), 205 (2023). https://doi.org/10.15251/CL.2023.203.205
[8] S. Thanikaikarasan, T. Mahalingam, T. Ahamad, S. M. Alshehr, Journal of Saudi Chemical Society, **24**, 955 (2020). https://doi.org/10.1016/j.jscs.2020.10.003

[9]   N. Jahan, R. Matin, M.S. Bashar, M. Sultana, M. Rahaman, M.A. Gafur, M.A. Hakim, et al., Am. Int. J. Res. Sci. Technol. Eng. Math, **1**, 69 (2016). http://iasir.net/AIJRSTEMpapers/AIJRSTEM16-141.pdf

[10] A. Weber, R. Mainz, and H.W. Schock, Journal of Applied Physics, **107**(1), 013516 (2010). https://doi.org/10.1063/1.3273495

[11] H. Borate, A. Bhorde, A. Waghmare, S. Nair, P. Subhash, A. Punde, P. Shinde, et al., ES Materials & Manufacturing, **11**, 30 (2020). http://dx.doi.org/10.30919/esmm5f934

[12] S. Mahjoubi, N. Bitri, M. Abaab, and I. Ly, Materials Letters, **216**, 154 (2018). https://doi.org/10.1016/j.matlet.2018.01.004

[13] D. Payno, S. Kazim, M. Salado, and S. Ahmad, Solar Energy, **224**, 1136 (2021). https://doi.org/10.1016/j.solener.2021.06.038

[14] H. Zhang, M. Xie, S. Zhang, and Y. Xiang, Journal of Alloys and Compounds, **602**, 199 (2014). http://dx.doi.org/10.1016/j.jallcom.2014.03.014

[15] S. Siebentritt, and S. Schorr, Progress in Photovoltaics: Research and Applications, **20**(5), 512 (2012). https://doi.org/10.1002/pip.2156

[16] G. Larramona, S. Levcenko, S. Bourdais, A. Jacob, C. Choné, B. Delatouche, C. Moisan, et al., Advanced Energy Materials, **5**(24), 1501404 (2015). https://doi.org/10.1002/aenm.201501404

[17] E.A. Botchway, F.K. Ampong, I. Nkrumah, R.K. Nkum, and F. Boakye, Open Journal of Applied Sciences, **9**(9), 725 (2019). https://doi.org/10.4236/ojapps.2019.99059

[18] J.J. Scragg, T. Ericson, T. Kubart, M. Edoff, and C. Platzer-Bjorkman, Chemistry of Materials, **23**(20), 4625 (2011). https://doi.org/10.1021/cm202379s

[19] S. Chen, J. Tao, H. Tao, Y. Shen, L. Zhu, J. Jiang, X. Zeng, and T. Wang, Materials Technology, **30**(5), 306 (2015). https://doi.org/10.1179/1753555715Y.0000000007

[20] X. He, H. Shen, J. Pi, C. Zhang, and Y. Hao, Journal of Materials Science: Materials in Electronics, **24**(11), 4578 (2013). https://doi.org/10.1007/s10854-013-1445-2

[21] T. Hreid, Doctoral dissertation, Queensland University of Technology, 2016.

[22] F. Jiang, S. Ikeda, Z. Tang, T. Minemoto, W. Septina, T. Harada, and M. Matsumura, Research and Applications, **23**(12), 1884 (2015). https://doi.org/10.1002/pip.2638

[23] S. Mondal, S.R. Bhattacharyya, and P. Mitra, Bulletin of Materials Science, **36**, 223 (2013). https://doi.org/10.1007/s12034-013-0462-3

[24] D.B. Puzer, I. Nkrumah, F.K. Ampong, M. Paal, E.A. Botchway, R.K. Nkum, F. Boakye, Chalcogenide Letters, **18**(8), 481 (2021). https://chalcogen.ro/481_PuzerDB.pdf

[25] J.J. Scragg, P.J. Dale, L.M. Peter, G. Zoppi, and I. Forbes, Physica Status Solidi B, **245**(9), 1772 (2008). https://doi.org/10.1002/pssb.200879539

[26] O.V. Goncharova, and V.F. Gremenok, Semiconductors, **43**, 96 (2009). https://doi.org/10.1134/S1063782609010199

[27] M. Paal, I. Nkrumah, F.K. Ampong, D.U. Ngbiche, R.K. Nkum, and F. Boakye, Science Journal of University of Zakho, **8**(3), 97 (2020). https://doi.org/10.25271/sjuoz.2020.8.3.752

[28] C.K. Bandoh, I. Nkrumah, F.K. Ampong, R.K. Nkum, and F. Boakye, Chalcogenide Letters, **18**(2), 81 (2021). https://chalcogen.ro/81_BandohCK.pdf

[29] M. Khammar, F. Ynineb, S. Guitouni, Y. Bouznit, and N. Attaf, Applied Physics A, **126**(6), 398 (2020). https://doi.org/10.1007/s00339-020-03591-6

ТОНКІ ПЛІВКИ CZTS, ВИРОЩЕНІ ШЛЯХОМ СУЛЬФУРИЗАЦІЇ ЕЛЕКТРООСАДЖЕНИХ МЕТАЛЕВИХ ПРЕКУРСОРІВ: ВПЛИВ ПІДВИЩЕННЯ ВМІСТУ ОЛОВА В МЕТАЛЕВИХ ПРЕКУРСОРАХ НА СТРУКТУРУ, МОРФОЛОГІЮ ТА ОПТИЧНІ ВЛАСТИВОСТІ ТОНКИХ ПЛІВОК

Є.А. Ботчвей, Френсіс Кофі Ампонг, Ісаак Нкрума, Д.Б. Пузер, Роберт Кваме Нкум, Френсіс Боак'є

Факультет фізики, Університет науки і технологій Кваме Нкрума, Кумасі, Гана

Було проведено дослідження впливу кількості Sn у розчині прекурсора на деякі фізичні властивості плівок CZTS, вирощених шляхом сульфування електроосаджених металевих прекурсорів. Зростання зразків CZTS було досягнуто шляхом послідовного електроосадження складових металевих шарів на скляних підкладках ITO з використанням 3-електродної електрохімічної комірки з графітом як протиелектродом та Ag/AgCl як електродом порівняння. Вміст Sn в металевому прекурсорі змінювали шляхом зміни часу осадження Sn. Складений елементний шар потім м'яко відпалювали в аргоні при 350°C, а потім сульфірували при 550°C для вирощування тонких плівок CZTS. Досліджено структуру, морфологію та оптичні властивості. Дослідження рентгенівської дифракції показали, що незалежно від вмісту Sn усі плівки були полікристалічними та демонстрували структуру кестериту CZTS з переважною орієнтацією вздовж площини (112). Однак спостерігалося збільшення кількості піків, індексованих до небажаних вторинних фаз, оскільки вміст Sn у металевому попереднику був збільшений. Вимірювання оптичного поглинання показало наявність прямого переходу зі значеннями забороненої зони, що зменшуються від 1,74 eB до 1,25 eB зі збільшенням кількості Sn. Менше значення ширини забороненої зони пояснюється наявністю вторинних фаз, утворених на додаток до плівки CZTS. Морфологія сульфурованих плівок показала компактну та кам'янисту текстуру з хорошим покриттям по всій підкладці. Однак плівки CZTS з більш високим вмістом Sn мали розплавлену металеву поверхню з глибокими тріщинами, які могли мати негативний вплив на електричні властивості плівки. Аналіз EDAX показав, що всі плівки відповідають утворенню CZTS. З усіх методів визначення характеристик очевидно, що збільшення вмісту Sn у складених металевих прекурсорах понад стехіометричні кількості мало несприятливий вплив на структурні та оптичні властивості плівок CZTS, вирощених цією технікою.

Ключові слова: *тонкі плівки CZTS; електроосадження, сульфуризація; дослідження*

MAGNETO-THERMOELECTRIC COEFFICIENTS OF HEAVILY DOPED N-TYPE Mg₂Si MATERIAL[†]

Mulugeta Habte Gebru

Department of Physics, Arba Minch University, Arba Minch, Ethiopia
E-mail: mulugeta1970@gmail.com
Received March 27, 2023; revised April 26, 2023; accepted April 27, 2023

In contrast to parabolic band model typically used in understanding electronic properties in general, thermoelectric and magneto-thermoelectric in particular, this study confirms non-parabolic band model results in better understanding of Seebeck coefficient and Nernst coefficient in the presence of magnetic field for Mg₂Si. The magneto Seebeck coefficient was found significantly enhanced from its zero-field value for different electron concentrations in the range 0.6 - 12×10^{25}/m³ and at room temperature due to the magnetic field in the range 0.2 – 1 T for non-parabolic model compared to parabolic band model. The result for Nernst coefficient shows increasing trend as function of magnetic field except for certain electron concentrations for parabolic band model while it is decreasing with magnetic field on average for non-parabolic band model.

Keywords: *Magneto-Seebeck coefficient; Nernst coefficient; heavily doped semiconductor; magneto-thermoelectricity; magnesium Silicide*
PACS: 72.20. My

INTRODUCTION

According to [1] Mg₂Si have been investigated both by experimental and theoretical methods. By contrast, transport properties have never been determined so far using calculation methods so that the present study is among such few studies. The crystal structure data revealed that Mg₂Si has space group of Fm3m with Mg occupied sites in 8c (1/4,1/4,1/4) coordinates and Si occupied sites in 4a (0,0,0) coordinates [2].

In n-type Mg₂Si crystal doped with more than 6×10^{16}/cm³ or shallower donors' concentration, the donor band merges with the conduction band [3]. The effect of heavily doping on the electronics properties of semiconductors is important. There are a number of papers in the literature [4,5] which show bit of data on electrical properties of heavily doped semiconductors. Recently, considerable interest has been aroused in the properties of heavily doped semiconductors because of their use in diodes and thin solar cells [6,7]. Heavily doped semiconductor based thermoelectric devices as a single device have been widely utilized as non-contact temperature sensors, flow sensors, gas sensors, accelerometers, and power generators while array of them as infrared (IR) imaging devices and micro-spectrometers [8]. It can be used for CNT application [9] and Lithium battery components [2].

Thermoelectric effects are in general dependent on magnetic field with the principal parameters, used in thermoelectric, the Seebeck and Peltier effects having the corresponding thermomagnetic coefficients the Nernst and Ettingshausen effects, respectively [10].

In [11] reported on the role of impurities on the lattice dynamics of nanocrystalline Si produced by a bottom-up process with respect to thermoelectric applications. In [12] accounts the fact that when the doping density increases there are at least four phenomena occurring simultaneously, on one hand the conduction band and valence band rigidly shift towards one another due to increasing interactions among free carriers, and between free carriers and dopant atoms, causing a reduction in the band gap, in addition to this the two band edges are perturbed and band tails are formed, arising from the random impurity distribution and the resulting potential energy fluctuation.The next phenomena occurred is the shallow dopant band, located slightly above the valence band and the last one is Fermi level shift.

The review work by [13] discusses the nature of main factors such as impurities, defects, electrically active thermal donors and other complexes that are formed due to direct impurity scattering, acoustic phonon scattering, and optical phonon scattering etc. do influence the energy band structure formation in semiconductors, basic electrophysical, optical, thermoelectrical, even mechanical properties. In [14] suggested the following expression for density of states of non-parabolic band having band tails

$$\rho(z) = \frac{m_b^{*\frac{3}{2}} 2^{\frac{3}{4}} \delta^{\frac{1}{2}}}{\pi^2 \hbar^3} y(z) \tag{1}$$

where,

$$y(x) = \frac{1}{\sqrt{\pi}} \int_{-\infty}^{z} \sqrt{z - \zeta} \exp(-\zeta^2) d\zeta \tag{2}$$

and

$$z = \frac{\varepsilon}{\sqrt{2}\delta} \tag{3}$$

For high density limit the potential energy fluctuation reduces to a Gaussian with the standard deviation of

$$\delta = \left(\frac{ne^4a_s}{8\pi\epsilon_0^2\epsilon_d^2}\right)^{\frac{1}{2}} = \left(\frac{N_de^4a_s}{8\pi\epsilon_0^2\epsilon_d^2}\right)^{\frac{1}{2}} \tag{4}$$

We have a screened coulomb potential of impurity atoms with ϵ_d (dielectric constant) of the given semiconductor. The Thomas-Fermi screening length for all ionized dopants ($n \cong N_d$) according to [15] is

$$a_s = \left(\frac{\pi^{\frac{4}{3}}\epsilon_0\epsilon_d\hbar^2}{3^{\frac{1}{3}}N_d^{\frac{1}{3}}e^2m_n^*}\right)^{\frac{1}{2}} \tag{5}$$

The density of states function given by equation (1) is very complicated and thus is not useful for making any calculation. Slotboom [16] has however; suggested the following approximation for y(z) as

$$\begin{cases} y(z) \cong z^{\frac{1}{2}}\left[1 - \frac{1}{16z^2}\right] \\ \quad ; \text{for } z > 0.601, equally, \varepsilon > 0.85\delta \\ y(z) \cong \frac{1}{2\pi^{\frac{1}{2}}}Exp(-z^2)\{1.225 - 0.906[1 - Exp(2z)]\} \\ \quad ; \text{for } z \leq 0.601 \end{cases} \tag{6}$$

We obtain the following expression of the electron concentration,

$$n = \frac{m_n^{*\frac{3}{2}}2^{\frac{5}{4}}\delta^{\frac{3}{2}}}{\pi^2\hbar^3}\Psi_0 \tag{7}$$

where,

$$\Psi_0 = \frac{1}{2\pi^{\frac{1}{2}}}\int_{-\infty}^{0.601} \exp(-z^2)\left(\frac{0.319+0.906Exp(2z)}{1+Exp\left\{1.494n_n^{\frac{5}{12}}z-\eta\right\}}\right)dz + \int_{0.601}^{\infty}\frac{z^{\frac{1}{2}}\left[1-\frac{1}{16z^2}\right]}{1+\exp\left\{1.494n_n^{\frac{5}{12}}z-\eta\right\}}dz \tag{8}$$

The corresponding expressions for parabolic density of state and the electron concentration are

$$\rho(\varepsilon) = \frac{8\sqrt{2}\pi m_n^{*\frac{3}{2}}}{h^3}\varepsilon^{\frac{1}{2}} \tag{9}$$

and

$$n = \int_0^{\infty}\rho(\varepsilon)f_0(\varepsilon)d\varepsilon = \frac{m_n^{*3}}{2\pi^2\hbar^3}\left(\frac{2k_BT}{m_n^*}\right)^{\frac{3}{2}}F_{\frac{1}{2}}(\eta) \tag{10}$$

where, the standard Fermi-Dirac integral is

$$F_i(\eta) = \int_0^{\infty}\frac{x^id\varepsilon}{(1+Exp[x-\eta])} \tag{11}$$

In terms of the reduced energy and Fermi energy $x = \frac{\varepsilon}{k_BT}$ and $= \frac{E_F}{k_BT}$, respectively. Thus, $F_{1/2}$ corresponds to i = ½.

It is more convenient to introduce normalized electron concentration n_n given by

$$n_n = \frac{n}{10^{25}/m^3}. \tag{12}$$

In this study the semi-classical and quantum treatments are applied in the calculations of scattering mechanisms under the assumptions of the electron concentrations from 0.6×10^{18} - $12\times10^{20}/cm^3$ and in the temperature range $77 - 300K$.

BOLTZMANN TRANSPORT EQUATION WITH RELAXATION TIME APPROXIMATION

We define a probability density function f(**r**,**k**,t) that describes the probability of finding an electron at position **r** with a wave vector **k** at time t. The distribution function can be written as

$$f = f_0 + f_1 \tag{13}$$

where f_0 is the thermal equilibrium distribution and f_1 is a small perturbation.

The Boltzmann transport equation is

$$\frac{\partial f}{\partial t} + \mathbf{v}.\nabla f + \dot{\mathbf{k}}.\nabla_k f = \left(\frac{\partial f}{\partial t}\right)_C \tag{14}$$

Making use of $v = \frac{1}{\hbar}\nabla_k\varepsilon$ and $\nabla_k f_0 = \frac{\hbar^2 k}{m_n}\frac{df_0}{d\varepsilon}$ and assumption that $\nabla_r T$, $\nabla_r\varepsilon_F$ as well as the electric field E are first order quantities and on equating the first order terms in equation (14) to obtain

$$\frac{f_1}{\tau} = -\mathbf{v}.\left(\nabla_r\varepsilon_f + (\varepsilon-\varepsilon_f)\nabla_r T\right)\left(\frac{df_0}{d\varepsilon}\right) = -\mathbf{v}.\boldsymbol{F}.\left(\frac{df_0}{d\varepsilon}\right) \tag{15}$$

where,

$$\mathbf{F} = \nabla_r\varepsilon_f + (\varepsilon-\varepsilon_f)\nabla_r T \tag{16}$$

In the presence of Lorenz force consisting of magnetic field that created second order perturbation where f$_1$ is assumed to behave as a negative scalar function of the energy ε as

$$f_1 = -\phi\frac{df_0}{d\varepsilon} \tag{17}$$

where,

$$\phi = \tau\mathbf{v}.\mathbf{G} \tag{18}$$

when **B** = 0 the general vector **G** reduces to **F** for electric field only.

We can say the collision process can be described such that the loss of momentum **P**/τ is described by the Lorenz equation

$$m_n^*\frac{d\mathbf{v}}{dt} = (-e)(\boldsymbol{E} + \mathbf{v}\mathbf{x}\mathbf{B}) - \frac{\mathbf{P}}{\tau} \tag{19}$$

Similarly,

$$\frac{\phi}{\tau} = \mathbf{v}.\left(\nabla_r\varepsilon_F + \frac{\varepsilon-\varepsilon_F}{T}\nabla_\mathbf{r}T\right) - (-e)(\boldsymbol{E} + \mathbf{v}\mathbf{x}\mathbf{B}) \tag{20}$$

For spherically symmetric $\varepsilon(k)$ with $\mathbf{n} = \frac{\mathbf{k}}{k} = \frac{\mathbf{v}}{v}$, and making appropriate coordinate transformations

$$e(\mathbf{v}\mathbf{X}B)\nabla_k\phi = \frac{ev}{k}(\mathbf{B}\mathbf{X}\,\phi)\mathbf{n} \tag{21}$$

We can express Eq. (20) as

$$\frac{\phi}{\tau} = \mathbf{v}.\left(\nabla_r\varepsilon_F + \frac{\varepsilon-\varepsilon_F}{T}\nabla_\mathbf{r}T\right) - \frac{ev}{\hbar k}(\mathbf{B}\mathbf{X}\phi).\mathbf{v} \tag{22}$$

For the case of transverse magnetic field **B** perpendicular to the field E = E$_x$ and thermal gradient in the x-y plane, the components of ϕ are

$$\frac{\phi_x}{\tau} = v_x\left(\frac{d\varepsilon_F}{dx} + \frac{\varepsilon-\varepsilon_F}{T}\frac{dT}{dx}\right) - \frac{ev_x^2}{\hbar k}B\phi_y \tag{23}$$

$$\frac{\phi_y}{\tau} = v_y\left(\frac{d\varepsilon_F}{dy} + \frac{\varepsilon-\varepsilon_F}{T}\frac{dT}{dy}\right) + \frac{ev_y^2}{\hbar k}B\phi_x \tag{24}$$

Solving for ϕ_x and ϕ_y gives

$$\phi_{x,y} = \left(\tau v_{x,y}^2 F_{x,y} \mp \omega\tau^2 v_{x,y}^2 F_{y.x}\right)/(1 + \omega^2\tau^2) \tag{25}$$

Where $\omega = \frac{eB}{m_n^*}$ is cyclotron frequency.

DERIVATION OF CONDUCTIVITY FOR PARABOLIC AND NON-PARABOLIC BAND STRUCTURES

In reality there is a dynamic equilibrium maintained between energy input in the form of both heat and the electromagnetic forces and the scattering processes which tend to randomize momentum and relax energies. In the derivation of conductivities, we have assumed that

(i) the electrons are behaving identically with a uniform velocity.

(ii) the ionized impurity scattering is the most important for the electronic transport processes in heavily doped semiconductor and it is energy dependent ($\tau = \tau_0\varepsilon^{3/2}$) since most phonon modes would be suppressed at low temperatures in the range 77-300 K and τ_0 is approximated to be 0.01 ns [17].

f$_1$ is responsible for the electric current density and the calculation of the electric current density lies within the first Brillouin zone with $\rho(k) = 1/4\pi^3$ is the local density of states in k-space to get after some steps.

$$J_{\mathbf{x}} = \int_0^\infty ev_x^2 \phi_x \left(\frac{df_0}{d\varepsilon}\right) \rho d\varepsilon$$

$$= \sigma_{xx}E_x - \sigma_{xy}E_y + \frac{1}{T}\frac{dT}{dx}\alpha_{xx} - \frac{1}{T}\frac{dT}{dy}\alpha_{xy} \tag{26}$$

and in the same way

$$J_y = \sigma_{yy}E_y - \sigma_{yx}E_x + \frac{1}{T}\frac{dT}{dy}\alpha_{yy} - \frac{1}{T}\frac{dT}{dx}\alpha_{yx} \tag{27}$$

In the general case, the electrical and thermoelectric conductance in a transverse magnetic field is expressed in terms of the tensor components σ_{ij} and α_{ij} as in the equations (26) and (27).

The most important consequence of the assumptions asserted previously is that all elements of the conductivity tensor are expressed as weighted averages over the density of states $\rho(\varepsilon)$, and zero field distribution, $f(\varepsilon)$ in the coming derivations in accordance with

$$\langle\tau(\varepsilon)\rangle = \frac{\int_0^\infty \varepsilon\tau(\varepsilon)\left(\frac{\partial f_0}{\partial \varepsilon}\right)\rho d\varepsilon}{\int_0^\infty \varepsilon\left(\frac{\partial f_0}{\partial \varepsilon}\right)\rho d\varepsilon} \tag{28}$$

We use Onsager symmetry [18] for diagonal $\left(\sigma_\parallel; \alpha_\parallel\right)$ and off-diagonal $(\sigma_\perp; \alpha_\perp)$ elements of electrical and thermoelectric conductivities to get

$$\sigma_{xx} = \sigma_{yy} = \frac{2e^2}{3m_n^*}\int_0^\infty \frac{\tau\varepsilon}{1+\omega^2\tau^2}\left(\frac{df_0}{d\varepsilon}\right)\rho d\varepsilon \tag{29}$$

$$\sigma_{xy} = -\sigma_{yx} = \frac{2e^2}{3m_n^*}\int_0^\infty \frac{\omega\varepsilon\tau^2}{1+\omega^2\tau^2}\left(\frac{df_0}{dE}\right)\rho d\varepsilon \tag{30}$$

$$\alpha_{xx} = \alpha_{yy} = \frac{2e}{3m_n^*}\int_0^\infty \frac{\tau\varepsilon}{1+\omega^2\tau^2}(\varepsilon-\varepsilon_F)\left(\frac{df_0}{dE}\right)\rho d\varepsilon \tag{31}$$

$$\alpha_{xy} = -\alpha_{yx} = \frac{2e}{3m_n^*}\int_0^\infty \frac{\omega\varepsilon\tau^2}{1+\omega^2\tau^2}(\varepsilon-\varepsilon_F)\left(\frac{df_0}{d\varepsilon}\right)\rho d\varepsilon \tag{32}$$

where for n-type semiconductor $df_0/d\varepsilon = -f_0/k_BT$.

Solving equations (26) and (27) for E_x and E_y gives

$$E_x = \frac{\begin{array}{c}-J_x\sigma_{yy}+\frac{1}{T}\frac{dT}{dx}\sigma_{yy}\alpha_{xx}-\frac{1}{T}\frac{dT}{dy}\sigma_{yy}\alpha_{xy}\\ -J_y\sigma_{xy}+\frac{1}{T}\frac{dT}{dy}\sigma_{xy}\alpha_{yy}-\frac{1}{T}\frac{dT}{dx}\sigma_{xy}\alpha_{yx}\end{array}}{-\sigma_{xx}\sigma_{yy}+\sigma_{xy}\sigma_{yx}} \tag{33}$$

and

$$E_y = \frac{\begin{array}{c}-J_x\sigma_{yx}+\frac{1}{T}\frac{dT}{dx}\sigma_{yx}\alpha_{xx}-\frac{1}{T}\frac{dT}{dy}\sigma_{yx}\alpha_{xy}\\ -J_y\sigma_{xx}+\frac{1}{T}\frac{dT}{dy}\sigma_{xx}\alpha_{yy}-\frac{1}{T}\frac{dT}{dx}\sigma_{xx}\alpha_{yx}\end{array}}{-\sigma_{xx}\sigma_{yy}+\sigma_{xy}\sigma_{yx}} \tag{34}$$

It can be written in vector form [17] as

$$\boldsymbol{E} = \rho\boldsymbol{J} + R_H(\boldsymbol{B}X\boldsymbol{J}) + S\nabla T + N(\boldsymbol{B}X\nabla T) \tag{35}$$

where, we have electric resistivity (ρ), hall effect factor (R_H) that appears due to the application of the magnetic field that leads to a decrease in longitudinal conductivity and induces an off-diagonal conductivity, which is called the hall effect. This is commonly called the magneto-resistance. We have also Seebeck coefficient(S) and Nernst coefficient (N). When a conductive solid is placed under a longitudinal temperature gradient and a transverse magnetic field, two types of thermoelectric responses occur, i.e., the magneto-Seebeck effect in the longitudinal direction and the Nernst effect in the other transverse direction.

We can get magneto-Seebeck coefficient by setting $j_x = j_y = 0$ and eliminating E_y in equation (33) under isothermal condition $\nabla_y T = 0$ as

$$s = \frac{E_x'}{\nabla_x T} = -\frac{1}{T}\frac{\sigma_{yy}\alpha_{xx} + \sigma_{xy}\alpha_{yx}}{\sigma_{xx}\sigma_{yy} + \sigma_{xy}\sigma_{xy}}$$

$$= -\frac{1}{eT}\frac{\langle\frac{\tau}{1+\omega^2\tau^2}\rangle\langle\frac{\tau\varepsilon}{1+\omega^2\tau^2}\rangle + \langle\frac{\omega\tau^2}{1+\omega^2\tau^2}\rangle\langle\frac{\omega\tau^2\varepsilon}{1+\omega^2\tau^2}\rangle}{\langle\frac{\tau}{1+\omega^2\tau^2}\rangle^2 + \langle\frac{\omega\tau^2}{1+\omega^2\tau^2}\rangle^2} = -\frac{k_B}{e}\left\{\frac{K_0K_1 + \mu^2B^2\mathcal{L}_0\mathcal{L}_1}{K_0^2 + \mu^2B^2\mathcal{L}_0^2}\right\} \tag{36}$$

where the mobility $\mu = \frac{e\tau_0}{m_n^*}$ and the integral functions in equation (36) are expressed with the help of the reduced energy $x = \varepsilon/k_B T$ and $\tau = \tau_0 x^{3/2}$ accordingly other quantities which appeared in the derivations were reduced to dimensionless for sake of unit consistency.

$$K_i = \left\langle \frac{\tau\varepsilon^i}{1+\omega^2\tau^2}\right\rangle = \int_0^\infty \frac{x^{i+3}f_0}{1+\mu^2 B^2 x^3}\,dx \tag{37}$$

and

$$\mathcal{L}_i = \left\langle \frac{\omega\tau^2\varepsilon^i}{1+\omega^2\tau^2}\right\rangle = \int_0^\infty \frac{x^{i+9/2}f_0}{1+\mu^2 B^2 x^3}\,dx \tag{38}$$

Furthermore, Nernst coefficient is obtained by setting $j_x = j_y = 0$ and eliminating E_x in equation (33) under isothermal condition $\nabla_y T = 0$

$$N = \frac{E_y'}{\nabla_x T} = \frac{1}{T}\frac{\sigma_{xx}\alpha_{xy} - \sigma_{xy}\alpha_{xx}}{\sigma_{xx}\sigma_{yy} + \sigma_{xy}\sigma_{xy}}$$

$$= -\frac{k_B}{e}(\mu B)\frac{K_0\mathcal{L}_1 - K_1\mathcal{L}_0}{K_0^2 + \mu^2 B^2 \mathcal{L}_0^2} \tag{39}$$

We can obtain the corresponding expression for magneto-Seebeck coefficient for the case of modified density of states based on standard model with parabolic density of states (which doesn't incorporate the effect of band tails) by substituting equation (1) for modified density of states and by extending the integration limits from $-\infty$ to ∞.

$$S = -\frac{k_B}{e}\left(\frac{\sqrt{2}\delta}{k_B T}\right)\frac{\psi_{5/2}'\psi_{7/2}' + c^2\psi_4'\psi_5'}{\psi_{5/2}'^2 + c^2\psi_4'^2} \tag{40}$$

where,

$$c = (\mu B)\left(\frac{\sqrt{2}\delta}{k_B T}\right)^{3/2} \tag{41}$$

and the integral functions in equation (40) are obtained by setting $\lambda = 5/2; 7/2; 4; 5$ into this equation respectively.

$$\psi_\lambda' = \frac{1}{2\pi^2}\int_{-\infty}^{0.601}\frac{|z'|^\lambda exp(-z'^2)(0.319 - 0.906\,exp(2z'))}{exp\left(\frac{\sqrt{2}\delta}{k_B T}z' - \eta\right)\left(1 + \frac{e^2 B^2 \tau_0^2}{m_n^{*2}}\left(\frac{\sqrt{2}\delta}{k_B T}\right)^3 z'^3\right)}\,dz' + \int_{0.601}^{\infty}\frac{z'^{\lambda+1/2}\left[1 - \frac{1}{16z'^2}\right]}{exp\left(\frac{\sqrt{2}\delta}{k_B T}z' - \eta\right)\left(1 + \frac{e^2 B^2 \tau_0^2}{m_n^{*2}}\left(\frac{\sqrt{2}\delta}{k_B T}\right)^3 z'^3\right)}\,dz' \tag{42}$$

The corresponding expression for Nernst coefficient is

$$N = \frac{k_B}{e}\frac{\sqrt{2}\delta}{k_B T}c\frac{\psi_{5/2}'\psi_5' - \psi_4'\psi_{7/2}'}{\psi_{5/2}'^2 + c^2\psi_4'^2} \tag{43}$$
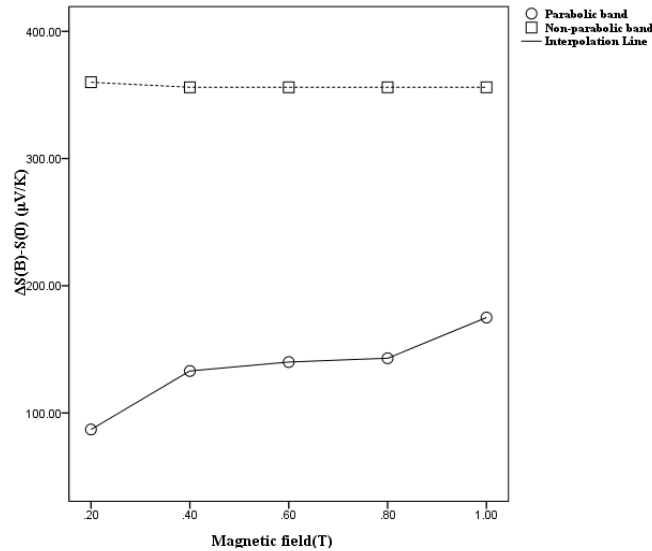
RESULTS

The calculation of Seebeck coefficient(S) for zero field used the expressions as $-\frac{k_B}{e}\frac{F_4}{F_3}$ and $-\frac{\sqrt{2}\delta}{eT}\frac{\psi_{7/2}}{\psi_{5/2}}$ for parabolic and non-parabolic bands respectively [19]. Similarly in the presence of magnetic field and temperature gradient equation (36) for Seebeck(S) and equation (39) for Nernst coefficient(N) in parabolic band and the corresponding equations (40) and (43) in non-parabolic are carried out under the assumption that the electron concentrations vary from $0.6 - 12\times10^{19}$/cm^3 and in the temperature range 77 – 300K. The effective mass of Mg$_2$Si is $m_n^* = 0.46m_0$(m_0 is mass of free electron) and its dielectric constant is $\epsilon = 20$ as well as the parameters a_s and δ were determined in the way as in [20].

Numerical values were obtained by using Matlab software in such a way that the reduced value of electron concentration $n_n = n/(10^{25}m^3)$ is used to get the corresponding reduced Fermi-energy η. A number of steps are required to obtain the write value of η for a given electron concentration through iterative method. Equation (11) for parabolic band was used and Equation (7) was for non-parabolic band in this iterative method in such a way that the integral on the LHS is evaluated for a given η and next one should get the write value which equates the given value of n_n on the RHS. In this way, we obtained the table of paired values. These values are the basis for calculations of thermomagnetic coefficients in the study with a magnetic field ranging from 0.2 to 1 T. Note that in this study, electron mobility is considered to be featureless and the relaxation time is typically 10^{-11}s without losing the generality as in [17, 21, 22].

Figure 1 is plotted with the calculated values of Seebeck coefficient for zero field case S(0) and S(B) in the presence of magnetic field that are used to determine $\Delta = S(B) - S(0)$ for parabolic and non-parabolic bands respectively. The change is significant for non-parabolic band consideration that is about 360μV/K on average compared to its value for parabolic band that is about 135.6 μV/k on average for magnetic field ranging in the interval 0.2 – 1 T. In both cases, the Seebeck coefficient is enhanced as a result of the magnetic field. As it is the case for this study, we need the modern approaches for better understanding of the thermomagnetic property of Mg$_2$Si–based

materials based on the consideration under non-parabolic band of heavily doped semiconductor rather than for that of parabolic band consideration. For this reason, the value 360μV/K value is a reliable value that shows that there is significant enhancement of Seebeck due to the magnetic field for Mg_2Si–based materials. The enhancement of Seebeck coefficient 360 μV/K is two orders of magnitude greater than the experimental uncertainty level ~ 10μV/K [23]. It is therefore possible to expect one would expect significant effect of magnetic field in heavily doped n-type Mg_2Si.

Figure 1. Change of Seebeck coefficient from zero field value S(0) to S(B) due to magnetic field for parabolic and non-parabolic bands

The result in figure 2 provides the value of Nernst coefficient(N) as a function of magnetic field ranging in the interval 0.2 – 1T for electron concentration in heavily doping range 0.6 – 12×10^{25}/m^3 for parabolic band consideration. There is slow variation of Nernst coefficient with its negative values for certain electron concentrations such as 2×10^{25}/m^3 and 4×10^{25}/m^3 compared to relatively rapid variations for the rest values of electron concentrations. When considering the parabolic band, the Nernst coefficient increases with the magnetic field for the latter case.
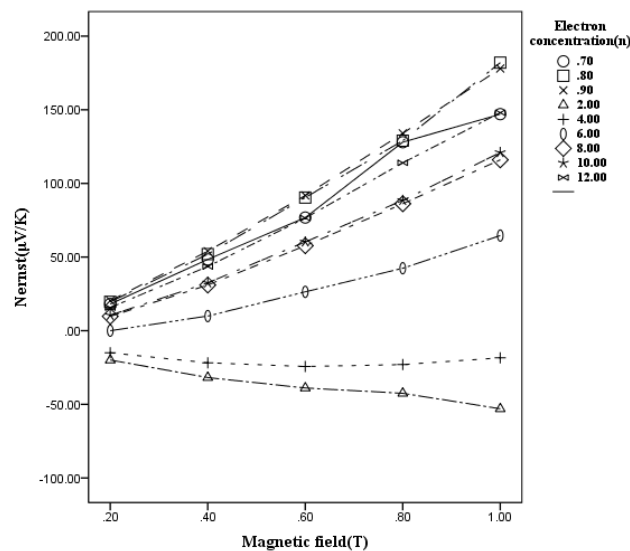
Figure 2. Nernst coefficient against the magnetic field for different electron concentrations in the parabolic band

The result in Figure 3 is the value of Nernst coefficient as a function of magnetic field ranging in the interval 0.2 - 1 T due to resolution problem in the graph it shows the average values for electron concentrations in the heavily doping range .6 – 12×10^{25}/m^3. In contrast to the result in Figure 2 for parabolic band the Nernst coefficient decreases with magnetic field for non-parabolic band consideration with its magnitude in the order of 10^{-9} V/K compared to the order of magnitude 10^{-6} V/K for parabolic band consideration as shown in Figure 2. There is a significant difference in the order of magnitude of the Nernst coefficient as a function of the magnetic field for the consideration of the parabolic band versus the parabolic non-parabolic consideration We again recommend using more modern approaches in considering non-parabolic bands with respect to parabolic considerations.
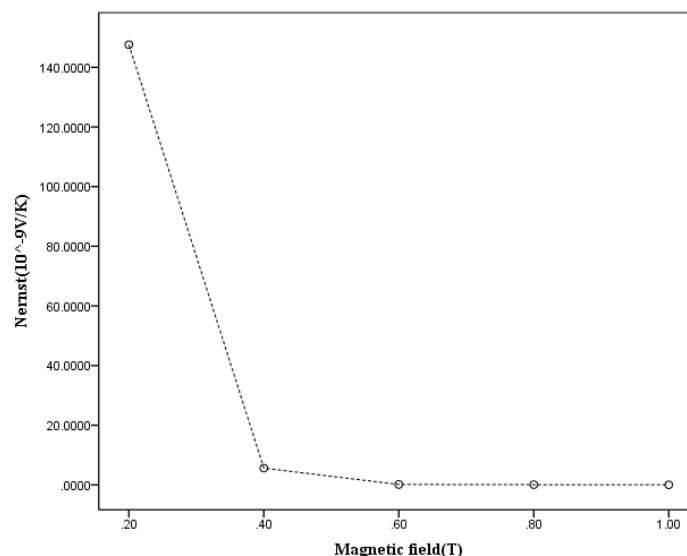
Figure 3. Nernst coefficient with respect to the magnetic field by averaging its values for various electron concentrations in the non-parabolic band.

The same behavior as in figure 1 and figure 2 are expected to be observed for similar experimental arrangements. Therefore, there is a huge potential for further experimental exploration and investigation on such behaviors. These values are not meant to be a good fit for measurements. Note that the results as shown are those we obtained with the help of Matlab software. Seebeck and Nernst coefficients should vary much with the magnetic field, so the results for these coefficients are closely agree with the first principal calculations as in [24] that show the importance of non-parabolic effects, in the thermoelectric properties of semiconductors. The same magneto behaviour of Seebeck and Nernst has been experimentally observed [25] for the semi-metallic Wely polycrystalline NbP.

CONCLUSION

Our theoretical calculation confirms that the material under study shows the general tendency to display higher values of the magneto-Seebeck coefficients for non-parabolic band consideration compared to parabolic band consideration. Our theoretical results also show that the magnitude of the Nernst coefficient is larger at lower temperatures, lower carrier concentrations, and magnetic fields with the exception of that for non-parabolic consideration where Nernst coefficient shows decreasing trend with magnetic field. These observations could prove useful in evaluating the Nernst coefficient in other materials having similar band structures as that of Mg$_2$Si, while it is true that the relaxation times may differ with carrier concentration and magnetic field dependent mobility for our result to well agree with experimental result these factors should be considered in future studies for better result.

ORCID ID

Mulugeta Habte Gebru, https://orcid.org/0000-0001-7341-2717

REFERENCES

[1] P. Boulet, M.J. Verstraete, J.P. Crocombette, M. Briki, and M.C. Record, "Electronic properties of the Mg$_2$Si thermoelectric material investigated by linear-response density-functional theory," Computational Materials Science, **50**(3), 847-851 (2011). https://doi.org/10.1016/j.commatsci.2010.10.020

[2] N.S. Naser, R.V. Denys, H.F. Andersen, L. Arnberg, and V.A. Yartsy, "Nanostructured Magnesium silicide Mg$_2$Si and its electrochemical performance as anode of a Lithium battery," Journal of Alloys and Compounds, **718**, 478-491 (2017). https://doi.org/10.1016/j.jallcom.2017.05.163

[3] T.H. Nguyen, *et al.*, "On the composition of luminescence spectra from heavily doped p-type Silicon under low and high excitation," Journal of luminescence, **181**, 223-229 (2016). https://doi.org/10.1016/j.jlumin.2016.08.036

[4] M.H. Gebru, "Electrical and thermal conductivity of heavily doped n-type silicon," Eur. Phys. J. Appl. Phys. **90**, 10102 (2020). https://doi.org/10.1051/epjap/2020190332

[5] P.W. Chapman, O.N. Tufte, J.D. Zook, and D. Long, "Electrical properties of heavily doped silicon," J. App. Phys. **34**(11), 3291-3295 (2004). https://doi.org/10.1063/1.1729180

[6] W.G. Spitzer, F.A. Trumbore, and R.L. Logan, "Properties of heavily doped n-type germanium," Journal of Applied Physics, **32**, 1822–1830 (1961). https://doi.org/10.1063/1.1728243

[7] A. Cuevas, P.A. Basore, G.G. Matlakowski, and C. Dubois, "Surface Recombination Velocity of Heavily Doped N-Type Silicon,"Journal of Applied Physics, **80**, 3370-3375 (1996). https://doi.org/10.1063/1.363250

[8] H. Zhou, P. Kropelnicki, J.M. Tsai, and C. Lee, "Study of the thermoelectric properties of heavily doped poly-Si in high temperature,"Procedia Engineering, **94**, 18-24 (2014). https://doi.org/10.1016/j.proeng.2013.10.011

[9] K. Kikuchi, K. Yamamoto, N. Nomura, and A. Kawasaki, "Synthesis of n-type Mg$_2$Si/CNT Thermoelectric Nanofibers," Nanoscale Res. Lett. **12**, 343 (2017). https://doi.org/10.1186/s11671-017-2120-y

[10] D.W. Rowe, editor, *Thermoelectric Handbook: Macro to Nano*, (CRC Press/Taylor & Francis, Boca Raton, FL, 2006). https://doi.org/10.1201/9781420038903

[11] H. Wiggers, M.M. Schober, R. Koza, and P. Hermann, "Effects of impurity on the lattice dynamics of nanocrystalline silicon for thermoelectric application," J. Mater. Sci, **48**(7), 2836-2845 (2013). https://doi.org/10.1007/s10853-012-6827-y

[12] C.J. Hwang, "Calculation of Fermi energy and band tail parameters in heavily doped and degenerate n-type GaAs," J. Appl. Phys. **41**, 2268-2674 (1970).http://dx.doi.org/10.1063/1.1659280

[13] P.I. Baranskii, V.M. Babich, and E.F. Venger, "Development of The Physical Insight into The Nature of The Factors That Control Electrophysical and Other Properties of Semiconductors, Semiconductor Physics, Quantum Electronics & Optoelectronics, **4**(1), 1-4 (2000). http://journal-spqeo.org.ua/users/pdf/n1_2001/001_4_1.pdf

[14] E.O. Kane, "Thomas-Fermi approach to impurity semiconductor band structure," Phys. Rev. **133**,79-88 (1963). https://doi.org/10.1103/PhysRev.131.79

[15] C. Kittel, *Introduction to solid state physics*, 7th ed. (John Wiley & Sons Inc., New York, 1996).

[16] J.W. Slotboom, "The pn-product in silicon," Solid-State Electronics, **20**(4), 279-283 (1977). https://doi.org/10.1016/0038-1101(77)90108-3

[17] P. Sengupta, Y. Wen, and J. Shi, "Spin-dependent magneto-thermopower in narrow gap lead chalcogenide quantum wells," Sci. Rep. **8**, 5972 (2018). https://doi.org/10.1038/s41598-018-23511-2

[18] V. Zlatić, and R. Monnier, *The Modern Theory of Electricity*, (Oxford University press, 2014).

[19] M.H. Gebru, "Thermoelectric coefficients of heavily doped n-type silicon," East. Eur. J. Phys. **4**, 189-196 (2021). https://doi.org/10.26565/2312-4334-2021-4-25

[20] M.H. Gebru, "Electrical and thermal conductivity of heavily doped n-type silicon", Eur. Phys. J. Appl. Phys. **90**, 10102 (2020), https://doi.org/10.1051/epjap/2020190332

[21] S.S. Lee, *Semiconducor physical electronics*, 2nd ed. (Springer, 2006).

[22] S. Majdi, N. Suntornwipat, M. Gabrysch, and J. Isberg, "Carrier scattering mechanisms: Identifications via the scaling properties of the Boltzmann transport equation," Advanced Theory and Simulations, **4**(1), 2000103 (2021). https://doi.org/10.1002/adts.202000103

[23] T.J. Salez, M. Kouyaté, C. Filomeno, M. Bonetti, M. Roger, G. Demouchy, E. Dubois, et al., "Magnetically enhancing Seebeck in ferrofluids," Nanoscale Adv. **1**, 2979-2989 (2019). https://doi.org/10.1039/C9NA00109C

[24] X. Chen, D. Parker, and D.J. Singh, "Importance of non-parabolic band effects, on the thermoelectric properties of semiconductors," Sci. Rep. **3**, 3168 (2013). https://doi.org/10.1038/srep03168

[25] E.F. Scott, K.A. Schlaak, P. Chakraborty, C. Fu, S.N. Guin, S. Khodabakhsh, A.E.P. y Puente, et al., "Doping as Tuning Mechanism for Magneto-Thermoelectric Effects to Improveζ T In Polycrystalline NbP," Phys. Rev. B, **107**, 115108 (2023), https://doi.org/10.1103/PhysRevB.107.115108

Appendix

Table 1. Calculated values for parabolic band model

Serial No	n_n	η	$\tau_{0,i}$	F_3	F_4	α_{xx} (µV/K)	B(T)	K_0	K_1	$\mathcal{L}_0$	$\mathcal{L}_1$	α_{xx} (µV/K)	N(µV/KT)
1	.6	-.26	1×10^{-11}s	4.62	18.5	-345		0.417	0.824	1.288	3.824	-244	-37.2
2	.7	-.11		5.38	21.5	-345		0.485	0.957	1.496	4.4428	-175.74	18.1
3	.8	.02		6.12	24.49	-348.9		0.552	1.09	1.704	5.06	-156	19.6
4	.9	.14		6.9	27.6	-34	0.2	0.622	1.229	1.921	5.705	-148.84	20.4
5	2	.94		15.36	61.4	-353.06		1.385	2.736	4.275	12.7	-194.199	-19.9
6	4	1.63		30.6	122.5	-345		2.762	5.454	8.523	25.31	-248.5	-15
7	6	2.04		46	184.6	-374.2		4.162	8.218	12.84	38.14	-285.2	-1.05
8	8	2.3		59.85	239.4	-385.2		5.397	10.66	16.66	49.47	-313.9	9.75
9	10	2.55		76.8	307.4	-396		6.930	13.69	21.39	63.52	-338	10.5
10	12	2.73		92	367.98	-407.8		8.297	16.38	25.6	76.04	-359.2	15.7
1	.6	-.26						0.153	0.2566	0.379	1.04	-102	14200
2	.7	-.11						0.177	0.298	0.44	1.209	-107.5	48.4
3	.8	.02						0.202	0.34	0.501	1.377	-112.7	52
4	.9	.14						0.228	0.383	0.565	1.55	-117.3	54.0
5	2	.94					0.4	0.506	0.85	1.257	3.456	-162.5	-31.8
6	4	1.63						1.01	1.7	2.51	6.89	-215.6	-21.8
7	6	2.04						1.521	2.56	3.78	10.38	-253.9	9.94
8	8	2.3						1.973	3.32	4.9	13.46	-284.9	31
9	10	2.55						2.53	4.26	6.29	17.29	-311.4	32.5
10	12	2.73						3.03	5.102	7.53	20.7	-334.7	43.6
1	.6	-.26						0.08	0.124	0.178	0.474	-95.7	130000
2	.7	-.11						0.09	0.144	0.207	0.551	-101.7	76.8
3	.8	.02						0.106	0.164	0.235	0.627	-107.3	90.4
4	.9	.14						0.119	0.185	0.265	0.707	-112.4	91.8
5	2	.94					0.6	0.266	0.41	0.59	1.57	-156.3	-38.9
6	4	1.63						0.529	0.819	1.177	3.14	-208.2	-24.3
7	6	2.04						0.798	1.23	1.77	4.73	-246	26.4
8	8	2.3						1.035	1.601	2.3	6.13	-276.8	57.7
9	10	2.55						1.33	2.056	2.95	7.87	-303.2	60.3
10	12	2.73						1.59	2.46	3.54	9.43	-326.6	76.5
1	.6	-.26					0.8	0.05	0.073	0.103	0.27	-93.7	14100

Serial No	n_n	η	$\tau_{0,i}$	F_3	F_4	α_{xx} (μV/K)	B(T)	K_0	K_1	$\mathcal{L}_0$	$\mathcal{L}_1$	α_{xx} (μV/K)	N(μV/KT)
2	.7	-.11						0.058	0.084	0.119	0.31	-99.6	128
3	.8	.02						0.066	0.096	0.136	0.36	-105.2	129
4	.9	.14						0.074	0.11	0.1534	0.402	-110.3	134
5	2	.94						0.165	0.24	0.34	0.895	-153.7	-42.5
6	4	1.63						0.328	0.48	0.68	1.78	-204.9	-23
7	6	2.04						0.495	0.725	1.025	2.69	-242.4	42.4
8	8	2.3						0.64	0.94	1.33	3.49	-272.93	86.2
9	10	2.55						0.82	1.207	1.71	4.476	-299.21	88.5
10	12	2.73						0.986	1.445	2.04	5.36	-322.5	114
1	.6	-.26						0.034	0.048	0.067	0.17	-92.5	15600
2	.7	-.11						0.039	0.056	0.078	0.2	-98.5	147
3	.8	.02						0.045	0.06	0.089	0.23	-104	182
4	.9	.14						0.05	0.07	0.1	0.259	-109.2	178
5	2	.94					1	0.11	0.159	0.22	0.58	152.2	-53
6	4	1.63						0.224	0.316	0.44	1.15	-203	-18.4
7	6	2.04						0.34	0.476	0.667	1.73	-240.3	64.6
8	8	2.3						0.438	0.62	0.865	2.24	-270.7	116
9	10	2.55						0.56	0.79	1.11	2.88	-296.9	121
10	12	2.73						0.67	0.95	1.33	3.45	-320	148

Table 2. Calculated values for non-parabolic band model

Serial No	n_n	η	τ_0	$\Psi_{5/2}$	$\Psi_{7/2}$	α_{xx} (μV/K)	B(T)	Ψ'_4	Ψ'_5	$\Psi'_{5/2}$	$\Psi'_{7/2}$	α_{xx} (μV/K)	N(μV/K)
1	.6	-.15	1X10⁻¹¹s	4.21	16.53	-334	0.2T	1.136	3.25	0.372	0.733	-243.6	26.9
2	.7	.029		3.99	14.87	-332		0.886	2.53	0.287	0.57	-175.7	8.8
3	.8	.22		13.14	13.15	-342.8		0.78	2.11	0.275	0.52	-156	4.97
4	.9	.4		3.63	12.18	-329.2		0.208	0.338	0.26	0.48	-148.8	-.28
5	2	1.57		3.19	7.07	-345.6		0.175	0.34	0.097	0.136	-194.2	.79
6	4	3.1		3	6.37	-332		0.166	0.292	0.094	0.13	-248.5	.23
7	6	4.28		3.46	6.89	-368.6		0.129	0.214	0.082	0.106	-285.2	.17
8	8	5.8		5.33	10.9	-379.8		0.13	0.228	0.075	0.104	-314	.16
9	10	6.8		6.14	12.57	-390.9		0.11	0.2	0.062	0.089	-338	.118
10	12	7.08		5.2	10.15	-402.2		0.082	0.14	0.048	0.066	-359.2	0.06
1	.6	-.15					0.4T	0.676	1.99	0.22	0.436	-102	1.8
2	.7	.029						0.26	0.685	0.098	0.173	-107.5	0.3
3	.8	.22						0.257	0.59	0.157	0.197	-112.6	0.6
4	.9	.4						0.197	0.49	0.083	0.138	-117.3	0.17
5	2	1.57						0.08	0.155	0.0455	0.0625	-162.5	0.004
6	4	3.1						0.044	0.076	0.027	0.0361	-215.6	0.001
7	6	4.28						0.033	0.055	0.02	0.027	-253.9	0.0007
8	8	5.8						0.0334	0.058	0.02	0.027	-284.9	0.001
9	10	6.8						0.0287	0.051	0.016	0.0227	-311.4	0.0007
10	12	7.08						0.021	0.035	0.013	0.017	334.7	0.0004
1	.6	-.15					0.6T	0.144	0.398	0.056	0.097	-95.7	0.008
2	.7	.029						0.118	0.309	0.047	0.081	-101.7	0.005
3	.8	.22						0.1007	0.256	0.039	0.069	-107.3	0.003
4	.9	.4						0.09	0.22	0.042	0.065	-112.4	0.003
5	2	1.57						0.036	0.07	0.02	0.029	-156.3	0.0006
6	4	3.1						0.02	0.034	0.0123	0.016	-208.2	0.0003
7	6	4.28						0.015	0.024	0.009	0.012	-246	0.0001
8	8	5.8						0.015	0.026	0.008	0.012	-276.8	0.0001
9	10	6.8						0.013	0.023	0.007	0.01	-303.2	0.0001
10	12	7.08						0.009	0.016	0.006	0.0075	-326.6	0.0001
1	.6	-.15					0.8T	0.676	1.99	0.22	0.436	-93.7	1.27
2	.7	.029						0.047	0.176	0.0218	0.044	-99.6	0.002
3	.8	.22						0.058	0.145	0.026	0.04	-105.2	0.002
4	.9	.4						0.051	0.124	0.02	0.036	-110.3	0.0007
5	2	1.57						0.02	0.039	0.013	0.016	-153.7	0.0003
6	4	3.1						0.01	0.019	0.007	0.009	-204.9	0.0001
7	6	4.28						0.011	0.019	0.0074	0.0094	-242.4	0.0001
8	8	5.8						0.008	0.015	0.005	0.007	-272.9	0.00007
9	10	6.8						0.007	0.013	0.004	0.006	-299.2	0.00004
10	12	7.08						0.005	0.009	0.003	0.004	-322.5	0.00003
1	.6	-.15					1T	0.054	0.145	0.04	0.038	-92.5	0.00000
2	.7	.029						0.044	0.11	0.02	0.03	-98.5	0.0008
3	.8	.22						0.038	0.094	0.0158	0.0263	-104	0.0005
4	.9	.4						0.034	0.08	0.0166	0.0244	-109.2	0.0005
5	2	1.57						0.013	0.025	0.008	0.01	-152.2	0.0001
6	4	3.1						0.007	0.012	0.0036	0.0057	-203	0.00000
7	6	4.28						0.005	0.009	0.003	0.004	-240.3	0.00002
8	8	5.8						0.0054	0.0093	0.003	0.0043	-270.7	0.00001
9	10	6.8						0.0046	0.008	0.003	0.0036	-296.9	0.00003
10	12	7.08						0.003	0.0056	0.002	0.0027	-320	0.00001

МАГНІТО-ТЕРМОЕЛЕКТРИЧНІ КОЕФІЦІЄНТИ СИЛЬНОЛЕГОВАНОГО МАТЕРІАЛУ N-ТИПУ Mg₂Si

Мулугета Хабте Гебру

Факультет фізики, Університет Арба Мінча, Арба Мінч, Ефіопія

На відміну від параболічної смугової моделі, яка зазвичай використовується для розуміння електронних властивостей загалом, термоелектричних і магнітотермоелектричних зокрема, це дослідження підтверджує результати непараболічної смугової моделі для кращого розуміння коефіцієнтів Зеєбека та Нернста в присутності магнітного поля для Mg₂Si. Коефіцієнт магнето Зеєбека був значно підвищений порівняно з ненульовим значенням поля як функція магнітного поля для різних концентрацій електронів у діапазоні $0.6\text{-}12\times10^{25}/m^3$ в середньому при кімнатній температурі для непараболічної моделі порівняно з параболічною. модель гурту. Результат для коефіцієнта Нернста демонструє тенденцію до зростання як функції магнітного поля, за винятком певних концентрацій електронів для моделі параболічної зони. Водночас вона зменшується з магнітним полем у середньому для моделі непараболічної зони.

Ключові слова: *коефіцієнт магнето-Зеєбека; коефіцієнт Нернста; сильнолегований напівпровідник; магнітотермоелектрика; силіцид магнію*

EXPERIMENTAL SIMULATION FOR TWO OPTICALLY FILTERED MODULATION WEIGHTS IN LASER DIODE AS A SELF-LEARNING LAYER[†]

Dhuha Raad Madhloom[a]*, Ayser A. Hemed[b†], Suha Musa Khorsheed[a‡]

aDepartment of Physics, College of Science, University of Al-Nahrain, Baghdad, Iraq
bDepartment of Physics, College of Education, Mustansiriyah University, Baghdad, Iraq
*Corresponding author's e-mail: duha.raad23@gmail.com
†E-mail: ayser.hemed@uomustansiriyah.edu.iq
‡E-mail: suhaalawsi@gmail.com
Received March 25, 2023; revised April 17, 2023; accepted April 19, 2023

In this study, the response of a nonlinear laser medium is experimentally studied. In the study, a hybrid version of the input layer that multiplies optically and accumulates electrically is compared with a wholly optical version that multiplies and accumulates optically. This medium is subjected to two different paths of optically filtered and attenuated feedback. With such a system, the variation of feedback weight in one of them is tested in correspondence to the second one. Observations for frequency spectra are carried out to simulate the resultant response with an input layer for a neural network based on chaotic carriers. Chaotic laser emission was observed as a function of several control parameters, which are D.C. bias voltage, branch optical attenuation, and feedback strengths based on filtration with fiber Bragg grating. This learning rule is linear in the difference between each input and output of a neuron. This is an enhancing/inhibiting rule. The thresholds are adjusted in such a way that the output of the neuron is either pushed in the same direction as the input (enhancing) or pushed in the opposite direction (inhibiting).

Keywords: *Machine Learning; Neural Network; Chaotic Modulation; Laser Diode; Light Brain*
PACS: 42.55.Wd, 42.65.Sf, 42.79.Hp, 42.79.Sz, 85.60._q

1. INTRODUCTION

Optical neural network development initially described the fundamentals of an optical matrix multiplier for linear operation based on the theory of artificial neural networks. The optical neural network created by waveguide optical interconnection and free-space optical interconnection is then introduced. Finally, we discuss optical neural networks' nonlinearity [1]. Both connection topologies and the response dynamics of individual neurons influence computations in biological brain networks. The Hodgkin-Huxley framework is the foundation for a broad and biologically plausible family of computational models for single neurons known as conductance-based neuron models. These nonlinear dynamical systems relate the ionic current flow into and out of the neuron to the temporal evolution of the voltage across the neuronal membrane. Instead of simulating a binary-valued train of spike events, they model the continuous-valued membrane voltage, which allows them to generate a diverse range of neuronal activities, such as subthreshold oscillations, spikes, and bursts of different waveforms. In addition, by appropriately simplifying the underlying dynamical system, their complexity may frequently be tailored to the particular situation at hand [2].

Machine learning, which includes deep learning, is a subset of the larger area of artificial intelligence. With its billions of interconnected neurons serving as processing units, the deep architecture of the human brain is the model that deep learning attempts to mimic. Our brains likewise function hierarchically, beginning with more basic thoughts and building upon them to understand more sophisticated notions. Deep learning models, which divide incoming data into features and then recombine them to complete the job at hand, reflect this way of learning (e.g., detection, classification). A deep learning model can be used to do tasks of a similar nature without human input once it has acquired important features during the training phase [3]. Early in the 1980s, optical neural networks had already been created. These systems were able to recognize faces, learn Boolean operations, and decode handwriting. Optical networks take advantage of any optical device's benefits over electrical ones, such as their capacity to transport data from a single point source to any number of recipients, whereas doing so with electronics would require a lot of cable volume. Compared to electrical systems, optical systems produce less heat. Yet, the bulk and lack of scalability of all these optical solutions are common flaws [4].

The current state of the system, $x(t)$ and the state of the system at a previous time point, $x(t - \tau)$, are frequently used to predict the temporal evolution of physical, biological, and technological systems. The output optical frequency modes of a laser are determined by the time it takes for light to complete one round-trip of the resonant cavity. Time delays are crucial to the mechanisms governing the formation of white blood cells and breathing rate in the human physiological system. Electronic and fiber-optic cable time delays are frequently assessed and taken into account in modern communication systems. The interaction of delay τ established by attenuation element and nonlinearity existing in the laser active medium $F(x) = \{x(t), x(t - \tau)\}$ in such systems can generate a rich array of chaotic dynamical effects that are sometimes intrinsic for maintaining proper operation and other times detrimental.

2. THEORETICAL CONCEPTS

A neural network is a system with inputs and outputs that consists of numerous straightforward processing components that are similar in nature. Each of the processing elements has several internal variables called "weights". The behavior of an element will change if its weights are changed, and the entire network's behavior will change as a result [5]. In 1943, Walter Pitts [6] developed the first artificial neural network (ANN) model based on arithmetic and algorithms that mimicked the principles and functions of biological nerve cells. This model was successful in performing logical operations, ushering in the era of ANNs [7]. A decades-old artificial intelligence method involves simulating brain neurons to develop sophisticated machine learning models. This method has produced both remarkable advancements and disappointing results. Because of tremendous advances in mathematical formulations and computational capacity, we can now build many more layers of virtual neurons than at any other time in the history of science [8]. By utilizing technology based on free space and an integrated platform, optical neural networks are able to process information in parallel. In this section, we'll discuss optical computing and how to design neural networks using optical techniques. Refers to an optical neural network (ONN), which has numerous linear layers connected in a convoluted manner. Due to optical interconnection's high degree of parallelism, the beam's ability to transverse the room without interfering with it, and the speed at which light propagates, time delay, and dispersion are essentially nonexistent [9]. Individual neurons in biological networks are stimulated by external currents, if any, as well as by currents received from other neurons that are presynaptic to them. DDF neurons are useful as effective network nodes in computational models of functional neural networks because the presynaptic voltage and the postsynaptic voltages describe the gap junction and synaptic current connections [10].

In terms of intensity, phase, and carrier dynamics, optical feedback in LDs can result in extensive nonlinear behavior [11]. The full scenario calls for reviewing laser dynamics with modulation for the communications application and researching the effects of direct modulation on laser rate equations. Let the laser bias component I_b, the sinusoidal component of wave amplitude I_m, then the modulation frequency f_m are combined to provide the injection current $I(t)$ [12] [13];

$$I(t) = I_b + I_m \sin(2\pi f_m t) \tag{1}$$

Chaotic behavior in semiconductor laser is well understood, where these lasers' peak output power varies in an unpredictable manner [14]. The possible application of chaotic encryption-based cryptography makes chaotic behavior in LDs important and with direct current modulation can be represented by the following rate equations for the photon density P, carrier density N, and the driving current I as follows [15]:

$$\frac{dN}{dt} = \frac{1}{\tau_e}\left[\frac{I_b + I_m \sin(\emptyset)}{I_{th}} - N - \frac{N-\delta}{1-\delta}P\right] \tag{2}$$

The modulation is not for the complex field but for the carrier density through the disturbance to the injection current, therefore using the rate equation of the photon number P and can be written below take the form [16]:

$$\frac{dP}{dt} = GP + R_{sp} - \frac{P}{\tau p} \tag{3}$$

$$\frac{dN}{dt} = \frac{I}{q} - \frac{N}{\tau c} - Gp \tag{4}$$

where the number of electrons N, change with time inside the active region.

For a single-mode laser $G = \Gamma V g \mathcal{G}m = G N(N - N_0)$, G is the net rate of stimulated emission and R_{sp} is the rate of spontaneous emission in to the lasing mode. Phase modulation can be included through the equation [16]:

$$\frac{d\varphi}{dt} = \frac{1}{2}\beta_c\left[GN(N - N_0) - \frac{1}{\tau p}\right] \tag{4}$$

where β_c is the amplitude-phase coupling parameter, commonly called the line width enhancement factor.

Circuit roles in the dynamics of OEF are played by the feedback delay time and feedback ratio [17]. There are two forms of OEF, the first of which is positive and the second of which is negative. In both circumstances, we can anticipate that the laser output power will exhibit regular pulsing, quasi-periodic pulsing, and chaotic pulsing states [18]. Only negative OEF is seen in the real experimental system; the region of the frequency-locked state is relatively small for positive OEF. The self-OEF system is one of the chaotic OEF with wave length filter systems proposed in LDs.

Many types of optical filter are using absorbing glass filter, color filter tunable filter, band pass filter, Notch filter, Edge filter, Fabry-Perot filter [19] and fiber Bragg grating filter [20]. Additional types are infrared filter, absorptive filter, ultraviolet filter, and Dichroic filter [21].

The processing element used in the layer simulation in this paper, is corresponding to minor Adaline [5], which is shown in Fig. 1. It has an input vector X = {x_i}, which contains n (=2) components subtracted from unique laser, and a single output y from itself, and a weight vector W={w_i}, which also contains n (=2) components. The weights are variable (two different Bragg wavelengths) coefficients indicated by circles with arrows. The output y equals the sum of inputs multiplied by the weights and then passed through a nonlinear function. When Adalines are connected together, the layer

will become feed-forward neural network. The optimization of a posterior distribution over the states at all time points and the unknown parameters might be used as an alternative to filtering methods. In addition to finding nonlinear parameters in nonlinear and even chaotic models, optimization-based techniques have been successfully employed to estimate linear parameters in neural networks [10].
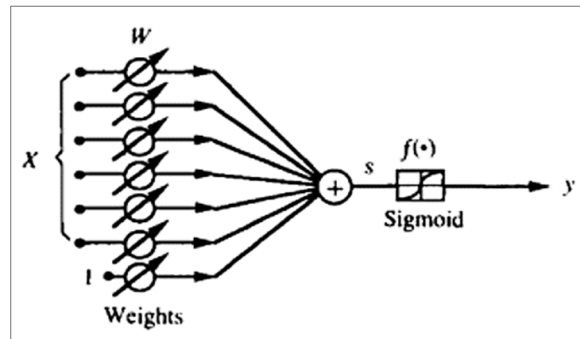

Figure 1. Adaline with sigmoid [5] [3].

Experimental Set-up

As shown in Figure 2(a), the experimental set-up includes a laser source; its model is HFCT5205A, which is a laser diode with an operational wavelength of 1310 nm and a maximum measured power of 0.048 mV at 25.5°C.
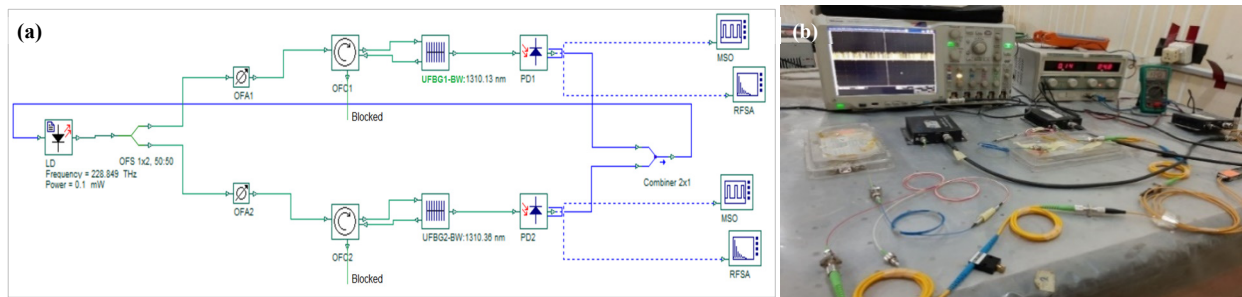
Figure 2. Experimental set-up for two branches filtered and attenuated optoelectronic feedback.

The light emitted from this source is divided into two parts via an optical fiber splitter (OFS); the first one is directed toward a first optical fiber attenuator (OFA1), then to a first fiber optical circulator (OFC1), with a blocked reflected port, and then enters a uniform fiber Bragg grating (UFBG1) with its fiber type SMF-28E, reflectivity 84%, and a Bragg wavelength (λ_B) equal to 1310.13 nm. The transmission or UFBG exit is connected with a first photodetector (PD1), whose model is BT-1VE-T, which gives the radio frequency (RF) signal to a mixed storage oscilloscope (MSO) and RF spectrum analyzer. The detect signal is also directed toward the laser bias to mix with its DC bias and then upload selected portions to the laser source. The same scenario is followed with the second output port signal that emerges from the OFS, passing through a second (OFA2), a third (UFBG2), and a fourth (PD2), then finally being added to the laser bias with selected portions. The UFBG2 has a fiber type of SMF-28E, a reflectivity of 83%, and a Bragg wavelength (λ_B) equal to 1310.36 nm. As a result, the laser is subject to selected amounts of opto-electronic feedback (OEF), which originated from itself but passed through two different optical paths. BW is λ_B, remaining abbreviations are given during the text. The figure is drawn by the Optisystem program only for clarity. Photographic picture for selected active run during the experiment operation based on Figure (2, b).

3. RESULTS AND DISCUSSIONS

Based on the configuration given in Figure 1, the laser is subjected to filtered optoelectronic feedback from two different narrow filters, with slightly different. This situation gives the facility for studying the weight of each feedback branch separately, even if both are returned to add to each other's. The laser responds nonlinearly to these feedbacks via optoelectronic feedback. Such a response can give a simulation idea inside the laboratory about the behaviors of nonlinear components in biological cells included in the brain. With such interactions, the communication system is of the electrochemical type. The focus of statistical inference has frequently been on monitoring dynamical variables, like membrane voltage, over time. The results are classified mainly according to optoelectronic feedback level, as shown in Table 1. In which, the measured parameters are the optical powers that flow after attenuation variation plus the laser bias current that resulted after tuning the observed time series by the MSO to recognize the shape of this signal from any side noise that may have been collected due to unwanted effects. The table's last two right columns, which represent the weighted feedback ratio with respect to the two branches, are summarized in the plot numbered with Figure 3.

Table 1. Experimentally measured parameters classified according to feedback strengths

No.	LD measured current (mA)	Measured power after OFA1 (uW)	Measured power after OFA2 (uW)	(OFA1-OFA2) /OFA1	(OFA2-OFA1) /OFA2
1	132.2	1.79	0	100.00%	-
2	131.1	1.79	56.7	-3067.60%	96.84%
3	129.5	27.8	2.5	91.01%	-1012.00%
4	129.5	33.6	6.5	80.65%	-416.92%
5	129.5	42.0	12.1	71.19%	-247.11%
6	129.9	57.02	32.8	42.48%	-73.84%
7	126	57.2	51	10.84%	-12.16%
8	131	67.5	158	-134.07%	57.28%
9	132	64.3	69.2	-7.62%	7.08%
10	130	63.4	8	87.38%	-692.50%
11	133	38.4	69.7	-81.51%	44.91%
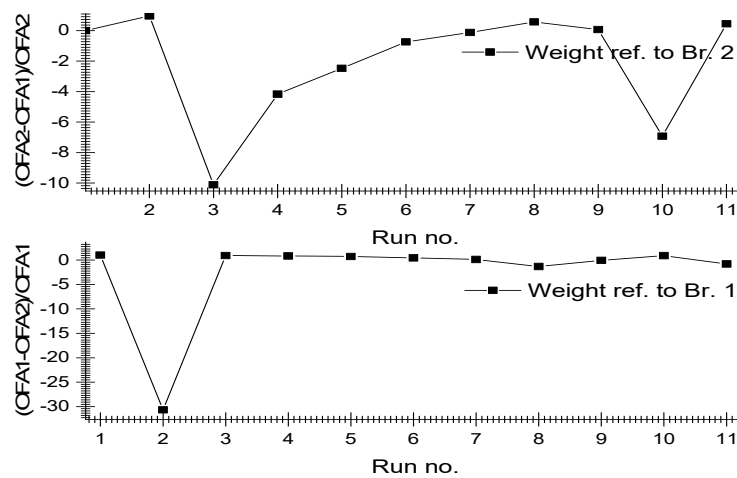
Figure 3. Summery for weighted optical feedback ratios before filtering and detection.

The first step is evaluating the weight of branch one; thus, our selection for operating is investigated with only one feedback branch, where the power is vanished in the second branch, and results show the spectra given in Figure 4.
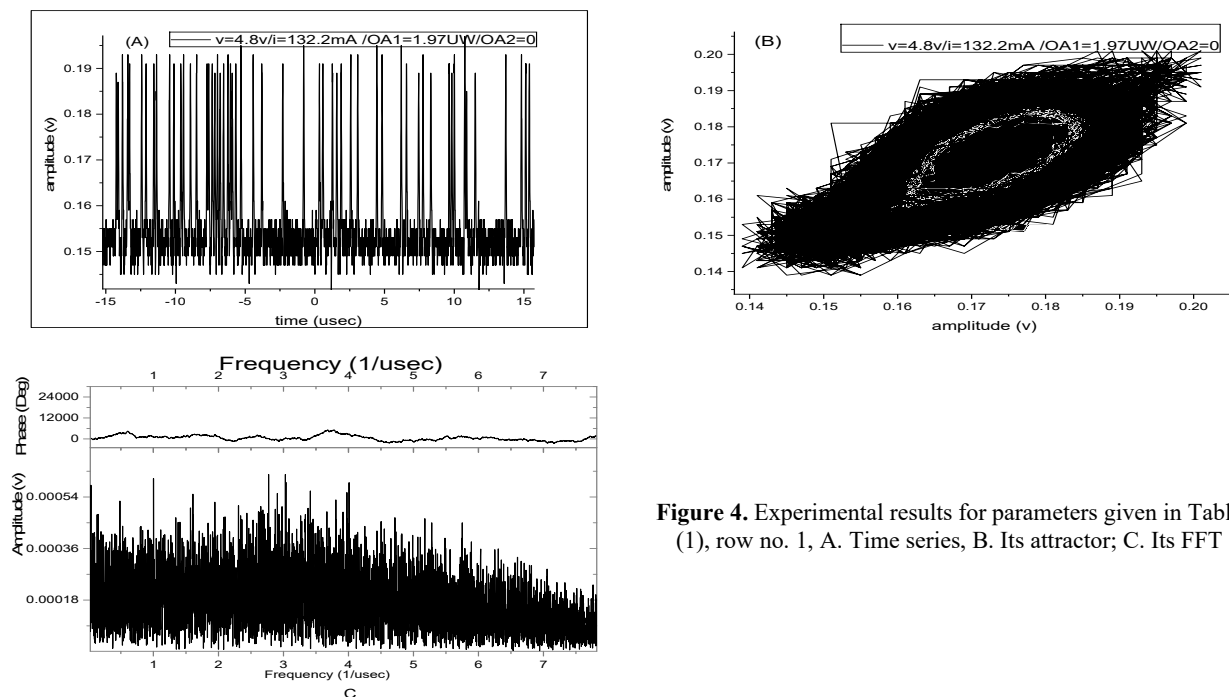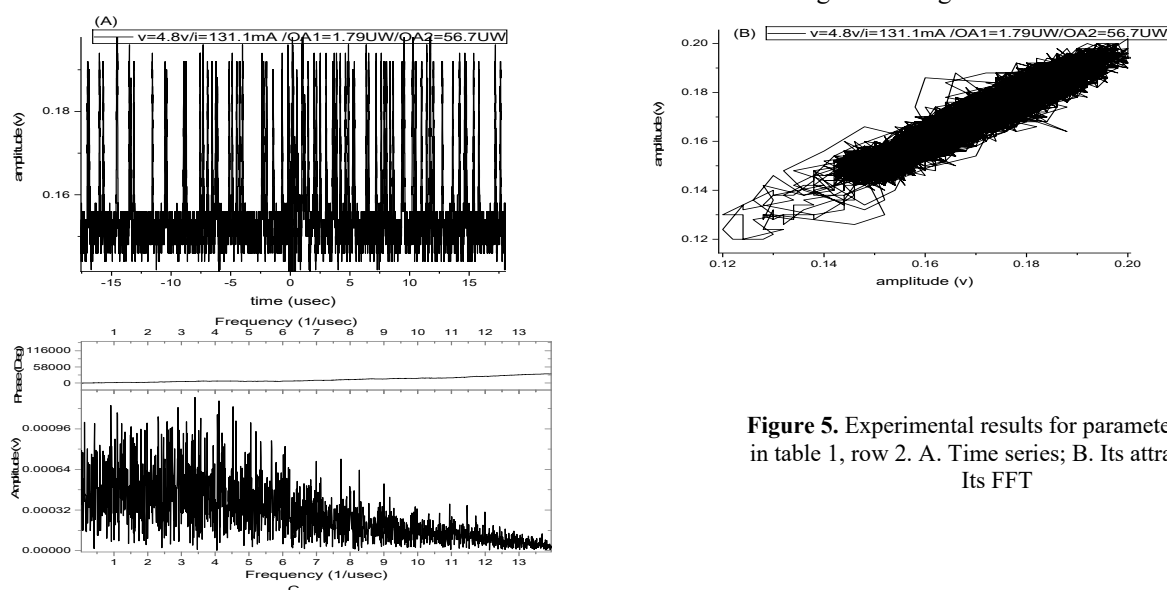

Figure 4. Experimental results for parameters given in Table (1), row no. 1, A. Time series, B. Its attractor; C. Its FFT

Observed time series, uSec scaled, in this figure shows period one and period two emission with a broad and extended limit circle attractor, while the frequency spectrum shows complete chaotic emission with around 7 MHz of

extended spectrum. This observation indicates and reinforces the assumption for the single branch weight in this experiment, where the laser is responding chaotically to its filtered feedback. This result is identical to the operation in single scaled attenuated optoelectronic feedback given in [22], but the difference is located in the feedback ratio after filtering, which is not recorded in that article, i.e., the border frequency spectrum is the result of this observation.

Introducing the second feedback branch contribution, with zero attenuation, affected the resulted spectrum directly; this is observable easily in Figure 5 via the phase and frequency spaces, furthermore time series. Phase space has turned into a fully contiguous area, indicating a huge number of newly generated chaotic modes. The frequency spectrum has a higher amplitude value, roughly twice that in Figure 4, and the overall shape of the signal is identical to a Gaussian curve with 13 MHz extended compared with less in the last-mentioned figure. This observation indicates the weight and contribution of the second feedback branch in the laser, as a nonlinear medium, resulting in dynamics.

Switching the feedback strengths ratio to roughly the same as that given in Figure (5), 91.01% reference to branch one, between the branches leads to different effects on the signal combination entering the laser medium, this being off course due to the difference in filter width that comes from it each branch weight or strength.
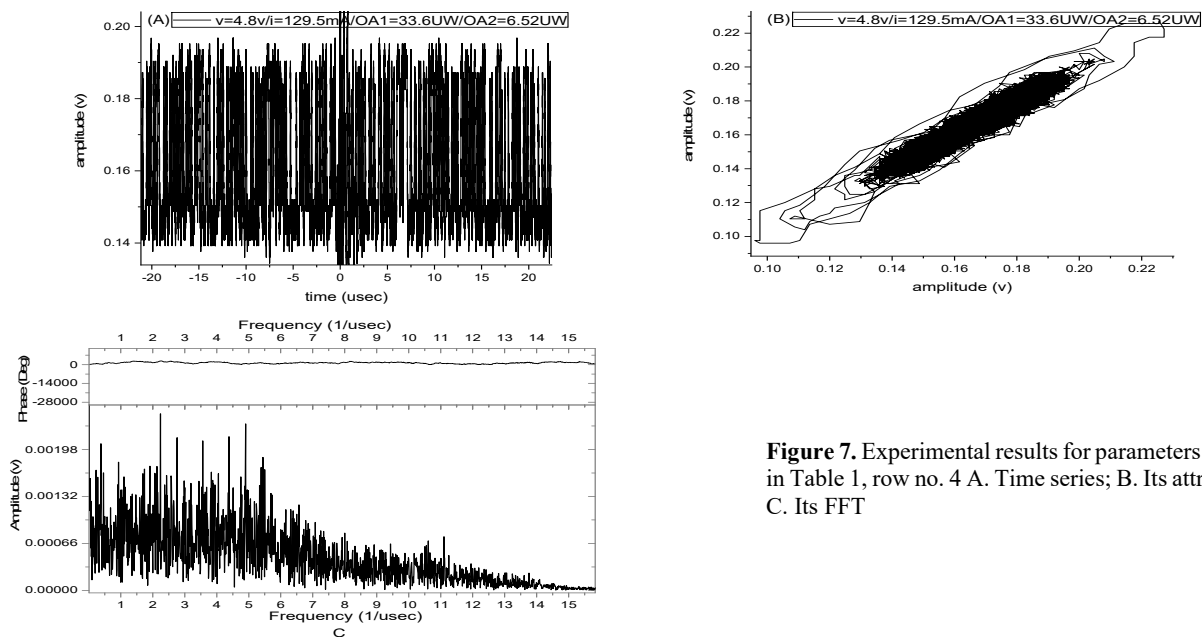

Figure 5. Experimental results for parameters given in table 1, row 2. A. Time series; B. Its attractor; C. Its FFT

As shown in Figure 6, time scale is developed to 2 uSec, and the frequency width for the chaotic signal is also extended to be 130 MHz with a higher amplitude signal, and the attractor having more smooth edges.
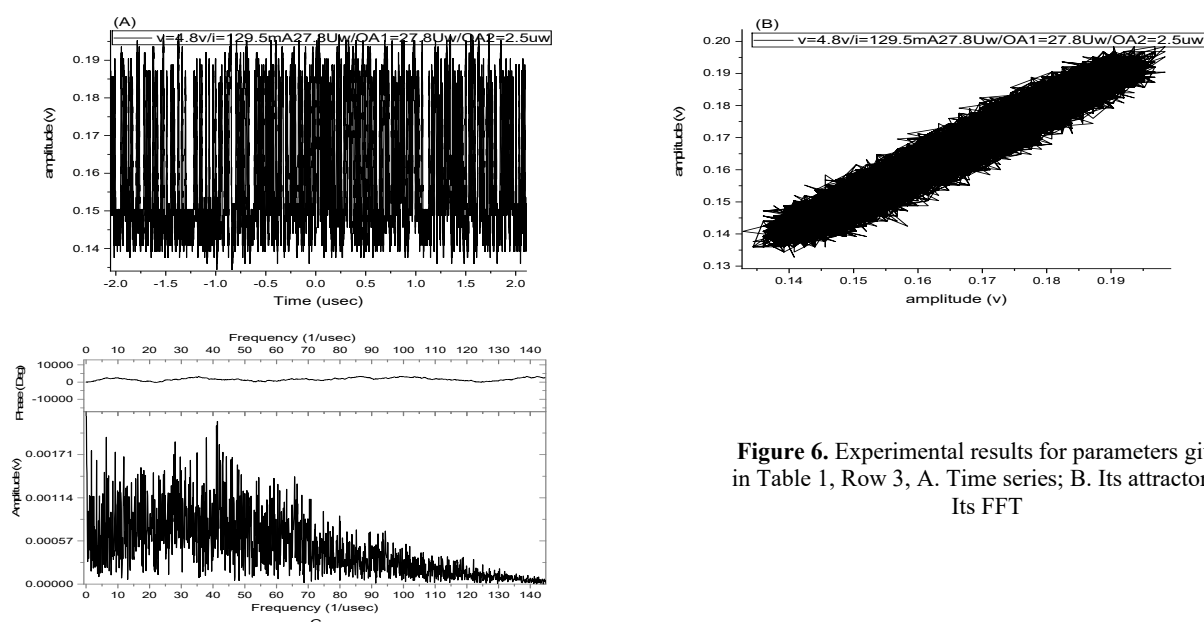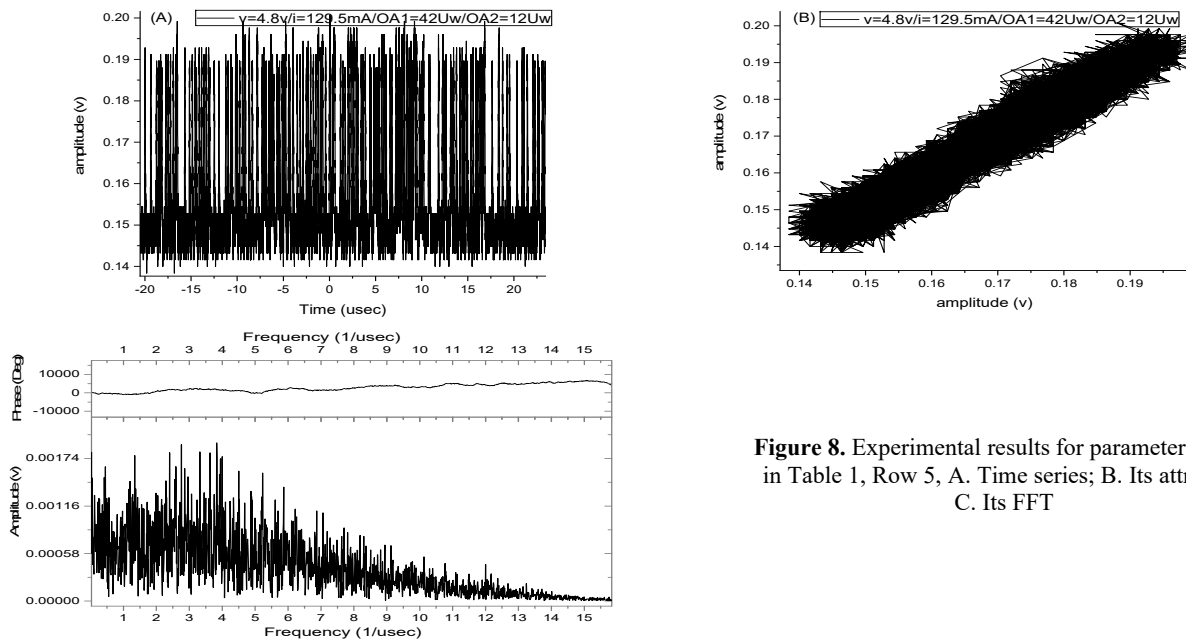

Figure 6. Experimental results for parameters given in Table 1, Row 3, A. Time series; B. Its attractor; C. Its FFT

Slightly deviating from the feedback filtering attenuation, precisely to a new ratio of 11.12 percent between branch one and branch two, the results given in Figure 7 recorded another variation in the observed spectrum, such that the attractor deviated from its original smooth edges to several distinguishable modes in the higher amplitude region. While the frequency spectrum is shrinking to only 13 MHz, the signal shape is now far away from its original Gaussian shape with a slightly higher amplitude.

Figure 7. Experimental results for parameters given in Table 1, row no. 4 A. Time series; B. Its attractor; C. Its FFT

Decreasing the difference between the two feedback branches, the ratio is now 3.5 percent between branch one and branch two, the time series is still chaotic, the phase space repeated its smooth edges, and the frequency spectrum kept its chaotic broadening with a slight difference in overall shape, as shown in Figure 8.

Figure 8. Experimental results for parameters given in Table 1, Row 5, A. Time series; B. Its attractor; C. Its FFT

A few fundamental presumptions form the foundation of theoretical neurophysiology. The nervous system is made up of a network of neurons, each with an axon and a soma. The axon of one neuron and the soma of another are always connected by adjunctions, or synapses. Refs. [5] and [3] reported that a neuron always has a threshold that stimulation must surpass in order to start an impulse. This level can be considered a starting point for the chaotic dynamics emission from the LD. This level of edge-emitted lasers was measured corresponding to the free-running laser threshold, i.e., applied bias voltage into the device with respect to that threshold. As it is mentioned inside all previewed results, the bias voltage selection is located at a faraway value from the laser threshold. The judgment in our selection of that value is the chaotic release that we need to be near from our application requirements. Figure 9 gives the resulted dynamics measurements, which have a ratio of 1.7 percent between branch one and branch two.

Generalization can be done when a layered feedforwarded as a neural network, that is by connecting Adalines to one another. The objective is to select the network's weights in order to obtain the appropriate input/output relationship. The network gets trained during this procedure. When the weights are kept constant, the output vector of the network can be said to be memoryless because it is independent of previous inputs and solely depends on the current input vector. As reported in Table 1 many weights are experimented to make the best selection from them.
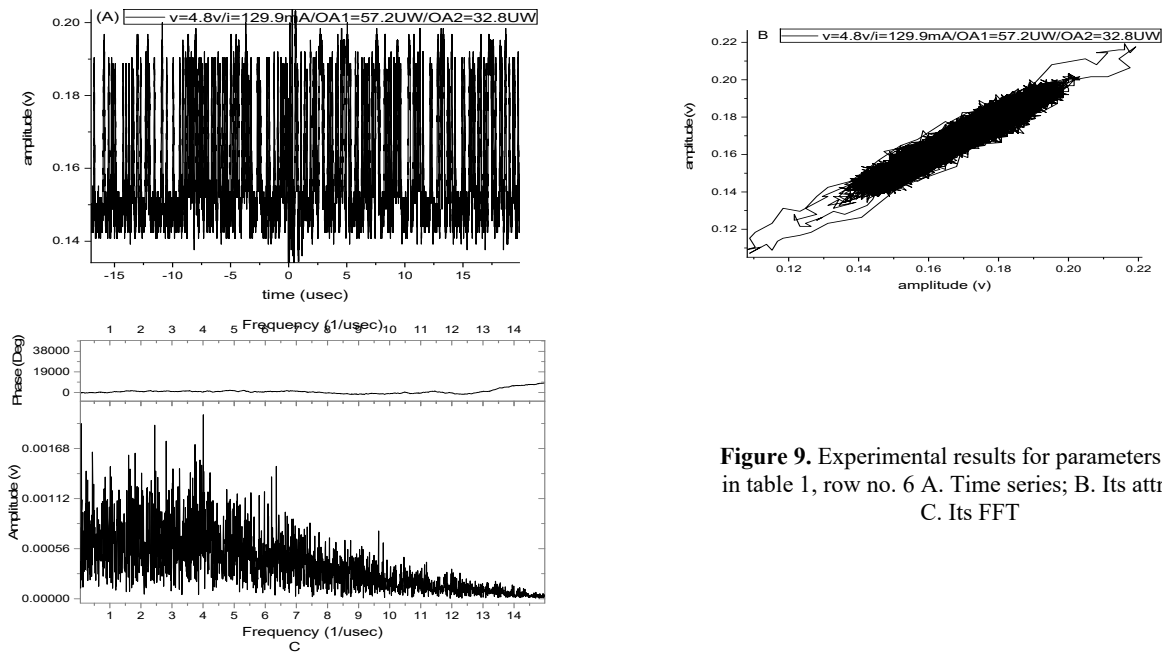
Figure 9. Experimental results for parameters given in table 1, row no. 6 A. Time series; B. Its attractor; C. Its FFT

With 1.13 percent between branch one and two, Figure 10, the lasing chaotic spectrum disappeared; instead, destructive behavior of the signal was observed, indicating only noise emission. The role of FBG is to give the operation loop a gate, i.e., in this operation level, the signal becomes larger in its wavelength spectrum spread, and if all included wavelets have a larger Bragg wavelength, they are blocked from transmission. Refs. [23] and [24] reported that the FBG gate can play the role of a wide or narrow filter to the incident signal according to the relation between the incident wavelength spectrum and its entire Bragg wavelength.
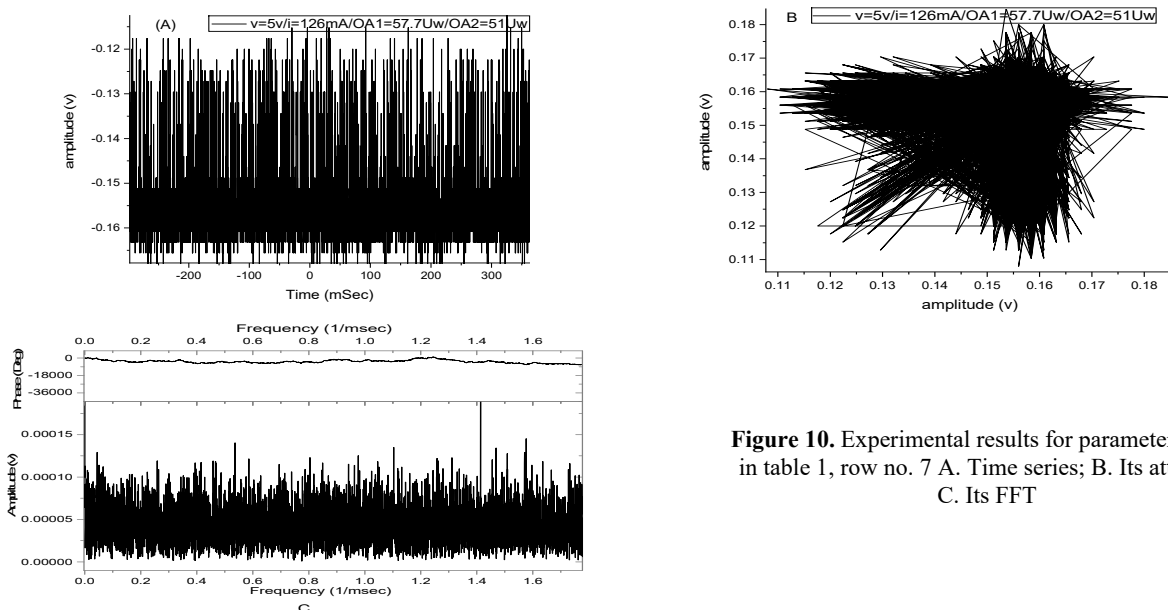
Figure 10. Experimental results for parameters given in table 1, row no. 7 A. Time series; B. Its attractor; C. Its FFT

Working with a 0.425 ratio between branches one and two (Figure 11), the maximum amplitudes return to be apparent, indicating matching between the incident signal and the Bragg wavelength for the filter. Around 7 MHz of chaotic signal width is observed with a circular attractor that includes several outer modes. When the output is modest due to laser medium nonlinearity, the Adaline filter behaves like a linear filter, but as the output amplitude increases, it saturates to +1 or -1. It should be noticed that the default setting for one of Adaline's inputs is +1. This gives the Adaline a technique to provide the weighted sum with a constant bias.

Working with an increased ratio of 0.895 in Figure 12, between branch one and two, the attractor is divided into three regions with a single mode outside of them. The frequency spectrum is extended to about 8 GHz, indicating large filter operation. Figures 13 and 14 give results for ratios of 7.925 and 0.548, respectively, between branches one and two. Both of these two measurements mention the existence of transmission, but with a slightly higher transmission ratio that appears as a broadening in the two observed spectra.
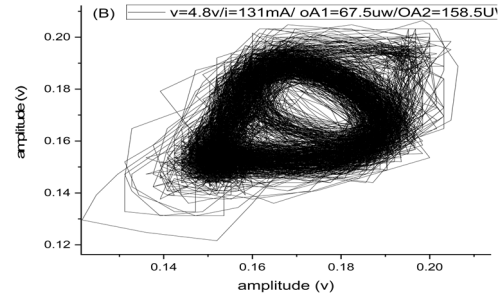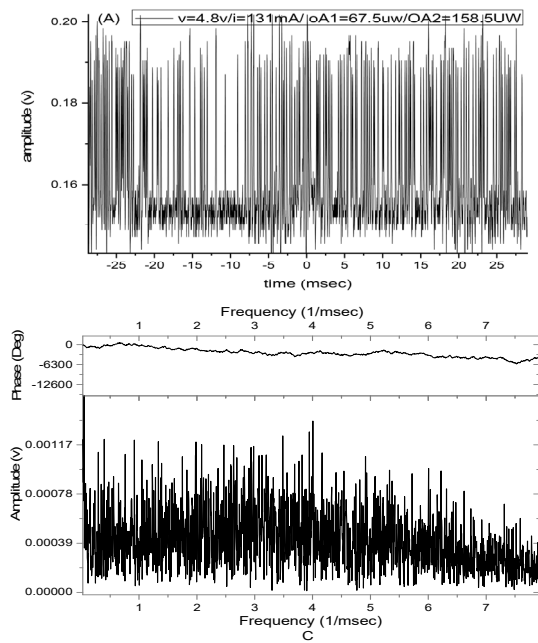
Figure 11. Experimental results for parameters given in table 1, row no. 8 A. Time series; B. Its attractor; C. Its FFT
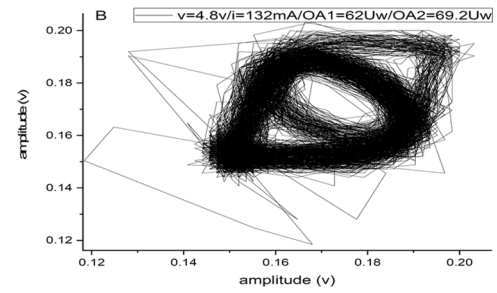

Figure 12. Experimental results for parameters given in table 1, row 9. A. Time series; B. Its attractor; C. Its FFT

Figure 13. Experimental results for parameters given in table 1, row no. 10 A. Time series; B. Its attractor; C. Its FFT
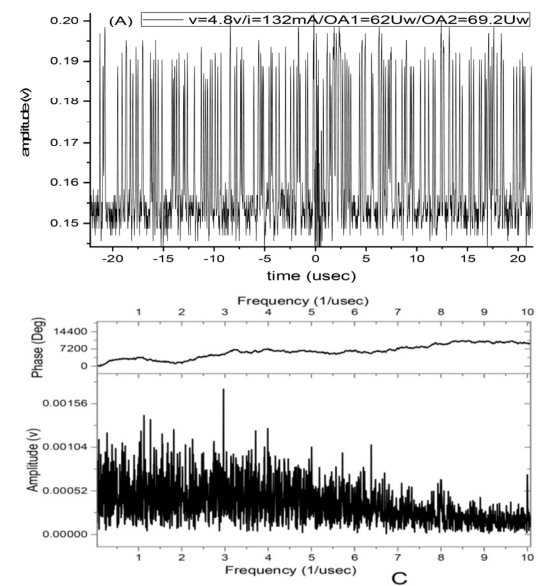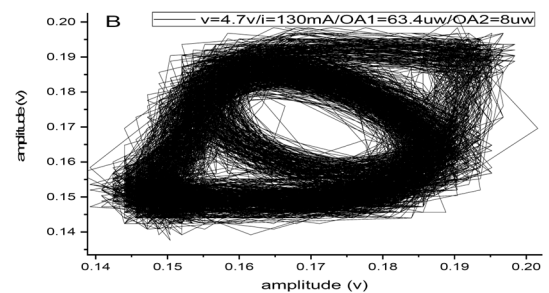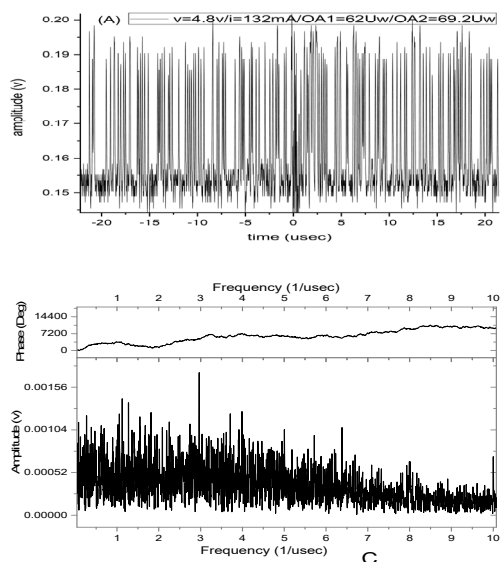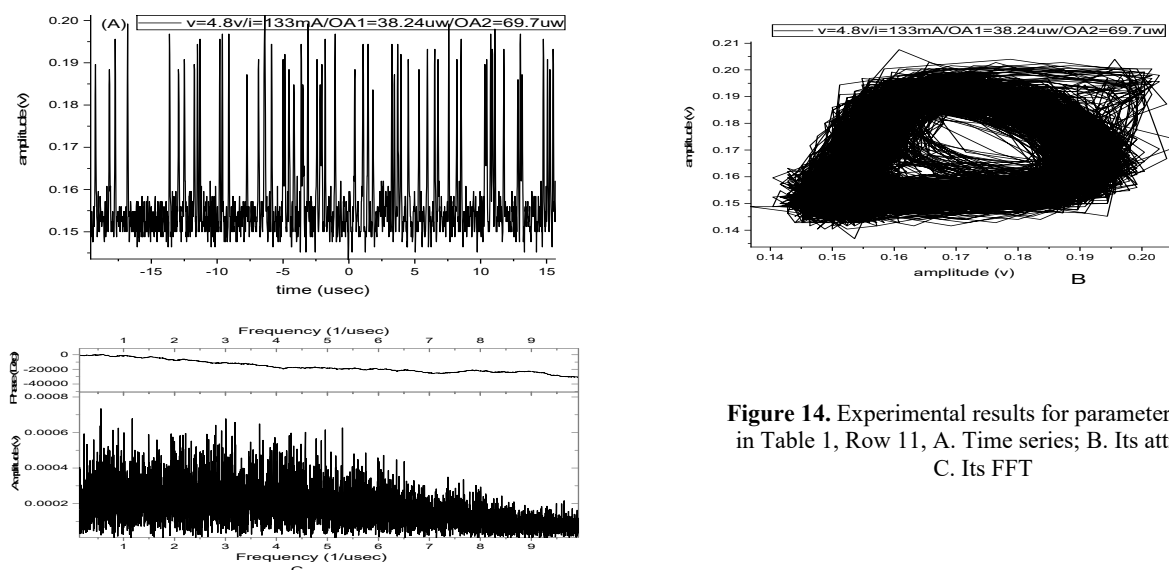
Figure 14. Experimental results for parameters given in Table 1, Row 11, A. Time series; B. Its attractor; C. Its FFT

CONCLUSIONS

The input layer experiment is satisfied, and through experimentation, the all-electrical architecture was contrasted with the hybrid and all-optical approaches. The all-optical technique is comparable to the hybrid strategy in terms of energy efficiency, outperforming the all-electrical approach. The hybrid architecture takes up much less space than the all-optical version because it only uses narrow filters. The feed-back versus feed-forward is tested as a step for the network's construction by combining an increased number of these layers. A ratio of 11.12 percent between branches one and two in this experiment gives a better contribution to the output chaotic signal compared with all measured values.

ORCID IDs

Dhuha Raad Madhloom, https://orcid.org/0009-0008-7053-2754; **Ayser A. Hemed,** https://orcid.org/0000-0003-0319-1650,
Suha Musa Khorsheed, https://orcid.org/0000-0002-9544-3677

REFERENCES

[1] X. Sui, Q. Wu, L. Jia, Q. Chen, and G. Gu, "A Review of Optical Neural Networks," IEEE Access, **8**, 70773-70783 (2020). https://doi.org/10.1109/ACCESS.2020.2987333

[2] N. Kadakia, "Optimal control methods for nonlinear parameter estimation in biophysical neuron models," bioRxiv preprint, 2022. https://doi.org/10.1101/2022.01.11.475951

[3] F.P. Sunny, E. Taheri, M. Nikdast, and S. Pasricha, "A Survey on Silicon Photonics for Deep Learning,"ACM Journal on Emerging Technologies in Computing Systems, **17**(4), 1-57 (2021). https://doi.org/10.1145/3459009

[4] E. Cohen, D. Malka, A. Shemer, A. Shahmoon, Z. Zalevsky, and M. London, "Neural networks within multi-core optic fibers," Scientific Reports, **6**, 1-14 (2016). https://doi.org/10.1038/srep29080

[5] D.H. Nguyen, and B. Widrow, "Neural Networks for Self-Learning Control Systems," IEEE Control Systems Magazine, **10**(3), 18-23 (1990). https://doi.org/10.1109/37.55119

[6] W.S. Mcculloch, and W. Pits, "A logical calculus of the ideas immanent in nervous activity," Bulletin of Mathematical Biophysics, **5,** 115-133 (1943). https://doi.org/10.1007/BF02478259

[7] R.F. Thompson, "The neurobiology of learning and memory," in: *Clinical neuropsychology and brain function: Research, measurement, and practice,* edited by T. Boll, and B.K. Bryant (American Psychological Association, Vashington, 1988). pp. 61-83, https://doi.org/10.1037/10063-002

[8] T. Staff, "Deep learning - 10 breakthrough technologies 2013," MIT Technology Review, 2013.

[9] F.-C.F. Tsai, C.J. O'Brien, N.S. Petrović, and A.D. Rakić, "Analysis of optical channel cross talk for free-space optical interconnects in the presence of higher-order transverse modes," Applied Optics, **44**(30), 6380-6387 (2005). https://doi.org/10.1364/AO.44.006380

[10] R. Clark, L. Fuller, J. Platt, and H.D.I. Abarbanel, "Reduced-Dimension, Biophysical Neuron Models Constructed From Observed Data," Neural Comput. **34**(7), 1545-1587 (2022). https://doi.org/10.1162/neco_a_01515.

A. Uchida, *Optical Communication with Chaotic Lasers: Applications of Nonlinear Dynamics and Synchronization*, (Wiley-VCH Verlag GmbH & Co., KGaA, 2012).

[11] M. Ahmed, A. Bakry, and F. Koyama, "Application of Strong Optical Feedback to Enhance the Modulation Bandwidth of Semiconductor Lasers to the Millimeter-Wave Band," International J. Physical and Mathematical Science, **9**(1), 17-22 (2015). https://doi.org/10.5281/zenodo.1337753

[12] D.R. Hjelme, and A. Mickelson, "On the theory of external cavity operated single-mode semiconductor lasers," IEEE Journal of Quantum Electronics, **23**(6), 1000-1004 (1987). https://doi.org/10.1109/JQE.1987.1073460

[13] G.P. Agrawal, "Effect of gain nonlinearities on period doubling and chaos in directly modulated semiconductor lasers," Applied Physics Letters, **49**(16), 1013-1015 (1986), https://doi.org/10.1063/1.97456

[14] V. Bindu, and V.M. Nandakumaran, "Chaotic encryption using long-wavelength directly modulated semiconductor lasers," Journal of Optics A: Pure and Applied Optics, **4**(2), 115-119 (2002). https://doi.org/10.1088/1464-4258/4/2/301

[15] G.P. Agrawal, and N.K. Dutta, *Semiconductor Lasers*, Second Edition, (Dordrecht: Kluwer Academic Publishers, 1993).

[16] F.-Y. Lin, and J.-M. Liu, "Nonlinear Dyanmic of Semiconductor Laser with Delayed Optoelectronic Feedback," IEEE Journal of Quantum Electronics, **39**(4), 562-568 (2003), https://doi.org/10.1109/JQE.2003.809338

[17] G. Giacomelli, M. Calzavara, and F.T. Arecchi, "Instabilities in a semiconductor laser with delayed optoelectronic feedback," Optics Communications, **74**(1-2), 97-101 (1989). https://doi.org/10.1016/0030-4018(89)90498-7

[18] H. Erzgraber, B. Krauskopf, D. Lenstra, A. Fischer and G. Vemuri, , *Phys Rev E Stat Nonlin Soft Matter Phys,* **76**, no. 2, (2007), https://doi.org/10.1103/PhysRevE.76.026212

[19] A. Hemed, Ph.D. dissertation, University of Baghdad-Iraq, 2011.

[20] V.L. Kalyani, and V. Sharma, "Different types of optical filter and their application," Journal of Management Engineering and Information Technology, **3**(3), 12-17 (2016).

[21] A.M. Suhail, B.T. Chead, H.J. Kbashi, and A.A. Hemed, "Studying the effect of variant optoelectronic feedback on chaos generation," Atti della Fondazione Giorgio Ronchi, Chaos, Anno, **LXV**(2), 147-154 (2010).

[22] Z.R. Ghayib, Ph.D. dissertation, College of Education at Mustansiriyah University, 2022.

[23] A. Hemed, and Z.R. Gaiab, in: *2022 International Conference on Computer Science and Software Engineering CSASE*, Duhok, Kurdistan Region – Iraq, 2022. https://doi.org/10.1109/csase51777.2022.9759612

[24] G. Fennessy, and Y. Vorobeychik, "Optical Neural Networks," https://doi.org/10.48550/arXiv.1805.06082

ЕКСПЕРИМЕНТАЛЬНЕ МОДЕЛЮВАННЯ ДВОХ ОПТИЧНО ФІЛЬТРОВАНИХ МОДУЛЯЦІЙНИХ ВАГ В ЛАЗЕРНОМУ ДІОДІ ЯК ШАРІ З САМОНАВЧАННЯМ

Дхуха Раад Мадлум[a], Айсер А. Хемед[b], Суха Муса Хоршід[a]
[a]Факультет фізики, Науковий коледж, Університет Аль-Нахрейн, Багдад, Ірак
[b]Факультет фізики, Педагогічний коледж, Університет Мустансірія, Багдад, Ірак

У цьому дослідженні експериментально досліджено відгук нелінійного лазерного середовища. У дослідженні гібридна версія вхідного шару, який розмножується оптично та накопичує електрично, порівнюється з повністю оптичною версією, яка розмножується та накопичує оптично. Це середовище зазнає двох різних шляхів оптично відфільтрованого та ослабленого зворотного зв'язку. У такій системі зміна ваги зворотного зв'язку в одному з них перевіряється відповідно до другого. Спостереження за частотними спектрами проводяться для моделювання результуючої реакції з вхідним рівнем для нейронної мережі на основі хаотичних несучих. Хаотичне лазерне випромінювання спостерігалося як функція кількох керуючих параметрів, якими є напруга зміщення постійного струму, оптичне загасання в гілці та інтенсивність зворотного зв'язку на основі фільтрації за допомогою волоконної ратки Брегга. Це правило навчання є лінійним у різниці між кожним входом і виходом нейрона. Це правило посилення/затримки. Пороги регулюються таким чином, що вихід нейрона або підштовхується в тому ж напрямку, що і вхід (посилення), або в протилежному напрямку (гальмування).

Ключові слова: *машинне навчання; нейронна мережа; хаотична модуляція; лазерний діод*

REEVALUATION BODY WEIGHT AND AGE WITH STANDARDIZED UPTAKE VALUE IN THE LIVER CANCER FOR [18F] FDG PET/CT[†]

Aya B. Hade[a], Satar M. Kadam[b], Samar I. Essa[a],*

aDepartment of Physics, College of Science, University of Baghdad, Baghdad, Iraq
bDepartment of Surgery, College of Medicine, University of Baghdad, Baghdad, Iraq
*Corresponding Author: samar.o@sc.uobaghdad.edu.iq

Standardized uptake values, often known as SUVs, are frequently utilized in measuring 18F-fluorodeoxyglucose (FDG) uptake in malignancies. In this work, we investigated the relationships between a wide range of parameters and the standardized uptake values (SUV) found in the liver. Examinations with 18F-FDG PET/CT were performed on a total of 59 patients who were suffering from liver cancer. We determined the SUV in the liver of patients with a normal BMI (between 18.5 and 24.9) and a high BMI (above 30) obese, after adjusting each SUV based on the results of the body mass index (BMI) and body surface area (BSA) calculations, which were determined for each patient based on their height and weight. Under various circumstances, SUVs were evaluated based on their means and standard deviations. Scatterplots were created to illustrate the different weight and SUV variances. In addition to that, the SUVs that are appropriate for each age group were determined. SUVmax in the liver was statistical significance in obese BMI and higher BSA, p-value < 0.001). Age appeared to be the most important predictor of SUVmax and was significantly associated with the liver SUVmax with mean value (58.93±13.57). Conclusions: Age is a factor that contributes to variations in the SUVs of the liver. These age-related disparities in SUV have been elucidated due to our findings, which may help clinicians conduct more accurate assessments of malignancies. However, the SUV overestimates the metabolic activity of every individual, and this overestimation is far more severe in people who are obese compared to people who have a body mass index that is normal (BMI).
Keywords: 18F-FDG-PET/CT); Standardized Uptake Value (SUV); Liver; BMI; Age Variation
PACS: 87.57.-s, 87.57.-C, 87.57.U-, 87.57.uk

1. INTRODUCTION

In the present day, (18F-FDG) PET/CT scan is frequently used for staging, restaging, recurrence identification, and tracking of therapeutic response in a variety of malignant diseases [1]. 18F-FDG PET/CT identifies malignant lesions by combining metabolic and anatomical information. To accomplish this, areas with rapid glycolytic metabolism and expression of membrane glucose transporter (GLUT) proteins are located and mapped out [2]. Malignant lesions aren't the only type of lesion that can have increased FDG uptake; infections and inflammatory lesions can also have this effect. Therefore, various more lesions that may demonstrate FDG uptake could be located in the head, neck, lung, mediastinum, belly, pelvis, bones, joints, lymph nodes, or vascular system [3].

Studies on the benefits and drawbacks of various methods of assessing tissue 18F FDG accumulation on PET/CT, such as glucose utilization rate (MRglu) [4], FDG clearance, and standardized uptake value, have been carried out in a number of different instances. Examples of these methods include glucose utilization rate (MRglu) (4). (SUV). The parameter SUV, which quantifies the amount of tissue FDG concentration per FDG unit, is the one that is used the most often and the most widely [5].

As a practical and semiquantitative indicator for FDG accumulation in tissue, the standardized uptake value (SUV) has been presented as a useful tool. To determine it, divide the patient's body weight by the ratio of the amount of activity present in the tissue per milliliter to the amount of activity contained in the injected dose [6]. The distribution absorption ratio, often known as the SUV, goes by a few distinct names. One of them is the differential uptake ratio [7,8].

On the other hand, mistakes in liver SUV could be the result of a number of different physiologic factors. These factors, which also include age, gender, body mass index, serum glucose level, hepatic function, and hyperthyroidism, might lead to inaccurate PET/CT findings that are either false-positive or false-negative [9]. Therefore, in order for medical professionals to properly interpret PET/CT images of the liver, it is necessary to first determine the normal SUV of the liver. According to an increasing number of studies, an SUV's age may have a major impact on its performance. It is essential to provide scientific rigor and enable repeatability by determining a precise range of liver SUVs using 18F-FDG PET/CT in multi-aged groups [10].

Despite the fact that many researchers have used SUV as a useful semiquantitative indicator for evaluating FDG uptake in tissue, it was recently shown that SUV has a substantial positive association with patient body weight, rising by 70%-98% from patients with low weight to those with high weight. This discovery was made despite the fact that many researchers have been using SUV in this capacity. Despite the fact that a large number of researchers have been used SUV as a helpful semiquantitative indicator for evaluating FDG uptake in tissue, this was found to be the case [11].

The purpose of this study was to examine the association between age and body weight and standardized uptake value in liver cancer patients.

---

2. MATERIALS AND METHODS

Between November 2022 and December 2022, participants aged 15 to 85 were referred to the Al-Andalus Specialist Hospital. The study included 59 participants (24 male and 35 female) individuals. The participants' average age was 58.01 ± 13.18 years. The hospital's ethical committee accepted our study, and informed patient consent was obtained prior to doing PET/CT scans.

In the course of our investigation, we made use of a Discovery IQ PET/CT scanner (GE Healthcare, Milwaukee, WI, USA). This scanner's detector was made up of $Bi_4Ge_3O_{12}$ (BGO) crystals, each of which measured 6.3 by 6.3 by 30 millimeters. At the one-bed position, the transaxial field of vision (FOV) measured 700 millimeters, the axial field of view measured 260 millimeters, and 79 axial slices were acquired. The window width for the energy range was 435-650 keV, and the window width for the coincidence time range was 9.5 ns. We obtained a matrix with a dimension of 192 by 192, and the thickness of each slice was 3.27 millimeters. The amount of slice overlap that occurred between beds was 19 slices.

Patients who had had a blood sugar concentration in their fasting blood that was more than 200 mg/dL at the time of the examination were not permitted to take part in any aspect of the study. Before receiving an injection of ^{18}F-FDG, all of the patients went without food for at least four to six hours. Before giving ^{18}F-FDG to the patient, an intravenous cannula was put in the patient's arm or hand, and a blood sample was obtained to determine the patient's glycemia. Images were taken 45–90 minutes following injection of the FDG. Patients were placed in a supine position with both of their arms elevated. The emission acquisition time per bed position was (1.5-3) minutes. By collecting or calculating these characteristics for each patient, the association between patient-dependent factors and ^{18}F-FDG PET image quality was studied. Height and body mass index (BMI) were retrieved from patient data. Determine the body mass index (BMI).

$$BMI = \frac{weight \ in \ kg}{\left(height \ in \ m\right)^2}. \tag{1}$$

The World Health Organization categorizes body mass index (BMI) as follows: underweight (BMI 18.5 kg/m^2), normal (18.5 – 24.99 kg/m^2), overweight (25 – 30 kg/m^2), and obese ($\leq$ 30 kg/m^2) [12].

Using the following formula, the body surface area (BSA) was calculated [13].

$$BSA(m^2) = (weight \ in \ kg)^{0.425} \times (height \ in \ m)^{0.725} \times 0.007184. \tag{2}$$

2.1. Statistical Analysis

To express all results, the mean and standard deviation (SD) were utilized. All statistical analysis was performed using Microsoft Office Excel 2013. The definition of statistical significance was a p-value less than 0.05.

3. RESULTS

The relationships between SUV and patient body weight are shown in Figure 1. There was statistically significant difference between the SUV and patient body weight ($p < 0.001$). The mean values and SD for body weight (kg) were 78.19 ± 16.18.
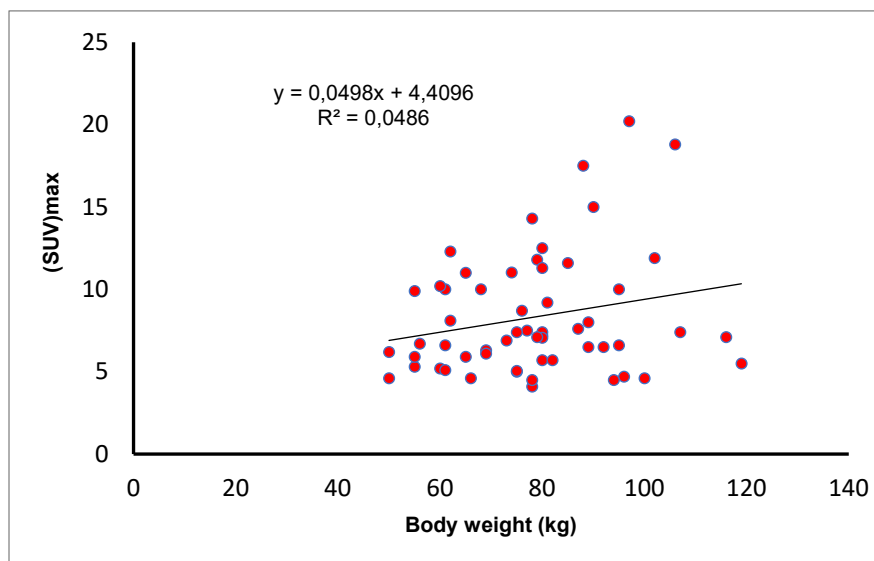

Figure 1. Relationships between patient body weight and SUV.

Statistically significant positive associations existed between BMI and SUVmax ($R^2 = 0.122$, $p < 0.0001$), as shown in Figure 2.
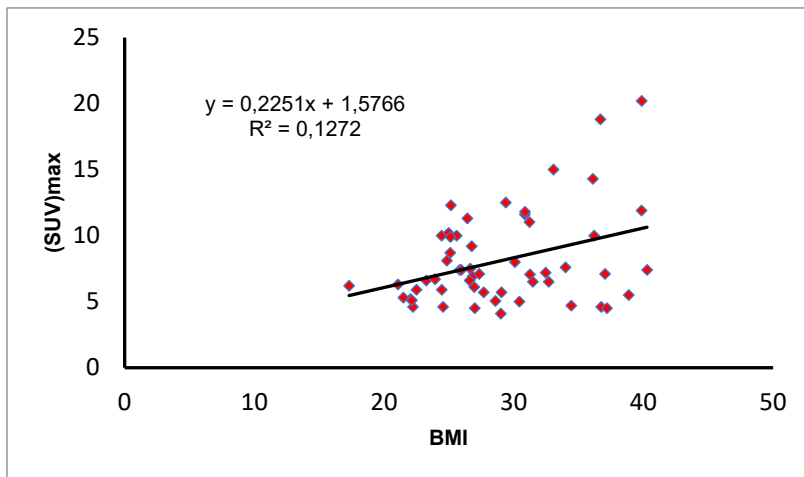
Figure 2. Relationships between BMI and SUV.

Mean BSA was 0.065 ± 0.0070 m². The results of the curve fitting of SUV and BSA shows for curve the ($R^2 = 0.0141$) with significant difference ($p < 0.0001$) (see Fig. 3).
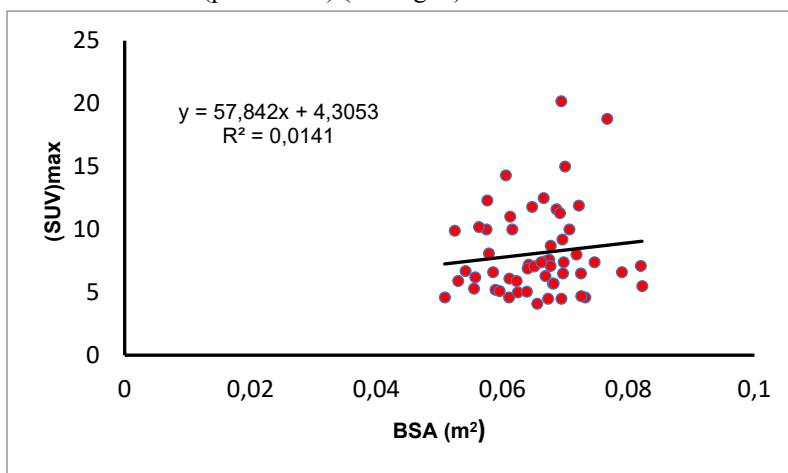
Figure 3. Relationships between BSA and SUV.

When we plotted the SUVmax versus patient age, there was a strong (and significant) $p < 0.001$) (Fig. 4).
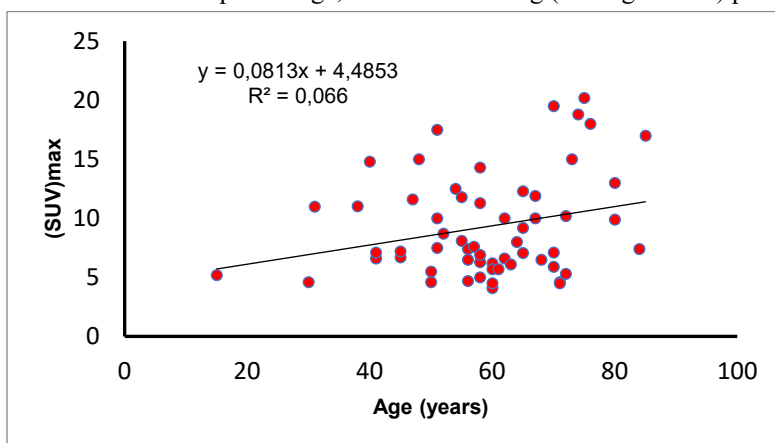
Figure 4. Relationships between age and SUV.

4.   DISCUSSION

Visually evaluating PET scans for regions of abnormal uptake is accurate and sufficient. However, depending on the PET investigation, a quantitative or semiquantitative technique can analyze factors such as metabolic activity, perfusion, and receptor density of lesions and tissues more precisely. These assessments are essential for establishing the grade of the cancer, determining the therapeutic agent dosage, and comparing post-treatment with pre-treatment studies [14].

SUV is the most common PET parameter used to evaluate radiopharmaceutical absorption in malignancies and healthy tissues. Although SUV can be affected by a variety of human, biological, and technological factors that could cause an overestimation or underestimating of activity, it nevertheless reliably predicts the degree of absorption in lesions and normal tissues. Suboptimal patient preparation, high blood sugar and insulin levels, diabetes, body mass index, age, sex, the time of imaging after radiotracer injection, significant extravasation of activity, the image acquisition and reconstruction parameters, circumstances during the post injection uptake period, and inaccurate entry of patient weight, height, and injected activity can all affect ^{18}F-FDG uptake [9].

The liver deoxyglucose metabolism of adolescents is significantly lower than that of adults. The increase in ^{18}F-FDG uptake during development may be a result of age-related alterations in hepatocyte quantity, number, and function [15]. A rise in ^{18}F-FDG uptake may also be explained by the substantial changes in body size, body composition, and blood volume that occur during development. In addition to body size and age, changes in uptake duration, plasma glucose, recovery coefficient, and partial volume artifacts affected SUV results [16]. Meier and colleagues postulated, however, that age-related hepatotoxins may have triggered cumulative inflammatory changes [17].

There are numerous possible biological causes for the observed age-related SUV changes in our study. We hypothesize that organ degeneration, organ metabolism, and molecular transport could explain the pertinent mechanisms. In overweight and obese patients, SUV is typically overstated in lesions and normal tissues; in heavy patients, SUVs of liver were up to twice as high as those in lighter patients (figure 1). Both body surface area and body mass index were calculated on the basis of patient body weight and height; there was a strong positive correlation between both indices with SUV, Figures 2 and 3.

5. CONCLUSION

SUV overestimates metabolic activity in all patients, although the effect is particularly pronounced in obese individuals. Age was found to have the greatest effect of all the variables that influence the liver SUV. We discovered age-related changes in the physiological absorption of FDG by the liver. Before analyzing oncologic whole-body PET/CT scans, it must be proven that the liver's background SUV is within the age-dependent reference limits.

ORCID IDs
Aya B. Hade, https://orcid.org/0000-0002-1246-3024; **Satar M. Kadam,** https://orcid.org/0000-0001-8519-8463
Samar I. Essa, https://orcid.org/0000-0001-9821-2279

REFERENCES

[1] M.R. Hasan, S.M. Kadam, and S.I. Essa, "Diffuse Thyroid Uptake in FDG PET/ CT Scan Can Predict Subclinical Thyroid Disorders," Iraqi Journal of Science, **63**(5), 2000-2005 (2022). https://doi.org/10.24996/ijs.2022.63.5.15

[2] R.L. Wahl, "Targeting glucose transporters for tumor imaging: "sweet" idea, "sour", result," J. Nucl. Med, **37**, 1038-1041 (1996). https://jnm.snmjournals.org/content/jnumed/37/6/1038.full.pdf

[3] A.D. Culverwell, A.F Scarsbrook, and F.U. Chowdhury, "False-positive uptake on2-[(1)(8)F]-fluoro-2-deoxy-D-glucose (FDG)positron-emission tomography/computed tomography (PET/CT) in oncological imaging," Clin. Radiol. **66**, 366-382 (2011). https://doi.org/10.1016/j.crad.2010.12.004

[4] S.G. Hasselbalch, G.M. Knudsen, B. Capaldo, A. Postiglione, and O.B. Paulson, "Blood-brain barrier transport and brain metabolism of glucose during acutehyperglycemia in humans," J. Clin. Endocrinol. Metab, **86**, 1986-1990 (2001). https://doi.org/10.1210/jcem.86.5.7490

[5] B. Bai, J. Bading, and P.S. Conti, "Tumor quantification in clinical positron emissiontomography", Theranostics, **3**(10), 787-801 (2013). https://doi.org/10.7150%2Fthno.5629

[6] L.G. Strauss, and P.S. Conti, "The application of PET in clinical oncology", J. Nucl. Med. **32**, 623-648 (1991). https://jnm.snmjournals.org/content/jnumed/32/4/623.full.pdf

[7] K. Kubota, T. Matsuzawa, M. Ito, K. Ito, T. Fujiwara, Y. Abe, S. Yoshioka, et al. "Lung tumor imaging by positron emission tomography using C-11 L methionine," J. Nucl. Med. **26**, 37-42 (1985). https://jnm.snmjournals.org/content/jnumed/26/1/37.full.pdf

[8] L.G. Strauss, J.H. Clorius, P. Schlag, B. Lehner, B. Kimmig, R. Engenhart, M. Marin-Grez, et al. "Recurrence of colorectal tumors: PET evaluation," Radiology, **170**, 329-332 (1989). https://doi.org/10.1148/radiology.170.2.2783494

[9] I. Sarikaya, A. Sarikaya, and P. Sharma, "Assessing effect of various blood glucose levels on ^{18}F-FDG activity in the brain, liver and blood pool," J. Nucl. Med. Technol. **47**(4), 313-318 (2019). https://doi.org/10.2967/jnmt.119.226969

[10] M.H. Mahmud, A.J. Nordin, F.F. Ahmad, and A.Z.F. Azman, "Impacts of biological and procedural factors on semiquantification uptake value of liver in fluorine-18 fluorodeoxyglucose positron emission tomography/ computed tomography imaging," Quant Imaging Med. Surg. **5**, 700-707 (2015). https://doi.org/10.3978%2Fj.issn.2223-4292.2015.05.02

[11] C.K. Kim, N.C. Gupta, B. Chandramouli, and A. Alavi, "Standardized Uptake Values of FDG: Body Surface Area Correction is Preferable to Body Weight Correction," J. Nucl. Med. **35**, 164-167 (1994). https://jnm.snmjournals.org/content/jnumed/35/1/164.full.pdf

[12] C.Y. Lin, W.Y. Lin, C.C. Lin, C.M. Shih, L.B. Jeng, and C.H. Kao, "The negative impact of fatty liver on maximum standard uptake value of liver on FDG PET," Clin. Imaging, **35**, 437-441 (2011). https://doi.org/10.1016/j.clinimag.2011.02.005

[13] C.P.W. Cox, D.M.E. van Assema, F.A. Verburg, T. Brabander, M. Konijnenberg, and M. Segbers, "A dedicated paediatric [^{18}F] FDG PET/CT dosage regimen," EJNMMI Res. **11**, 65 (2021). https://doi.org/10.1186/s13550-021-00812-8

[14] G.G. Bural, D.A. Torigian, A. Burke, M. Houseni, K. Alkhawaldeh, A. Cucchiara, S. Basu, and A. Alavi, "Quantitative assessment of thehepatic metabolic volume product in patients with diffuse hepatic steatosisand normal controls through use of FDG-PET and MR imaging: a novelconcept," Mol. Imaging Biol. **12**, 233-239 (2010). https://doi.org/10.1007/s11307-009-0258-4

[15] WHO, *Building foundations for health, progress of member states: report of the WHO Global observatory for health*, (World Health Organization, 2006).

[16] M. Fani, G.P. Nicolas, and D. Wild, "Somatostatin receptor antagonists for imaging and therapy," J. Nucl. Med. **58**(Suppl. 2), 61S-66S (2017). https://doi.org/10.2967/jnumed.116.186783

[17] J. Sastre, F.V. Pallardó, R. Plá, A. Pellín, G. Juan, J.E. O'Connor, J.M. Estrela, J. Miquel, and J. Viña, "Aging of the liver: age-associated mitochondrial damage in intact hepatocytes," Hepatology, **24**(5), 1199-1205 (1996). https://doi.org/10.1002/hep.510240536

ПЕРЕОЦІНКА МАСИ ТІЛА ТА ВІКУ ЗА СТАНДАРТИЗОВАНИМ ЗНАЧЕННЯМ ПОГЛИНАННЯ ПРИ РАКУ ПЕЧІНКИ ДЛЯ [¹⁸F] FDG PET/CT

Ая Б. Хаде[a], Сатар М. Кадам[b], Самар I. Есса[a]

[a]*Департамент фізики, Науковий коледж, Багдадський університет, Багдад, Ірак*
[b]*Департамент хірургії, Медичний коледж, Багдадський університет, Багдад, Ірак*

Стандартизовані значення поглинання, часто відомі як SUV, часто використовуються в процесі вимірювання поглинання ¹⁸F-фтордезоксиглюкози (FDG) при злоякісних пухлинах. У цій роботі ми досліджували зв'язки між широким діапазоном параметрів і стандартизованими значеннями поглинання (SUV), виявленими в печінці. Обстеження за допомогою ПЕТ/КТ ¹⁸F-FDG проведено 59 пацієнтам, які страждали на рак печінки. Ми визначали SUV у печінці пацієнтів із нормальним ІМТ (від 18,5 до 24,9) та високим ІМТ (вище 30) із ожирінням. Після коригування кожного SUV на основі результатів розрахунків індексу маси тіла (ІМТ) і площі поверхні тіла (ППТ), які визначали для кожного пацієнта на основі їх росту та ваги. За різних обставин позашляховики оцінювали на основі їх середніх значень і стандартних відхилень. Діаграми розсіювання були створені, щоб проілюструвати різні відхилення ваги та SUV. Крім того, були визначені позашляховики, які підходять для кожної вікової категорії. SUVmax у печінці був статистично значущим при ІМТ із ожирінням та вищим BSA, p-значення <0,001. Вік виявився найважливішим предиктором SUVmax і був суттєво пов'язаний із SUVmax печінки із середнім значенням (58,93±13,57). Висновки: вік є чинником, який сприяє змінам SUV печінки. Ці вікові відмінності в SUV були з'ясовані в результаті наших висновків, що може допомогти клініцистам у більш точному оцінюванні злоякісних новоутворень. Однак SUV переоцінює метаболічну активність кожного окремого індивідуума, і це переоцінка є набагато серйознішим у людей з ожирінням порівняно з людьми з нормальним індексом маси тіла (ІМТ).

Ключові слова: *¹⁸F-FDG-PET/CT); стандартизоване значення поглинання (SUV); печінка; ІМТ; вікова варіація*

THE EFFECT OF DIFFUSENESS PARAMETER ON THE QUASI-ELASTIC SCATTERING OF THE ^{25}Mg + ^{90}Zr and ^{28}Si + (^{120}Sn, ^{150}Nd) SYSTEMS USING WOOD-SAXON POTENTIAL[†]

Farah J. Hamood[§], Khalid S. Jassim*

Department of Physics, College of Education for pure Sciences, University of Babylon, Iraq.
[§]E-mail: pure.farah.jabar@uobabylon.edu.iq
Corresponding Author e-mail: khalidsj@uobabylon.edu.iq
Received march 12, 2023; revised April 30, 2023; accepted May 2, 2023

In this research, the effect of changing the values of the diffusion parameter on the semi-elastic scattering ($\frac{d\sigma qel}{d\sigma R}$) and distribution (D) calculations for single channel (SC) and coupled channel (CC) have been studied. Three values were taken from the diffusion for each system parameter. It is assumed that the nuclear potential has a Woods-Saxon form, which is indicated by the surface diffuseness, potential depth, and radius parameters for (^{25}Mg + ^{90}Zr), (^{28}Si + (^{120}Sn, ^{150}Nd) Systems. The chi square (χ^2) is applied to compare the best fitted value of the diffuseness parameter between the theoretical calculations and the experimental data. According to the results of (χ^2), we noticed that some systems achieved a good match between the theoretical calculations and experimental data of semi-elastic scattering ($\frac{d\sigma qel}{d\sigma R}$) and the distribution calculations at the standard value of the diffusion parameter (a_0=0.63) or at a value higher and lower than the standard value .In the case of channel is single SC the best fit was at a value less than the standard value of the diffusivity parameter, but in the case of CC the fit was better at a value higher than the standard value of the surface diffuseness parameter because the potential barrier in the single SC, while in CC calculations it is multiple.
Keywords: *Quasi-elastic scattering; Woods-Saxon potential; Single channel; Coupled channels; Surface diffuseness parameter; Heavy-ion system*
PACS: 21.60.-n, 21.10.-k, 21.60.Jz, 25.70.Bc, 25.70.

1. INTRODUCTION

The Nuclear reactions at sub-barrier energy are crucial in nature, since they are responsible for the basic behavior of stars, their development, and many aspects of element production. The nucleus potential is consist from Coulomb $V_C(r)$ and nuclear $V_N(r)$ parts [1][2]. The Woods-Saxon (WS) form is often used to represent the nuclear component, which is characterized by the deepness V_0, radius r_0, and diffuseness a_0 parameters. It is significant in nuclear physics because it is regarded as a realistic potential [3]. Experiments indicate that coupling to collective states results in a distribution of Coulomb barrier heights, which may be calculated directly from the fusion excitation function σ_{fus} (E) or from back scattered quasi elastic events for many nuclear systems. A significant method for the investigation of barrier distributions near to the Coulomb barrier is large back-angle quasi elastic scattering [4]. It may be described as the total of elastic scattering, inelastic scattering, and transfer reaction. It is very similar to the fusion process which is defined as a reaction in which two discrete nuclei combine to produce a compound system [5]. Heavy-ion collisions at energies around the Coulomb barrier are strongly affected by the internal structure of colliding nuclei [6]. The coupling channel model is the best instrument for simultaneously reproducing the experimental data for a variety of events, including particle transfers, fusion, elastic and inelastic scattering [7]. The inter-nuclear potential is the most crucial factor in calculations involving coupled channels. Since it has an impact on the coupling strengths and the breadth of the barrier. The transfer reactions, as well as the collective vibrational and rotational movements, are coupled with the relative motion of the colliding nuclei to produce the channel coupling [8]. A heavy-ion reaction to fusion has a counterpart in quasi-elastic heavy-ion scattering at reverse angles. At energies near to the Coulomb barrier, these inclusive procedures are vulnerable to channel coupling effects (due to collective inelastic excitations of the colliding nuclei). The likelihood of reflection at the Coulomb barrier causes quasi-elastic scattering, whereas transmission is connected to fusion. This fact was exploited, and barrier distributions were obtained [9]. Fusion is one of the most significant near-barrier processes. The interaction between the relative velocity of two colliding nuclei and their internal structures is well known to result in a significant increase in fusion cross sections at sub-barrier energy [1]. Several studies on quasi elastic scattering have been studied by Khalid S. Jassim for some heavy ions systems [10-12].

The aim of this research study is to study quasi elastic scattering at near energies from high the coulomb potential barrier to determine the surface diffuseness parameters of the inter-nucleus potential for the systems ^{25}Mg+^{90}Zr and (^{28}Si, ^{120}Sn)+^{150}Nd single and coupled channels calculations were performed using the CQEL program [7], which includes all orders of coupling and is the most recent iteration of the computer code CCFULL.

The chi square (χ^2) approach has been used to find the diffuseness parameters' best fitted values in comparison to the experimental data.

2. THEORY

The potential between two nuclei consists of two parts, the first part being the nuclear potential Vn, which may be adequately and reasonably characterized by the two parts that make up the nucleus-nucleus potential. The Woods-Saxon (WS) form provided by [12].

$$V_N(r) = -\frac{V_\circ}{1+e^{\left[\frac{r-R_\circ}{a}\right]}}, \tag{1}$$

where r is the center-of-mass separation between the target nucleus of mass number A_T and the projectile nucleus of mass number A_P, and R_0 denotes the system's radius $R_0 = r_0\left(A_T^{\frac{1}{3}} + A_P^{\frac{1}{3}}\right)$. When they do not interact, the second part being the Coulomb potential V_C between two spherical nuclei with uniform charge density distributions is given by [12]:

$$V_c(r) = \frac{Z_P Z_T\, e^2}{r}, \tag{2}$$

here **r** is the distance between the centers of mass of the colliding nuclei and Z_p and Z_T are the atomic numbers of the projectile and target, respectively.

The Coulomb potential is produced when the nuclei interact, and it is determined by[13].

$$V_c(r) = \frac{Z_P Z_T\, e^2}{2R_C}\left[3 - \left(\frac{r}{R_c}\right)^2\right], \tag{3}$$

where R_c is the radius of the equivalent sphere, which corresponds to the projectile and target nuclei.

The coupling between the nuclear intrinsic motion and the relative motion of the centers of mass of the colliding nuclei, r = (r, r), which causes the collision of two nuclei. The Hamiltonian system's is provided by [4] :

$$H(\vec{r}.\xi) = -\frac{\hbar^2}{2\mu}\nabla^2 + V(r) + H_0(\xi) + V_{coup}(\vec{r}.\xi), \tag{4}$$

where V (r) is the bare potential in the absence of coupling where V(r)= V N (r)+V c (r) , $H_0(\xi)$ is the Hamiltonian for the intrinsic motion, and Ccoup is the stated coupling, r stands for the center of mass distance between the colliding nuclei.

The entire wave function's Schrodinger equation is given by[14].

$$\left(-\frac{\hbar^2}{2\mu}\nabla^2 + V(r) + H_0(\xi) + V_{coup}(\vec{r}.\xi)\right)\psi(\vec{r}.\xi) = E\psi(\vec{r}.\xi), \tag{5}$$

Generally, the internal degree of freedom has a limited spin. The coupling Hamiltonian in complexities can be written as [4] :

$$V_{coup}(\vec{r}.\xi) = \sum_{\lambda>0,\mu} f_\lambda(r) Y_{\lambda\mu}(\hat{r}).\mathrm{T}_{\lambda\mu}(\xi), \tag{6}$$

The spherical harmonics and spherical tensors, which are constructed from the internal coordinate, are denoted by $Y_{\lambda\mu}(\hat{r})$ and $\mathrm{T}_{\lambda\mu}(\xi)$, respectively. That when it was taken into account in V (r), the total is taken over all values of excluding for λ = 0. (r). For a constant total angular momentum J and its z-component M, the expansion basis for the wave function in Eq. (5) is given by [4] :

$$\langle \vec{r}\,\xi|(nlI)JM\rangle = \sum_{m_l m_I}\langle lm_l\, Im_I|JM\rangle Y_{lm_l}(\hat{r})\, \varphi_{nIm_I}(\xi), \tag{7}$$

where in l denotes the orbital, I denotes internal angular momenta, and $\varphi_{nIm_I}(\xi)$ denotes the wave function for the internal motion that which fulfills by equation below[4] :

$$H_0(\xi)\,\varphi_{nIm_I}(\xi) = \epsilon_n\,\varphi_{nIm_I}(\xi), \tag{8}$$

With this basis, the total wave function $\psi(\vec{r}.\xi)$ has been expansion as [15]:

$$\psi(\vec{r}.\xi) = \sum_{n.l.I}\frac{u_{nlI}^J(r)}{r}\langle \vec{r}\,\xi|(nlI)JM\rangle, \tag{9}$$

It is possible to write the Schrödinger equation [Eq. (3)] as a group of coupled equations for $u_{nlI}^J(r)$ [14] :

$$\left[-\frac{\hbar^2}{2\mu}\frac{d^2}{dr^2} + V(r) + \frac{l(l+1)\hbar^2}{2\mu r^2} - E + \epsilon_n\right]u_{nlI}^J(r) + \sum_{\acute{n}.\acute{l}.\acute{I}}V_{nlJ;\acute{n}.\acute{l}.\acute{I}}^J(r)u_{\acute{n}.\acute{l}.\acute{I}}^J(r) = 0, \tag{10}$$

The coupling matrix elements $V_{nlJ;\acute{n}.\acute{l}.\acute{I}}^J(r)$, According to [4] are as follows:

$$V_{nlJ;\acute{n}.\acute{l}.\acute{I}}^J(r) = \langle JM\,(nlI)|V_{coup}(\vec{r}.\xi)|(\acute{n}.\acute{l}.\acute{I})JM\rangle = \sum_\lambda(-1)^{I-\acute{I}+\acute{l}+J}f_\lambda(r)\langle l||Y_\lambda||\acute{l}\rangle\langle nI||T_\lambda||\acute{n}\acute{I}\rangle \times$$
$$\sqrt{(2l+1)(2I+1)}\begin{Bmatrix}\acute{I} & \acute{l} & J\\ l & I & \lambda\end{Bmatrix}, \tag{11}$$

Where the reduced matrix elements in Eq. (8) is defined as follows [4]:

$$\langle l_{ml}|Y_{\lambda\mu}|l'_{ml'}\rangle = \langle l'_{ml'}\,\lambda\mu|l_{ml}\rangle\,\langle l||Y_\lambda||l'\rangle, \tag{12}$$

where $V^J_{nlJ;\acute{n}.l'.\acute{l}}(r)$ are separate of the index M, the index has been suppressed as seen in Eq. (11). Coupled-channels equations are the name given to the equation (10). For heavy-ion fusion reactions, these equations are usually solved using the incoming wave boundary conditions[14].

$$u^J_{nlI}(r) \sim \mathcal{T}^J_{nlI}\,exp\left(-1\int_{r_{abs}}^r k_{nlI}(\acute{r})d\acute{r}\right).r \leqslant r_{abs}, \tag{13}$$

$$\frac{i}{2}\left(H_l^{(-)}(k_{nIr})\delta_{n,n_i}\delta_{l,l_i}\delta_{I,I_i} + \sqrt{\frac{k_{nIi}}{k_{nI}}}\,S^J_{lI}H_l^{(+)}(k_{nIr})\right),r \longrightarrow \infty, \tag{14}$$

where $k_{nIr} = \sqrt{2\mu(E-\epsilon_{nI})/\hbar^2}$, $k_{nIi} = k = \sqrt{2\mu E/\hbar^2}$ and the following formula defines the local wave number k_{nlI}:

$$k_{nlI}(r) = \sqrt{\frac{2\mu}{\hbar^2}\left(E-\epsilon_{nI}-\frac{l(l+1)\hbar^2}{2\mu r^2}-V(r)-V^J_{nlJ;nlJ}(r)\right)}, \tag{15}$$

After obtaining the transmission coefficients T nlIJ, the penetrability via the Coulomb barrier is given by:

$$P^J_{l_iI_i}(E) = \sum_{n.l.I}\frac{k_{nlI}(r_{abs})}{k}|\mathcal{T}^J_{nlI}|^2, \tag{16}$$

The computation of quasi-elastic cross sections typically needs a high value of angular momentum in order to provide convergent results, unlike the calculation of fusion cross sections. For such a huge angular momentum, the potential pocket at (r = rabs) becomes shallow or even vanishes. Therefore, it is impossible to precisely identify the incoming flux in Eq. (13). In order to avoid employing the incoming wave boundary conditions, the quasi-elastic problem often executes the regular boundary conditions at the origin. A complex potential V N (r)= V N$_0$ (r)+iw(r) is required to model the fusion reaction when utilizing the usual boundary conditions. Following the acquisition of the nuclear S-matrix in Equation (Eq11), the scattering amplitude may be computed as

$$f^J_{lI}(\theta.E) = i\sum_{Jl}\sqrt{\frac{\pi}{kk_{nI}}}i^{J-l}\,e^{i[\sigma_J(E)+\sigma_l(E-\epsilon_{nI})]}\sqrt{2J+1}\,Y_{l0}(\theta)\left(S^J_u-\delta_{I.I_2}\delta_{l.l_2}\right)+f_c(\theta.E)\delta_{I.I_2}\delta_{l.l_2} \tag{17}$$

The Coulomb phase shift is σ_l.and given by the equation,

$$\sigma_l = |\Gamma(l+1+i\eta)|, \tag{18}$$

As for f_c, which is the Coulomb scattering amplitude and is determined by [14]:

$$f_c(\theta.E) = \frac{\eta}{2k\sin^2\left(\frac{\theta}{2}\right)}e^{\left[-i\eta\ln\left(\sin^2\left(\frac{\theta}{2}\right)\right)+2i\sigma_0(E)\right]}, \tag{19}$$

here η = is the Sommerfeld parameter which is given by $\eta = Z_1Z_2\,e^2/\hbar v$, and utilizing Equation (16), the differential cross section may be evaluated

$$\frac{d\sigma_{qel}(\theta.E)}{d\Omega} = \sum_{JlI}\frac{k_{nI}}{k}|f^J_{lI}(\theta.E)|^2, \tag{20}$$

may be evaluate the Rutherford cross section.

$$\frac{d\sigma_R(\theta.E)}{d\Omega} = |f_c(\theta.E)|^2 = \frac{\eta^2}{4k^2}csc^4\left(\frac{\theta}{2}\right), \tag{21}$$

The distribution of the barrier of fusion is defined as [4] :

$$D_{fus}(E) = \frac{d^2}{dE^2}\left[E\,\sigma_{fus}(E)\right], \tag{22}$$

The definition of the total scattering distribution of the barrier of scattering D $_{tot}$ (E) is [4]:

$$D_{tot}(E) = -\frac{d}{dE}\left[\frac{d\sigma_{tot}}{d\sigma_R}(E)\right], \tag{23}$$

3. RESULTS AND DISCUSSION

Calculations for single-channel and coupled channels were performed using the CQEL code last version [7], which is thought to be the most recent iteration of the computer code CCFULL . This program precisely resolves the linked equations and the Schrödinger equation. The chi square methods have been used in the present work to prevent systematic mistakes, where the data with dqel /dR>1 were omitted from the fitting procedures. The chi square technique χ^2 was regarded as a normalizing factor between the theoretical calculation and the experimental data. the main potential in this work is Wood-Saxon (WS), which has both real and fictitious components. The fairly tiny internal potential was explained by the fictitious potential. A change has been made to done on the real potential's parameters to determine how best to fit the experimental data, and it was then repeated for all interactions. The value of 0.63 is

considered a constant for the diffuseness parameter [15], and a higher and lower value is taken for each system, It differs from one system to another and the radius parameter is assumed to be r_0 1.2 fm.

4-1. The ^{24}Mg + ^{90}Zr reaction

In this system, the results were processed in two cases, the first case, where both the projectile and target nuclei were considered inert (SC) at different values of the diffusion parameter (0.69, 0.63, and 0.57) fm, respectively and we considered the diffusion parameter 0.63 fm is the standard value. In the second case, the projectile nucleus was ^{24}Mg rotates with a deformation coefficient of $\beta_2 = 0.374$ to the state 2^+ (1.368672 MeV) and this was deduced according to the ratio $E_{4+}/E_{2+} = 3.012$ while the target core ^{90}Zr was vibrating with a deformation coefficient of $\beta_2 = 0.089$ to the state 2^+ (2.186273 MeV), where $E_{4+}/E_{2+} = 1.4$ at coupled-channel (CC). We used the single phonon state of the quadrupole excitation of the projectile and target nuclei, the potential depth $V_0 = 58.8$ MeV, and the radius parameter $r_0 = 1.2$ fm.

Table 1. The values of the **WS** potential's parameters and χ^2 fitting between experimental and theoretical data for the ^{24}Mg + ^{90}Zr reaction.

System	Channel	V_0 (MeV)	r_0 (fm)	a_0 (fm)	θ_{cm} (deg.)	χ^2	
						σ_{qel}/σ_R	D_{qel}
^{24}Mg + ^{90}Zr	SC	58.8	1.2	0.57	158	0 .28177	0.07342
				0.63		3.47134	0.33499
				0.69		12.68139	0.88261
	CC	58.8	1.2	0.57	158	0.01071	0.04572
				0.63		0.02178	0.02036
				0.69		0.07305	0.02015

From Table (1), it is shown that, according to the results of the χ^2, the calculated ratio of the quasi-elastic to the Rutherford cross sections $\left(\frac{d\sigma_{qel}}{d\sigma_R} \right)$ is 0.28177 at the diffuseness parameter 0.57 fm, $V_0 = 58.8$ MeV, which was obtained from the SC data analysis where the projectile ^{24}Mg nucleus and target ^{90}Zr nucleus are inert and is represented by the hard red line in Fig. 1.a. (A),
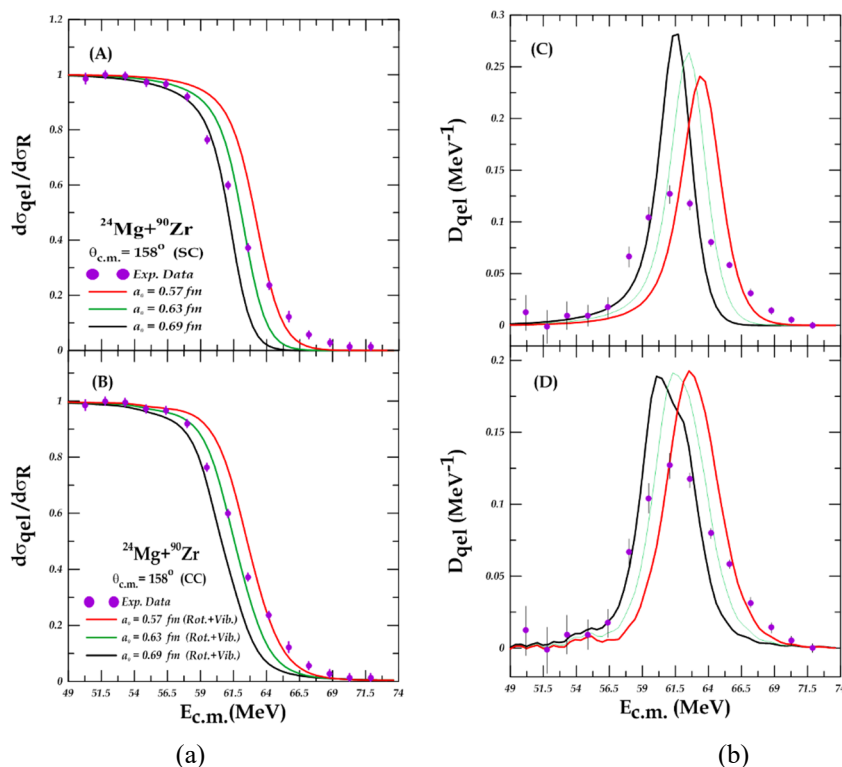
Figure 1.a. The ratio of the quasi-elastic scattering to the Rutherford cross sections for ^{25}Mg+^{90}Zr system at sub-barrier energies. Banal A and B using the single channel and coupled-channels calculations, respectively. **Figure 1.b.** (C, D) shows the distribution at sub-barrier energies, using the single and coupled channels calculations, respectively. The experimental data are taken from Ref [16].

It is the curve closest to the curve of the experimental data; the best value of the distribution D is 0.33499 at the same value of a_0 which is represented by the black colored. According to the coupled-channel calculation with a rotating projectile (P) and a vibrating target (T), the best value of $\left(\frac{d\sigma_{qel}}{d\sigma_R} \right)$ is 0.01071 at the diffuseness parameter $a_0 = 0.57$ fm is represented by the hard red line in Fig. 1.b (B). From the Fig. 1.b. (C) the best value of the distribution D is 0.015 at the diffuseness parameter of 0.69 fm, which is represented by the black colored.
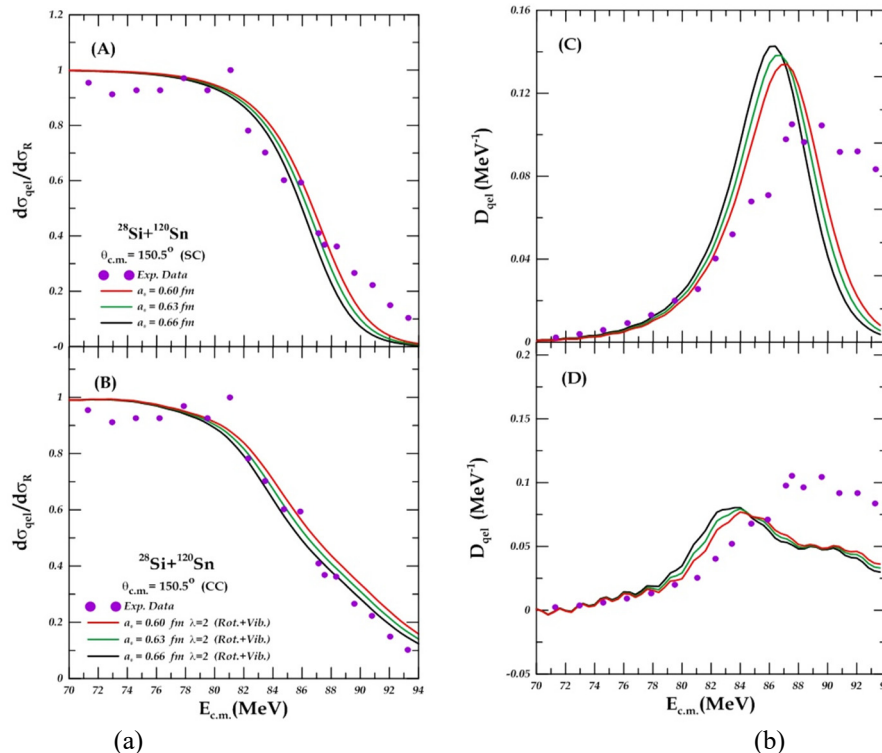
4-2. The ^{28}Si+^{120}Sn system

From Throughout this system, the findings were processed in two distinct ways. In the first case, we assumed that the diffusion parameter 0.63fm was the standard value and that both the projectile and target nuclei were inert (SC) at various values (0.60, 0.63, and 0.66) fm respectively. In the second instance, the target core ^{120}Sn was vibration with a deformation coefficient of $\beta_2 = 0.107$ to the state 2^+(1.171265 Mev), $E_{4^+}/E_{2^+} = 1.8$ at coupled-channel (CC), whereas the projectile nucleus was ^{28}Si rotation with a deformation coefficient of $\beta_2 = -0.478$ to the state 2^+(1.77903 MeV), where $E_{4^+}/E_{2^+} = 2.59$. The potential depth V$_0$= 45.8 MeV, the radius parameter r$_0$ =1.2 fm, and the single phonon state of the quadruple excitation of the projectile and target nuclei were employed.

Table 2. The values of the **WS** potential's parameters and χ^2 fitting between experimental and theoretical data for the ^{28}Si+^{120}Sn reaction

System	Channel	V_0 (MeV)	r_0 (fm)	a_0 (fm)	θ_{cm} (deg.)	χ^2	
						σ_{qel}/σ_R	D_{qel}
^{28}Si+^{120}Sn	SC	45.8	1.2	0.60	150.5	0.06072	0.03304
				0.63		0.10359	0.05258
				0.66		0.17721	0.08379
	CC	45.8	1.2	0.60	150.5	0.01259	0.01686
				0.63		0.00794	0.01954
				0.66		0.00475	0.02127

According to Table (2), the results of χ^2 show that the calculated ratio of the quasi-elastic to the Rutherford cross sections $\left(\frac{d\sigma_{qel}}{d\sigma_R}\right)$ is 0.06072 at the diffuseness parameter of 0.60 fm, which was obtained from single channel (SC) data analysis where the projectile ^{28}Si nucleus and target ^{120}Sn nucleus are inert, and is represented by the hard red line in Fig. 2.a. (A) It is the curve that is closest to the experimental data curve; the best value for the distribution D is 0.03304, which is represented by the hard red line in Fig. 2.b. while the coupled-channel calculations with a rotating projectile (P) and vibrating target (T), it was found that the best value of $\left(\frac{d\sigma_{qel}}{d\sigma_R}\right)$ is 0.00475 at the diffuseness parameter 0.66 fm, which is represented by the solid black line in Fig. 2.b. (B), where V$_0$ = 45.8 MeV. It is the curve closest to the curve of the experimental data, the best value for the distribution D is 0.01686 at the diffuseness parameter 0.60 fm denoted by the red-colored curve.

Figure 2.a. The ratio of the quasi-elastic scattering to the Rutherford cross sections for ^{28}Si+^{120}Sn system at sub-barrier energies. Banal A and B using the single channel and coupled-channels calculations, respectively. **Figure 2.b.** (C, D) shows the distribution at sub-barrier energies, using the single and coupled channels calculations, respectively. The experimental data are taken from ref [17].

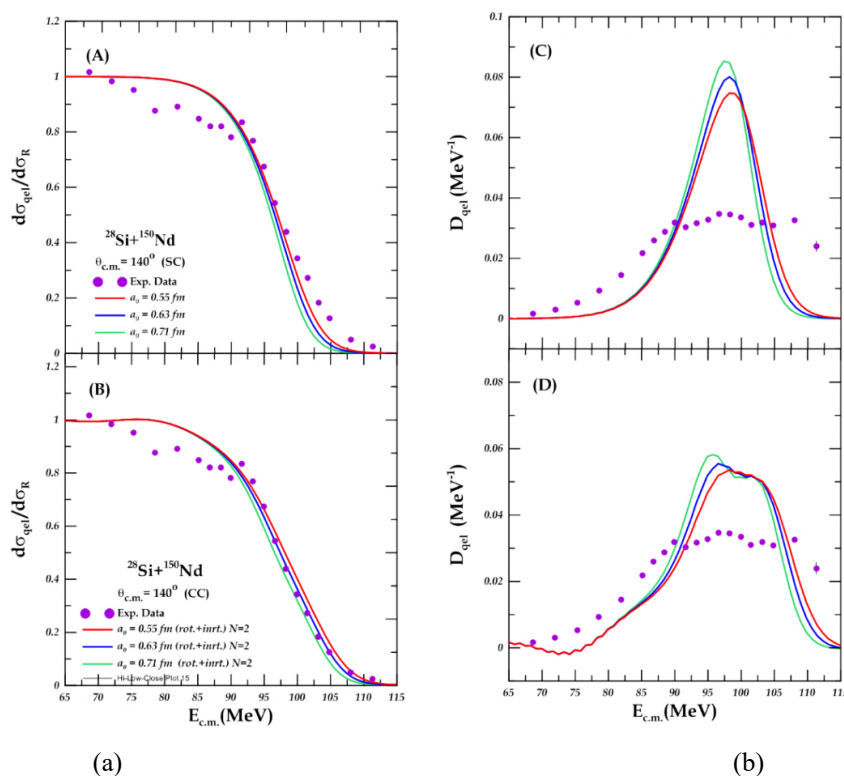### 4-3. The ^{28}Si+^{150}Nd system

In this system, the change of quasi elastic scattering with the angle was studied, depending on the change in the values of the diffusion parameter, and the study was carried out in two cases, in the first case The projectile and target

nuclei were each considered to be inert, single channel (SC) at different values from diffuseness parameter (0.55, 0.63, and 0.71) fm, and 0.63fm was taken to be the standard value. in the second case, we assumed that the projectile nucleus ^{28}Si is rotation coupled to the state 2^+(1.77903 MeV), $E_{4+}/E_{2+} = 2.59$ with deformation parameter $\beta_2 = -0.478$ where the target nucleus ^{150}Nd was inert. The potential depth $V_0 = 42.2$ MeV, the radius parameter $r_0 = 1.2$ fm, and the single phonon state of the quadrupole excitation to the projectile nuclei were employed.

Table 3. The values of the **WS** potential's parameters and χ^2 fitting between experimental and theoretical data for the **^{28}Si**+**^{150}Nd** reaction

System	Channel	V_0 (MeV)	r_0 (fm)	a_0 (fm)	θ_{cm} (deg.)	χ^2	
						σ_{qel}/σ_R	D_{qel}
^{28}Si+^{150}Nd	SC	42.2	1.2	0.55	140	0.01936	0.03100
				0.63		0.05279	0.05130
				0.71		0.17076	0.10976
	CC	42.2	1.2	0.55	140	0.00843	*0.00880*
				0.63		*0.00597*	0.01078
				0.71		0.00828	0.01623

In Table (3), According to the results of the χ^2 data, the red line in Fig. 3.a. (A) represents the calculated ratio of the quasi-elastic to the Rutherford cross sections $\left(\frac{d\sigma_{qel}}{d\sigma_R}\right)$, which is 0.01936 at the diffuseness parameter *0.55* fm, $V_0 = 42.2$ MeV obtained from single channel (SC) data analysis with the projectile ^{28}Si nucleus and target ^{150}Nd nucleus being inert.

Figure 3.a. The ratio of the quasi-elastic scattering to the Rutherford cross sections for ^{28}Si+^{150}Nd system at sub-barrier energies. Banal A and B using the single channel and coupled-channels calculations, respectively. **Figure 3.b.** (C, D) shows the distribution at sub-barrier energies, using the single and coupled channels calculations, respectively. The experimental data are taken from ref [18].

It is the curve that is most nearby to the curve of the experimental data. The optimum value for the distribution D is *0.03100*, shown by the hard red line in Fig. 3.b. (C) at the same diffuseness parameter value. According to the coupled-channel calculations with a rotating projectile (P) and inert target (T), it was found that the best value of $\left(\frac{d\sigma_{qel}}{d\sigma_R}\right)$ is *0.00597* at the diffuseness parameter a_0 of *0.63* fm, which is represented by the hard blue line in Fig. 3.b. (B). It is the curve closest to the curve of the experimental data, the best value of the distribution D is *0.00880* at the diffuseness parameter of *0.55* fm denoted by the red-colored curve.

5. CONCLUSIONS

We conclude from this study the following:

1- The standard value of the diffuseness parameter a_0 is not the only one that shows the best match between the theoretical calculations and the practical values, but it is possible to take lower and higher values than the standard value of the diffuseness parameter by 9, and thus we were able to obtain the best match within this range of values.

2- From the calculations of (CC) we notice that it has a significant impact on improving quasi elastic scattering calculations ($\frac{d\sigma_{qel}}{d\sigma_R}$) ,and this was clearly shown on the results of (χ^2) regardless of the value of a_0.

3- We notice in the calculations of (SC) that the theoretical calculations coincide with the practical values at the value of a_0 which is less than the standard diffusion parameter, because the larger the value of the diffuseness parameter, the greater the diffusion of nuclear potential. In addition, the potential barrier in the (SC) is single, while in (CC) calculations it is multiple.

ORCID IDs

◉**Khalid S. Jassim,** https://orcid.org/0000-0002-5990-3277

REFERENCES

[1] M. Dasgupta, D.J. Hinde, N. Rowley, and A. M. Stefanini, "Measuring Barriers To Fusion," Annual Review of Nuclear and Particle Science, **48**, 401-461 (1998). https://doi.org/10.1146/annurev.nucl.48.1.401

[2] V.Y. Denisov, "Superheavy element production, nucleus-nucleus potential and μ-catalysis," in AIP Conference Proceedings, **704**(1), 92-101 (2004). https://doi.org/10.1063/1.1737100

[3] L.R. Gasques, M. Evers, D.J. Hinde, M. Dasgupta, P.R.S. Gomes, R.M. Anjos, M.L. Brown, *et al.*, "Systematic study of the nuclear potential through high precision back-angle quasi-elastic scattering measurements," Phys. Rev. C - Nucl. Phys. **76**(2), 024612 (2007). https://doi.org/10.1103/PhysRevC.76.024612

[4] K. Hagino, and N. Rowley, "Large-angle scattering and quasielastic barrier distributions," Phys. Rev. C, 69(5), 054610 (2004). https://doi.org/10.1103/PhysRevC.69.054610

[5] M. Zamrun, K. Hagino, S. Mitsuoka, and H. Ikezoe, "Coupled-channels analyses for large-angle quasi-elastic scattering in massive systems," Phys. Rev. C, **77**(3), 034604 (2008). https://doi.org/10.1103/PhysRevC.77.034604

[6] A.B. Balantekin, and N. Takigawa "Quantum Tunneling in Nuclear Fusion," Rev. Mod. Phys. **70**, 77 (1998). https://doi.org/10.1103/RevModPhys.70.77

[7] K. Hagino, N. Rowley, and A.T. Kruppa, "A program for coupled-channel calculations with all order couplings for heavy-ion fusion reactions," Comput. Phys. Commun. **123**(1-3), 143-152 (1999). https://doi.org/10.1016/S0010-4655(99)00243-X

[8] K. Washiyama, K. Hagino, and M. Dasgupta, "Probing surface diffuseness of nucleus-nucleus potential with quasielastic scattering at deep sub-barrier energies," Phys. Rev. C, **73**, 034607 (2006). https://doi.org/10.1103/PhysRevC.73.034607

[9] K. Hagino, and K. Washiyama, "Probing internucleus potential with large-angle quasi-elastic scattering," AIP Conference Proceedings, **853**, 86-93 (2006). https://doi.org/10.1063/1.2338360

[10] Q.J. Tarbool, K.S. Jassim, and A.A. Abojassim, "Surface diffuseness parameter with quasi-elastic scattering for some heavy-ion systems," Int. J. Nucl. Energy Sci. Technol. **13**(2), 110-119 (2019). https://www.inderscience.com/info/inarticle.php?artid=100758

[11] N.H. Hayef, and K.S. Jassim, "Coupled channels for quasi-elastic scattering of determining diffuseness parameters in Woods-Saxon potential for nuclear reaction," AIP Conference Proceedings, **2414**(1), 030012 (2023). https://doi.org/10.1063/5.0117002

[12] A.J. Hassan, and K.S. Jassim, "Effect of Surface Diffuseness Parameter on Quasi-elastic Scattering Calculations for ^{6}He+^{64}Zn, ^{7}Li+^{64}Zn and ^{8}Li+^{90}Zr Systems," NeuroQuantology, **18**(9), 40-44 (2020). https://doi.org/10.14704/nq.2020.18.9.NQ20214

[13] R.D. Woods, and D.S. Saxon, "Diffuse surface optical model for nucleon-nuclei scattering," Phys. Rev. **95**(2), 577 (1954). https://doi.org/10.1103/PhysRev.95.577

[14] P. Fröbrich, and R. Lipperheide, *Theory of nuclear reactions*, Vol. 18, 1st ed. (Clarendon Press, Oxford Studies, 1996). pp. 18.

[15] M. Dasgupta, D.J. Hinde, J.O. Newton, and K. Hagino, "The nuclear potential in heavy-ion fusion," Prog. Theor. Phys. Suppl. **154**, 209-216 (2004). https://doi.org/10.1143/PTPS.154.209

[16] R.A. Broglia, and A. Winther, *Heavy Ion Reactions: Elastic and inelastic reactions*, (Advanced B. Cummings Publishing Company, 1981).

[17] Y.K. Gupta, B.K. Nayak, U. Garg, K. Hagino, K.B. Howard, N. Sensharma, M. Şenyiğit, *et al.*, "Determination of hexadecapole (β4) deformation of the light-mass nucleus ^{24}Mg using quasi-elastic scattering measurements," Phys. Lett. Sect. B Nucl. Elem. Part. High-Energy Phys. **806**, 135473 (2020). https://doi.org/10.1016/j.physletb.2020.135473

[18] M. Sharma, A. Rani, S. Manda, S. Nath, N. Madhavan, J. Gehlot, Gonika, *et al.*, "Quasi-Elastic Scattering Measurements for ^{28}Si+^{116,120,124}Sn Systems near Coulomb Barrier," Proceedings of the DAE Symp. on Nucl. Phys. **65**, 433-434 (2021). https://inspirehep.net/files/f1ec2021066b5c813665ad770c13244c

[19] S. Biswas, A. Chakraborty, A. Jhingan, D. Arora, B.R. Behera, R. Biswas, N.K. Deb, *et al.*, "Barrier distribution for the ^{28}Si+^{150}Nd system through quasi-elastic excitation function measurement," DAE Symp. Nucl. Phys. **64**, 439-440 (2019). https://inspirehep.net/literature/1803955

ВПЛИВ ПАРАМЕТРУ ДИФУЗНОСТІ НА КВАЗІПРУЖНЕ РОЗСІЮВАННЯ СИСТЕМ
^{25}Mg+^{90}Zr та ^{28}Si+(^{120}Sn, ^{150}Nd) З ВИКОРИСТАННЯМ ПОТЕНЦІАЛУ ВУДА-САКСОНА
Фарах Дж. Хамуд, Халід С. Джасім
Факультет фізики, Освітній коледж чистих наук, Вавилонський університет, Ірак

Було вивчено вплив зміни значень параметра дифузії на розрахунки напівпружного розсіювання (*dσqel*)/*dσR*) і розподілу (D) для одного каналу (SC) і зв'язаного каналу (CC). Три значення були взяті з дифузії для кожного параметра системи. Передбачається, що ядерний потенціал має форму Вудса-Саксона, на яку вказують поверхнева дифузність, глибина потенціалу та параметри радіуса для систем (^{25}Mg +^{90}Zr), (^{28}Si+(^{120}Sn, ^{150}Nd). Хі-квадрат (χ2) застосовується для порівняння найкраще підігнаного значення параметра дифузності між теоретичними розрахунками та експериментальними даними. Згідно з результатами (χ2), ми зазначаємо, що деякі системи досягли гарної відповідності між теоретичними розрахунками та експериментальними даними напівпружнього розсіювання (*dσqel*)/*dσR*) і розрахунками розподілу при стандартному значенні параметра дифузії (a$_0$=0,63) або при значенні вище або нижче стандартного значення. У випадку (SC) найкраще відповідність було при меншому, ніж стандартне значення параметра дифузії, але у випадку (CC) відповідність була кращою при значенні, вищому за стандартне значення параметра дифузії, оскільки потенційний бар'єр у (SC) одинарний, тоді як у (CC) розрахунки кратні.

Ключові слова: *квазіпружне розсіювання; потенціал Вудса-Саксонса; один канал; сполучені канали; поверхневий параметр дифузності; система важких іонів*